Modeling of Polymer Electrolyte Membrane devices for hydrogen energy carrier

Maha Rhandi

THÈSE

Pour obtenir le grade de

DOCTEUR DE L'UNIVERSITÉ GRENOBLE ALPES

Spécialité : MEP : Mécanique des fluides Energétique, Procédés.

Arrêté ministériel : 25 mai 2016.

Présentée par :

Maha RHANDI

Thèse dirigée par **Florence Druart**, Maître de conférences, Grenoble-INP, Université Grenoble Alpes.
et codirigée par **Jonathan Deseure**, Maitre de Conférences, Université Grenoble Alpes.

Préparée au sein du **Laboratoire d'Electrochimie et de Physico-Chimie des Matériaux et des Interfaces,**
dans **l'École Doctorale I-MEP2 - Ingénierie - Matériaux, Mécanique, Environnement, Energétique, Procédés, Production.**

Modélisation de procédés électrochimiques de type PEM (Proton Electrolyte Membrane) pour le développement du vecteur Hydrogène.

Modeling of Polymer Electrolyte Membrane Devices for Hydrogen Energy Carrier

Thèse soutenue publiquement le **22 Janvier 2021**,
devant le jury composé de :

Madame Florence Druart
MAITRE DE CONFERENCE, Grenoble-INP, LEPMI, Directrice de thèse.
Monsieur Gaël Maranzana
PROFESSEUR, Université de Lorraine, LEMTA, Rapporteur.
Madame Nadia Yousfi Steiner
PROFESSEUR, Université de Franche-Comté, FEMTO-ST, Rapportrice.
Madame Delphine Riu
PROFESSEUR, Grenoble-INP, G2Elab, Présidente du jury.
Monsieur Christophe Turpin
DIRECTEUR DE RECHERCHE, CNRS, LAPLACE, Examinateur.
Monsieur Jonathan Deseure
MAITRE DE CONFERENCE, Université Grenoble Alpes, LEPMI, Co-directeur de thèse.

UNIVERSITE GRENOBLE ALPES

Laboratoire de rattachement : LEPMI

THÈSE
Pour obtenir le grade de
DOCTEUR DE LA COMMUNAUTE UNIVERSITE GRENOBLE ALPES

Spécialité : MEP : Mécanique des fluides Energétique, Procédés

Présentée et soutenue publiquement
Le 22 Janvier 2021 par

Maha RHANDI

Modeling of Polymer Electrolyte Membrane Devices for Hydrogen Energy Carrier

Sous la direction de Dr. Florence Druart & Dr. Jonathan Deseure.

Acknowledgements

The past three years have been one of the most challenging years of my life, specially the writing process. I had to question everything starting from my work to the essence of my being. But I guess it is a path that many took before me and it is an honor for my person to have been allowed this opportunity.

I would like to express my sincere appreciation to Pr. Maranzana Gaël and Pr. Yousfi Steiner Nadia for becoming the reviewers of my thesis. I would like to express my acknowledgement also to Pr. Riu Delphine and Dr. Turpin Christophe (Directeur de Recherche) for their participation in the jury.

I am incredibly grateful to Dr. Druart Florence and Dr. Deseure Jonathan for supervising my research work and helping me every step of the way on this amazing journey. I want to thank you not only for the knowledge you have passed me but also for being there when I needed help. I will be forever grateful to everything you have done for me.

I would like to express my deepest acknowledgements to Pr. Bessarabov Dmitri for giving me the opportunity to do an internship at his lab HySa Infrastructure, Potchefstroom, South Africa. I would like to also thank his team: Leandri, Boitumelo, Carel, Faan, Cédric, Alex, Alina, Faan, and Nicolaas who have been so helpful and kind to me. This trip has made me also meet the best people I met in years not only at the hySa lab, but also at the E13 residence. Ellen, Jordan, Izzy, Christoph, Oskar, Nicolo and all the others. A specific thank you to this people who have pulled me out of my routine and reminded me that amazing people still exist.

A special appreciation and acknowledgements to my two-favorite people in the LEPMI, François and Killian, I cannot even begin to express the role you have played in my life for the last few years. The days I have spent with you around were my favorite. Without forgetting of course Marine and Delphine who has taken the time to listen to me when I needed someone to talk to. Another special thank you to Nicolas, Olivier, Laurent, Jonathan, Lenka, Nadine and Noel for the "fun" lunch discussions we have had. I want to thank Khadidja, Parfait, Mireia and all the interns with whom I shared my office for all the joy they have brought to it. I want to express my gratitude to all the PhD students of the 3rd floor, the ones who left and the ones who

are still here, for all the fun I have had with you guys in the few times I went out with you. I should not forget to express my acknowledgments to all the LEPMI staff and researchers for their helpfulness.
I am extremely grateful to my lovely best friends, Imane, Asmae, Hugo, Salim and Yassine. The people whom I am more than honored to call my people. They were here for years before this thesis, well some of them, and they have helped me grow to the person I am today. Thank you, guys, for being so patient with my mood swings during these hard times and thank you for staying in my life despite everything I put you through lately.

Last but not least, to the people I am profoundly indebted to, my family. Thank you, Mama, for teaching how a strong smart woman should be and thank you baba for make me who I am today. I would have achieved nothing if it were not for both of you. To my younger siblings, Tapha, Chouchou and Zaidou, thank you for giving me the motivation to always be the good older sister you need and deserve (I'm not all the time but I'm trying my best). My aunts: Swalika, Amina, Mbarka, Guibel and Yaya, thank you for motivating me and loving me unconditionally all these years.

All the amazing solo trips, the hard-darkest days, the people I have lost and gained these past three years have been worth it. I am glad I choose this career path and if time goes back, I will do it all over again.

It was not easy, but it was SO worth it.

“And lower to them the wing of humbleness out of mercy and say: 'My Lord, be merciful to them, as they raised me since I was little.' (24)”

Sura AL-ISRA (ISRA') 17

وَاخْفِضْ لَهُمَا جَنَاحَ الذُّلِّ مِنَ الرَّحْمَةِ وَقُلْ رَبِّ ارْحَمْهُمَا كَمَا رَبَّيَانِي صَغِيرًا ﴿٢٤﴾

سورة الإسراء

Articles and Conference Communications During this Thesis

Articles:

- **Maha Rhandi**, Marine Trégaro, Florence Druart, Jonathan Deseure and Marian Chatenet. *Electrochemical hydrogen compression and purification versus competing technologies – Part I: pros and cons*. Chinese Journal of Catalysis 2020. DOI: S1872-2067(19)63404-2.

- Marine Trégaro, **Maha Rhandi**, Florence Druart, Jonathan Deseure and Marian Chatenet. *Electrochemical hydrogen compression and purification versus competing technologies – Part II: challenges in electrocatalysis*. Chinese Journal of Catalysis 2020. DOI: S1872-2067(19)63438-8.

- Farid AUBRAS, **Maha RHANDI***, Jonathan Deseure, Amangoua Jean-Jacques Kadjo, Miloud Bessafi, Brigitte Grondin-Perez, Florence Druart and J-P Chabriat. *Dimensionless approach of a Polymer Electrolyte Membrane Water Electrolysis: Advanced Analytical Modelling*. Journal of power sources 2021. *Corresponding author. https://doi.org/10.1016/j.jpowsour.2020.228858.

Posters:

- **National Conferences:**

    - *Study of Proton Exchange Membrane at high current density for Electrochemical Hydrogen Compressor*, poster*. Maha RHANDI*, Florence DRUART and Jonathan DESEURE, "Hydrogène, Systèmes et Piles à Combustible", Research grouping n°3652 from CNRS [GdR HySPàC]: Grenoble, France, 23-25 May 2018.

- **International Conferences:**

    - *Modelling of Electrochemical Hydrogen Pumping: fundamental 1D approach*, poster*. Maha RHANDI*, Florence DRUART and Jonathan DESEURE, 8th International Conference on Fundamentals & Development of Fuel Cells. FDFC2019, Nantes, France, from February 12th to February 14th, 2019.

    - *Electrochemical compression and separation of hydrogen mixtures*, poster*. Leandri KRIEK*, Maha RHANDI, Dmitri BESSARABOV, Carel MINNAAR, Faan DU PREEZ, Faan OELOFSE, Florence DRUART and Jonathan DESEURE, 15th HYdrogen POwer THeoretical and Engineering Solutions International Symposium. HYPOTHESIS XV, Cape Town, South Africa, from May 3rd to May 6th, 2020.

Presentations:

- **National Conferences:**

    - *Caractérisation d'une cellule d'électrolyseur à membrane échangeuse de protons : approche numérique, analytique et expérimentale*, oral*. Farid Aubras, Jean.-Jacques Amangoua Kadjo*, Maha Rhandi, Jonathan Deseure, Miloud Bessafi, Brigitte Grondin-Perez, Florence Druart, Jean-Pierre Chabriat, 5ème réunion plènières du GDR 3652 HysPàC « Hydrogène, Système et Piles à Combustible », Le Croisic, France, from June 11 th to June 13 th, 2019,

- **International Conferences:**

    - *Dimensionless approach of a pressurized proton exchange membrane water electrolysis*, oral*. Maha RHANDI*, Farid AUBRAS, Amangoua Jean-Jacques KADJO, Florence DRUART, Brigitte GRONDIN-PEREZ, Jonathan DESEURE, 12th EUROPEAN CONGRESS OF CHEMICAL ENGINEERING. ECCE12, Florence, Italy, from September 15th to September 19th, 2019.

List of symbols

Latin letters:

A	Membrane geometric area (m²)
a	Activity (-)
c	Concentration (mol.m^{-3})
c_f	Fixed charge site concentration in the membrane (mol.m^{-3})
C_{dl}	Double layer capacitance (F)
D_{H_2O}	Water Diffusion coefficient in membrane (m².s^{-1})
D_i	Diffusivity coefficient (m² s^{-1})
EA	Activation Energy (K)
E_{eq}	Equilibrium Potential (V)
EW	Equivalent weight of the PEM (kg.mol^{-1})
F	Faraday constant (C.mol^{-1})
i	Electric current density (A.m^{-2})
i_0	Exchange current density (A.m^{-2})
J	Total current density (A m^{-2})
J_0	Operating Current density (A.m^{-2})
K	Integration constant (-)
k_i	Gas permeability coefficient (mol m^{-1} s^{-1} Pa^{-1})
M	Molar mass (kg mol^{-1})
$\dot{m}$	Mass flow (kg s^{-1})
N	Molar flux (mol.m^{-2}.s^{-1})
n	Mole number (mol)
P	partial pressure (Pa)
p	total Pressure (Pa)
p_0	standard Pressure (Pa)
Q_w^{EHC}	Isothermal specific compression work (J/kg)
R	Universal gas constant (J mol^{-1} K^{-1})
R	Membrane resistance (Ω)
R_{cell}	Cell resistance (Ω cm^2)
R_f	Charge transfer resistance (Ω cm^2)
r	equations roots
t_n	Dimensionless transference coefficient ()
T	Temperature (K)
u	function used in analytical integration (Ricatti Equation)
U_{cell}	Cell voltage (V)
V_{ex}	PEM expansion coefficient (-)
v_m	Velocity inside the membrane (m s^{-1})
V_{theor}	Theoretical compression work (J/kg)
W	Theoretical power (W)
x	space coordinate in the thickness of MEA (m)
z	function used in analytical integration (Ricatti equation)
z_f	Charge of fixed sites in membrane (-)

Greek letters:

α	charge transfer coefficient (-)
β	model constant defined in (-)
γ	roughness coefficient, (m^2 .m^{-2})
ΔP	Pressure gradient (bar)
δ	thickness of the layer (m)
ζ	model constant defined (-)
η	Overpotential (V)
κ_Φ	Electrokinetic permeability (m^2)
κ_n	Molar permeability coefficient (mol s^{-1}m^1)
κ_p	Hydraulic permeability (m^2)
λ	Water content (-)
μ	Water dynamic viscosity (kg m^{-1} s^{-1})
ρ_{dry}^m	Dry density of the PEM (kg m^{-3})
σ	Conductivity (Ω^{-1} m^{-1})
Φ	Electrical potential (V)
ω	Frequency (Hz)
$\omega_{a,c}$	Wagner number (-)

Superscripts & subscripts:

a	Anode
act	Active
c	Cathode
eff	Effective
elec	Electronic
eq	Equilibrium
H	Homogeneous
H^+	Protonic
H_2	Hydrogen
H_2O	Water
m	Membrane
p	Particular
sat	Saturated
t	Total
*	Dimensionless

Acronyms:

1D	One dimension
BP	Bipolar plates
CL	Catalyst Layer
ECSA	Electrochemically Active Surface Area
EHC	Electrochemical Hydrogen Compression
EIS	Electrochemical Impedance *Spectroscopy*
FC	Fuel Cell
FITR	Fourier-transform infrared
GDL	Gas Diffusion Layer
HER	Hydrogen Evolution Reaction
HFCT	Hydrogen and Fuel Cell Technology
HOR	Hydrogen Oxidation Reaction
LHV	Lower Heating Value
MC	Mechanical Compression
MEA	Membrane Electrode Assembly
PEM	Polymer Electrolyte Membrane
PEM-E	Proton Exchange Membrane Electrolysis
PEMFC	Proton Exchange Membrane Fuel Cell
PEMWE	Polymer Electrolyte Membrane Water Electrolysis
PFSA	Perfluoro sulfonic Acid
PGM	Platinum group metal
PSA	Pressure Swing Adsorption
RH	Relative humidity
TSA	Temperature Swing Adsorption

List of figures

List of Tables

Table of contents

Introduction:

Hydrogen gas was firstly produced in 1671 by Robert Boyle. It was recognized as an element by Henry Cavendish in 1766 which he called “inflammable air” due to its high flammability. However, the name hydrogen was introduced by Antoine Laurent de Lavoisier in 1787. “hydro” is the Greek name for “water” and “genes” is for “generating”. H is the chemical symbol of hydrogen. Usually, the word hydrogen used currently refers to dihydrogen (H_2). On earth it exists hardly in pure form, hydrogen most occurs as a water or an organic compound. Thus, the production step is necessary. the need for the production [1]. Hydrogen fulfils the main characteristics to achieve the performance required for an efficient energy carrier, but its low volume density remains a weak point. A very high energy-efficient compression is a necessary step.

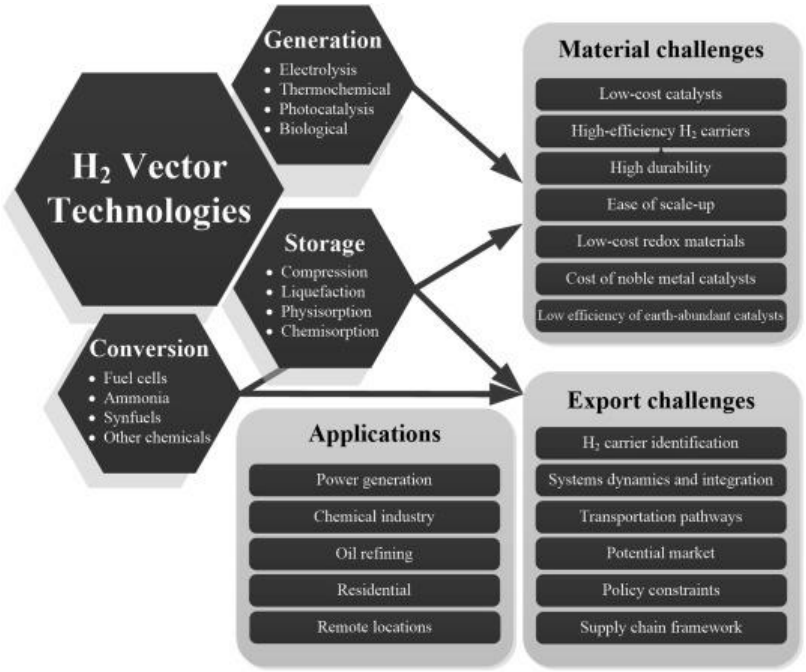

Figure 1: Challenges in hydrogen production and applications [2]

As demonstrated in Figure 1, the H_2 needs to be produced first using electrolysis (as discussed in this thesis), photo catalysis, thermochemical or biological processes. Before it is used, it must be stored, for instance by compression. Many types of compressors exist currently, such as mechanical compressors or electrochemical compressor (which is also detailed in this thesis). There is also liquefaction,

physisorption and chemisorption as other storage options. Lastly, the stored hydrogen is converted and used as a product or a reactant in an application like Fuel Cells.

The shortage of fossil fuels puts renewable energy under a lot of attention economically, scientifically, and even politically. The hydrogen energy carrier is considered as one of the key solutions of the current climate challenges. As shown Figure 2, the hydrogen demand went from less than 20Mt in 1975 to more 70Mt in 2018. It is expected to keep growing in the following years. Today's hydrogen production is still largely based on fossil fuels and can therefore not be considered pure. Thus, purification of hydrogen is mandatory, at a large scale. In addition, hydrogen being the lightest gas, its volumetric energy content is well-below its competing fuels, unless it is compressed at high pressures (typically 70 MPa = 700 bar), making compression unavoidable as well. As a result, the CO_2 emissions released for this whole process is also growing. Hence, the existing controversy about the actual impact of this component.

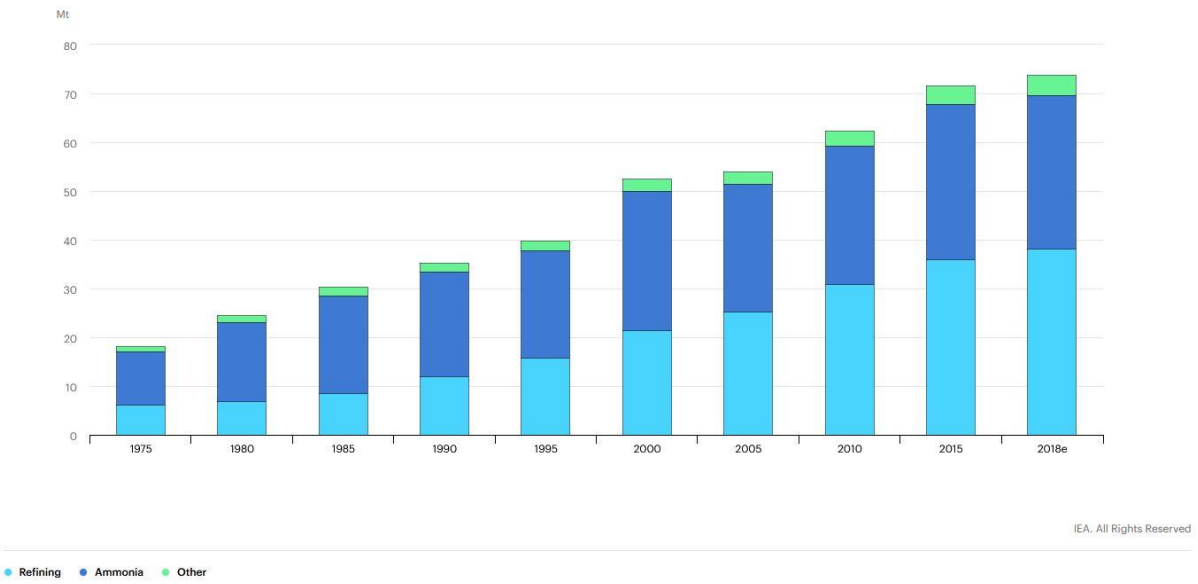

Figure 2: Global demand for pure hydrogen, 1975-2018 [3]

Currently, many roadmaps have been introduced describing the role of hydrogen within the energy sector, in the United States, European Union and Japan. Around 470 Hydrogen stations were operating internationally by the end 2019. The main three leaders currently are Japan, Germany, and the United States. 32 other countries have agreed on expanding the research and development of hydrogen energy.

As exhibited in Figure 3, the global fuel cell electric vehicle (FCEV) reserve has approximately doubled by the end of 2019 [4].

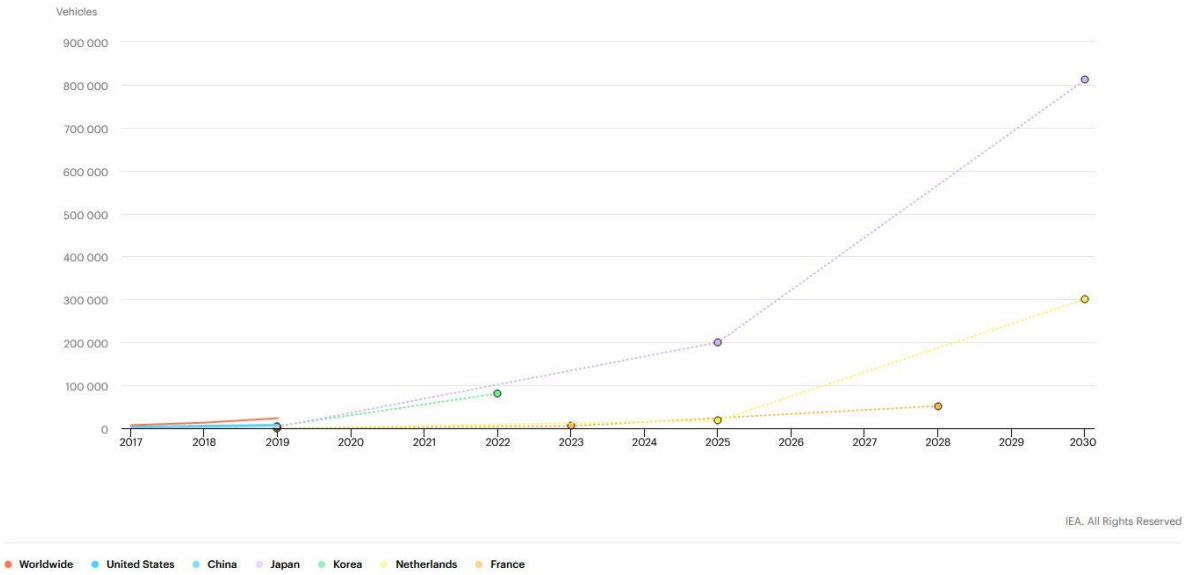

Figure 3: Fuel cell EV deployment and national targets for selected countries [4]

In the same purpose of hydrogen research many thesis and internships were launched to study the multiple aspects of this issue. Either on the different applications or the challenges that face this global target. This research dissertation addresses the modelling aspect of some of the microscopic phenomena in the Proton Electrolyte Membrane devices that produces or operates on Hydrogen. This manuscript contains a general state of art of the PEM Water Electrolysis (PEMWE) as a production and compression device, the PEM Fuel Cell (PEMFC) as an electricity generator and the Electrochemical Hydrogen Compressor (EHC) as a purification and compression device. The aim of this thesis is modeling of Polymer Electrolyte Membrane devices for hydrogen energy carrier, more precisely PEMWE and EHC.

References:

[1] Shell, “Energy of the future? Shell Hydrogen Study,” 2017. https://www.shell.com/energy-and-innovation/new-energies/hydrogen/_jcr_content/par/keybenefits_150847174/link.stream/1496312627865/6a3564d61b9aff43e087972db5212be68d1fb2e8/shell-h2-study-new.pdf.

[2] Z. Abdin, A. Zafaranloo, A. Rafiee, W. Mérida, W. Lipiński, et K. R. Khalilpour, “Hydrogen as an energy vector”, *Renew. Sustain. Energy Rev.*, vol. 120, p. 109620, mars 2020, doi: 10.1016/j.rser.2019.109620.

[3] P. IEA, “IEA, Global demand for pure hydrogen, 1975-2018”, 2018. https://www.iea.org/data-and-statistics/charts/global-demand-for-pure-hydrogen-1975-2018.

[4] P. IEA, “IEA, Fuel cell EV deployment, 2017-2019, and national targets for selected countries,” 2019. https://www.iea.org/data-and-statistics/charts/fuel-cell-ev-deployment-2017-2019-and-national-targets-for-selected-countries.

Thesis Structure

This dissertation consists of 4 chapters:

Chapter 1, State of art on Polymer Electrolyte Membrane (PEM) devices for hydrogen carrier, in context of the work, which illustrates the different PEM bases technologies and the most used currently. The chapter describes a generic basic concept of a PEM and the phenomena within the device. A portion of the review about the electrochemical hydrogen compression is included.

Chapter 2, Modeling of Polymer Electrolyte Membrane cells (steady state, DC modeling), of a preliminary study, discusses an 1D analytical steady state model taking into account mass balance, charge balance of the membrane and electrochemical kinetics of catalytic layers using dimensionless numbers.

Chapter 3, Polymer Electrolyte Membrane Cells Experimental Application: Electrochemical hydrogen compression, presents the test bench as well as the single cell used during the experimental tests. The compression was performed between 0 and 30 bars. For these experiments, using a galvanostatic procedure, temperature, relative humidity, and pressure measurement were conducted. In addition, an electrochemical impedance spectroscopy (EIS) measurement was also performed. These experiments ran on both pure hydrogen and hydrogen/nitrogen mixture.

Chapter 4, Polymer Electrolyte Membrane Cells Electrochemical Impedance Spectroscopy Modeling, describes an 1D analytical Electrochemical Impedance Spectroscopy (EIS) model describing the electrochemical kinetics of the cell. The results and validation of the model are presented.

Chapter 1: State of art on Polymer Electrolyte Membrane devices for hydrogen carrier

1. State of art on Polymer Electrolyte Membrane devices for hydrogen carrier

The COP21 in Paris demonstrated that most countries are willing to reduce their carbon footprint. One convenient manner to do so is to increase renewable energies (*e.g.* solar panel and windmills) and to store their excess production into chemicals via a power-to-gas (and in particular power-to-hydrogen) strategy by water electrolysis, so that "green" electricity can be produced on demand peaks by converting the gas (hydrogen) into electricity, for instance in fuel cells [1]. Commercial electrolysis systems have a maximum delivery pressure equal to 44.8 MPa with untreated hydrogen gas purity equal to 99.5%, excluding water vapor. The Impurity is mainly O_2 and after deoxidizer, the treated gas purity reaches 99.999% [2]. Therefore, purification is not required for water electrolysis except for O_2 and water vapor. This is the ideal scenario, and unfortunately, the present hydrogen is still not widely produced using this strategy. However, the electrolysis production capacity is still low and costs higher than traditional way of production.

Today, more than 95% of hydrogen is produced from fossils (and in a minor amount from bio-processes) and is therefore not pure [3]. Nevertheless, supplementary hydrogen sources from biomass can contribute to the penetration of renewable energies ([4], [5]), e.g. photo-biohydrogen exhibits a positive global warming potential, low acidification potential, relevant social cost of carbon and a low potential production cost [6]. Hence, the biomass processes appear as promising technologies to renewable hydrogen [7], but with a large amount of impurities.

This means that widespread usage of hydrogen, *e.g.* in fuel cell vehicles, stationary power production or for specialty chemistry, requires its efficient purification. If one takes the case of proton electrolyte membrane fuel cells (PEMFC) for automotive applications as a benchmark, the level of purity required is as follows: H_2 > 99.97 mol%, hydrocarbons CO < 0.2 ppm (mol), H_2S < 0.004 ppm (mol), NH_3 < 0.1 ppm (mol), O_2 < 5 ppm (mol), N_2 and Ar < 300 ppm (mol) ([8], [9]). Besides, the volumetric energetic content of hydrogen being small at room pressure, this gas needs to be compressed to fairly high pressures to compete with usual fuels [10] [11].

For example, at 300 bar the density of energy is 0.75 kWh/m^3 in comparison to 3.4 kWh/m^3 for Natural Gas or 8.8 kWh/m^3 for gasoline. The targeted pressure by transport applications is at 700 bar.

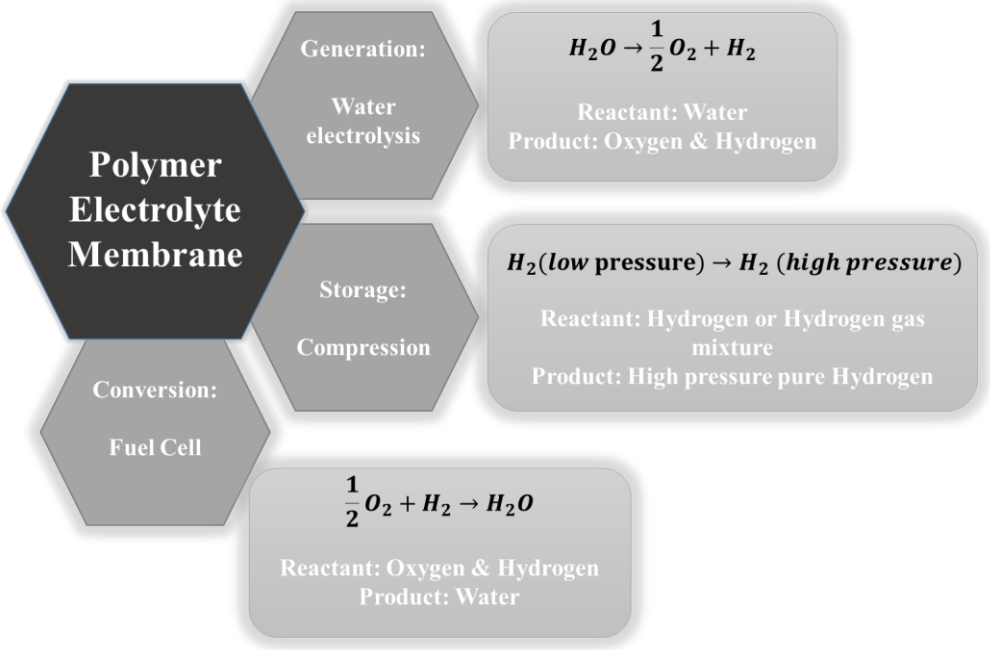

Figure 1.1 : Polymer Electrolyte membrane devices

In this state of art, the PEM devices in Figure 1.1 will be detailed, precisely the materials, the cell structure, and the operating principle. This work will focus on EHC and PEMWE devices.

1.1. Polymer Electrolyte Membrane devices

The most common Proton Electrolyte Membrane devices are Proton Electrolyte Membrane Fuel Cells (PEMFCs) and Proton Electrolyte Membrane Water Electrolysis (PEMWEs). As shown in Figure 1.2, unlike the fuel cell, the polarity of the water electrolysis on the anode is positive and on the cathode is negative [12]. The Electrochemical Hydrogen Compressor (EHC) is one of the devices that will be also discussed in this paragraph (subsection 1.1.3). Its cell has the same structure as these two previous devices and the reactant gas feed consists of a hydrogen gas mixture at low pressure and the product is high pressure hydrogen. The core of the system is usually called membrane electrode assembly (MEA).

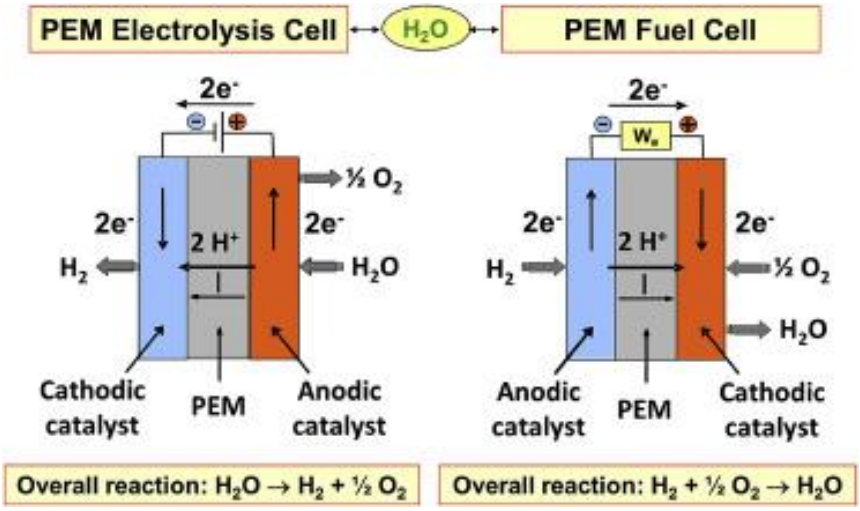

Figure 1.2: Comparison between Proton Electrolyte Membrane Fuel Cells and Proton Electrolyte Membrane Water Electrolysis [13]

PEMFC, EHC and PEMWE are currently developing to be an alternative for hydrocarbon fuel demands and environmental concerns [14]. These devices will play a substantial part in the sustainable advancement in the hydrogen and fuel cell technology (HFCT) market in international industries via transportation, stationary and portable applications.

1.1.1. Polymer Electrolyte Membrane Water Electrolysis

Water electrolysis for hydrogen production has many advantages, the first one is the simple process: only water and electricity are required to produce hydrogen. Several technologies are available: Solid oxide electrolysis, alkaline electrolysis, PEM electrolysis. According to Joshua Mermelstein and Oliver Posdziech [15] an electrochemical device based on solid oxide electrolysis cells can reach an electrical efficiency close to 100% lower heating value (LHV). Moreover, this system could be combined with different strategies of power to gas (e.g. methanation reactor) [16]. However, due to high operating temperatures of these cells, the material stability is affected which decreases the cell performance [17]. Commercial alkaline electrolysis has been used since the 20th century [18]. This alkaline electrolysis uses non-noble and less expensive catalysts. Which makes the quality of the utilized water insignificant since they are less sensitive to poisoning. Nonetheless, these technologies lead to a long-term corrosion problem [19]. The PEM technology is now compatible with fast start-up/shutdown, hence with intermittent operation [20] . Furthermore, the operation at ambient temperature makes it easier to real application. Among the electrolysis technologies, the Proton Electrolyte Membrane Water Electrolysis (PEMWE) is the best possible compromise in the current industrial process. PEMWE can electrolyze water with low energetic consumption and directly deliver pressurized hydrogen [21].

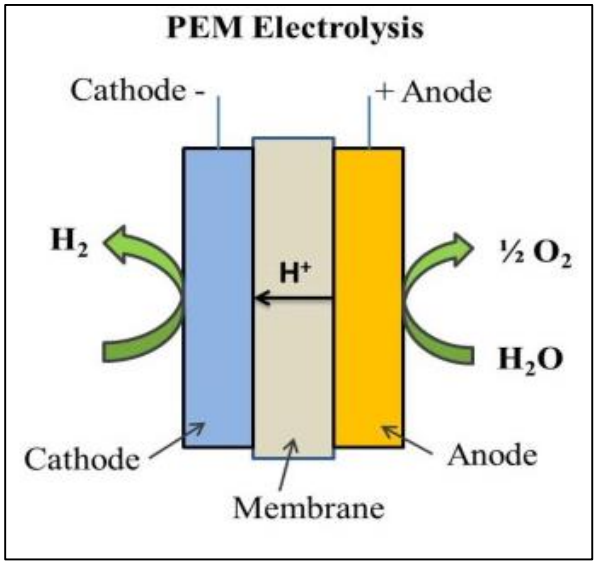

Figure 1.3: Operation principle of a PEM Electrolysis [22]

PEMWE energy conversion system converts electrical energy into chemical energy (Figure 1.3). The reactant involved is liquid water and the products are oxygen and hydrogen gas as represented in Equations (1.3) below:

Anodic reaction: $H_2O \rightarrow \frac{1}{2}O_2 + 2H^+ + 2e^-$ (1.1)

Cathodic reaction: $2H^+ + 2e^- \rightarrow H_2$ (1.2)

Overall reaction: $H_2O \rightarrow \frac{1}{2}O_2 + H_2$ (1.3)

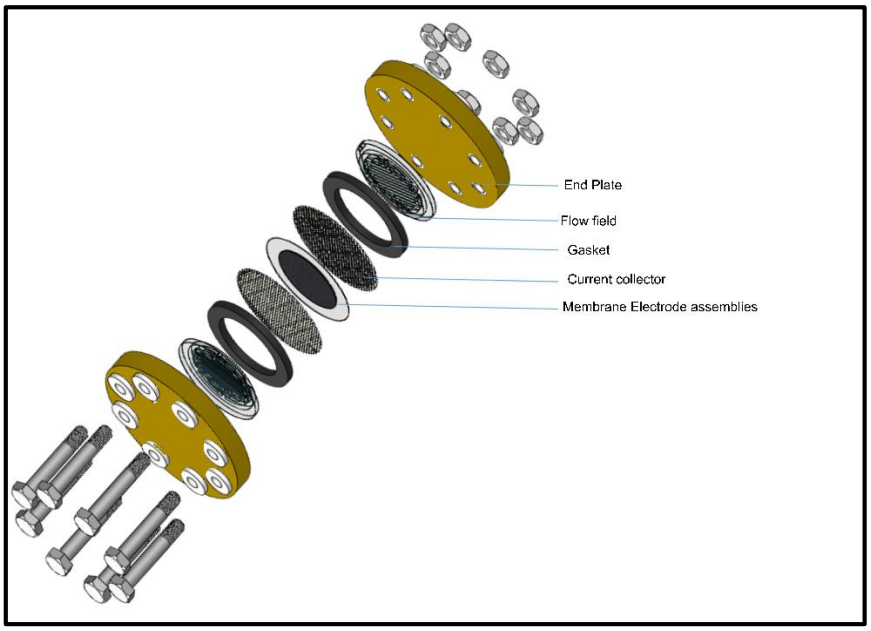

Figure 1.4 : Single cell proton electrolyte membrane electrolysis (PEMWE) [23]

Figure 1.4 shows a schematic representation of a single cell of the Proton Electrolyte Membrane Water Electrolysis (PEMWE). The single cell consists of a proton electrolyte membrane, two electrodes, and flow field plates having flow channels machined in them, through which electrical energy is supplied to the electrodes. The flow channels are required to achieve circulation of the reactant (H_2O at the anode side) and products (O_2 at the anode side and H_2 at the cathode side). The architecture of PEMWE is similar to proton electrolyte membrane fuel cells (PEMFC). The water flow at the inlet of the channels is distributed toward the anodic current collector. The protons pass through the membrane from the anode to the cathode and re-associating with the electrons to form gaseous hydrogen. The resulting hydrogen diffuses through the cathodic current collector and toward the outlet of the cathodic distribution channel. Simultaneously, oxygen bubbles are removed from the electrode into the anodic current collector and the water flow sweeps the bubbles away.

1.1.2. Polymer Electrolyte Membrane Fuel cells

Sir Humphry Davy introduced a simple fuel cell concept in 1802. However, the invention credit in 1839, based on reverse water electrolysis, went to Sir William Grove, also known as the father of the fuel cell. In 1889, the term "fuel cell" was first used by Charles Langer and Ludwig Mond [24]. Before the invention of the proton electrolyte membrane other fuel cell types existed such as solid-oxide fuel cells.

Due to their lightweight and their wide power ranges, PEMFCs are most suited for three broad areas [25], [26]:

- For transportations such as cars, buses, trains and trams, etc. [27], [28]
- For portable power, including military applications, small and large personal electronics, etc.
- For stationary power generation

The operating principle can be summarized in three chemical reactions:

$$\text{Anodic reaction: } H_2 \rightarrow 2H^+ + 2e^- \tag{1.4}$$

$$\text{Cathodic reaction: } \frac{1}{2}O_2 + 2H^+ + 2e^- \rightarrow H_2O \tag{1.5}$$

$$\text{Overall reaction: } \frac{1}{2}O_2 + H_2 \rightarrow H_2O \tag{1.6}$$

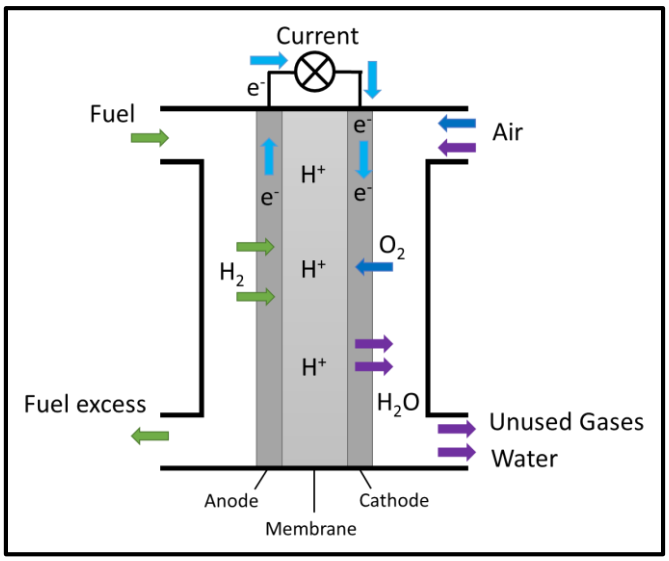

Figure 1.5: Operation principle of a Fuel Cell

As shown in Figure 1.5, hydrogen fuel enters from the anode side. The protons are separated from the electrons on the surface of the catalyst. These protons will go through the membrane to the cathode side

and the electrons pass in an external circuit generating electricity. On the cathode side, the hydrogen protons are combined with oxygen (from the air) to produce water.

1.1.3. Polymer Electrolyte Membrane compressor/concentration

Despite its name, EHC, also allows the purification of hydrogen. These devices are based on an assembly comprising anode and cathode gas-diffusion electrodes, and a solid (usually polymer-based) electrolyte situated between the electrodes. In an EHC system, electric energy is supplied to the cell to promote the transport of hydrogen (and only hydrogen) from the anodic to the cathodic compartment. To that goal, the operating principle of an electrochemical compressor (EHC) is simply to oxidize impure hydrogen at the positive electrode (anode) and to evolve hydrogen at the negative electrode; in the meantime, the protons produced at the positive electrode selectively migrate to the negative electrode through the proton-conductive membrane (Figure 1.6). This process can be summarized by the two electrochemical reactions (1.7) and (1.8):

$$\text{Anodic reaction: } H_2 \rightarrow 2H^+ + 2e^- \quad (1.7)$$

$$\text{Cathodic reaction: } 2H^+ + 2e^- \rightarrow H_2 \quad (1.8)$$

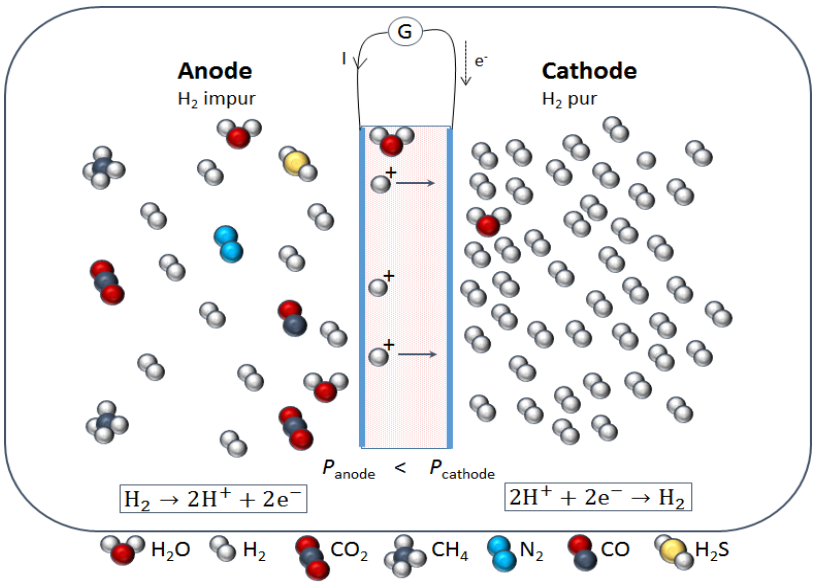

Figure 1.6: Operation principle of an electrochemical hydrogen compressor [29]

The operating principle is simple. However, building a reliable efficient PEM device can be complicated due to many challenging technical details.

1.2. Polymer Electrolyte Membrane cell basic concept

1.2.1. Single Cell Design

Every Polymer Electrolyte Membrane (PEM) device discussed in this thesis will be structured in the same architecture. The materials such as catalyst load or the reactants and the products are not similar, but the order of the structure remains the same, a multilayer assembly. As it is shown in Figure 1.7, on the edges Bipolar Plate (BP), which also support the feed flow channels (1), ensure electric connection between cells and the fluid distribution . The Gaskets (2) or the seals are generally inserted between the distribution channels and the Membrane Electrode Assembly (MEA).

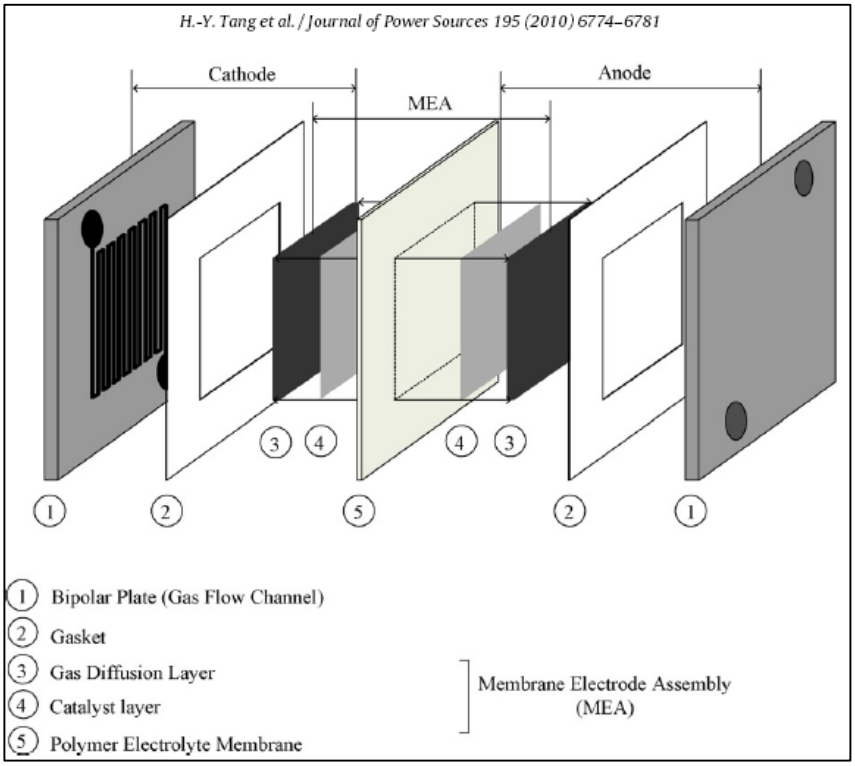

Figure 1.7: Representation of a PEM fuel cell device [30]

MEA is mainly composed of two Gas Diffusion Layers (3) on both sides, two Catalyst Layers (4) with a Polymer Electrolyte membrane (PEM) (5) in the center.

1.2.2. Polymer Electrolyte Membrane

All the devices in this present work have a PEM. The membrane is the central element of the single cell. This electrolyte prevents the reactants present at the anode side to mix with the products present at the cathode side. It also allows the migration of protons from the anode to the cathode [31]. One of the most used membranes is the Nafion® membrane. In the 1960's, Nafion® was introduced by DuPont [32]. The thickness of the commercialized membranes varies between 20 and 254 µm. It is a fluoropolymer made by sulfonated tetrafluorethylene [33]. Structurally (Figure **1.8**), PEM membranes is a perfluorosulfonic acid (PFSA) polymer consisting of two elements: the sulfonate acid and a polymer matrix of Teflon® [34]. These membranes have the chemical and thermal stability of Teflon® [35] and the hydrophilic property of sulfonate acid sites [36].

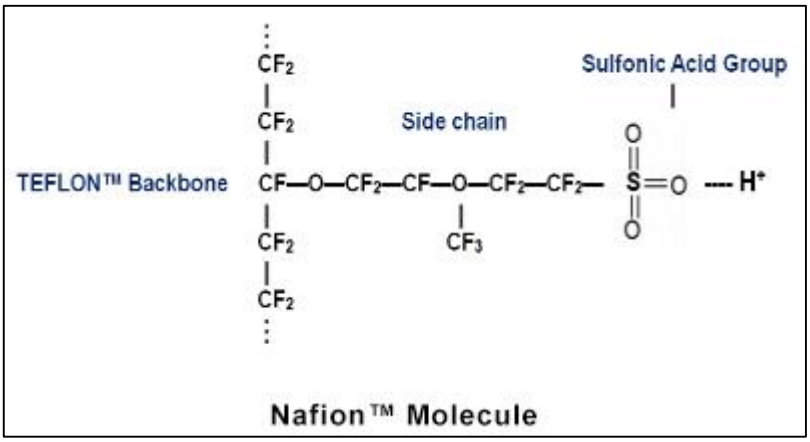

Figure 1.8: Nafion® Molecule structure [37]

The most important characteristics sought in a membrane are the proton conductivity, the water permeability, the chemical resistance and the mechanical resistance [33]. One of the disadvantages of Nafion® membranes is that they are known to lose water at temperatures exceeding 100°C therefore the ionic conductivity sharply declines [38].

The Nafion® membrane is mainly characterized by (λ_m) the water content of the Nafion®, (σ_{H^+}) the proton conductivity (S / m), (δ_m) the membrane thickness (m) and (D_m) the diffusion coefficient in the membrane (m^2 / s) [31].

The membrane conductivity formula differs in the literature. The ones commonly used are:

For Neubrand [39][40]:

$$\sigma_{H^+} = (0.0013\lambda^3 + 0.0298\lambda^2 + 0.2658\lambda) \exp\left(EA\left(\frac{1}{353} - \frac{1}{T}\right)\right) \quad (1.9)$$

with (T) the temperature in K.

For Springer *et al.* [41] used for Nafion® 117 in PEMFC:

$$\sigma_{H^+} = (0.005139\lambda - 0.00326) \exp\left(1268\left(\frac{1}{303} - \frac{1}{T}\right)\right) \quad (1.10)$$

The effective proton conductivity is [31]:

$$\sigma_{H^+}^{eff} = \epsilon.\sigma_{H^+} \quad (1.11)$$

ε is the porosity of the Nafion® membrane.

1.2.3. Catalyst Layer

The catalytic layer (or active layer / reaction layer) is where the electrochemical half-reactions occur. Therefore, a thin coating layer is needed to speed up the reactions. As shown in Figure 1.9, this acts as a porous active layer on both sides of the membrane [42].

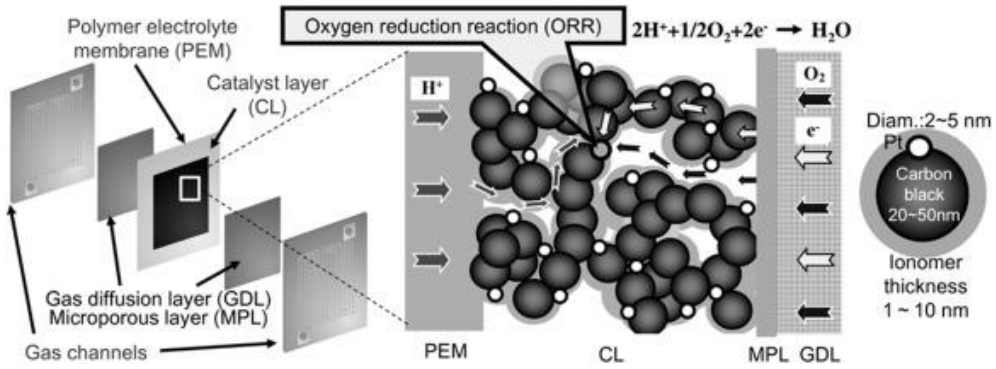

Figure 1.9: Graphic demonstration reaction and mass transport in the catalyst layer (CL) [43]

In this PEMFC, the electro catalyst is often a noble metal such as platinum or its alloys/composites like carbon-supported Pt-based particles loaded on a Nafion® ionomer. This catalyst is chosen for its high kinetics towards the hydrogen oxidation reaction and hydrogen evolution reaction (ORR, HORHER). However, due to the high cost of the raw materials used, most of the efforts research is currently based on optimizing electro-catalysis. Thus, to lower the cost, the use of Pt-based electro-catalysts must be reduced. To do so, enlarging its electrochemically active surface area (ECSA) using nanoparticles can be one of the solutions [44]. Accordingly, the best compromise for platinum nanoparticles between the mass activity and the stability was a diameter of 4 nm [45].

The different materials need to be chosen depending on the system operating conditions (targeted performances), and the nature of the impurities in the hydrogen feed. For example, in the case of the PEMWE, at the anode, since it is an oxygen evolution reaction (OER), the electro catalyst is commonly the iridium (Ir, IrO_2). However, at the cathode side it is a HER, so it is a platinum-based electro catalyst.

In Hydrogen pumping devices, specially the EHC for compression and purification, currently, platinum is considered the leading electro catalyst for the hydrogen oxidation reaction (HOR) and the hydrogen evolution reaction (HER) [29].

The parameters needed for modeling the catalytic layers (CL) will be ($i_{0,a,c}$) the current density (A / m²), ($\alpha_{a,c}$) the electrochemical exchange coefficient, ($\sigma_{a,c}$) the proton conductivity (S / m), δ_{cc} the catalytic layer thickness (m), (ε_{cc}) the porosity and ($\gamma_{a,c}$) roughness coefficient [31].

1.2.4. Gas Diffusion Layer (GDL)

The GDL provides a structural backing of the CL by allowing a good electrical conductivity and a transport of the reactants through its hydrophobic porous structure. They also play a crucial role in heat discharge and water management [46].

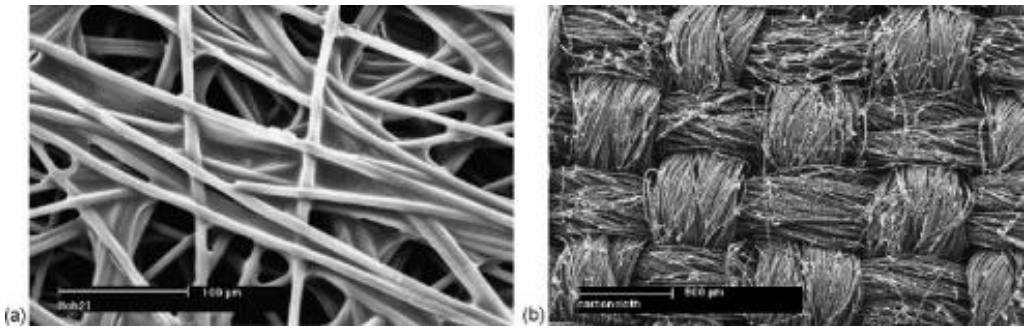

Figure 1.10: Microscopic image of: (a) carbon paper and (b) carbon cloth [47]

On the Hydrogen side, the most common Gas Diffusion Layers (GDL) are carbon paper and carbon cloth, such as the figure shows for a PEMFC [48] (Figure 1.10). Same GDL is used for the EHC. As for the oxygen side, porous titanium GDLs are mostly used in the PEM electrolysis [49][50] (Figure 1.11).

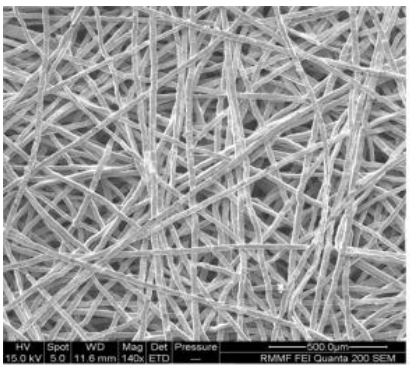

Figure 1.11: Microscopic image of titanium fiber [48]

The porosity of GDL differs between 30% and 90% with pore size between 12 μm to 95 μm. This difference affects its characteristics such as electrical conductivity, thermal conductivity, and permeability. Therefore, the porosity is important for the cell efficiency [48]. Hwang *et al.* [51] have claimed that Ti-felt GDLs in Fuel cell mode, reduced porosity enhances the efficiency in wet conditions by lowering the resistance of mass transport. Grigoriev *et al.* [52] have stated that the porosity of GDL

in PEM electrolysis should lie between 30% and 50%. Because a higher porosity GDLs simplify gas removal however it boosts the ohmic losses.

The GDL thickness can affect the water management and the thermal and electrical resistance. The thickness of titanium GDL in PEMWE varies between 250 µm and 1000 µm [48] while the carbon GDL in PEMFC varies between 200 µm and 300 µm [46].

The GDLs are characterized by the following variables: (σ_{GDL}) the electrical conductivity (S / m), (δ_{GDL}) the diffusion layer thickness (m) and (ε_{GDL}) the porosity [31].

1.2.5. Bipolar Plates

The Bipolar Plates (BP) are the distribution channels that ensure the distribution of reactants as well as the evacuation of products and excess reactants. As shown in Figure 1.12, many designs exist to supply a path for reactants in PEM devices. However, since PEMFC and EHC both have gas feed, the shape has less impact compared to the PEMWE which is due to the water feed. Therefore, the more convenient geometry is parallel channels.

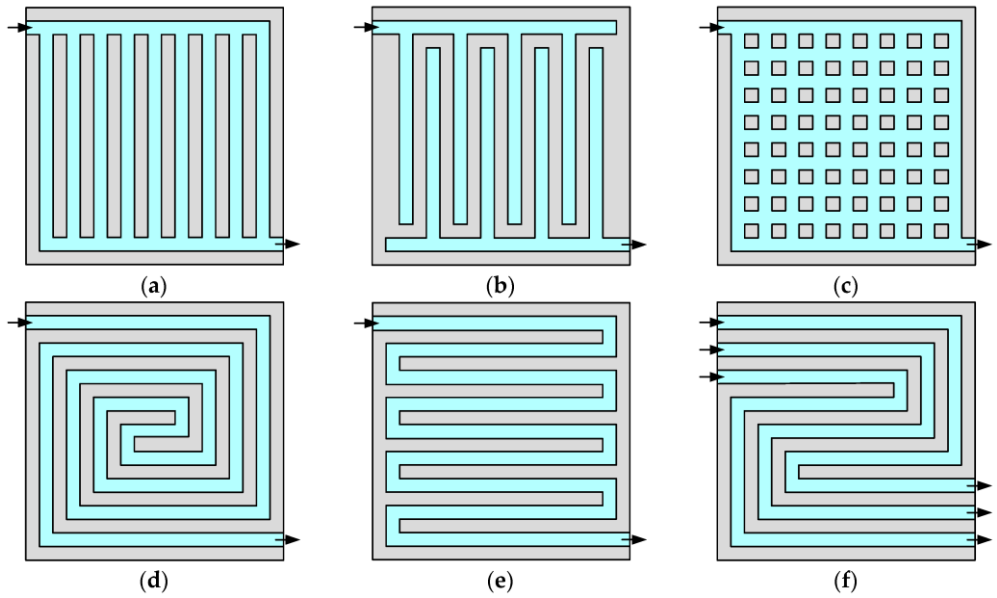

Figure 1.12: The most typical geometries of Bipolar Plates: (a) straight parallel; (b) interdigitated; (c) pin-type; (d) spiral; (e) single-channel serpentine; (f) multiple-channel (triple) serpentine [53]

The ratio between channel area and land area is crucial. A large channel area allows to supply enough reactants and a bigger land area ensures a better electrical connection between the BPs and the GDL. A compromise should be achieved to establish an optimum cell performance [46]. The BPs must also conduct electricity, act as a current collector, and allow heat evacuation. They must also have sufficient mechanical strength to seal the cell and resist corrosion, while being impermeable to gas leaks[54]. Various studies have been made, on both the material (Graphite, Carbon composites, Metal) and the manufacturing processes in order to reach several technical and economic criteria [55].

The most convenient material that is commonly used in bipolar plates is graphite. Due to its high electrical and thermal conductivity, low corrosion rate, and lightweight. Nonetheless, it is still an expensive material. Carbon composites are also manufactured for BPs PEMFC and EHC [46]. However, for the PEMWE it is more common to use stainless steel BP.

The commercially marketed stacks today have more metal alloy metallic BP than graphite BP due to the manufacturing difficulties of achieving a good compactness of the material. For example, the French producer Symbio makes PEMFC stacks using metal BP.

1.2.6. Polymer Electrolyte Membrane Cell Performance and Phenomena

1.2.6.1. General layout on PEM devices' performance

One of the most common methods used to analyze the PEM devices behaviors and performance is the polarization curves. It represents the cell voltage as a function of the current density. Using usually a potentiostat that applies a current and measures the voltage. The curves are later compared to other data found in the literature to characterize the performance. Each PEM device has a specific pattern that the measurements frequently revolves around. The variations around the theoretical shape is due to variation of the temperature, the relative humidity, the catalyst loading thickness and material, the types of membranes used, and so on.

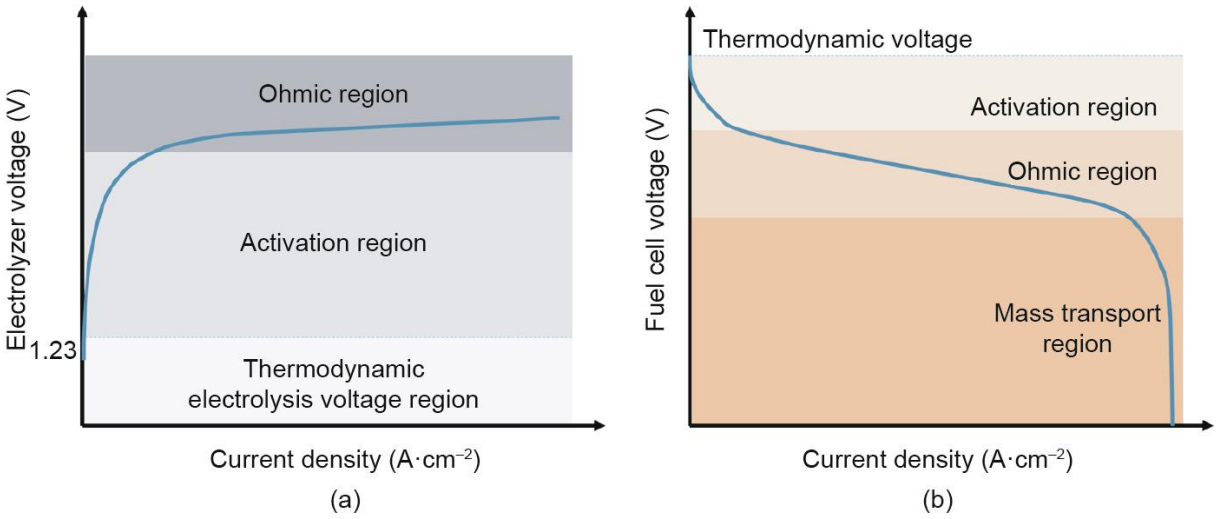

Figure 1.13 : Pattern polarization curves: (a) PEMWE & (b) PEMFC [56]

Figure 1.13 exhibits the theoretical polarization curves frequently presented in the literature for (a) PEMWE and (b) PEMFC. Several phenomena contribute to the performance and thus to the obtaining of this Voltage-Current curve. The thermodynamic potential imposed by the redox couple determines the minimum potential in the case of the PEMWE and the maximum in the case of the PEMFC. When the current flows, the ohmic losses and the activation over potential appear, they are added to the thermodynamic potential in the case of the PEMWE. However, in the case of the PEMFC, the ohmic

losses and activation over potential are deducted. For the PEMFC, the over potential appear due to the mass transport on the active sites at high current.

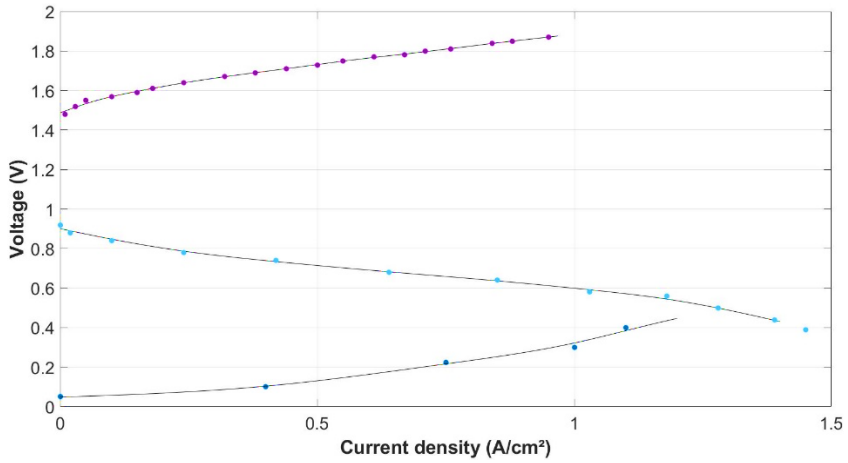

Figure 1.14 : Polarization curves comparison (EHC (-•-); PEMWE (-•-); PEMFC (-•-))

Figure 1.14 illustrates some experimental data from the literature [57] [58] [59]. This figure demonstrates that even if the architecture of the PEM devices is similar. The difference of flow feed (gas/water) materials (catalyst loading) is crucial to the device behavior and purpose. The difference in these curves, beside the different functionality of each cell (Generation/Storage/Conversion) is the effect of the PEM membrane ohmic resistance.

The methods of characterization like the polarization curves are needed to understand better the areas that still need to be improved in these devices. Even though they reached remarkably high performances in the market, these PEM cells still have many drawbacks which limits their efficiency.

For EHC, Casati *et al.* [60] have investigated some fundamental aspects in the EHC using a PEMFC; this work has unveiled some performing parameters of the system, such as:

- The membrane hydration is a critical issue: galvanostatic operating conditions can damage the membrane due to the improper water management. Therefore, potensiostatic operating conditions must be favored.
- The feed flow has an important impact on the amount of hydrogen recovered. The recovered fraction rises when the inlet hydrogen flow rate decreases. The recovery rate is maximum when the inlet flow of hydrogen is equal to the flow rate through the membrane (determined by the cell current). Therefore, this maximum is determined by the hydrogen production (at the outlet).
- The specific energy consumption depends only on the applied voltage, which is divided into:
    - Thermodynamic potential: due to the compression ratio of the hydrogen

- Kinetic potential: that depends on cell current, or in other words the flowrate of hydrogen treated across the MEA (overvoltage)
- Dissipative potential: defined by the useless forces (Ohmic drop)

1.2.6.2. Water management in PEMFC and EHC

Water transport through a proton electrolyte membrane (PEM) is a critical issue for both a fuel cell and an electrochemical compressor. Most of the studies that focused on water management were related to the case of fuel cells (FC). Water transport inside the membrane is induced by three mechanisms: the electro-osmotic drag caused by proton transport (from the anode to the cathode side), the back-diffusion flux (from the cathode to the anode side) due to gradient of water content and the Darcy like flux involved with the pressure gradient due to the pressure rise of the compression at the cathode side (in the case of EHC). The difference between the FC and the EHC for this particular issue is that at the cathode side of a FC, water is produced by the electrochemical reaction, which might cause an excess of water in the system (flooding); in the case of an EHC water is not involved in any of the reactions at stake; this does however not mean that water is useless to the operation of an EHC. Indeed, the lack of water production coupled to the need for non-negligible proton transport in the PEM from the anode to the cathode (being admitted that protons are accompanied by water molecules and that the present membranes need to be well-hydrated to promote fast proton transport) might cause a water drainage in the membrane; if uncontrolled, it will eventually stop any proton transport, hence the compression process.

The water content parameter is used to describe the water quantity in the membrane. Both Zawodzinksi *et al.* [61] and Springer *et al.* [41] have presented a correlation between the equilibrium water vapor pressure and the water content value for Nafion® at atmospheric pressure and a temperature of $T = 30°C$. Hinatsu *et al.* [62] demonstrated an empirical formula describing the previous correlation at a temperature of $T = 80°C$ and Ge *et al*. [63] gave an equation predicting the water content in a PEM for $30 < T < 80°C$. As for Kusoglu *et al.* [64], they talked about the internal balance between chemical and mechanical forces determining the water content in Nafion® membranes. For the diffusion coefficient, it is also a function of the water content; Majsztrik *et al*. [65] have provided insight into the different measurement methods considered in the literature to quantify water diffusion, whilst distinguishing sorption and desorption effects. For PEMFC, PEMWE and EHC many equations must be solved such as thermodynamic equilibrium, mass, momentum, and charge balance. Therefore, steady-state mass balance in the membrane for incompressible fluid flow simplifies the water equation as follows (equation (1.12)):

$$D_{H_2O}\Delta c_{H_2O} = \vec{v}_m.\vec{\nabla}c_{H_2O} \quad (1.12)$$

where c_{H_2O} is the bulk concentration of water in the membrane (mol.m^{-3}), $\vec{v}_m$ is the velocity inside the membrane (m s^{-1}) and the term D_{H_2O} is the effective diffusion coefficient of water (m^2.s^{-1}).

The momentum balance is described by a form of Schlögl's equation of motion, electric potential and pressure gradients generate convection within the pores of the ion-exchange membrane [66], as expressed by equation (1.13).

$$\vec{v}_m = -\frac{\kappa_\Phi}{\mu} z_f c_f F \frac{\vec{j}}{\sigma} - \frac{\kappa_p}{\mu}\vec{\nabla}p \quad (1.13)$$

where μ denotes the water viscosity (kg m^{-1} s^{-1}), κ_Φ is the electro-kinetic permeability (m^2), z_f is the fixed-charge number in the membrane, c_f is the fixed-charge concentration (mol.m^{-3}), κ_p is the hydraulic permeability (m^2), σ is the ionic conductivity (Ω^{-1} m^{-1}) and $\vec{j}$ is the current density inside the membrane (A m^{-2}).

This type of equation can be difficult to solve due to the different parameters that should be considered, such as the current density, the pressure, the water concentration, and the membrane characteristics.

Modeling of the EHC properties therefore requires a clear distinction between the internal driving forces for water fluxes and external conditions [67]. According to them, the hydrogen dehumidification is an interesting issue observed during compression. Compression of the gases leads to the pressure rise of the hydrogen at the cathode side unlike for water vapor that is condensed.

1.2.6.3. Gas permeation

As two compartments with different partial pressures are separated by a membrane, permeation of any species could occur downward the partial pressure gradient. Gas permeation is therefore driven by partial pressure gradient, and depends on the operating conditions, such as temperature and relative humidity (water management) and is determined by the nature of the membrane and its thickness. Kocha *et al*. described the principle of gas permeation and gave the expression of gas permeation rate N_i (mol s^{-1} m^{-2}) of species *i* (equation (1.14)):

$$N_i = D_i \frac{H_i^h p_i^h - H_i^l p_i^l}{\delta} \quad (1.14)$$

and the definition of k_i, the gas molar permeability coefficient, (mol m^{-1} s^{-1} Pa^{-1}) (equation (1.15)):

$$k_i = D_i H_i \quad (1.15)$$

with H_i the solubility coefficient, (mol m^{-3} Pa^{-1}), D_i the effective diffusion coefficient in the membrane, m^2 s^{-1}, p_i the partial pressure of gas (Pa), and δ the thickness of the membrane. These expressions demonstrate that the solubility and diffusion coefficient of the species are of equal importance in the permeation phenomenon.

1.2.6.4. Hydrogen crossover

A lot of study exists on hydrogen crossover in PEMFC ([68], [69], [70], [71], [72], among others), due to its severe impact on both the efficiency and durability of the fuel cell. For example, Brunetti *et al* [71] evaluated mass-transport, including hydrogen crossover, for Nafion® 117. The gas permeability coefficient depends on temperature, relative humidity, and nature of the membrane, while the transport is strongly depending on the water content and on the hydrothermal history of membrane. Truc *et al.* [70] proposed a numerical model including hydrogen crossover and the dependence of permeability with membrane water content and temperature.

In addition, the hydrogen crossover is linked to the pressure gradient. According to Schalenbach *et al.* [73] in the case of a pressurized PEMWE the hydrogen permeation is three times higher than a PEMWE at balanced pressure. If only electrochemical purification is targeted, the cell could be operated by applying a total pressure gradient of zero across the PEM [74]. For a one-step electrochemical compressor, the total pressure gradient varies greatly from one experiment to another. Indeed, several cells are usually included in a stack: even if the overall compression ratio is specified, it is difficult to know the pressure difference on either side of the membrane for one cell within the stack. It is nevertheless commonly known that 50 bar is a large pressure gradient for low-temperature commercial PEMs [67]. At laboratory scale, with reinforced or high-temperature membranes, higher gradients have been obtained [75], hence large compression (a positive effect). However, such large gradients enhance gas permeation (a negative effect). It is therefore a matter of compromise.

For a standard membrane, back-diffusion does not limit the compression ratio. The faradaic equivalent current ($j_{f,eq}$) can be estimated from the hydrogen permeation rate, and it is low in front of the current imposed on the cell. Bessarabov *et al.* [67] showed some experimental data for commercial low temperature (for the differential pressure, ΔP = 50 bar, the maximum value is $j_{f,eq}$ < 80 mA cm^{-2}) and high temperature membranes (for ΔP = 250 bar, $j_{f,eq}$ < 10 mA cm^{-2}).

Accordingly, Baik *et al.* [72] showed that the equivalent current due to hydrogen crossover is below $j_{f,eq}$ < 2 mA cm^{-2}. These authors gave an empirical model thanks to multiple linear regressions (equation (1.16)):

$$\varphi = a_0 + a_1 T + a_2 RH + a_3 k_{H_2} + \frac{a_3}{\ln(\delta)} \qquad (1.16)$$

where φ is the hydrogen crossover rate, *RH* is the Relative humidity and δ is the membrane thickness? Of course, this empirical model is validated only for moderate gradients for Nafion® membranes thickness from 258 < δ < 135 µm.

The permeability coefficient for low temperature membrane PFSA ([60], [68] , [67]) varies between $2.10^{-14} < k_{H2} < 5.10^{-14}$ mol m^{-1} s^{-1} Pa^{-1}. Its value is mainly conditioned by the state of hydration of the membrane and the operating temperature of the cell. According to equation (1.14) and (1.15) an estimation is calculated, using mean value of permeability coefficient ($k_{H2} = 3.10^{-14}$ mol m^{-1} s^{-1} Pa^{-1}) for Nafion® 117 (thickness =183 µm) and ΔP =50 bar. With these values, the equivalent current of hydrogen crossover flow is then: $j_{f,eq}$ = 16 mA cm^{-2}, which is a mere 3% of the current imposed in the cell at j = 0.5 A cm^{-2}, and is negligible for larger cell current densities (which is targeted in practice).

Nevertheless, as molecular hydrogen back-diffusion reduces the efficiency of the hydrogen pump and impacts the hydrogen purity, several strategies of mitigation of the back-diffusion have been suggested:

- Add a molecular hydrogen barrier (this strategy is used by HyET), or a modified PEM [57].
- Avoid excessive pressure differences on either side of a membrane and use a stack of cells for the overall compressor (several steps of (intermediate) compression).
- Find an optimal value of current density and adapt water management to avoid permeate backflow and electrical resistance.

1.2.6.5. Limiting physical phenomena

The limiting physical phenomena in the PEM devices are due to the conditions of the cell, such as temperature and relative humidity. The catalyst loading also affects the electrochemical behaviors of the device. The type of the used membrane changes the conductivity in certain situations which is causally linked to the proton diffusion in the membrane. The pressure gradient in the case of an EHC or a pressurized PEMWE also adds another parameter to the mathematical representation of the cell. Therefore, it is particularly important to determine which device and the materials used for its construction to characterize the limiting phenomena of the considered PEM device.

In the literature, the most discussed and analyzed physical phenomena are (Figure **1.15**):

- Proton diffusion in the membrane and the catalytic layer
- The diffusion of water in the membrane
- Electrochemical kinetics at catalytic layers
- Electro-osmotic transport in the membrane
- Heat flow (mostly considered for high temperature applications)
- Osmotic pressure transport in the membrane (in the case of a pressure variation between the inlet and the outlet)

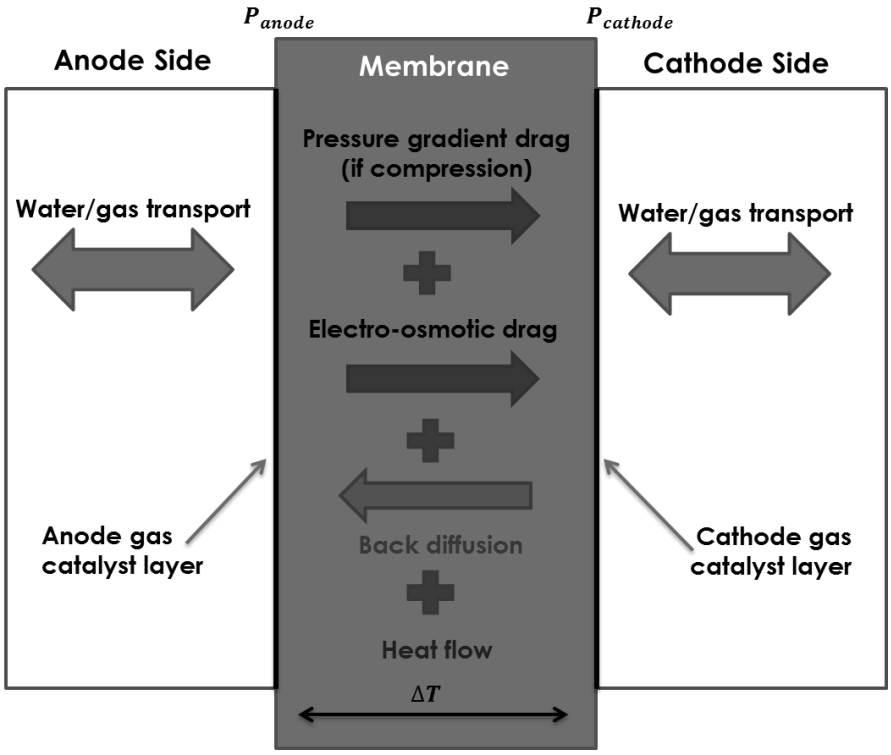

Figure 1.15 Limiting physical phenomena of PEM device

1.3. Polymer Electrolyte Membrane Electrochemical hydrogen compression

In this part, the focus is on EHC, which is the most recently developed device. This part is a portion from our review work [11]. At present, there are many ways to purify and to compress hydrogen. It will notably be shown that electrochemical hydrogen compression (EHC) systems enable both purification and compression at reasonable efficiency and could therefore be the technological solution for such application.

1.3.1. Purification methods

In order for hydrogen to become a widespread renewable-energy carrier, its purification and compression are unavoidable industrial processes [10]. Currently, these two processes are usually physically separated in, firstly, a purification step to convert impure hydrogen into ultra-pure hydrogen, and then a compression step to make the purified (and low-pressure) hydrogen gas storage sufficiently dense (in terms of gravimetric and volumetric density) to compete with the usual energy vectors (*e.g.* gasoline, natural gas, etc.). The sections below will detail the different ways to purify and to compress hydrogen gas with present technologies, but also with "future" ones.

1.3.1.1. Different purification methods

Several approaches enable hydrogen purification in the industry. Hydrogen can be recovered by condensing the impurities (cryogenic process), by adsorbing the impurities (Pressure Swing Adsorption, PSA) or by using perm-selective membranes.

Many research works propose to mix various polymer materials in composite membranes to improve their apparent selectivity and permeability [76]. The performances reached still do not meet the industrial targets, though, and the most advanced technologies for hydrogen separation use dense metal membranes. The most common metallic membrane for hydrogen separation consists of palladium membrane. Nevertheless, such metal membranes (including Pd membranes) also bear drawbacks: they can fail due to hydrogen embrittlement and remain expensive (Pd is an expensive element [77]).

Pressure Swing Adsorption (PSA) is the most widely used method to produce high-purity hydrogen from steam methane reforming: several hundred PSA–H_2 process units are currently installed in various

parts of the world. It is difficult to compare these three processes, though, because the scale and maturity of these technologies can be strongly different.

Temperature swing adsorption (TSA) is also widely used to purify hydrogen. However, according to Bonjour et al [78], the main drawbacks of the TSA systems is the large energy consumption it requires as well as large masses of adsorbents that are needed.

1.3.1.2. Electrochemical Hydrogen Compressor/Concentrator (EHC)

Obtaining pure hydrogen at the outlet of EHC requires a minimum electrical work to be supplied to the cell: the theoretical work of purification is given by the Nernst equation [79]. In practice, though, this theoretical work is not sufficient, and kinetics limitations should be overcome. They depend on the ohmic resistance of the cell (both owing to non-infinity conductivity of the proton-exchange membrane and electrode materials, and the electrical contacts), some charge-transfer limitations (although the HER and HOR are known to be very fast reactions on platinum-based electrodes, their overvoltage values are strictly not zero) and some mass-transport limitations (molecular hydrogen and proton transport to/from the catalytic sites,). These kinetics limitations increase when the current density increases, which means that the efficiency of an EHC will decrease when its productivity (flux of pure H_2) increases. In addition, the EHC purification assumes that there are electro catalysts that enable fast oxidation of impure hydrogen, which is not granted on present anode materials, that usually display low tolerance to some poisons (*e.g.* H_2S and CO).

At a geometric current density of $j = 2$ A cm^{-2}, EHC reaches the performance of the best membrane process, thus EHC is an attractive solution for hydrogen purification.

1.3.1.3. Comparison of purification methods

As stated above, direct comparison of these different processes of hydrogen purification is not straightforward (Table 1-1). Whatever this bias, it was decided to attempt such comparison; it is based on five markers, which have been particularly chosen to benchmark the EHC versus the present industrial hydrogen purification means.

The first marker is the *gas recovery*. It was set close to 1 for the membrane process and EHC, because in these cases, the purges exhibit a weak percent of feed gas (*e.g.* near to 1% or below – they can operate in dead-end mode), whereas it is higher for the PSA and cryogenic processes (their purge-to-feed ratio

is usually higher than 20%), resulting in lower *gas recovery* marker value. The second marker is the *operating temperature convenience*: the choice was made to set this value of quotation of the operating temperature to 1 if the operating temperature is between room temperature and 200°C material durability and sealing system are very convenient, to 0.5 for temperature comprised between $200 < T < 500$°C (less convenient) and 0.2 for negative temperature ($T < 0$°C) or very high temperature ($T > 500$°C) (very detrimental and energetically costly in practice). The third marker is the compatibility of the process with *continuous operation*; it is set to 1 for the regenerative swing method (fully-compatible with *continuous operation*), to 0.5 for the non-regenerative method, and to 0 for external regenerative systems. Non-regenerative methods are based on chemical trap [80] and are not presented here. Although temperature swing adsorption (TSA) could be used to remove the adsorbed impurities from the mixture, this method is limited to low productivities as compared to the PSA. TSA or Vacuum Swing Adsorption (VSA) exhibit more energy consumption than PSA [81], thus these methods are not detailed here. The fourth marker is the *energetic cost* of the process: a value of 1 corresponds to the minimal work for the purification. Agrawal *et al.* [82] proposed a classification for the energetic consumption of purification processes: membrane > cryogenic. The fifth marker is the *gas purity* that can be reached with the process, which is in favor of the membrane and EHC processes (both use membranes, in fact, which provides and selects to the separation and therefore high purity of the obtained hydrogen). The results of this quotation are gathered in Figure 1.16 which demonstrates that the EHC has many advantages over the other hydrogen purification techniques: EHC offers the best compromise between these five markers.

Another thing that must not be forgotten is, as specified in the previous sections, that the EHC (and the Pd membrane process) are compatible with small units of purification, which render them well-suited for fuel cell vehicles refilling systems.

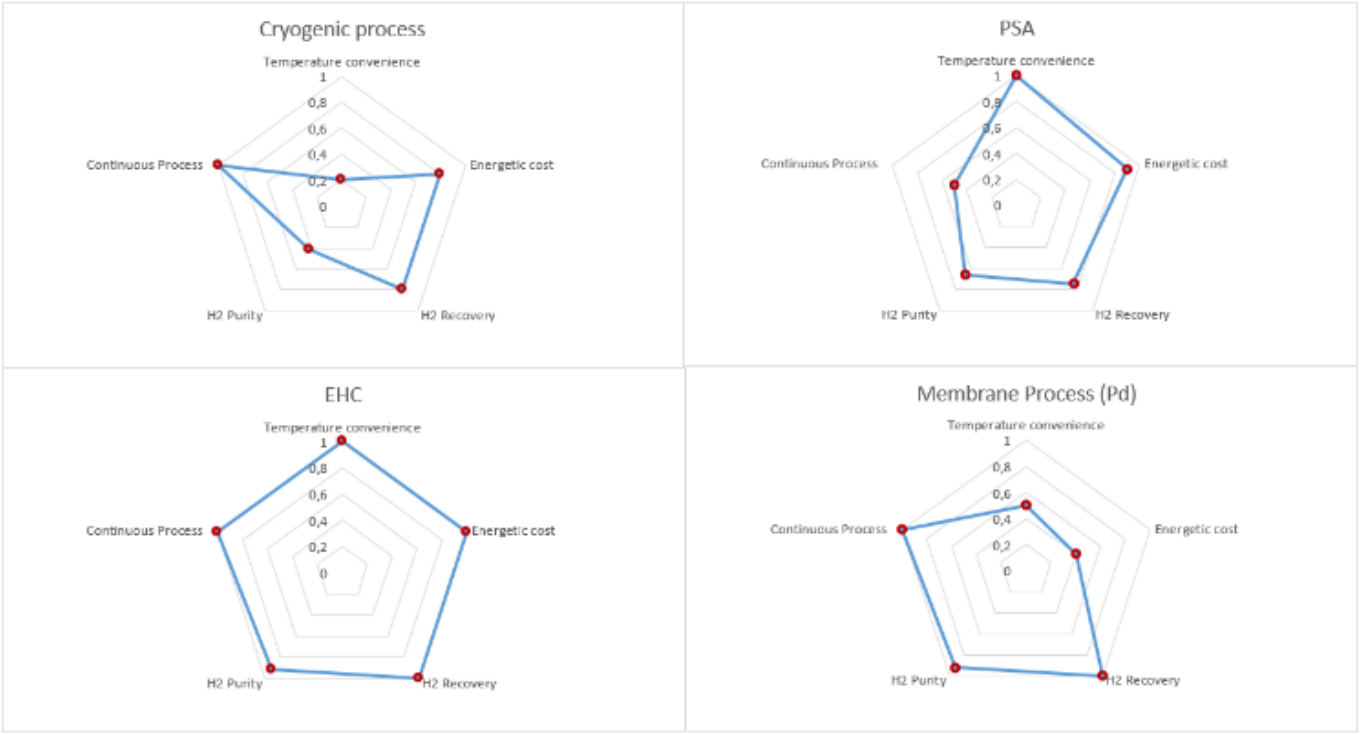

Figure 1.16: Comparative diagram of the performances of several hydrogen purification methods [11]

Table 1-1: Additional literature information of several hydrogen purification methods [11]

	Reference	**Temperature range °C**	**Pressure range**
Cryogenic	[83] [84]	25- (-) 253	1-10 bars
PSA	[85] [86] [87] [88] [89] [90]	25-80	1-10 bars
Porous membranes	[91] [92]	25- 500	20 bars
Palladium membrane	[91] [93]	350-500	>10 bars
Polymeric membrane	[94] [95]	25- 65	Vacuum : 10^{-2} mbar
Protonic ceramic membrane	[96], [97]	700 -1000	>10 bars

1.3.2. Comparison of Hydrogen Compression

As stated in preamble, most industrial techniques of hydrogen post-treatment upon production use different steps for the purification and the compression. Hereafter are detailed the classical means that are used to compress hydrogen at an industrial scale. Most of them are based on a mechanical compression (MC).

According to Petitpas *et al.* [98] the ideal gas law is available until 100 bar for hydrogen (23°C). At 23°C between 100 to 800 bar, the isentropic coefficient γ increases. The adiabatic energy loss is undervalued (by 15% to 20 %) with the assumption of the ideal gas law versus real gas. Therefore, the ideal gas assumption presents a non-favorable case for this comparison. Hence the isothermal compression (Nernst law) is used as a means of comparison.

1.3.2.1. Assessment on efficiency of Electrochemical hydrogen compression (EHC)

As stated above, whereas in the most conventional compressors (*e.g.* mechanical compressors), the purification is separated from the compression process, electrochemical hydrogen compression (EHC) combines the purification and the compression in one single step. This makes EHC interesting alternatives from usual (purification + compression) systems; their intrinsically high efficiency but also the fact they do not use moving parts (except for cooling systems) are also to their advantages. As illustrated in Figure 1.6, the cathode side is the origin of the compression (and purification) in these devices [99]. According to the research data, only the back-diffusion of hydrogen from the (high-pressure cathode side) and the intrinsic mechanical properties of the membrane cause a pressure limitation and not the electrochemical operating principle of the EHC [100], which means that very high compression ratios are achievable in principle [75].

Studies usually show that efficient proton exchange membrane (PEM)-based EHCs can be built for output pressures ranging from $34 < P_{out} < 100$ bar (starting from room pressure). The pressure upgrade depends on the sealing construction and the design of the cell. More practically, the output pressure can be increased by stacking several cells in series (in that case, the overall output pressure increases in cascade from one cell to the other), while the hydrogen flow can be increased using larger units. The literature makes clear that the reduction of materials production cost achieved for the PEM fuel cells (PEMFC) for the last decade can also be applied to PEM hydrogen compressors (PEM-EHC) [100]. Some researchers such as Casati *et al.* [60] have used a PEMFC to test the different aspects of the PEM-

EHC. Besides the cross-cutting aspects of PEM-based technologies, either for fuel cells or electrolysis, the PEM-EHC has no moving part. Therefore, it does neither generate noise nor vibrations, and no gas-contaminating lubricants are needed in the process [101]. The heat production of the process is small (because both the HER and the HOR are fast reactions in PEM environments [102], at least when the incoming hydrogen gas is pure), inducing low temperature rise upon compression, which implies that the EHC does not need an expensive pre-chilling equipment.

Catalano *et al.* [103] have demonstrated the maximum efficiency (η) of electrochemical gas compressors, following its mathematical calculation (equation (1.17)):

$$\eta = \frac{\sqrt{1+\beta}-1}{\sqrt{1+\beta}+1} \tag{1.17}$$

where β is the figure-of-merit for electro-kinetic compression in the gas phase (equation (1.18))?

$$\beta = (RT/F^2)(t_n{}^2\,\sigma/\kappa_n) \tag{1.18}$$

where R is the gas constant (8.31 J mol^{-1} K^{-1}), T is the temperature (K), F is the faraday constant (96487 C mol^{-1}), t_n is the dimensionless transference coefficient of the volatile species (H_2 and methanol, in their study), σ is the ionic conductivity (S m^{-1}) and κ_n is the molar permeability coefficient (mol s^{-1} m^{-1}) for zero current density.

Using the estimation for the gas transport properties of Nafion® with pure H_2 from Sakai *et al.* [104] and with H_2 and methanol transport from [105], the figure-of-merit and the efficiency were calculated as follows (Table 1-2).

Table 1-2: Calculation of efficiency for different Nafion® with pure H_2 and Nafion® with H_2 and methanol [103]

	κ_n (mol s^{-1} m^{-1})	t_n	σ (S m^{-1})	β	η (%)
Nafion® with pure H_2	9 x 10^{-9}	1/2	10	74	79
Nafion® with H_2 and methanol	5 x 10^{-6}	5	4.8	32	70
		10	1.2		
		20	0.3		

1.3.2.2. Comparison of the compression methods (MHC & EHC)

Although EHCs seem to have a very high efficiency, these devices still suffer from disadvantages, such as the (still too) low power density and the (possibly large) over potential needed to dissociate hydrogen at the anode (especially if impure), which have not been taken into account in the previous estimation of the efficiency [103]. Note that the cathode reaction (recombination of protons into H_2 at the cathode) is believed to be only mildly limiting the overall process (there are no impurities on the cathode side, because the PEM enables high selectivity in proton transport). Contrary to the mechanical hydrogen compression (MHC), which is accomplished using diaphragm and piston pumps in an adiabatic process, that requires to be divided into stages in order to reduce the heating of the system and increase the efficiency, the EHC is an isothermal and single-stage process, as claimed by HyET company. HyET has also stated that single-stage electrochemical hydrogen compression can even reach 100 MPa [106] starting from room pressure, a very impressive performance (but obtained for a small demonstration cell: 1 cm^2 geometric area). In practice for large units, compression to these high-pressure levels will likely be made with several stages of intermediate compression. The thermodynamic process taking place in an EHC is described using the isothermal compression formula. The minimum electrical work needed for the system is the theoretical work of compression, as defined by the Nernst equation [107] (equation (1.19)).

$$V_{\text{theor}} = \frac{RT}{nF} \ln\left(\frac{P_2}{P_1}\right) \tag{1.19}$$

Where n is the mole number (mol), P_1 is the pressure at the anode (inlet) side and P_2 is the pressure at the cathode (outlet) side. According to Faraday's law (equation (1.20)):

$$\dot{m} = \frac{MI}{nF} \tag{1.20}$$

where $\dot{m}$ is the hydrogen mass flow (kg s^{-1}), I is the current (A), M is the molar mass (kg mol^{-1})?

The power needed for transporting hydrogen is given by equation (1.21):

$$W = IV_{\text{theor}} \tag{1.21}$$

By combining (Eq. (1.16)) and (Eq. (1.17)), the theoretical power needed to transfer hydrogen from the anode to the cathode can be calculated according to equation (1.22).

$$W = \frac{\dot{m}RT}{M} \ln\left(\frac{P_2}{P_1}\right) \tag{1.22}$$

Comparing the adiabatic specific compression work (equation (1.23)):

$$Q_{\mathrm{w}}^{\mathrm{MHC}} = \left[\frac{\gamma}{\gamma - 1}\right] p_1 V_1 \left[\left({}^{p_2}/_{p_1}\right)^{{}^{\gamma-1}/_{\gamma}} - 1\right] \tag{1.23}$$

And hydrogen to the hydrogen isothermal specific compression work (equation (1.24)):

$$Q_{\mathrm{w}}^{\mathrm{EHC}} = \frac{RT}{M} \ln\left(\frac{P_2}{P_1}\right) \tag{1.24}$$

Comparing the different compression energies in Figure 1.17, it is clearly more interesting using isothermal compression, *i.e.* in a EHC device, versus an MC compressor (Figure 1.17). Since for the different conditions, even at low efficiency the compression energy for EHC is still lower than the MC compression energy.

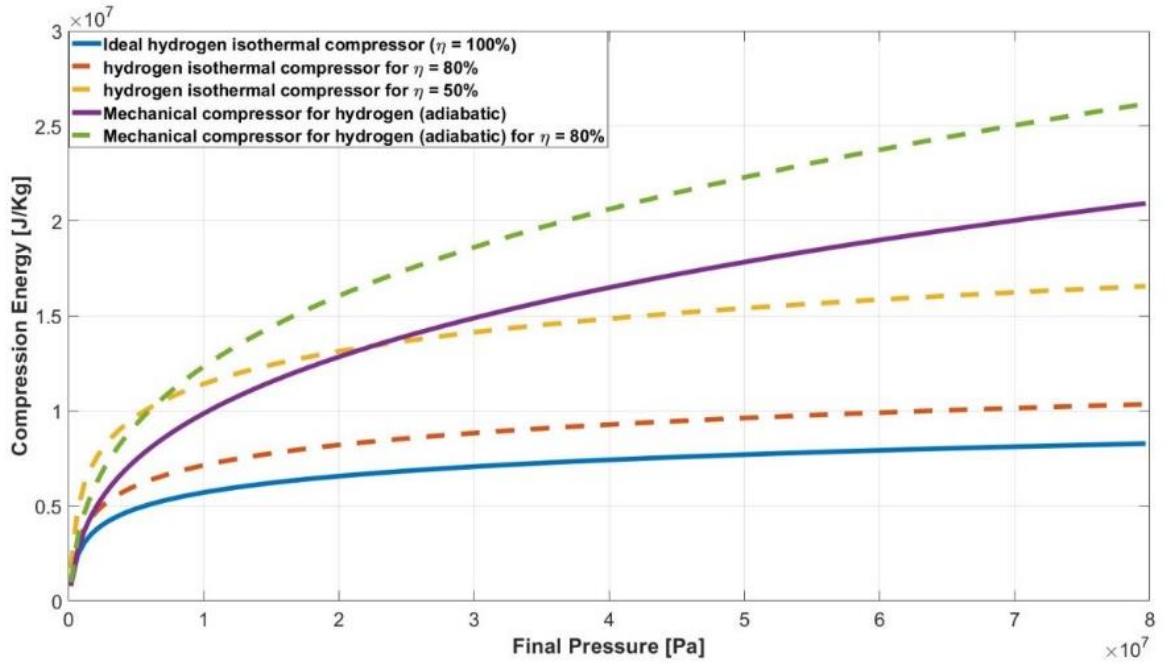

Figure 1.17: Compression energy of isothermal compression versus adiabatic compression (25°C) [11]

1.3.3. Applied aspect of electrochemical compression/purification

Besides these previous results relative to the EHC performance, the selective permeability of the membrane is another advantage of this process. Only purified hydrogen and water vapor are present at the cathode [100].

1.3.3.1. Gas permeation of impurities and other gas

At that stage, one has to underline the advantages of hydrogen pump against (non-electrochemical) membrane separation: the selectivity is imposed by the difference between the migration flow of proton and the gas permeation of impurities; the former flow is driven by the current density, while the latter depends on the gradient of partial pressure. For example in EHC, Bouwman *et al.* [75] extract hydrogen (10%) from nitrogen with a good yield of extraction. Lee *et al.* [74], achieves high-purity hydrogen from mixture (N_2, CO_2, H_2) from 10% to 90% of hydrogen. Table 1-3 represents the gas permeability coefficient and diffusivity coefficient for the usual impurities for different operating conditions.

Table 1-3: Permeability and diffusion of gases in several Nafion® membranes

	Gas permeability coefficient k_i (mol m^{-1} s^{-1} Pa^{-1})	**Diffusivity coefficient D_i (m^2 s^{-1})**	**Type of Nafion®**	**Operating conditions**	**References**
H_2	4.16 10^{-15}	104 10^{-12}	Dry N211	35°C, 2 atm	[108]
O_2	6.01 10^{-16}	5.9 10^{-12}	Dry N211	35°C, 2 atm	[108]
CO	No Data	18.0 10^{-12}	Humidified N112	35 °C	[109]
CO_2	1.36 10^{-15}	2.7 10^{-12}	Dry N211	35°C, 2 atm	[108]
	4.8 10^{-15}	14.6 10^{-12}	Dry N115	70°, 1 atm	[74]
N_2	1.4 10^{-16}	1.8 10^{-12}	Dry N211	35°C, 2 atm	[108]
	1.25 10^{-15}	6.2 10^{-12}	Dry N115	70°, 1 atm	[74]
H_2S	No Data	8.48 10^{-12}	Humidified N112	35 °C	[109]
CH_4	4.94 10^{-17}	0.45 10^{-12}	Dry N211	35°C, 2 atm	[108]
NH_3	35.7 10^{-14}	No Data	Humidified Nafion	50°C, 1 atm	[110]
	63.7 10^{-14}	1 10^{-8}	No Data	100°C, 2 atm	[111]

1.3.4. Operating conditions

The operating conditions (T, ΔP, j, U_{cell}) of the system depend on the purpose of the utilization.

When only compression is targeted, optimal energy consumption is obtained for a cell current density of j = 0.5 A cm^{-2}, and the corresponding cell voltage is close to U_{cell} = 200 mV (cell resistance is ca. 0.3 < R_{cell} < 0.4 Ω cm^2 [112]) and the pressure gradient (ΔP) between both chambers rises to 50 bar at 80°C. From a thermodynamic point of view, operating at large pressure gradient enhance the benefit of EHC over mechanical compressor.

If the device is used for the purification as well, the required current density shall reach j = 2 A cm^{-2} in order to compete with the existing (non-electrochemical) membrane compression systems, and the cell voltage shall be maintained at a reasonably-low value, typically below 1 V (*e.g.* $U_{cell} \cong$ 0.72 V).

To achieve the treatment flow, the choice of the surface area is directly related to the operating current density and the MEA resistivity. For example, for a lower current density the surface area shall be larger, but this is a balance between the capital cost (geometric area of the membrane and electrodes) and the operating costs (cell voltage, which directly depends on the applied current density).

In conclusion, among the different means to purify and compress hydrogen, the electrochemical hydrogen compressor (EHC) exhibits a wealth of assets. This system appears the best compromise if one needs to simplify the purification / compression steps of hydrogen. Compared to classical means of hydrogen purification, the EHC combines a low energetic cost, high H_2 recovery and purity, little maintenance, low cost and low temperature of operation, which neither the pressure swing adsorption, the cryogenic or the membrane processes can do. Unlike the widely used mechanical compressor, EHCs are compatible with an efficient compression even for small systems, do not lead to contamination of the output hydrogen gas and exhibit moderate capital and operational costs. On the side of compression, EHC systems are also of lower cost, and higher efficiency. Finally, EHC can do both the purification and compression in a single system (if not a single cell).

In addition, this application is compact and easily adaptable, which allows use on new applications. Barbir *et al*, 2006 [113], operate EHC for recirculation of hydrogen in a fuel cell stack, EHC cells are inserted between fuel cells of the stack avoiding additional pipe. In the same way, EHC should be used for recycling of exhaust gas of industrial processes (for example semiconductor industries) to increase sustainability because EHC is a device easy for adapting to different exhaust flow and separate hydrogen even at low concentration.

Despite their numerous assets for the purification and compression of hydrogen, electrochemical hydrogen compressors, in order to be competitive to their mechanical/thermal counterparts, need to operate at high current density (above j = 1 A cm^{-2}) at a cell voltage below U_{cell} = 0.25 V, which remains challenging with an impure feed of hydrogen; these objectives are yet to be met with pure hydrogen inlet [101]. In other words, the needs for EHC to operate at very high current density (likely above j = 2 A cm^{-2} or even j = 5 A cm^{-2}), low cell voltage (likely below U_{cell} = 0.5 V) and high differential pressure per cell (likely ΔP = 50 – 70 bar) to be (economically) competitive. The electrochemical hydrogen purification and compression requires to employ very efficient core materials for the EHC. This is true for the membrane, that ensures the gas separation, hence the purity, and enables the compression, but also for the electro catalysts, at least the one used in the anode of the first stage of the device, *i.e*. the one that operates under impure hydrogen. This electro catalyst (at the anode side of the purification cell) not only must demonstrate remarkably high HOR activity, but also be very tolerant to the poison molecules.

CONCLUSION

The common ground between these three PEM applications enable to create a structural analogy for the different phenomena. Which allows a certain parallelism between the current existing research on PEMFC and the work on PEMWE and EHC. The advancement of these applications is crucial for the development of the hydrogen sector. This work focuses mainly on the PEMWE and EHC that represents the generation and the storage of hydrogen. As a matter of fact, achieving a final state of pure hydrogen under pressure is the preliminary stage for its use and a key step for the energy efficiency of the entire chain.

The following chapters will be focusing on: First, a preliminary study was carried out using a dimensionless analytical steady state model of PEM electrolysis cells operating with large pressure gradients. This approach enables the estimation of performance using three dimensionless parameters that govern the electrochemical reaction at the catalyst layer and the mass transport through the membrane. The dimensionless numbers are: (i) a Wagner like numbers at the anode and cathode side which is the ratio between the protonic conductivity and the electrochemical kinetic at the catalyst layer, (ii) a number similar to Thiele modulus at the catalyst layers that describes the effective protonic conductivity and the operational current density, (iii) a dimensionless ratio describing the water transport process through the membrane. The model was applied to the PEMWE and it was in good agreement with the experimental data.

Secondly, hydrogen compression and purification experiments were conducted using an EHC. During these tests, the compression was performed between 0 and 30 bars for different temperatures and relative humidity. In addition, an electrochemical impedance spectroscopy (EIS) measurement was also performed. These experiments ran on both pure hydrogen and hydrogen/nitrogen mixture. After the data entropy analysis and the postmortem characterization using FTIR and SEM imaging it was found that the azote is not a benign component for this application. Surprisingly, the N_2 can lead to the degradation of the membrane due to local NH_3 synthesis.

Finally, an electrochemical impedance spectroscopy (EIS) model was developed. The EIS is a strong characterization method which inclines both theoretical and experimental approaches by modelling the different physics and electrochemical processes into a very complex system. The one-dimensional analytical model describes the electrochemical kinetics of the cell in the EIS regime. This method allows to highlight the limiting process and to predict the artefacts.

References

[1] A. F. Ghoniem, “Needs, resources and climate change: Clean and efficient conversion technologies”, *Prog. Energy Combust. Sci.*, vol. 37, nº 1, p. 15-51, Feb. 2011, doi: 10.1016/j.pecs.2010.02.006.

[2] N. Kelly, T. Gibson, et D. Ouwerkerk, “A solar-powered, high-efficiency hydrogen fueling system using high-pressure electrolysis of water: Design and initial results”, *Int. J. Hydrog. Energy*, vol. 33, nº 11, p. 2747-2764, June2008, doi: 10.1016/j.ijhydene.2008.03.036.

[3] “U.S. Department of Energy”. www.energy.gov (consulted Feb. 06, 2019).

[4] M. Yáñez, A. Ortiz, B. Brunaud, I. E. Grossmann, et I. Ortiz, “Contribution of upcycling surplus hydrogen to design a sustainable supply chain: The case study of Northern Spain”, *Appl. Energy*, vol. 231, p. 777-787, Dec. 2018, doi: 10.1016/j.apenergy.2018.09.047.

[5] T. da Silva Veras, T. S. Mozer, D. da Costa Rubim Messeder dos Santos, et A. da Silva César, “Hydrogen: Trends, production and characterization of the main process worldwide”, *Int. J. Hydrog. Energy*, vol. 42, nº 4, p. 2018-2033, Jan. 2017, doi: 10.1016/j.ijhydene.2016.08.219.

[6] I. Dincer et C. Acar, “Review and evaluation of hydrogen production methods for better sustainability”, *Int. J. Hydrog. Energy*, vol. 40, nº 34, p. 11094-11111, sept. 2015, doi: 10.1016/j.ijhydene.2014.12.035.

[7] J.-P. Magnin et J. Deseure, “Hydrogen generation in a pressurized photobioreactor: Unexpected enhancement of biohydrogen production by the phototrophic bacterium Rhodobacter capsulatus”, *Appl. Energy*, vol. 239, p. 635-643, Apr. 2019, doi: 10.1016/j.apenergy.2019.01.204.

[8] “ISO 14687-2:2012: Hydrogen fuel -- Product specification -- Part 2: Proton exchange membrane (PEM) fuel cell applications for road vehicles”. 2012, [En ligne]. Disponible sur: https://www.iso.org/standard/55083.html.

[9] “ISO 14687-3:2014: Hydrogen fuel -- Product specification -- Part 3: Proton exchange membrane (PEM) fuel cell applications for stationary appliances”. 2014, [En ligne]. Disponible sur: https://www.iso.org/standard/55078.html.

[10] G. Sdanghi, G. Maranzana, A. Celzard, et V. Fierro, “Review of the current technologies and performances of hydrogen compression for stationary and automotive applications”, *Renew. Sustain. Energy Rev.*, vol. 102, p. 150-170, Mar2019, doi: 10.1016/j.rser.2018.11.028.

[11] M. Rhandi, M. Trégaro, F. Druart, J. Deseure, et M. Chatenet, “Electrochemical hydrogen compression and purification versus competing technologies: Part I. Pros and cons”, *Chin. J. Catal.*, vol. 41, nº 5, p. 756-769, May2020, doi: 10.1016/S1872-2067(19)63404-2.

[12] S. Srinivasan, *Fuel cells: from fundamentals to applications*. New York, NY: Springer, 2006.

[13] C. Lamy, “From hydrogen production by water electrolysis to its utilization in a PEM fuel cell or in a SO fuel cell: Some considerations on the energy efficiencies”, *Int. J. Hydrog. Energy*, vol. 41, nº 34, p. 15415-15425, Sept. 2016, doi: 10.1016/j.ijhydene.2016.04.173.

[14] B. G. Pollet, I. Staffell, et J. L. Shang, “Current status of hybrid, battery and fuel cell electric vehicles: From electrochemistry to market prospects”, *Electrochimica Acta*, vol. 84, p. 235-249, Dec. 2012, doi: 10.1016/j.electacta.2012.03.172.

[15] J. Mermelstein et O. Posdziech, “Development and Demonstration of a Novel Reversible SOFC System for Utility and Micro Grid Energy Storage”, *Fuel Cells*, vol. 17, nº 4, p. 562-570, Aug. 2017, doi: 10.1002/fuce.201600185.

[16] Y. Luo, X. Wu, Y. Shi, A. F. Ghoniem, et N. Cai, “Exergy analysis of an integrated solid oxide electrolysis cell-methanation reactor for renewable energy storage”, *Appl. Energy*, vol. 215, p. 371-383, Apr. 2018, doi: 10.1016/j.apenergy.2018.02.022.

[17] Y. Yan, Q. Fang, L. Blum, et W. Lehnert, “Performance and degradation of an SOEC stack with different cell components”, *Electrochimica Acta*, vol. 258, p. 1254-1261, Dec. 2017, doi: 10.1016/j.electacta.2017.11.180.

[18] Department of Interface Chemistry and Surface Engineering, Max-Planck-Institut für Eisenforschung GmbH, Max-Planck-Strasse 1, 40237 Düsseldorf, Germany et M. Schalenbach,

"A Perspective on Low-Temperature Water Electrolysis – Challenges in Alkaline and Acidic Technology", *Int. J. Electrochem. Sci.*, p. 1173-1226, Feb. 2018, doi: 10.20964/2018.02.26.
[19] P. MILLET, "Électrolyseurs de l'eau à membrane acide", *Tech. Ing. Génie Procédés*, nº J4810, 2007.
[20] K. Zeng et D. Zhang, "Recent progress in alkaline water electrolysis for hydrogen production and applications", *Prog. Energy Combust. Sci.*, vol. 36, nº 3, p. 307-326, June2010, doi: 10.1016/j.pecs.2009.11.002.
[21] F. Barbir, "PEM electrolysis for production of hydrogen from renewable energy sources", *Sol. Energy*, vol. 78, nº 5, p. 661-669, May2005, doi: 10.1016/j.solener.2004.09.003.
[22] S. Shiva Kumar et V. Himabindu, "Hydrogen production by PEM water electrolysis – A review", *Mater. Sci. Energy Technol.*, vol. 2, nº 3, p. 442-454, Dec. 2019, doi: 10.1016/j.mset.2019.03.002.
[23] F. Aubras *et al.*, "Dimensionless approach of a polymer electrolyte membrane water electrolysis: Advanced analytical modelling", *J. Power Sources*, vol. 481, p. 228858, Jan. 2021, doi: 10.1016/j.jpowsour.2020.228858.
[24] F. T. Bacon, "Fuel cells, past, present and future", *Electrochimica Acta*, vol. 14, nº 7, p. 569-585, Jul. 1969, doi: 10.1016/0013-4686(69)87042-8.
[25] Y. Wang, D. F. Ruiz Diaz, K. S. Chen, Z. Wang, et X. C. Adroher, "Materials, technological status, and fundamentals of PEM fuel cells – A review", *Mater. Today*, vol. 32, p. 178-203, Jan. 2020, doi: 10.1016/j.mattod.2019.06.005.
[26] D. Hart, F. Lehner, S. Jones, et J. Lewis, "The Fuel Cell Industry Review 2019." Dec. 2019, [En ligne]. Disponible sur: http://www.afhypac.org/documents/publications/rapports/TheFuelCellIndustryReview2019.pdf.
[27] Y. Nonobe, "Development of the fuel cell vehicle mirai: DEVELOPMENT OF THE FUEL CELL VEHICLE MIRAI", *IEEJ Trans. Electr. Electron. Eng.*, vol. 12, nº 1, p. 5-9, Jan. 2017, doi: 10.1002/tee.22328.
[28] Y. Wang, K. S. Chen, J. Mishler, S. C. Cho, et X. C. Adroher, "A review of polymer electrolyte membrane fuel cells: Technology, applications, and needs on fundamental research", *Appl. Energy*, vol. 88, nº 4, p. 981-1007, Apr. 2011, doi: 10.1016/j.apenergy.2010.09.030.
[29] M. Trégaro, M. Rhandi, F. Druart, J. Deseure, et M. Chatenet, "Electrochemical hydrogen compression and purification versus competing technologies: Part II. Challenges in electrocatalysis", *Chin. J. Catal.*, vol. 41, nº 5, p. 770-782, May2020, doi: 10.1016/S1872-2067(19)63438-8.
[30] H.-Y. Tang, A. Santamaria, J. Kurniawan, J. W. Park, T.-H. Yang, et Y.-J. Sohn, "Developing a 3D neutron tomography method for proton exchange membrane fuel cells", *J. Power Sources*, vol. 195, nº 19, p. 6774-6781, oct. 2010, doi: 10.1016/j.jpowsour.2010.03.060.
[31] F. Aubras, « Contribution à l'étude de l'influence des régimes biphasiques sur les performances des électrolyseurs de type PEM basse pression» : approche numérique, analytique et expérimentale, université de la réunion, LE2P, 2018.
[32] D. J. Connolly et W. F. Gresham, "Fluorocarbon Vinyl Ether Polymers, US Patent", 3,282,875, Nov. 01, 1966.
[33] G. G. Gagliardi, A. Ibrahim, D. Borello, et A. El-Kharouf, "Composite Polymers Development and Application for Polymer Electrolyte Membrane Technologies—A Review", *Molecules*, vol. 25, nº 7, p. 1712, Apr. 2020, doi: 10.3390/molecules25071712.
[34] J. A. Kerres, "Development of ionomer membranes for fuel cells", *J. Membr. Sci.*, vol. 185, nº 1, p. 3-27, Apr. 2001, doi: 10.1016/S0376-7388(00)00631-1.
[35] "Nafio, Ion Exchange Materials. Safety in Handling and Use", Technical Bulletin T-01. [En ligne]. Disponible sur: https://ion-power.eu/wp-content/uploads/2020/05/Nafion-safety-handling-technical-information-Chemours-Bulletin-T-01.pdf.
[36] A. Z. Weber et J. Newman, "Transport in Polymer-Electrolyte Membranes", *J. Electrochem. Soc.*, vol. 150, nº 7, p. A1008, 2003, doi: 10.1149/1.1580822.
[37] "Ion Polymer". https://ion-power.eu/nafion/.

[38] S. S. Ivanchev, “Fluorinated proton-conduction nafion-type membranes, the past and the future”, *Russ. J. Appl. Chem.*, vol. 81, nº 4, p. 569-584, Apr. 2008, doi: 10.1134/S1070427208040010.
[39] J. Ramousse, J. Deseure, O. Lottin, S. Didierjean, et D. Maillet, “Modelling of heat, mass and charge transfer in a {PEMFC} single cell”, *J. Power Sources*, vol. 145, nº 2, p. 416-427, 2005, doi: http://dx.doi.org/10.1016/j.jpowsour.2005.01.067.
[40] S. Battersby, P. W. Teixeira, J. Beltramini, M. C. Duke, V. Rudolph, et J. C. D. da Costa, “An analysis of the Peclet and Damkohler numbers for dehydrogenation reactions using molecular sieve silica (MSS) membrane reactors”, *Catal. Today*, vol. 116, nº 1, p. 12-17, 2006.
[41] T. E. Springer, “Polymer Electrolyte Fuel Cell Model”, *J. Electrochem. Soc.*, vol. 138, nº 8, p. 2334, 1991, doi: 10.1149/1.2085971.
[42] M. Chatenet, L. Dubau, N. Job, et F. Maillard, “The (electro)catalyst|membrane interface in the Proton Exchange Membrane Fuel Cell: Similarities and differences with non-electrochemical Catalytic Membrane Reactors”, *Catal. Today*, vol. 156, nº 3-4, p. 76-86, oct. 2010, doi: 10.1016/j.cattod.2010.02.028.
[43] G. Inoue et M. Kawase, “Understanding formation mechanism of heterogeneous porous structure of catalyst layer in polymer electrolyte fuel cell”, *Int. J. Hydrog. Energy*, vol. 41, nº 46, p. 21352-21365, Dec. 2016, doi: 10.1016/j.ijhydene.2016.08.029.
[44] F. Maillard, S. Pronkin, et E. R. Savinova, “Influence of size on the electrocatalytic activities of supported metal nanoparticles in fuel cells related reactions”, in *Handbook of Fuel Cells*, W. Vielstich, A. Lamm, H. A. Gasteiger, et H. Yokokawa, Éd. Chichester, UK: John Wiley & Sons, Ltd, 2010.
[45] E. Guilminot *et al.*, “Membrane and Active Layer Degradation upon PEMFC Steady-State Operation”, *J. Electrochem. Soc.*, vol. 154, nº 11, p. B1106, 2007, doi: 10.1149/1.2775218.
[46] H. Wu, “Mathematical Modeling of Transient Transport Phenomena in PEM Fuel Cells”, University of Waterloo, Canada, 2009.
[47] Y. Wang, C.-Y. Wang, et K. S. Chen, “Elucidating differences between carbon paper and carbon cloth in polymer electrolyte fuel cells”, *Electrochimica Acta*, vol. 52, nº 12, p. 3965-3975, Mar. 2007, doi: 10.1016/j.electacta.2006.11.012.
[48] R. Omrani et B. Shabani, “Review of gas diffusion layer for proton exchange membrane-based technologies with a focus on unitised regenerative fuel cells”, *Int. J. Hydrog. Energy*, vol. 44, nº 7, p. 3834-3860, Feb. 2019, doi: 10.1016/j.ijhydene.2018.12.120.
[49] S. A. Grigoriev, P. Millet, S. A. Volobuev, et V. N. Fateev, “Optimization of porous current collectors for PEM water electrolysers”, *Int. J. Hydrog. Energy*, vol. 34, nº 11, p. 4968-4973, Jun. 2009, doi: 10.1016/j.ijhydene.2008.11.056.
[50] P. Millet, S. A. Grigoriev, et V. I. Porembskiy, “Development and characterisation of a pressurized PEM bi-stack electrolyser: PEM water electrolysis”, *Int. J. Energy Res.*, vol. 37, nº 5, p. 449-456, Apr. 2013, doi: 10.1002/er.2916.
[51] C. M. Hwang *et al.*, “Influence of properties of gas diffusion layers on the performance of polymer electrolyte-based unitized reversible fuel cells”, *Int. J. Hydrog. Energy*, vol. 36, nº 2, p. 1740-1753, Jan. 2011, doi: 10.1016/j.ijhydene.2010.10.091.
[52] S. A. Grigoriev, I. G. Shtatniy, P. Millet, V. I. Porembsky, et V. N. Fateev, “Description and characterization of an electrochemical hydrogen compressor/concentrator based on solid polymer electrolyte technology”, *Int. J. Hydrog. Energy*, vol. 36, nº 6, p. 4148-4155, Mar2011, doi: 10.1016/j.ijhydene.2010.07.012.
[53] D. M. Neto, M. C. Oliveira, J. L. Alves, et L. F. Menezes, “Numerical Study on the Formability of Metallic Bipolar Plates for Proton Exchange Membrane (PEM) Fuel Cells”, *Metals*, vol. 9, nº 7, p. 810, Jul. 2019, doi: 10.3390/met9070810.
[54] T. Anthony, «Transferts d’eau et de chaleur dans une pile à combustible à membrane : mise en évidence expérimentale du couplage et analyse des mécanismes», Université de Lorraine, LEMTA, 2013.
[55] X. Z. Yuan, H. Wang, J. Zhang, et D. Wilkinson, “Bipolar Plates for PEM Fuel Cells-From Materials to Processing”, 2006.

[56] L. Peng et Z. Wei, “Catalyst Engineering for Electrochemical Energy Conversion from Water to Water: Water Electrolysis and the Hydrogen Fuel Cell”, *Engineering*, vol. 6, nº 6, p. 653-679, Jun. 2020, doi: 10.1016/j.eng.2019.07.028.
[57] S. A. Grigoriev, I. G. Shtatniy, P. Millet, V. I. Porembsky, et V. N. Fateev, “Description and characterization of an electrochemical hydrogen compressor/concentrator based on solid polymer electrolyte technology”, *Int. J. Hydrog. Energy*, vol. 36, nº 6, p. 4148-4155, Mar. 2011, doi: 10.1016/j.ijhydene.2010.07.012.
[58] C. Rozain et P. Millet, “Electrochemical characterization of Polymer Electrolyte Membrane Water Electrolysis Cells”, *Electrochimica Acta*, vol. 131, p. 160-167, June2014, doi: 10.1016/j.electacta.2014.01.099.
[59] L. Wang, “A parametric study of PEM fuel cell performances”, *Int. J. Hydrog. Energy*, vol. 28, nº 11, p. 1263-1272, Nov. 2003, doi: 10.1016/S0360-3199(02)00284-7.
[60] C. Casati, P. Longhi, L. Zanderighi, et F. Bianchi, “Some fundamental aspects in electrochemical hydrogen purification/compression”, *J. Power Sources*, vol. 180, nº 1, p. 103-113, May 2008, doi: 10.1016/j.jpowsour.2008.01.096.
[61] T. A. Zawodzinski, M. Neeman, L. O. Sillerud, et S. Gottesfeld, “Determination of water diffusion coefficients in perfluorosulfonate ionomeric membranes”, *J. Phys. Chem.*, vol. 95, nº 15, p. 6040-6044, Jul. 1991, doi: 10.1021/j100168a060.
[62] J. T. Hinatsu, “Water Uptake of Perfluorosulfonic Acid Membranes from Liquid Water and Water Vapor”, *J. Electrochem. Soc.*, vol. 141, nº 6, p. 1493, 1994, doi: 10.1149/1.2054951.
[63] S. Ge, X. Li, B. Yi, et I.-M. Hsing, “Absorption, Desorption, and Transport of Water in Polymer Electrolyte Membranes for Fuel Cells”, *J. Electrochem. Soc.*, vol. 152, nº 6, p. A1149, 2005, doi: 10.1149/1.1899263.
[64] A. Kusoglu, B. L. Kienitz, et A. Z. Weber, “Understanding the Effects of Compression and Constraints on Water Uptake of Fuel-Cell Membranes”, *J. Electrochem. Soc.*, vol. 158, nº 12, p. B1504, 2011, doi: 10.1149/2.097112jes.
[65] P. W. Majsztrik, M. B. Satterfield, A. B. Bocarsly, et J. B. Benziger, “Water sorption, desorption and transport in Nafion membranes”, *J. Membr. Sci.*, vol. 301, nº 1-2, p. 93-106, sept. 2007, doi: 10.1016/j.memsci.2007.06.022.
[66] D. M. Bernardi et M. W. Verbrugge, “Mathematical model of a gas diffusion electrode bonded to a polymer electrolyte”, *AIChE J.*, vol. 37, nº 8, p. 1151-1163, Aug 1991, doi: 10.1002/aic.690370805.
[67] D. Bessarabov, H. Wang, H. Li, et N. Zhao, Éd., *PEM Electrolysis for Hydrogen Production: Principles and Applications*. CRC Press, 2015.
[68] S. S. Kocha, J. Deliang Yang, et J. S. Yi, “Characterization of gas crossover and its implications in PEM fuel cells”, *AIChE J.*, vol. 52, nº 5, p. 1916-1925, May 2006, doi: 10.1002/aic.10780.
[69] X. Cheng *et al.*, “Hydrogen crossover in high-temperature PEM fuel cells”, *J. Power Sources*, vol. 167, nº 1, p. 25-31, May 2007, doi: 10.1016/j.jpowsour.2007.02.027.
[70] N. T. Truc, S. Ito, et K. Fushinobu, “Numerical and experimental investigation on the reactant gas crossover in a PEM fuel cell”, *Int. J. Heat Mass Transf.*, vol. 127, p. 447-456, Dec. 2018, doi: 10.1016/j.ijheatmasstransfer.2018.07.092.
[71] A. Brunetti *et al.*, “New approach for the evaluation of membranes transport properties for polymer electrolyte membrane fuel cells”, *J. Power Sources*, vol. 205, p. 222-230, May 2012, doi: 10.1016/j.jpowsour.2012.01.108.
[72] K. D. Baik, B. K. Hong, et M. S. Kim, “Effects of operating parameters on hydrogen crossover rate through Nafion® membranes in polymer electrolyte membrane fuel cells”, *Renew. Energy*, vol. 57, p. 234-239, sept. 2013, doi: 10.1016/j.renene.2013.01.046.
[73] M. Schalenbach, M. Carmo, D. L. Fritz, J. Mergel, et D. Stolten, “Pressurized PEM water electrolysis: Efficiency and gas crossover”, *Int. J. Hydrog. Energy*, vol. 38, nº 35, p. 14921-14933, Nov. 2013, doi: 10.1016/j.ijhydene.2013.09.013.
[74] H. K. Lee, H. Y. Choi, K. H. Choi, J. H. Park, et T. H. Lee, “Hydrogen separation using electrochemical method”, *J. Power Sources*, vol. 132, nº 1-2, p. 92-98, May 2004, doi: 10.1016/j.jpowsour.2003.12.056.

[75] P. J. Bouwman *et al.*, "(Invited) Electrochemical Hydrogen Compression", *ECS Trans.*, vol. 64, nº 3, p. 1009-1018, Aug. 2014, doi: 10.1149/06403.1009ecst.
[76] D. Bastani, N. Esmaeili, et M. Asadollahi, "Polymeric mixed matrix membranes containing zeolites as a filler for gas separation applications: A review", *J. Ind. Eng. Chem.*, vol. 19, nº 2, p. 375-393, Mar. 2013, doi: 10.1016/j.jiec.2012.09.019.
[77] P. C. K. Vesborg et T. F. Jaramillo, "Addressing the terawatt challenge: scalability in the supply of chemical elements for renewable energy", *RSC Adv.*, vol. 2, nº 21, p. 7933, 2012, doi: 10.1039/c2ra20839c.
[78] J. Bonjour, J.-B. Chalfen, et F. Meunier, "Temperature Swing Adsorption Process with Indirect Cooling and Heating", *Ind. Eng. Chem. Res.*, vol. 41, nº 23, p. 5802-5811, Nov. 2002, doi: 10.1021/ie011011j.
[79] J. Sedlak, J. Austin, et A. Laconti, "Hydrogen recovery and purification using the solid polymer electrolyte electrolysis cell", *Int. J. Hydrog. Energy*, vol. 6, nº 1, p. 45-51, 1981, doi: 10.1016/0360-3199(81)90096-3.
[80] R. Lambert Michael et Grant, Robert, Bruce, "Solid-state gas purifier", Oct. 04, 2007.
[81] A. Golmakani, S. Fatemi, et J. Tamnanloo, "Investigating PSA, VSA, and TSA methods in SMR unit of refineries for hydrogen production with fuel cell specification", *Sep. Purif. Technol.*, vol. 176, p. 73-91, Apr. 2017, doi: 10.1016/j.seppur.2016.11.030.
[82] R. Agrawal, S. R. Auvil, S. P. DiMartino, J. S. Choe, et J. A. Hopkins, "Membrane/cryogenic hybrid processes for hydrogen purification", *Gas Sep. Purif.*, vol. 2, nº 1, p. 9-15, Mar. 1988, doi: 10.1016/0950-4214(88)80036-7.
[83] G. Q. Miller et Stoecker, J, "Selection of a hydrogen separation process", présenté à ational Petroleum Refiners Association annual meeting, San Francisco, CA (USA), 19-21, San Francisco, Jan. 1989.
[84] R. Agrawal, S. R. Auvil, S. P. DiMartino, J. S. Choe, et J. A. Hopkins, "Membrane/cryogenic hybrid processes for hydrogen purification", *Gas Sep. Purif.*, vol. 2, nº 1, p. 9-15, Mar. 1988, doi: 10.1016/0950-4214(88)80036-7.
[85] S. Sircar et T. C. Golden, "Purification of Hydrogen by Pressure Swing Adsorption", *Sep. Sci. Technol.*, vol. 35, nº 5, p. 667-687, Jan. 2000, doi: 10.1081/SS-100100183.
[86] A. Abdeljaoued, F. Relvas, A. Mendes, et M. H. Chahbani, "Simulation and experimental results of a PSA process for production of hydrogen used in fuel cells", *J. Environ. Chem. Eng.*, vol. 6, nº 1, p. 338-355, Feb. 2018, doi: 10.1016/j.jece.2017.12.010.
[87] J. Xiao, L. Fang, P. Bénard, et R. Chahine, "Parametric study of pressure swing adsorption cycle for hydrogen purification using Cu-BTC", *Int. J. Hydrog. Energy*, vol. 43, nº 30, p. 13962-13974, Jul. 2018, doi: 10.1016/j.ijhydene.2018.05.054.
[88] A. Yokozeki et M. B. Shiflett, "Hydrogen purification using room-temperature ionic liquids", *Appl. Energy*, vol. 84, nº 3, p. 351-361, Mar. 2007, doi: 10.1016/j.apenergy.2006.06.002.
[89] M. Mondal et A. Datta, "Energy transfer in hydrogen separation from syngas using pressure swing adsorption (PSA) process: a thermodynamic model: Hydrogen separation using PSA", *Int. J. Energy Res.*, vol. 41, nº 3, p. 448-458, Mar. 2017, doi: 10.1002/er.3627.
[90] V. I. Agueda *et al.*, "Adsorption and diffusion of H 2 , N 2 , CO, CH 4 and CO 2 in UTSA-16 metal-organic framework extrudates", *Chem. Eng. Sci.*, vol. 124, p. 159-169, Mar2015, doi: 10.1016/j.ces.2014.08.039.
[91] N. A. Al-Mufachi, N. V. Rees, et R. Steinberger-Wilkens, "Hydrogen selective membranes: A review of palladium-based dense metal membranes", *Renew. Sustain. Energy Rev.*, vol. 47, p. 540-551, Jul. 2015, doi: 10.1016/j.rser.2015.03.026.
[92] M. Hong, S. Li, J. L. Falconer, et R. D. Noble, "Hydrogen purification using a SAPO-34 membrane", *J. Membr. Sci.*, vol. 307, nº 2, p. 277-283, Jan. 2008, doi: 10.1016/j.memsci.2007.09.031.
[93] M. D. Dolan, D. M. Viano, M. J. Langley, et K. E. Lamb, "Tubular vanadium membranes for hydrogen purification", *J. Membr. Sci.*, vol. 549, p. 306-311, Mar. 2018, doi: 10.1016/j.memsci.2017.12.031.

[94] R. D. Noble et S. A. Stern, Éd., *Membrane separations technology: principles and applications*. Amsterdam ; New York: Elsevier, 1995.
[95] D. Bastani, N. Esmaeili, et M. Asadollahi, "Polymeric mixed matrix membranes containing zeolites as a filler for gas separation applications: A review", *J. Ind. Eng. Chem.*, vol. 19, nº 2, p. 375-393, Mar. 2013, doi: 10.1016/j.jiec.2012.09.019.
[96] Z. Zhu, J. Hou, W. He, et W. Liu, "High-performance Ba(Zr 0.1 Ce 0.7 Y 0.2)O 3−δ asymmetrical ceramic membrane with external short circuit for hydrogen separation", *J. Alloys Compd.*, vol. 660, p. 231-234, Mar. 2016, doi: 10.1016/j.jallcom.2015.11.065.
[97] E. Rebollo *et al.*, "Exceptional hydrogen permeation of all-ceramic composite robust membranes based on $BaCe_{0.65}Zr_{0.20}Y_{0.15}O_{3-\delta}$ and Y- or Gd-doped ceria", *Energy Environ. Sci.*, vol. 8, nº 12, p. 3675-3686, 2015, doi: 10.1039/C5EE01793A.
[98] G. Petitpas et S. M. Aceves, "The isentropic expansion energy of compressed and cryogenic hydrogen", *Int. J. Hydrog. Energy*, vol. 39, nº 35, p. 20319-20323, Dec. 2014, doi: 10.1016/j.ijhydene.2014.10.031.
[99] B. Michael, P. K. D, P. A. I, S. Panos, et V. Spyros, "An electrochemical hydrogen compression model", *Chem. Eng. Trans.*, p. 1213–1218, 2018008, doi: 10.3303/CET1870203.
[100] R. Ströbel, M. Oszcipok, M. Fasil, B. Rohland, L. Jörissen, et J. Garche, "The compression of hydrogen in an electrochemical cell based on a PE fuel cell design", *J. Power Sources*, vol. 105, nº 2, p. 208-215, Mar. 2002, doi: 10.1016/S0378-7753(01)00941-7.
[101] H. Monjid, "Electrochemical Compression". DOE Hydrogen & Fuel Cells Program, June14, 2018, [En ligne]. Disponible sur: https://www.hydrogen.energy.gov/pdfs/review18/pd136_hamdan_2018_o.pdf.
[102] W. Vielstich, H. Yokokawa, et H. Gasteiger, Éd., *Advances in electrocatalysis, materials, diagnostics, and durability ; part 2*. Chichester: Wiley, 2009.
[103] J. Catalano, A. Bentien, D. N. Østedgaard-Munck, et S. Kjelstrup, "Efficiency of electrochemical gas compression, pumping and power generation in membranes", *J. Membr. Sci.*, vol. 478, p. 37-48, Mar2015, doi: 10.1016/j.memsci.2014.12.042.
[104] T. Sakai, "Gas Permeation Properties of Solid Polymer Electrolyte (SPE) Membranes", *J. Electrochem. Soc.*, vol. 132, nº 6, p. 1328, 1985, doi: 10.1149/1.2114111.
[105] R. P. W. J. Struis, S. Stucki, et M. Wiedorn, "A membrane reactor for methanol synthesis", *J. Membr. Sci.*, vol. 113, nº 1, p. 93-100, May1996, doi: 10.1016/0376-7388(95)00222-7.
[106] P. Bouwman, "Electrochemical Hydrogen Compression (EHC) solutions for hydrogen infrastructure", *Fuel Cells Bull.*, vol. 2014, nº 5, p. 12-16, May 2014, doi: 10.1016/S1464-2859(14)70149-X.
[107] L. Lipp, "Electrochemical Hydrogen Compressor", DOE--FCE003727, 1235441, Jan. 2016. doi: 10.2172/1235441.
[108] M. Mukaddam, E. Litwiller, et I. Pinnau, "Gas Sorption, Diffusion, and Permeation in Nafion", *Macromolecules*, vol. 49, nº 1, p. 280-286, Jan. 2016, doi: 10.1021/acs.macromol.5b02578.
[109] V. A. Sethuraman, S. Khan, J. S. Jur, A. T. Haug, et J. W. Weidner, "Measuring oxygen, carbon monoxide and hydrogen sulfide diffusion coefficient and solubility in Nafion membranes", *Electrochimica Acta*, vol. 54, nº 27, p. 6850-6860, Nov. 2009, doi: 10.1016/j.electacta.2009.06.068.
[110] S. Suzuki, H. Muroyama, T. Matsui, et K. Eguchi, "Fundamental studies on direct ammonia fuel cell employing anion exchange membrane", *J. Power Sources*, vol. 208, p. 257-262, Jun 2012, doi: 10.1016/j.jpowsour.2012.02.043.
[111] Y. He et E. L. Cussler, "Ammonia permeabilities of perfluorosulfonic membranes in various ionic forms", *J. Membr. Sci.*, vol. 68, nº 1-2, p. 43-52, Apr. 1992, doi: 10.1016/0376-7388(92)80148-D.
[112] W. Vielstich, Éd., *Fuel cell technology and applications: pt. 1*, Reprinted. Chichester: Wiley, 2007.
[113] F. Barbir et H. Görgün, "Electrochemical hydrogen pump for recirculation of hydrogen in a fuel cell stack", *J. Appl. Electrochem.*, vol. 37, nº 3, p. 359-365, Feb. 2007, doi: 10.1007/s10800-006-9266-0.

Chapter 2: Modeling of Polymer Electrolyte Membrane cells (steady state, DC modeling)

2. Modeling of Polymer Electrolyte Membrane cells (steady state, DC modeling)

2.1 State of art on modeling PEM

The most common models in the literature are one-dimensional (1D) models. These studies often investigate critical issues of PEM devices. For example, water transport is an essential matter for both a fuel cell and an electrochemical compressor. The two-phase flow in the anode side is another critical point for PEMWE.

The model presented by S. S. Lafmejani *et al.* [3] is a comprehensive CFD model that comprises multiphase flow in porous media and micro-channel, electro-chemistry in catalyst layers, ion transport in membrane. Moreover, this model can help to investigate the gas–liquid flow impacts on the electrolysis performance. In addition, the modeling results can be used for improved porous transport layer, catalyst layer and flow field design for water electrolysis cells. According to A. Nouri-Khorasani *et al.* [4], the wettability of the catalyst proves to be the most influential material property for bubble-flow initiation. Modeling and CFD simulations are powerful tools to understand the bubble flow behavior [5], however the computation time required is not compatible with online analysis of real patterns of electrolysis cells. The best experimental way consists of in-situ neutron imaging [6], [7]. This technique has highlighted that the water management through the membrane plays a critical role in cell performances [8]. In a previous work of Aubras *et al.* [9], a 1D model of a membrane electrode assembly (MEA) has been performed to analyze the cell behavior [9]. However, the computing results of numerical modeling do not provide characteristic parameters to access a faster analysis of experimental data.

The 1D study can also focus on the different phenomena (such as charge and mass transport balances) at the anodic CL, the cathodic CL, and the membrane [2].

Analytical modeling is a mathematical analysis that has a closed-form solution. It is the mathematical solution of differential equations representing the internal phenomenology present within a given system as a mathematical analytic function. In addition to this, the dimensionless approach allows to obtain a set of dimensionless mathematical equations. This approach is used to discuss mean values and spatial distributions of current densities, over potential, water contents and membrane resistance. In the literature, studies on the analytical modeling approaches have essentially focused on fuel cells.

Jeng *et al.* [10] proposed an analytical resolution of mass transport, electrochemical kinetics and charge balance at the catalytic layer and the cathodic diffusion layer. Nevertheless, the work provides no

information concerning the mass transport inside the membrane as well as on its state of hydration. These authors exhibit a phenomenological approach based on dimensionless numbers.

Gyenge [11] proposed an original study of the dimensionless numbers present at the MEA of a PEM fuel cell by means of the Quraishi-fahidy method [12]. Experimentally validated, the model makes it possible to obtain spatial quantities such as water content, over potentials and current densities. Another interesting aspect of this study is the array of dimensionless numbers specific to fuel cells including the Wagner number [13] and the number of Damkholer [14]. These dimensionless numbers will be presented in this study.

Current literature suggests that the analytical modeling and dimensionless methods are currently underutilized in fuel cell (PEMFC) and electrolysis (PEMWE) domain. Therefore, this work presents an innovative analytic approach to quantify electrochemical performances based on the dimensionless methodology. The model is based on reported studies in the literature on the dimensionless modeling of the MEA of a fuel cell [11][10].

2.2 Polymer Electrolyte Membrane Cell Model

In this section, the different assumptions and equations used in the approach will be presented. The goal is to obtain a set of equations that can be solved analytically. As part of a first approach, the water content gradient is neglected in the diffusion and catalytic layer, species gradient is also neglected. Therefore, no mass balance is performed, and it is assumed that water content is equal to a constant in the catalytic layers. Therefore, the diffusion layer is not included in this model. This phenomenological description is based on mass and charge balance in the membrane, a charge balance in catalytic layers.

The catalytic layers and the membrane are assumed to be isothermal. The system is assumed to be one dimensional and considered to be functioning with a steady state $\frac{d}{dt} = 0$. The protonic conductivity occurs the main part of ohmic drop.

.

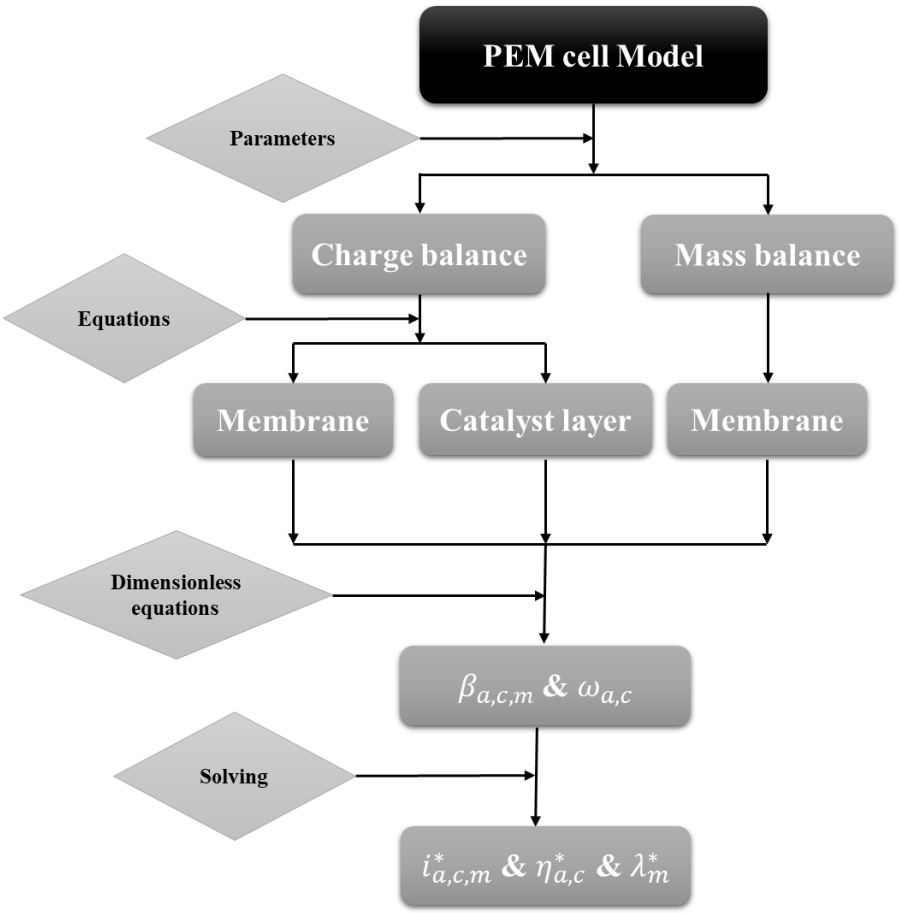

Figure 2-1 : PEM cell model equations & solving steps

As shown in Figure 2-1, the model starts by defining all the basic parameters used to describe the cell functioning or the material characteristics. Then the equations are outlined for mass balance in the membrane and charge balance in the catalyst layer and the membrane. Next using the dimensionless method, a new set of equations is determined. This will reveal the form of the dimensionless number which represents the different phenomena in the cell. Finally, the new equations will be solved both analytically and numerically to give a mathematical solution of this system.

2.2.1 Charge balance in the catalytic layer

Whether it is the anode or cathode, the equations will be the same. It is necessary to focus on the current densities involved in the catalytic layer, as a volume electrode. Catalytic layer is composed of an ionic conductor and an electronic conductor, it is also the location of the electrochemical reaction.

i_{ion} is ionic current density in protonic conductor, i_{elect} is electronic current density in electronic conductor, and J is current density in the cell.

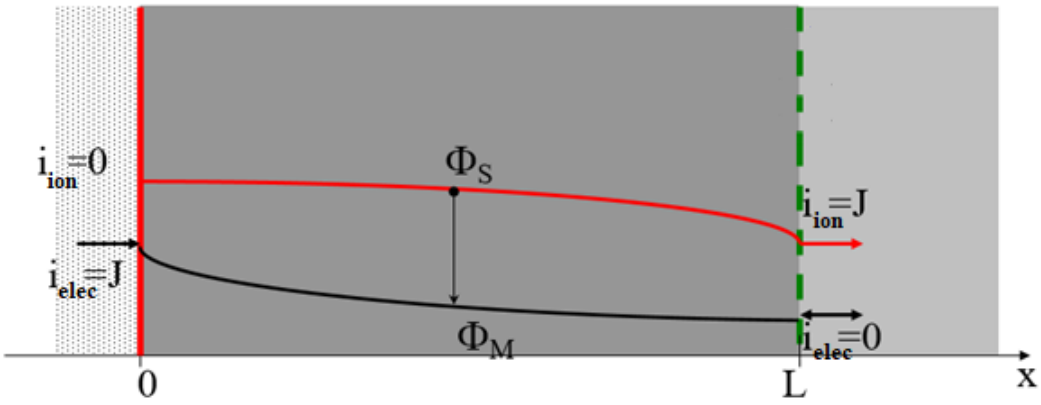

Figure 2-2 : Schematic representation of potential variation at the catalyst layer

At both limits of the catalytic layer is J= i_{ionic} for membrane/catalytic layer side and J= $i_{electronic}$ for gas diffusion/catalytic layer side (Figure 2-2).

However, through the catalyst layer:

$$J = i_{ionic} + i_{electronic} \tag{2.1}$$

The current conservation gives:

$$\vec{\nabla}J = \vec{\nabla}i_{ionic} + \vec{\nabla}i_{electronic} = 0 \rightarrow \vec{\nabla}i_{ionic} = -\vec{\nabla}i_{electronic} \quad (2.2)$$

Butler-Volmer's law describes electrochemical kinetics at the electrode [15] [16]:

$$i_k = i_{0,k}\left(e^{\frac{\alpha_k F\eta_k}{RT}} - e^{\frac{-(1-\alpha_k)F\eta_k}{RT}}\right) \quad (2.3)$$

In the 1D approach charge balance becomes:

$$\nabla_x i_k = \frac{di_k}{dx} = \frac{\gamma_k}{\delta_{act,k}} i_{0,k}\left(e^{\frac{\alpha_k F\eta_k}{RT}} - e^{\frac{-(1-\alpha_k)F\eta_k}{RT}}\right) \quad (2.4)$$

However, at high current density (quite far from the equilibrium potential $E_{eq}^{a,c}$(V) it is possible to simplify the Butler Volmer's law in Tafel's law and describes the steady state charge balance as follows: $e^{\frac{\alpha_k F\eta_k}{RT}} \gg e^{\frac{-(1-\alpha_k)F\eta_k}{RT}}$

Then electrochemical kinetics leads to the following equation:

$$\frac{di_k}{dx} = \frac{\gamma_k}{\delta_{act,k}} i_{0,k} e^{\frac{\alpha_k F\eta_k}{RT}} \quad (2.5)$$

Where, $i_{0,a}$ denotes the current exchange density (A.m^{-2}), $\gamma_{a,c}$ roughness factor (m².m^{-2}), $\alpha_{a,c}$ the anodic and cathodic exchange coefficients (-), R gas constant (J.mol^{-1}.K^{-1}), F the Faraday constant (C.mol^{-1}), T temperature (K), $\delta_{a,c}$ layer thicknesses of the anodic, cathodic catalytic layer, $\eta_{a,c,}$ the over potential at anode, cathode and membrane (V), $i_{a,c}$ the current density through the anode, cathode (A.m^{-2}) and x the axis of the system (m).

The catalytic layer is composed of an ionic phase and an electric phase. The over potential at the active layer is the difference between the ionic potential Φ_{ionic}(V) and the electric potential Φ_{elec}(V) and equilibrium potential $E_{eq}^{a,c}$ (V):

$$\eta_k = \Phi_{elec} - \Phi_{ionic} - E_{eq}^{k} \quad (2.6)$$

According to Ohm's law:

$$\begin{cases} \nabla_x \Phi_{elec} = -\dfrac{i_{k,elec}}{\sigma_{elec,}^{eff}} = -\dfrac{J - i_k}{\sigma_{elec,k}^{eff}} \\ \nabla_x \Phi_{ionic} = -\dfrac{i_k}{\sigma_{H^+,k}^{eff}} \end{cases} \quad (2.7)$$

In 1D, the derivative of the equation is:

$$\nabla_x \eta_k = \nabla_x \Phi_{elec} - \nabla_x \Phi_{ionic} \quad (2.8)$$

On the other hand, as stated in the assumptions, the protonic conductivity is very low compared to the electrical conductivity [17]: $\sigma_{elec,a}^{eff} \gg \sigma_{H^+,a}^{eff}$

As a result:

$$\nabla_x \eta_k = \frac{i_{k,ionic}}{\sigma_{H^+}^{eff}} \tag{2.9}$$

Where $\sigma_{H^+,a,c}^{eff}$ is the effective protonic conductivity (S.m) of the Nafion® phase in the catalytic layer.

Thus, for an isothermal system and a constant water content, the $\sigma_{H^+}^{eff}$ could be consider constant

By associating equations (2.5) and (2.9):

The result is a nonlinear second order differential equation, involving the current density at the active layer i_k:

$$\frac{d^2 i_k}{dx^2} = \frac{\gamma_k i_{0,k}}{\delta_{act,k}} \frac{\alpha_k F \eta_k}{RT} e^{\frac{\alpha_k F \eta_k}{RT}} \frac{d\eta_k}{dx} = \frac{\alpha_k F}{RT \sigma_{H^+,k}^{eff}} . \frac{di_k}{dx} . i_k \tag{2.10}$$

The differential equation of current density at the active layer can be written as follows:

- At the anode

$$i_a'' = \frac{\alpha_a F}{RT_a \sigma_a^{H^+}} i_a' i_a \tag{2.11}$$

- At the cathode

$$i_c'' = \frac{\alpha_c F}{RT_c \sigma_c^{H^+}} i_c' i_c \tag{2.12}$$

2.2.2 Charge balance in the membrane

The current is represented using the Ohm's law: $\vec{J} = -\sigma^m \vec{\nabla}\Phi$ And the current conservation for one dimensional approach, expressed as:

$$\vec{\nabla}.\vec{J} = 0 \leftrightarrow \Delta\Phi = 0 \leftrightarrow \vec{\nabla}\Phi = cste \tag{2.13}$$

$$\eta_m = \Phi_{elec} - \Phi_{ionic} - E_{eq}^m \tag{2.14}$$

$$\nabla\eta_m = \nabla\Phi_{elec} - \nabla\Phi_{ionic} - \nabla E_{eq}^m \rightarrow \nabla\eta_m = -\nabla\Phi_{ionic} = cste \tag{2.15}$$

The membrane is electrically isolated. Only protons can migrate from the anodic side to the cathodic side. In a case of a theoretically perfect functioning, the accumulation of protons is not taken into consideration. The distribution of the ohmic voltage drop is written using ohmic law:

$$\nabla\eta_m = \frac{i_m}{\sigma_{H^+,m}^{eff}} \tag{2.16}$$

The current density at the membrane is considered constant and equal to the operating current density imposed by the user J_0 ($i_m = J_0$). The 1D distribution of the over potential is written using a differential equation of the first order charge balance:

$$\frac{\mathrm{d}\eta_m}{\mathrm{d}x} = \frac{J_0}{\sigma_{H^+,m}^{eff}} \tag{2.17}$$

Where J_0 is the operating current density (A.m^{-2}) and the effective proton conductivity $\sigma_{H^+,m}^{eff}$ will be referred to as σ^m to simplify the notation.

2.2.3 Mass balance in the membrane

The conservation of mass for water is defined using the following equation:

$$\frac{\partial c_{H_2O}}{\partial t} + \vec{\nabla} \cdot \vec{N}_{H_2O} = 0 \tag{2.18}$$

The flux is defined using $\vec{N}_{H_2O} = -D_{H_2O}\vec{\nabla}c_{H_2O} + \vec{v}_m c_{H_2O}$. The steady-state material balance expression is $\vec{\nabla} \cdot \vec{N}_{H_2O} = 0$. Therefore:

$$\vec{\nabla} \cdot \vec{N}_{H_2O} = D_{H_2O}\Delta c_{H_2O} + \vec{\nabla}.\vec{v}_m c_{H_2O} + \vec{v}_m.\vec{\nabla}c_{H_2O} = 0 \tag{2.19}$$

Where c_{H_2O} is the bulk concentration of water (mol.m^{-3}) in the membrane, where $\vec{v}_m$ is the water velocity (m.s^{-1}) inside the membrane and D_{H_2O} is the effective diffusion coefficient of water in the membrane (m².s^{-1}).

The fluid flow at the membrane is assumed to be an incompressible thus the continuity equation is written as follow: $\vec{\nabla}.\vec{v}_m = 0$

These assumptions simplify the equation (2.19) as:

$$D_{H_2O}\Delta c_{H_2O} = \vec{v}_m.\vec{\nabla}c_{H_2O} \tag{2.20}$$

Schlögl's equation of motion describes the convective term of the mass-transfer: electric potential and pressure gradients generate convection within the pores of the ion-exchange membrane (Bernardi & Verbrugge 1991) [18]:

$$\vec{v}_m = \frac{\kappa_\Phi}{\mu} z_f c_f F \vec{\nabla}\Phi - \frac{\kappa_p}{\mu}\vec{\nabla}p \tag{2.21}$$

Where μ denotes the water viscosity (kg.m^{-1}.s^{-1}), κ_Φ is the electro-kinetic permeability (m^2), z_f is the fixed-charge number in the membrane, c_f is the fixed-charge concentration (mol.cm^{-3}) and κ_p is the hydraulic permeability (m^2).

The $\vec{\nabla}p$ is also constant by assuming in this case that it is equal to the pressure difference between the anode and the cathode. This can be proven using both the current conservation and the continuity equation for one dimensional approach:

$$\vec{\nabla}.\vec{v}_m = \frac{\kappa_\Phi}{\mu} z_f c_f F \Delta\Phi - \frac{\kappa_p}{\mu}\Delta p \;\leftrightarrow\; \Delta p = 0 \leftrightarrow\; \vec{\nabla}p = cste \tag{2.22}$$

The equation (2.20) becomes:

$$D_{H_2O}\Delta c_{H_2O} = -\frac{\kappa_\Phi}{\mu} z_f c_f F \frac{\vec{j}}{\sigma^m}.\vec{\nabla}c_{H_2O} - \frac{\kappa_p}{\mu}\vec{\nabla}p.\vec{\nabla}c_{H_2O} \quad (2.23)$$

Water molecules that are transported through the PEM from the anode to the cathode along with protons (H^+) will be referred to as water content λ_m transport in the PEM, where λ_m is the dimensionless quantity defined as follows [19]:

$$\lambda_m = \frac{EWV_{ex}c_{H_2O}}{\rho_{dry}^m} \leftrightarrow c_{H_2O} = \frac{\rho_{dry}^m \lambda_m}{EWV_{ex}} \quad (2.24)$$

Where ρ_{dry}^m (kg.m^{-3}) is the dry density of the PEM, EW is the equivalent weight (mass) of the PEM (kg.mol^{-1}), c_{H_2O} is the water concentration (mol.m^{-3}) and V_{ex} is the coefficient of expansion of the PEM.

The water mass balance can be written as follows:

$$D_{H_2O}\Delta\lambda_m = -\frac{\kappa_\Phi}{\mu} z_f c_f F \frac{\vec{j}}{\sigma^m}.\vec{\nabla}\lambda_m - \frac{\kappa_p}{\mu}\vec{\nabla}p.\vec{\nabla}\lambda_m \quad (2.25)$$

In the 1D approach mass balance becomes:

$$D_{H_2O}\Delta_x\lambda_m = -\frac{\kappa_\Phi}{\mu} z_f c_f F \frac{J}{\sigma^m}.\nabla_x\lambda_m - \frac{\kappa_p}{\mu}\nabla_x p.\nabla_x\lambda_m \quad (2.26)$$

2.3 Dimensionless approach & equation solving

It is well known that the analytical solution of the differential equations assumes a linear equation set to attain analytical solutions.

The main objective is to obtain a set of differential equations using dimensionless numbers. In order to achieve this aim, a dimensionless method should be introduced using dimensionless parameters gathered in the Table 2-1.

Table 2-1: Dimensionless parameters

Dimensionless current density	$i^*_{a,c,m} = \frac{i_{a,c,m}}{J_0}$
Dimensionless activation over potential	$\eta^*_{a,c} = \frac{\eta_{a,c}}{\frac{RT_{a,c}}{\alpha_{a,c}F}}$
Dimensionless ohmic voltage drop	$\eta^*_m = \frac{\eta_m}{\frac{RT_m}{F}}$
Characteristic length	$x^*_{a,c,m} = \frac{x_{a,c,m}}{\delta_{a,c,m}}$
Dimensionless water content	$\lambda^*_m = \frac{\lambda_m}{\lambda^{sat}_m}$
Dimensionless pressure	$p^*_m = \frac{p_m}{p^0_m}$

2.3.1 Dimensionless equations

2.3.1.1 Charge balance in the catalyst layer

- At the anode

Considering the differential equation (2.11) and the dimensionless variables (Table 2-1), the dimensionless current density i^*_a is governed by the following differential equation:

$$i^{*\prime\prime}_a = \beta_a i^{*\prime}_a i^*_a \qquad where \;\; \beta_a = \alpha_a \frac{J_0 \delta_a F}{2RT\sigma^{eff}_{H^+,a}} \tag{2.27}$$

The dimensionless over potential is obtained using the equation (2.5):

$$i_a^{*\prime} = \zeta_a \exp(\eta_a^*) \quad where\ \zeta_a = \frac{\gamma_a}{J_0} i_{0,a} \tag{2.28}$$

- At the cathode

The approach is similar at the cathode side:

$$i_c^{*\prime\prime} = \beta_c i_c^{*\prime} i_c^* \qquad where\ \beta_c = \alpha_c \frac{J_0 \delta_c F}{2RT\sigma_{H^+,c}^{eff}} \tag{2.29}$$

The dimensionless over potential is:

$$i_c^{*\prime} = -\zeta_c \exp(-\eta_c^*) \quad where\ \zeta_c = \frac{\gamma_c}{J_0} i_{0,c} \tag{2.30}$$

Table 2-2: Boundary conditions

a theoretically perfect operation, the protonic current is zero at the interface diffusion layer / anodic reaction layer	$i_a^*(0) = 0$
At the diffusion layer / cathodic catalytic layer interface, the protonic current will be considered as zero	$i_c^*(1) = 0$
Considering a constant current at the membrane equal to the operating current density	$i_a^*(1) = -1$
	$i_c^*(0) = 1$

2.3.1.2 Mass balance in the membrane

By associating equation (2.26) with the dimensionless numbers described by the parameters of Table 2-1, the mass transport at the membrane is written as follows:

$$\lambda_m^{*\prime\prime} + \beta_m \lambda_m^{*\prime} = 0 \qquad where\ \beta_m = \frac{\delta_m}{D_{H_2O}} \left(\frac{\kappa_\Phi}{\mu} z_f c_f F \frac{J_0}{\sigma^m} + \frac{\kappa_p}{\mu} \nabla p\right) \tag{2.31}$$

The boundary conditions are Dirichlet conditions, the dimensionless water content is a known constant at both ends of the membrane. For x_m^* = 0, it is equal to $\lambda_a{}^*$ and for x_m^* = 1, it is equal to $\lambda_c{}^*$.

2.3.2 Analytical solution of the dimensionless equations

In this section, the previously obtained differential equations and boundary conditions are solved, to obtain the spatial distributions and the averaged values of the current densities, over potential and water content at the membrane.

2.3.2.1 Charge balance

2.3.2.1.1 Over potential at the catalytic layer

At the anode and the cathode, the limiting processes considered are the electrochemical reactions and the proton resistance of the polymer phase. The coupling of these two phenomena is at the origin of the over potential at the catalytic layers named $\eta^*_{a,c}$ obtained previously with the differential equations involving the current density $i_{a,c}$.

At the anode, according to the equation (2.27):

$$\frac{d^2 i_a^*}{dx_a^{*\,2}} = \frac{d}{dx_a^*}\left(\beta_a . i_a^{*\,2}\right) \rightarrow \frac{d}{dx_a^*}\left(\frac{di_a^*}{dx_a^*} - \beta_a . i_a^{*\,2}\right) = 0 \rightarrow \frac{di_a^*}{dx_a^*} - \beta_a . i_a^{*\,2} = K_a^1 \qquad (2.32)$$

The equation (2.32) is non-linear. Therefore, the problem-solving method of the Riccati equation will be used to have an approximate analytical solution to the current density differential equation. The general solution is obtained as:

$$i_a^* = z_a^* + i_{a_p}^* \quad where \;\; i_{a_p}^* = cste \qquad (2.33)$$

At first, the particular solution needs to be defined:

$$\frac{di_{a_p}^*}{dx_a^*} - \beta_a . i_{a_p}^{*\,2} = -(K_a^1)^2 \;\; \rightarrow \;\; i_{a_p}^{*\,2} - \frac{\left(K_a^1\right)^2}{\beta_a} = 0 \;\; \rightarrow \;\; i_{a_p}^* = \pm\frac{|K_a^1|}{\sqrt{\beta_a}} \qquad (2.34)$$

Combining (2.32) and the equation (2.33):

$$\frac{d\left(z_a^* + i_{a_p}^*\right)}{dx_a^*} - \beta_a . \left(z_a^* + i_{a_p}^*\right)^2 = \frac{dz_a^*}{dx_a^*} - \beta_a . z_a^{*\,2} - 2\beta_a . i_{a_p}^* . z_a^* - \beta_a . i_{a_p}^{*\,2} = -(K_a^1)^2 \qquad (2.35)$$

According to (2.34):

$$i_{a_p}^{*\,2} - \frac{(K_a^1)^2}{\beta_a} = 0 \rightarrow \frac{dz_a^*}{dx_a^*} - 2\beta_a . i_{a_p}^* . z_a^* - \beta_a . z_a^{*2} = 0 \tag{2.36}$$

The equation (2.36) needs a substation to be solved. Hence: $z_a^* = \frac{1}{u_a^*} \rightarrow \frac{dz_a^*}{dx_a^*} = -\frac{1}{u_a^{*2}} \frac{du_a^*}{dx_a^*}$

The equation (2.36) can be written as follow:

$$\frac{du_a^*}{dx_a^*} + 2\beta_a . i_{a_p}^* u_a^* + \beta_a = 0 \text{ Where } u_a^* = u_{a_H}^* + u_{a_p}^* \ \& \ u_{a_p}^* = cste \tag{2.37}$$

The particular solution of the equation is:

$$\frac{du_{a_p}^*}{dx_a^*} + 2\beta_a . i_{a_p}^* u_{a_p}^* = -\beta_a \rightarrow u_{a_p}^* = -\frac{1}{2i_{a_p}^*} \tag{2.38}$$

Therefore, the general solution is:

$$\frac{du_a^*}{dx_a^*} + 2\beta_a . i_{a_p}^* u_a^* = 0 \rightarrow \frac{du_{a_H}^*}{dx_a^*} + 2\beta_a . i_{a_p}^* u_{a_H}^* = 0 \rightarrow u_{a_H}^* = K_a^2 e^{-2\beta_a . i_{a_p}^* . x_a^*} \tag{2.39}$$

Combining (2.38) and (2.39), the solution for the equation (2.37) is written as follow:

$$u_a^* = K_a^2 e^{-2\beta_a . i_{a_p}^* . x_a^*} - \frac{1}{2i_{a_p}^*} \rightarrow z_a^* = \frac{1}{K_a^2 e^{-2\beta_a . i_{a_p}^* . x_a^*} - \frac{1}{2i_{a_p}^*}} \tag{2.40}$$

The current density's analytical solution of the equation (2.28) obtained using (2.33), (2.38) and (2.40) is:

$$i_a^* = z_a^* + i_{a_p}^* \rightarrow i_a^* = \frac{1}{K_a^2 e^{-2\sqrt{\beta_a} . |K_a^1| . x_a^*} - \frac{\sqrt{\beta_a}}{2|K_a^1|}} + \frac{|K_a^1|}{\sqrt{\beta_a}} \tag{2.41}$$

At the cathode, the same equation form and problem-solving method using Riccati equation and Bernoulli equation, the current density's analytical solution will be written as follows:

$$i_c^* = \frac{1}{K_c^2 e^{-2\sqrt{\beta_c}.|K_c^1|.x_c^*} - \frac{\sqrt{\beta_c}}{2|K_c^1|}} + \frac{|K_c^1|}{\sqrt{\beta_c}} \tag{2.42}$$

With K_a^1, K_a^2, K_c^1 and K_c^2 integration constants. These constants will be determined using the boundary conditions (Table 2-2). A system of equations will be defined at both the anode and the cathode side.

At the anode:

$$\begin{cases} i_a^*(0) = \dfrac{1}{K_a^2 - \frac{\sqrt{\beta_a}}{2|K_a^1|}} + \dfrac{|K_a^1|}{\sqrt{\beta_a}} = 0 \;\rightarrow K_a^2 = -\dfrac{\sqrt{\beta_a}}{2|K_a^1|} \\ i_a^*(1) = \dfrac{1}{K_a^2 e^{-2\sqrt{\beta_a}.|K_1^a|} - \frac{\sqrt{\beta_a}}{2|K_a^1|}} + \dfrac{|K_a^1|}{\sqrt{\beta_a}} = -1 \rightarrow \dfrac{1 - e^{-2\sqrt{\beta_a}.|K_a^1|}}{1 + e^{-2\sqrt{\beta_a}.|K_a^1|}} = \dfrac{\sqrt{\beta_a}}{|K_a^1|} \end{cases} \tag{2.43}$$

At the cathode:

$$\begin{cases} i_c^*(0) = \dfrac{1}{K_c^2 - \frac{\sqrt{\beta_c}}{2|K_c^1|}} + \dfrac{|K_c^1|}{\sqrt{\beta_c}} = 1 \;\rightarrow\; K_c^2 = \dfrac{1 + \frac{\sqrt{\beta_c}}{|K_c^1|}}{2\left(1 - \frac{|K_c^1|}{\sqrt{\beta_c}}\right)} \\ i_c^*(1) = \dfrac{1}{K_c^2 e^{-2\sqrt{\beta_c}.|K_1^c|} - \frac{\sqrt{\beta_c}}{2|K_c^1|}} + \dfrac{|K_c^1|}{\sqrt{\beta_c}} = 0 \;\rightarrow \dfrac{|K_c^1|}{\sqrt{\beta_c}} - \left(1 + \dfrac{|K_c^1|}{\sqrt{\beta_c}}\right) e^{2\sqrt{\beta_c}.|K_c^1|} = 1 \end{cases} \tag{2.44}$$

Giving the complexity of these systems (2.43) & (2.44), the integration constants will be determined using a numerical solving method.

2.3.2.1.2 Activation over potential

The over potential will firstly be defined using the equations (2.28) & (2.30) allow to write that:

$$\eta_a^* = \ln\left(\frac{i_a^{*\prime}}{\zeta_a}\right) = \ln\left(\frac{\sqrt{\beta_a}K_a^2K_a^1}{\zeta_a} \frac{\exp\left(-\sqrt{\beta_a}K_a^2x_a^*\right)}{\left(K_a^1\exp\left(-\sqrt{\beta_a}K_a^2x_a^*\right) - \frac{\sqrt{\beta_a}}{2K_a^2}\right)^2}\right) \quad where\ \zeta_a = \frac{\gamma_a}{J_0} i_{0,a} \tag{2.45}$$

Highlighting the Wagner number ($\omega_{a,c}$):

$$\eta_a^* = \ln\left(-\frac{\beta_a^{\frac{3}{2}}K_a^2|K_a^1|}{\omega_a}\frac{\exp\left(-2\sqrt{\beta_a}|K_a^1|x_a^*\right)}{\left(K_a^2\exp\left(-2\sqrt{\beta_a}|K_a^1|x_a^*\right)-\frac{\sqrt{\beta_a}}{2|K_a^1|}\right)^2}\right) \quad where\ \omega_a = \zeta_a\beta_a = \frac{\gamma_a i_{0,a}\delta_a F}{2RT_a\sigma_a^{H^+}} \tag{2.47}$$

$$\eta_c^* = -\ln\left(-\frac{i_c^{*\prime}}{\zeta_c}\right) = -\ln\left(\frac{\sqrt{\beta_c}K_c^2K_c^1}{\zeta_c}\frac{\exp\left(-\sqrt{\beta_c}K_c^2x_c^*\right)}{\left(K_c^1\exp\left(-\sqrt{\beta_c}K_c^2x_c^*\right)-\frac{\sqrt{\beta_c}}{2K_c^2}\right)^2}\right) \quad where\ \zeta_c = \frac{\gamma_c}{J_0}i_{0,c} \tag{2.46}$$

$$\eta_c^* = -\ln\left(-\frac{\beta_c^{\frac{3}{2}}K_c^2|K_c^1|}{\omega_c}\frac{\exp\left(-2\sqrt{\beta_c}|K_c^1|x_c^*\right)}{\left(K_c^2\exp\left(-2\sqrt{\beta_c}|K_c^1|x_c^*\right)-\frac{\sqrt{\beta_c}}{2|K_c^1|}\right)^2}\right) \quad where\ \omega_C = \zeta_c\beta_c = \frac{\gamma_c i_{0,c}\delta_c F}{2RT_c\sigma_c^{H^+}} \tag{2.48}$$

The average anodic and cathodic activation over potential are obtained by the relation:

$$\overline{\eta_{a,c}^*} = \int_0^1 \eta_{a,c}^*\, dx_{a,c}^* \tag{2.49}$$

The calculation of this average will be done also using a numerical solving method, due to complexity of this integration, for example at the anode side the average anodic activation over potential is calculated as follows:

$$\overline{\eta_a^*} = \int_0^1 \eta_a^*\, dx_a^* = \ln\left(\frac{\sqrt{\beta_a}K_a^2K_a^1}{\zeta_a}\right) + \frac{-\sqrt{\beta_a}K_a^2x_a^*}{2} + \int_0^1 2\ln\left(K_a^1\, exp\left(-\sqrt{\beta_a}K_a^2x_a^*\right)-\frac{\sqrt{\beta_a}}{2K_a^2}\right)dx_a^* \tag{2.50}$$

The last term of this integral is the part where the numerical calculation will be needed. The same thing goes for the cathode side.

2.3.2.1.3 Over potential through the membrane

The distribution of the ohmic drop to the membrane is written as follows:

$$\eta_m = \frac{i_m}{\sigma_{H^+,m}^{eff}}x_m + K \;\leftrightarrow\; \eta_m^* = K_m^1\, x_m^* + K_m^2 \quad where\ \ K_m^1 = \frac{-\frac{i_m}{\sigma_{H^+,m}^{eff}}}{\frac{RT_m}{F}}\delta_m\ \&\ K_m^2 = \frac{RT_m}{F}K \tag{2.51}$$

The distribution of the dimensionless ohmic drop to the membrane is written as follows:

$$\eta_m^* = K_m^1x_m^* + K_m^2 \quad where\ K_m^2 = \eta_{a,int}^* \tag{2.52}$$

The average ohmic drop is then calculated as follow:

$$\overline{\eta_m^*} = -|\eta_m^*(0) - \eta_m^*(1)| \tag{2.53}$$

2.3.2.1.4 Total over potential

The total dimensionless theoretical over potential of a single cell is the sum of the activation over potential and the ohmic voltage drop:

$$\overline{\eta_t^*} = \overline{\eta_a^*} + \overline{\eta_c^*} + \overline{\eta_m^*} \tag{2.54}$$

2.3.2.2 Mass balance

The dimensionless water content distribution to the λ_m^* membrane is the solution to the first-order linear differential equation defined in equation (2.31). The characteristic equation can be written as follows:

$$\lambda_m^{*\prime\prime} + \beta_m \lambda_m^{*\prime} = 0 \;\rightarrow\; ar^2 + br + c = 0 \;\; where\; a = 1, b = \beta_m \; and \; c = 0 \;\; \leftrightarrow \Delta = B^2 > 0 \tag{2.55}$$

The solution in this case is written as follows:

$$\lambda_m^* = C_1 e^{r_1 z} + C_2 e^{r_2 z} \;\; (C_1, C_2 \in \mathbb{R}) \; and \; (r_1 = 0, r_2 = -\beta_m \; are \; the \; equation \; roots) \tag{2.56}$$

C_1 and C_2 are the integration constants that will be determined using the boundary conditions:

At x_m^* =0: $\lambda_a{}^* = C_1 + C_2$

At x_m^* = 1: $\lambda_c{}^* = C_1\left(1 + \frac{C_2}{C_1} e^{-\beta_m L_m}\right)$

Thus, the distribution of water content to the membrane is written as follows:

$$\lambda_m^* = C_1\left(1 + \frac{C_2}{C_1} e^{-\beta_m x_m^*}\right) \quad where \begin{cases} C_1 = \lambda_a{}^* - \dfrac{\lambda_c{}^* - \lambda_a{}^*}{e^{-\beta_m} - 1} \\ C_2 = \dfrac{\lambda_c{}^* - \lambda_a{}^*}{e^{-\beta_m} - 1} \end{cases} \tag{2.57}$$

The dimensionless water content averaged to the membrane is:

$$\overline{\lambda_m^*} = \int_0^1 \lambda_m^* \, dx_m^* = \int_0^1 C_1\left(1 + \frac{C_2}{C_1} e^{-\beta_m x_m^*}\right) dx_m^* \; = \; C_1 - \frac{C_2}{\beta_m}\left(e^{-\beta_m} - 1\right) \tag{2.58}$$

2.4 Modeling Results: Polymer Electrolyte Membrane Water Electrolysis for hydrogen

The dimensionless approach of pressurized PEMWE has not yet been proposed. In the literature [20], there has been evidenced three apparent two-phase flow regimes: a non-coalesced bubble regime (NCB regime) for small current densities, a coalesced bubble regime (CB regime) for average current densities and a bullous blockage regime called the "slug flow regime" for high current densities. The boundary conditions of this 1D model depends on two-phase flow regimes.

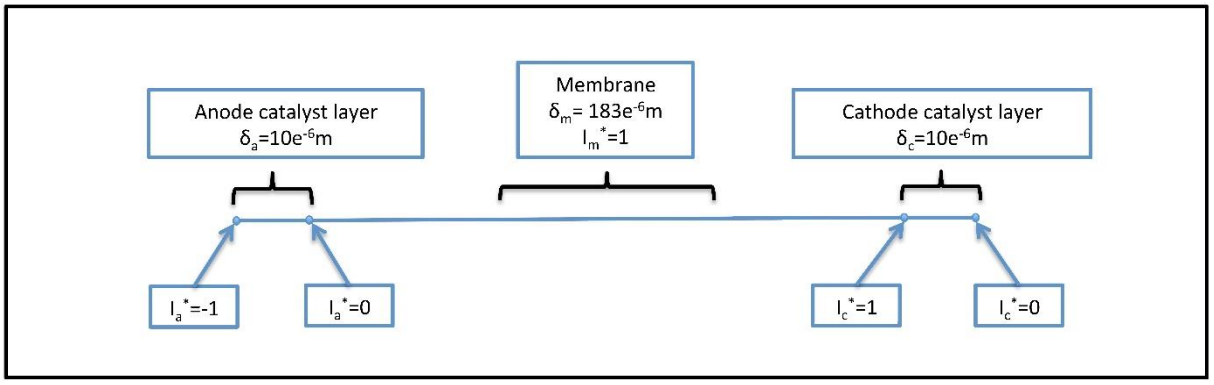

Figure 2-3: One dimensional schematic representation of PEMWE with $\delta_{a,c,m}$ are the common PEM assembly thicknesses

Figure 2-3 shows the geometry and the dimensionless current density boundary conditions used in this study. While the diffusion layer is completely saturated with water, only the catalytic layers and the membrane are represented. However, this assumption is well assumed for the cathodic side of PEMWE.

- At the hydrated anode

In this approach, the anodic catalytic layer is completely saturated with water.

- At the anode

As stated in the assumptions of the model, the diffusion and the reaction anodic layers are saturated with water, thus the water content at these layers is constant and equal to saturation water content $\lambda_{a,c,m}^{sat}$. The water content at the anode depends on the operating conditions such as flow regime and the topological parameters of the membrane. According to experimental work [9], at the catalytic layer/diffusion layer interface, the saturation water content appears as a function of the operating bubbly flow regime in the cathodic channel side. Certainly, it is possible that weak temperature gradients in catalyst layer involves

a non-equilibrium condition in catalyst layer because the cooling effect of water flux while thr electrolysis is clogged by thin bubbles like a thin gas film. Therefore, large bubbles can provide fresh water to catalyst layer: two apparent saturated values are possible $\lambda_a = \lambda_a^{sat,liq} = 22\ or\ \lambda_a = \lambda_a^{sat,vap} = 18$.

$$\lambda_a = \lambda_a^{sat,liq} = cste\ or\ \lambda_a = \lambda_a^{sat,vap} = cste \tag{2.59}$$

At $x_m^* = 0$: $\lambda_a{}^* = 0.3 + 10.8\ a_a - 16\ {a_a}^2 + 14.1\ {a_a}^3\ \ where\ \left(a_a = \frac{P_{H_2O}}{P_{sat}} = 0.5\right)$

- At the cathode

The diffusion layer and the reaction layer have a homogeneous water distribution. In the simulations, to investigate the entire experimental measurements, both values are used:

$$\lambda_c = \lambda_c^{sat,liq} = cste\ \ or\ \lambda_c = \lambda_c^{sat,vap} = cste \tag{2.60}$$

At $x_m^* = 1$: $\lambda_c{}^* = 0.3 + 10.8a_c - 16{a_c}^2 + 14.1{a_c}^3\ where\ \left(a_c = \frac{P_{H_2O}}{P_{sat}} = 1\right)$

In the case of a hydrated cathode: $\lambda_c = \lambda_c^{sat,liq} = 22\ or\ \lambda_c = \lambda_c^{sat,vap} = 18$.

The parameter chosen for the model in the case of this application are as follow (Table 2-3):

Table 2-3 : Model parameters

Parameter	Value
$\boldsymbol{T}$	58°C
$\boldsymbol{\delta_m}$	183.10^{-6} m
$\boldsymbol{F}$	96485
$\boldsymbol{D_{H_2O}}$	3.10^{-10} m².s^{-1}
$\boldsymbol{R}$	8.31
$\boldsymbol{\kappa_\Phi}$	$1.13.10^{-19}$ m²
$\boldsymbol{\mu}$	For 80°C: $3.565.10^{-4}$ kg.m^{-1}.s^{-1}
	For 20°C: 1.10^{-3} kg.m^{-1}.s^{-1}
$\boldsymbol{z_f}$	1
$\boldsymbol{c_f}$	$1.2.10^{-11}$ mol.cm^{-3}
$\boldsymbol{\kappa_p}$	$1.58.10^{-18}$ m²
$\boldsymbol{\sigma_{H^+,k}^{eff}}$	$(0.005139.22 - 0.00326) * exp(1268 * (\frac{1}{303} - \frac{1}{T}))$
$\boldsymbol{\delta_{a,c}}$	10^{-6} m

2.4.1 Dimensionless ionic current density distribution in catalyst layer

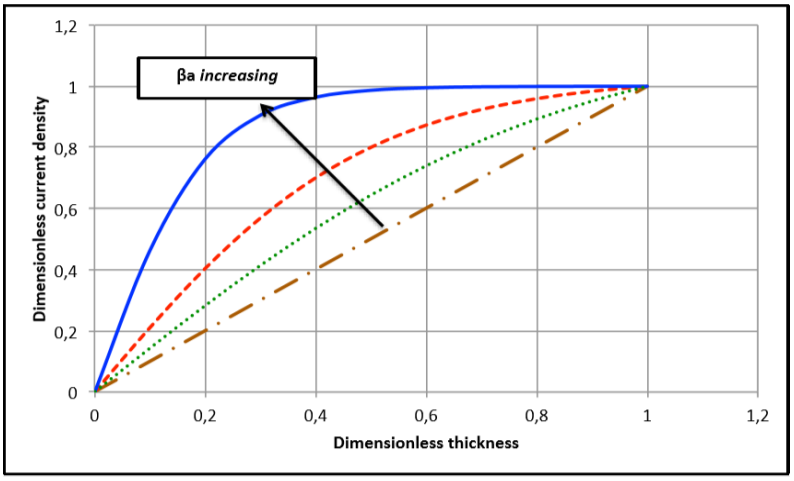

Figure 2-4: Dimensionless current density distribution for β_a= 0,01 [–•–]; β_a= 1 [•]; β_a= 5 [– –]; β_a= 10 [–] at the room temperature and atmospheric pressure

The Figure 2-4 exhibits the current density distribution at the anode side as a function of β_a. As β_a decreases, the through-plane current density distribution becomes more linear.

$$\beta_a = \alpha_a \frac{J_0 \delta_a F}{2RT\sigma_{H^+,a}^{eff}} \tag{2.61}$$

According to the equation (2.57), the analytical result shows that the effective protonic conductivity and the operational current density, which can be described by β_a (2.61), affect the distribution of the ionic current density at the catalyst layer.

As a result, the catalyst layer produces more faradic currents throughout the thickness of the catalyst layer at high current density (trivial result). The same result is also valid at low ionic conductivity. In the same way when the ionic conductivity decreases (non-trivial result). Ratio of applied current/effective ionic conductivity drives the performances of anode. The evolution of this ratio can reveal the optimum operating conditions of the anode for a given temperature and catalyst thickness.

2.4.2 Dimensionless water content distribution in membrane

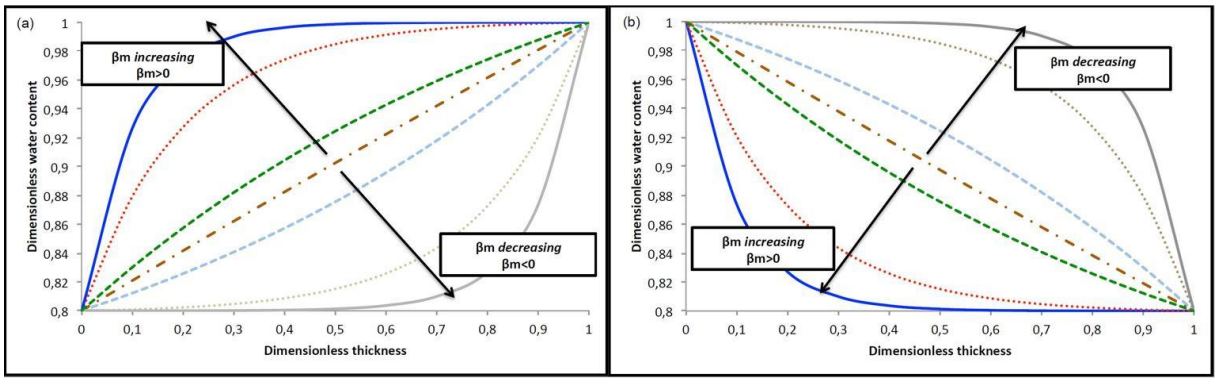

Figure 2-5: Dimensionless water content distribution at the membrane ((a) full hydrated cathode, (b) full hydrated anode) for β_m= 0,1 [–•–]; β_m= 1 [– –]; β_m= 5 [•]; β_m= 10 [–]; β_m= -1 [– –]; β_m= -5 [•]; β_m= -10 [–] at the room temperature and atmospheric pressure

The Figure 2-5 (a) and (b) exhibit the water content distribution at the membrane for different β_m.

$$\beta_m = \frac{\delta_m}{D_{H_2O}}\left(\frac{\kappa_\Phi}{\mu} z_f c_f F \frac{J_0}{\sigma^m} + \frac{\kappa_p}{\mu}\nabla p\right) \tag{2.62}$$

β_m represents the diffusion water, the electro-osmotic transport, the protonic conductivity, and the flux due to gradient pressure at the membrane. This analytical result shows that the β_m affects the shape of the water content distribution. For a $\beta_m \approx 0$, the water content distribution at the membrane is linear according to a pure Laplacian equation. In addition, the positive or a negative increase of the β_m induces a more homogenous water composition through the membrane. Consequently, the ohmic drop can be controlled by the pressure gradient and the cathodic water content e.g. for high cathodic pressure, a full hydrated cathode is needed to reduce ohmic drop.

2.4.3 Dimensionless over potential variation

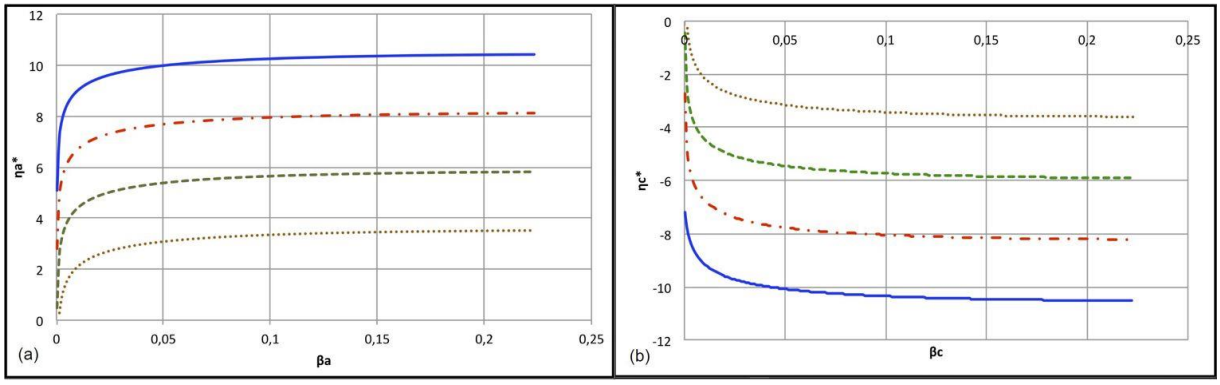

Figure 2-6: (a) Dimensionless anodic over potential variation with β_a (b) Dimensionless cathode over potential variation with βc at the atmospheric pressure and room temperature for $\omega_a = 10^{-5}$ [–•–]; $\omega_a = 10^{-6}$ [– –]; $\omega_a = 10^{-3}$ [•]; $\omega_a = 10^{-4}$ [–] at the room temperature and atmospheric pressure

The Figure 2-6 (a) and (b) exhibits the polarization curve for various Wagner numbers (2.63) at anode and cathode side.

$$\omega_{a,c} = \frac{\gamma_{a,c} i_{0,a,c} \delta_{a,c} F}{2RT_{a,c}\sigma_{a,c}^{H^+}} \tag{2.63}$$

These analytical results show that an increase of ω_a improves the electrochemical performance of the PEMWE. According to the equations ((2.45) & (2.46)) a decrease of the electrochemical kinetics or an increase of the protonic conductivity at the catalyst layers involved better electrochemical performance of the PEMWE. This theoretical results are in agreement with the literature [21], which suggests that the topological aspect of the catalyst layers is an important parameter for the optimization of the electrochemical performance of the PEMWE.

2.5 Experimental comparison with analytical dimensionless model: Polymer Electrolyte Membrane Water Electrolysis for hydrogen

The model is compared with experimental data of a low-pressure electrolysis conducted in collaboration with Electrochemical Innovation Lab (EIL) in University College London (UCL). The cell used for this work is an experimental device dedicated to the flow visualization. The PEMWE single cell used in this study had an active surface area of 8 cm^2, acrylic end plates, titanium pins for cell compression and current supply and platinum-coated titanium is used as the gas diffusion layers. A torque of 1.5 N.m was applied to each of the 8 bolts used to compress the cell. The cell pistons were pneumatically compressed to 20 bar, and deionized water was circulated through both sides from separate storage tanks via a peristaltic pump (Watson Marlow) at the room temperature 20°C. The inlet deionized water was supplied to the anode and cathode compartments by a peristaltic pump at the various flow rates using a recirculation loop with gas removal. The membrane electrode assembly (MEA) used in the cell was obtained from ITM Power. It consisted of two electrodes containing catalysts: 3 $mg.cm^{-2}$ platinum black at the cathode side and 3 $mg.cm^{-2}$ of iridium oxide at the anode side, laminated to either side of a proton conducting solid polymer membrane (Nafion® 117). At the anode (gas diffusion layer) titanium sinter had a thickness equal to 0.35 mm and with 80% of porosity 80 % and at the cathode carbon paper TGP-H-060 with 78% of porosity 78 % and 0.19 mm of thickness was used. The circular membrane has an active surface area of 8 cm^2 and was delivered in dry state.

To obtain optimal performance and minimize resistance, they were activated first ex-situ then in-situ as follows. First, immersion in deionized water at 60 °C for about 18 h then they were left in fresh deionized water for another 2 h at room temperature. Finally, the MEA was conditioned in the cell at a constant current density of 1 $A.cm^{-2}$ for about 18 h (activation process).

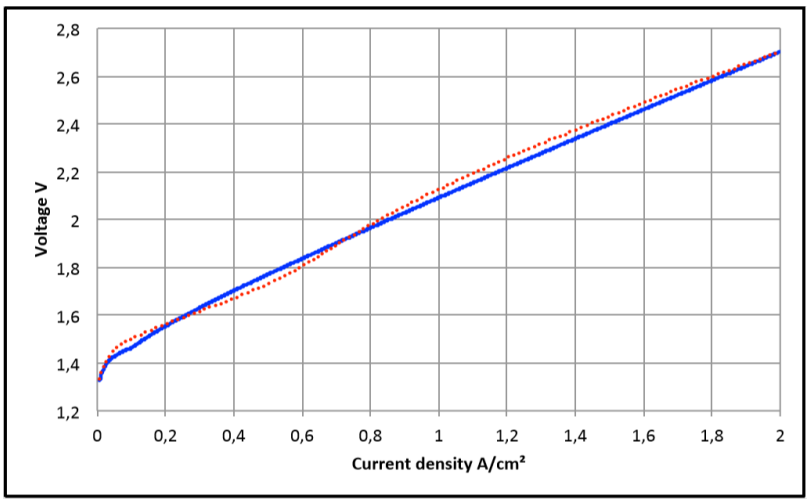

Figure 2-7: Experimental (•) and analytical (–) IV curve with a Nafion® 117 membrane at the atmospheric pressure and room temperature.

Figure 2-7 exhibits the simulated polarization curve and the experimental data with a flow rate of 200 ml.min^{-1}. Only the Wagner numbers $\omega_{a,c}$ at the anode and cathode sides are used as fitting parameters in equation ((2.47) & (2.48)). The analytical model can predict the IV curve of the pressurized PEMWE (Figure 2-7 & Figure 2-8). The Wagner number is the dimensionless key number of the approach. The Wagner number is the ratio between the protonic conductivity and the electrochemical kinetic at the catalyst layer [22][11].

$$\omega_{a,c} = \frac{Electrochemical\ kinetic}{Protonic\ conductivity} \tag{2.64}$$

$$\omega_{a,c} = \frac{\gamma_{a,c} i_{0,a,c} \delta_{a,c} F}{2RT_{a,c}\sigma_{a,c}^{H^+}} \tag{2.65}$$

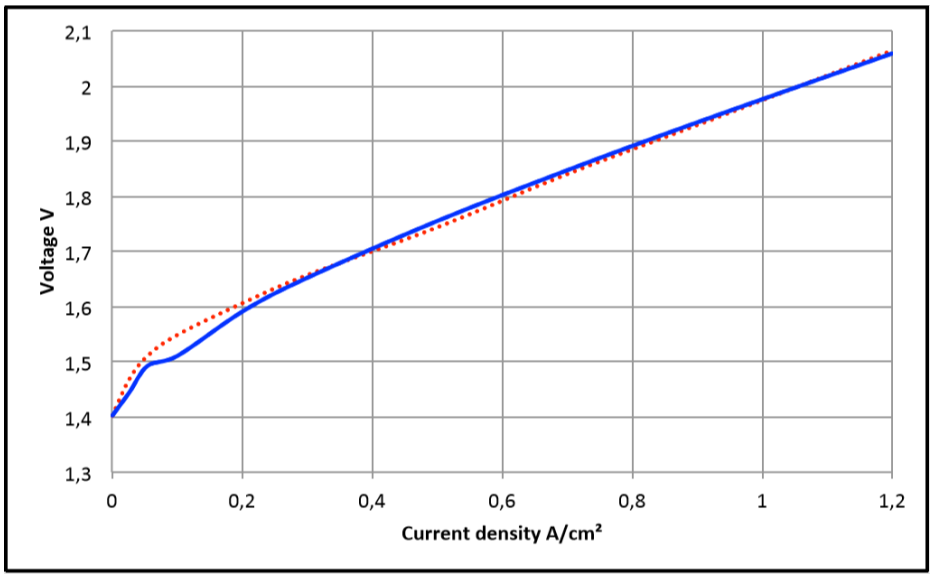

Figure 2-8: Experimental (•) and analytical (–) IV curve with a Nafion® 117 membrane with a pressure of 7 bars at the cathode side and a temperature of 58 °C.

A second set of data were compared to the simulation on Figure 2-8. This experimental data deals with a pressurized cell from literature experiments of Santarelli *et al.* [23].

A good agreement is observed between simulations and experiments in both cases. The parametric optimization is achieved using Nelder-Mead Simplex Method algorithm and at least five tests have been completed to avoid a local minimum. A gradient calculation analysis (Appendix B) was conducted to verify the values of the model compared to the experimental data. The gradient was stable.

The data fitting process synchronizes the parameters of the model and the experimental data in order to have the closest mathematical approach of the system. These experimental data are also used to validate the model. Therefore, the data fitting needs a thorough analysis and methodology to reach compatible results.

Therefore, this model is a really powerful tool because only two parameters (β, ω) are used to describe the cell efficiency. However, the ionic conductivity of polymeric electrolyte, physical characteristics of membrane and exact thicknesses are required, but no kinetic parameters are required.

The literature [20] exhibits that at the anode side two apparent bubbly flow regimes can appear in the PEMWE : for a range of [0-300 $A.m^{-2}$], there is a non-coalesced bubble regime (NCB regime), for a range of [300-1500 $A.m^{-2}$], there is a coalesced bubble regime (CB regime) and for a higher value of current density flow regime of two-phase flow in the channel changed from bubbly to slug flow (SF regime) [24]. Here, the main assumption is that the Wagner number can be linked to each different regime of two-phase flow.

According to the literature [9], for the CB regime, the appearance of larger bubbles increases the free surface at the electrode. The catalyst layer has full access in fresh water and a high protonic conductivity. The Wagner number at anode for the CB regime is constant. For the Slug Flow regime >1000 A.m^{-2}, it was assumed that an exponential decrease of the Wagner number at anode. According to H. Ito *et al.* [24], the transition between bubbly flow (CB) and Slug Flow (SF) is not linear. Therefore, the proposed expression is the following:

$$\omega_a = \omega_{a0}\, e^{(-a(J_0 - J_{trans}))} \tag{2.66}$$

At the cathode it is assumed that the Wagner number was constant, yet the value of ω_c was not fixed in all range of operating current density. ω_c can take two values, ω_{c1} for $J_0 < J_{trans}$ and ω_{c2} for $J_0 > J_{trans}$. In both experimental sets J_{trans} was close to 100 A.m^{-2}.

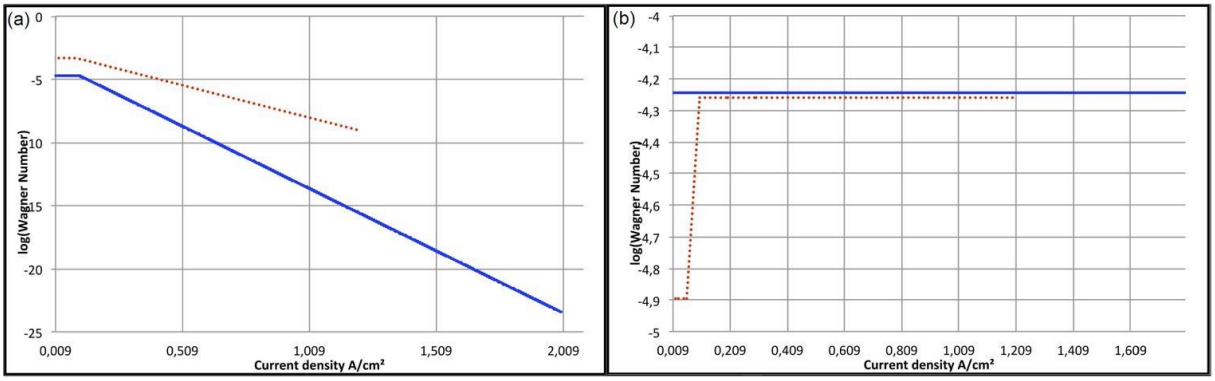

Figure 2-9: Evolution of the Wagner number at the catalyst layer for the anode (a) or for the cathode (b) side function the current density J_o (A.cm^{-2}) at the atmospheric pressure at room temperature (–) and with a pressure of 7 bars at the cathode side at 58 °C (•) (logarithmic scale).

Figure 2-9 (a) exhibits the evolution of the anodic Wagner numbers during the electrolysis process. As expected, at high current density, the slug flow regime may clog the channel flow and decrease the active surface area of the MEA [24]. For the slug flow regime, the analytical result shows that the exponential decrease has good agreement with experimental measurements (Figure 2-7 and Figure 2-8). This decrease is due to the decrease of anode catalyst layer performance. The Wagner number depends on the effective exchange current density (equation (2.62)). The effective anode exchange current density $\left(\overline{\gamma_a}.\, i_{0,a}\right)\overline{\gamma_a} i_{0,a}$ is directly linked to the distribution of specific active area $(\frac{\gamma_a}{\delta_a})$ [25] where, γ_a (called roughness factor) is equal to 0 when the catalytic material is not in contact with reactants [26], accordingly the average coefficient of $\bar{\gamma}_a$ decreases when the slug flow regime blocks the water in the channel flow.

Surprisingly, Figure 2-9 (b), the Wagner number at the cathode, was enhanced in the case of pressurized operations when the current density increases. This phenomenon is due to the water management through the membrane (Figure 2-5): the water flux is directly linked to oxygen permeation [27] and oxygen affects the catalyst performance of cathode. This phenomenon is more clearly evidenced in the case of pressurized electrolysis.

CONCLUSION

This approach performed on an analytic dimensionless model of PEMWE enables the finding of the three parameters that governed the electrochemical reaction at the catalyst layer and the mass transport through the membrane, namely: The Wagner numbers $\omega_{a,c}$ at the anode and cathode side, $\beta_{a,c}$ at the catalyst layers, and the dimensionless ratio of water transport process through the membrane β_m.

The experimental data exhibited a good agreement with simulations. Moreover, the computations allowed obtaining analytical solutions of the water content in the membrane, the over potential and the current density distribution in the membrane and the catalyst layers. This approach offered a useful tool for the ability of water management through the PEMWE. The dependence of the membrane hydration, total over potential on the Wagner number $\omega_{a,c}$ et β_m was depicted, which can be conveniently referred to when assessing the performance of the PEMWE system.

Exponential reduction of the Wagner numbers at the anode catalyst layer, $\omega_{a,}$ shows the impact of slug flow on cell efficiency at high current density. This result would show that the PEMWE undergoes an important decrease of the electrochemical reaction for the high current densities mainly due to gas exhaust. Furthermore, this approach is original and an easy-to-use method that will help with experimental analysis. This closed-form analytic solution of dimensionless model will have many applications for optimization of cell performances:

- the fast-computing ability of this dimensionless model will provide large amount of data for hierarchical learning
- the model is adapted to advanced method of process control to model predictive control (MPC)
- this approach can be inserted in a control loop for fault detection methods

The next chapters will be concentrating on a Polymer Electrolyte Membrane Cells Experimental Application using Electrochemical hydrogen compression. This will be followed by a Polymer Electrolyte Membrane Cells Electrochemical Impedance Spectroscopy Modeling.

References

[1] J. Deseure, “How to Build Simple Models of PEM Fuel Cells for Fast Computation”, in *Thermodynamics and Energy Engineering*, P. Vizureanu, Éd. IntechOpen, 2020.

[2] F. Aubras *et al.*, “Dimensionless approach of a polymer electrolyte membrane water electrolysis: Advanced analytical modelling”, *J. Power Sources*, vol. 481, p. 228858, Jan. 2021, doi: 10.1016/j.jpowsour.2020.228858.

[3] S. S. Lafmejani, A. C. Olesen, et S. K. Kær, “VOF modelling of gas–liquid flow in PEM water electrolysis cell micro-channels”, *Int. J. Hydrog. Energy*, vol. 42, nº 26, p. 16333-16344, Jun. 2017, doi: 10.1016/j.ijhydene.2017.05.079.

[4] A. Nouri-Khorasani, E. Tabu Ojong, T. Smolinka, et D. P. Wilkinson, “Model of oxygen bubbles and performance impact in the porous transport layer of PEM water electrolysis cells”, *Int. J. Hydrog. Energy*, vol. 42, nº 48, p. 28665-28680, Nov. 2017, doi: 10.1016/j.ijhydene.2017.09.167.

[5] J. Schillings, O. Doche, M. Tano Retamales, F. Bauer, J. Deseure, et S. Tardu, “Four-way coupled Eulerian–Lagrangian Direct Numerical Simulations in a vertical laminar channel flow”, *Int. J. Multiph. Flow*, vol. 89, p. 92-107, Mar. 2017, doi: 10.1016/j.ijmultiphaseflow.2016.10.006.

[6] O. Panchenko *et al.*, “In-situ two-phase flow investigation of different porous transport layer for a polymer electrolyte membrane (PEM) electrolyzer with neutron spectroscopy”, *J. Power Sources*, vol. 390, p. 108-115, Jun. 2018, doi: 10.1016/j.jpowsour.2018.04.044.

[7] F. de Beer, J.-H. van der Merwe, et D. Bessarabov, “PEM Water Electrolysis: Preliminary Investigations Using Neutron Radiography”, *Phys. Procedia*, vol. 88, p. 19-26, 2017, doi: 10.1016/j.phpro.2017.06.002.

[8] O. F. Selamet, U. Pasaogullari, D. Spernjak, D. S. Hussey, D. L. Jacobson, et M. Mat, “In Situ Two-Phase Flow Investigation of Proton Exchange Membrane (PEM) Electrolyzer by Simultaneous Optical and Neutron Imaging”, Boston, MA, 2011, p. 349-362, doi: 10.1149/1.3635568.

[9] F. Aubras *et al.*, “Two-dimensional model of low-pressure PEM electrolyser: Two-phase flow regime, electrochemical modelling and experimental validation”, *Int. J. Hydrog. Energy*, vol. 42, nº 42, p. 26203-26216, Oct. 2017, doi: 10.1016/j.ijhydene.2017.08.211.

[10] K. T. Jeng, C. P. Kuo, et S. F. Lee, “Modeling the catalyst layer of a PEM fuel cell cathode using a dimensionless approach”, *J. Power Sources*, vol. 128, nº 2, p. 145-151, 2004.

[11] E. L. Gyenge, “Dimensionless numbers and correlating equations for the analysis of the membrane-gas diffusion electrode assembly in polymer electrolyte fuel cells”, *J. Power Sources*, vol. 152, p. 105-121, 2005.

[12] M. S. Quraishi et T. Z. Fahidy, “A simplified procedure for dimensional analysis employing si units”, *Can. J. Chem. Eng.*, vol. 59, nº 4, p. 563-566, 1981.

[13] M. Matlosz, C. Creton, C. Clerc, et D. Landolt, “Secondary current distribution in a hull cell boundary element and finite element simulation and experimental verification”, *J. Electrochem. Soc.*, vol. 134, nº 12, p. 3015-3021, 1987.

[14] S. Battersby, P. W. Teixeira, J. Beltramini, M. C. Duke, V. Rudolph, et J. C. D. da Costa, “An analysis of the Peclet and Damkohler numbers for dehydrogenation reactions using molecular sieve silica (MSS) membrane reactors”, *Catal. Today*, vol. 116, nº 1, p. 12-17, 2006.

[15] D. A. Noren et M. A. Hoffman, “Clarifying the Butler–Volmer equation and related approximations for calculating activation losses in solid oxide fuel cell models”, *J. Power Sources*, vol. 152, p. 175-181, 2005.

[16] M. Carmo, D. L. Fritz, J. Mergel, et D. Stolten, “A comprehensive review on PEM water electrolysis”, *Int. J. Hydrog. Energy*, vol. 38, nº 12, p. 4901–4934, 2013.

[17] L. F. L. Oliveira, S. Laref, E. Mayousse, C. Jallut, et A. A. Franco, “A multiscale physical model for the transient analysis of PEM water electrolyzer anodes”, *Phys. Chem. Chem. Phys.*, vol. 14, nº 29, p. 10215-10224, 2012.

[18] D. M. Bernardi et M. W. Verbrugge, “Mathematical model of a gas diffusion electrode bonded to a polymer electrolyte”, *AIChE J.*, vol. 37, nº 8, p. 1151-1163, 1991.

[19] K. M. S. Uddin, L. K. Saha, et N. Oshima, “Water transport through the membrane of PEM”, *Fuel Cell*, vol. 4, p. 225-238, 2014.
[20] F. Aubras *et al.*, “Two-dimensional model of low-pressure PEM electrolyser: Two-phase flow regime, electrochemical modelling and experimental validation”, *Int. J. Hydrog. Energy*, vol. 42, nº 42, p. 26203-26216, Oct. 2017, doi: 10.1016/j.ijhydene.2017.08.211.
[21] S.-D. Yim *et al.*, “Optimization of PtIr electrocatalyst for PEM URFC”, *Int. J. Hydrog. Energy*, vol. 30, nº 12, p. 1345-1350, 2005.
[22] C. Wagner, “Theoretical analysis of the current density distribution in electrolytic cells”, *J. Electrochem. Soc.*, vol. 98, nº 3, p. 116-128, 1951.
[23] M. Santarelli, P. Medina, et M. Calì, “Fitting regression model and experimental validation for a high-pressure PEM electrolyzer”, *Int. J. Hydrog. Energy*, vol. 34, nº 6, p. 2519-2530, Mar. 2009, doi: 10.1016/j.ijhydene.2008.11.036.
[24] H. Ito *et al.*, “Effect of flow regime of circulating water on a proton exchange membrane electrolyzer”, *Int. J. Hydrog. Energy*, vol. 35, nº 18, p. 9550-9560,Sept. 2010, doi: 10.1016/j.ijhydene.2010.06.103.
[25] J. Ramousse, J. Deseure, O. Lottin, S. Didierjean, et D. Maillet, “Modelling of heat, mass and charge transfer in a {PEMFC} single cell”, *J. Power Sources*, vol. 145, nº 2, p. 416-427, 2005, doi: http://dx.doi.org/10.1016/j.jpowsour.2005.01.067.
[26] S. J. Lee, S. Mukerjee, J. McBreen, Y. W. Rho, Y. T. Kho, et T. H. Lee, “Effects of Nafion impregnation on performances of PEMFC electrodes”, *Electrochimica Acta*, vol. 43, nº 24, p. 3693-3701, août 1998, doi: 10.1016/S0013-4686(98)00127-3.
[27] P. Trinke, B. Bensmann, et R. Hanke-Rauschenbach, “Experimental evidence of increasing oxygen crossover with increasing current density during PEM water electrolysis”, *Electrochem. Commun.*, vol. 82, p. 98-102,Sept. 2017, doi: 10.1016/j.elecom.2017.07.018.

Chapter 3: Polymer Electrolyte Membrane Cells Experimental Application: Electrochemical hydrogen compression/concentrator (or purification)

3. Polymer Electrolyte Membrane Cells Experimental Application: Electrochemical hydrogen compression/concentrator (or purification)

Electrochemical hydrogen compression is a potential high efficient, environmentally friendly, low-maintenance and silent operation technology used to produce high pressure hydrogen [1].

In this context, the electrochemical hydrogen compressor can act as a purification device, producing pure hydrogen [2]. Therefore, direct electrochemical compression is mainly advantageous for hydrogen to become a widespread renewable-energy carrier.

According to chapter 1, the hydrogen purification using EHC combines a low energetic cost, high H_2 recovery and purity, little maintenance, low cost, and low temperature of operation. The mass transfer across the membrane only allows selective hydrogen transport which enables simultaneous purification Hence, EHC can do the purification and compression in a single stage. Despite all these advantages, there are still a few issues such as water management for a high rate of compression/purification that need to be optimized.

This chapter focuses on examining the compression of pure hydrogen and the effect of impurities such as N_2 on the EHC cell during the compression/separation of a N_2/H_2 gas mixture. To perform the observations of electrochemical behavior during compression on hydrogen several electrochemical measurements have been achieved.

The work has been performed within the facilities of Hydrogen South Africa (HySA) at the North-West University (NWU), Potchefstroom Campus, South Africa. HySa Infrastructure is becoming a world leader research facility where they develop fuel cell technologies and the hydrogen chain from production to delivery. HySa is equipped with a laboratory-scale photovoltaic, wind turbine, electrolysis, and fuel-cell educational demonstration kits, a small and larger-scale electrochemical hydrogen compressor and a PEM-based H_2 production system [3].

In this chapter, it starts by presenting the experimental setups: the test bench as well as the single cell electrochemical hydrogen compression. Followed by a detailed display of the results for the membrane conductivity measurements, the compression of pure hydrogen, and the compression/separation of hydrogen/nitrogen gas mixture. The compression was performed between 0 and 30 bars. For these experiments, using a galvanostatic procedure, temperature, relative humidity, and pressure measurement were conducted. In addition, an electrochemical impedance spectroscopy (EIS) measurement was also performed. Finally, a discussion and analysis of the data is carried out detailing the impact of nitrogen impurities on the cell behavior.

3.1 Experimental setups

3.1.1 Conductivity measurement Setup

Figure 3-1: Conductivity measurements experimental Setup

The experiments consisted of a through-plane conductivity measurement of PEM membrane for platinum group metal-based (PGM) electrochemical systems (**Figure 3-1**). Electrochemical impedance spectroscopy (EIS) was used to measure the membrane's resistance using a potentiostat (Solartron SI 1287 Electrochemical Interface) and a frequency response analyser (Solartron analytical 1252A), the frequency range was [3.10^{-1} Hz; 3.10^{5} Hz]. Each membrane was placed in a cylindrical cell with a gold based GDL (Appendix B). The standard diameter was around 60 mm and the cell were tightened at 1 N.m. These PEM were all Nafion® membranes with different thicknesses. For the Nafion® N117 and Nafion® N115, the conductivity was measured for different temperatures (30°C - 40°C - 50°C - 60°C) and different Relative Humidity (RH) (10% - 40% - 70% - 100%) to analyse the effect of these parameters on the material resistance. Six layers of Nafion® N117 membranes were also staked to determine the effect of the thickness on the conductivity. After each experiment, a layer was taken, and the rest were measured. This variation of thickness was done at T=25°C and RH=100%. A blank test, without a membrane, was preformed to define the cell's resistance which was estimated to 0.0007 Ω.

Table 3.1: Types of Nafion® PEM membranes used in these experiments [4]

Nafion® type	Thickness (µm)
N1110	254
N117	177.8
N115	127
NR-212	50,8
NR-211	25,4

After being sealed, **Figure 3-2**, the cell is placed in a humidification chamber (espec SH-222) [5] where the temperature and RH are fixed.

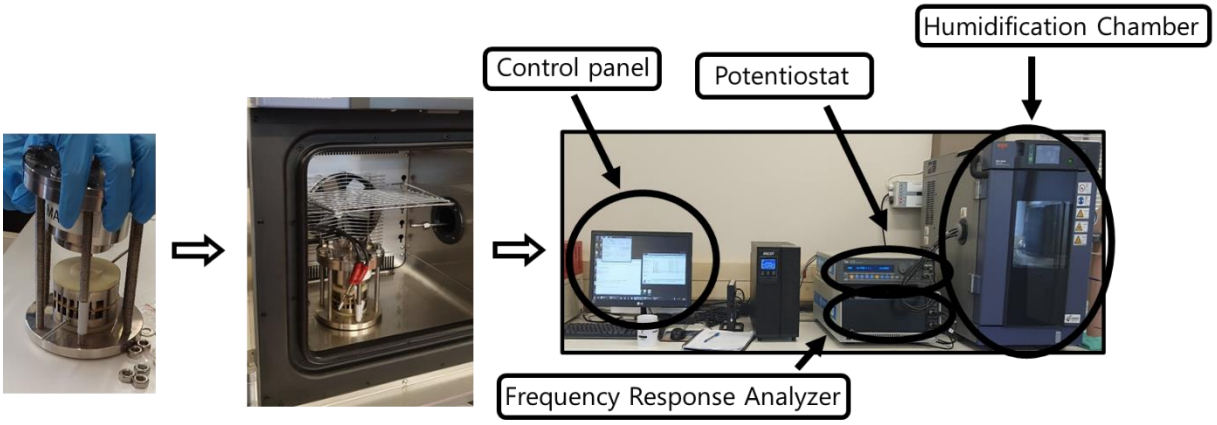

Figure 3-2: Conductivity measurements experimental installation

After a few test runs, it was observed that the membrane needs almost 60 minutes to reach an equilibrium of hydration and temperature. The relative humidity was fixed in the morning and the temperatures modified during the day. After an hour, approximately three test measurements were conducted in order to verify that the value measured is constant.

The system measures the membrane's resistance. Then the conductivity is calculated using the following formula:

$$\sigma = \frac{\delta}{A \,.\, R} \tag{3.1}$$

Where (σ) the membrane conductivity (S / m), (δ) the membrane thickness (m), (A) the membrane geometric area (m^2), (R) the membrane resistance (Ω).

3.1.2 Electrochemical Hydrogen Compression Setup

Figure 3-3 : Compression/Separation experimental Setup

Electrochemical characterization of compression and separation is characterized using IV curve, galvanostatic and EIS measurements (**Figure 3-3**). This bench has been used for the two tests:

- Compression characterization with pure H_2 with various humidity, temperature, and pressure
- Compression and Separation characterization with Hydrogen mixture (dilute hydrogen in Nitrogen) with various humidity, temperature, and pressure

Single cell electrochemical hydrogen compression (EHC) has been done over a Nafion® N1110 membrane (δ=254 µm) with a platinum catalyst load (0.2045 ± 0.0065 mg Pt/cm²).

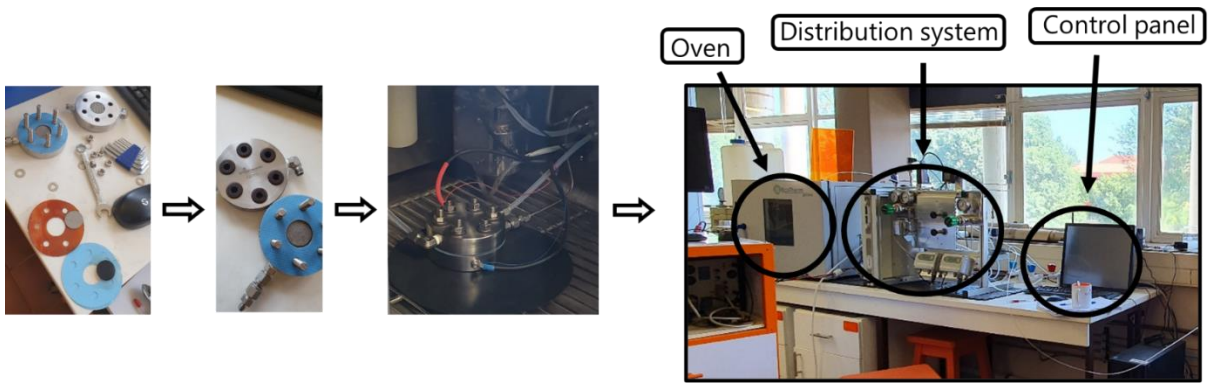

Figure 3-4: Electrochemical Hydrogen Compression experimental installation

The compression was performed between 0 bars and 30 bars. For these experiments, using a galvanostatic procedure, temperature, relative humidity, and pressure measurements were conducted. In addition, an electrochemical impedance spectroscopy measurement was also performed using a Gamry potentiostat before and after each compression experiment, the frequency range was [10^{-1} Hz - 3.10^{5}

Hz]. These experiments ran on both pure hydrogen and hydrogen/nitrogen mixture. The experiments were done for three imposed temperatures: 25°C – 40 °C – 60 °C and four relative humidity: 20% - 40% - 70% - 100%. Usually the RH was fixed in the morning and the temperatures modified during the day. After each temperature, the system was left for an hour approximately to reach a steady state before each measurement. The cell is sealed and placed in the oven and connected to a humidifier (**Figure 3-4**). to control the humidity and the temperature.

The small scale EHC test set-up, located at HySa Infrastructure Centre of Competence, was designed, and constructed to accommodate testing of small EHC. The cells can either be powered by a Gamry potentiostat or a programmable DC power supply. The test set-up can function using a fixed current (galvanostatic mode) or a fixed voltage (potentiotstatic mode). In these experiments, the measurements were done under a fixed current value and due to safety reasons, the setup was designed to reach a maximum voltage value of 600 mV. On the anode side, this system can control the temperature, humidity, pressure (up to 2 bars) and mass flow rate of the hydrogen or gas mixture that is supplied to the anode of the EHC cell. The system also has the functionality to control the cathode pressure (up to 30 bars).

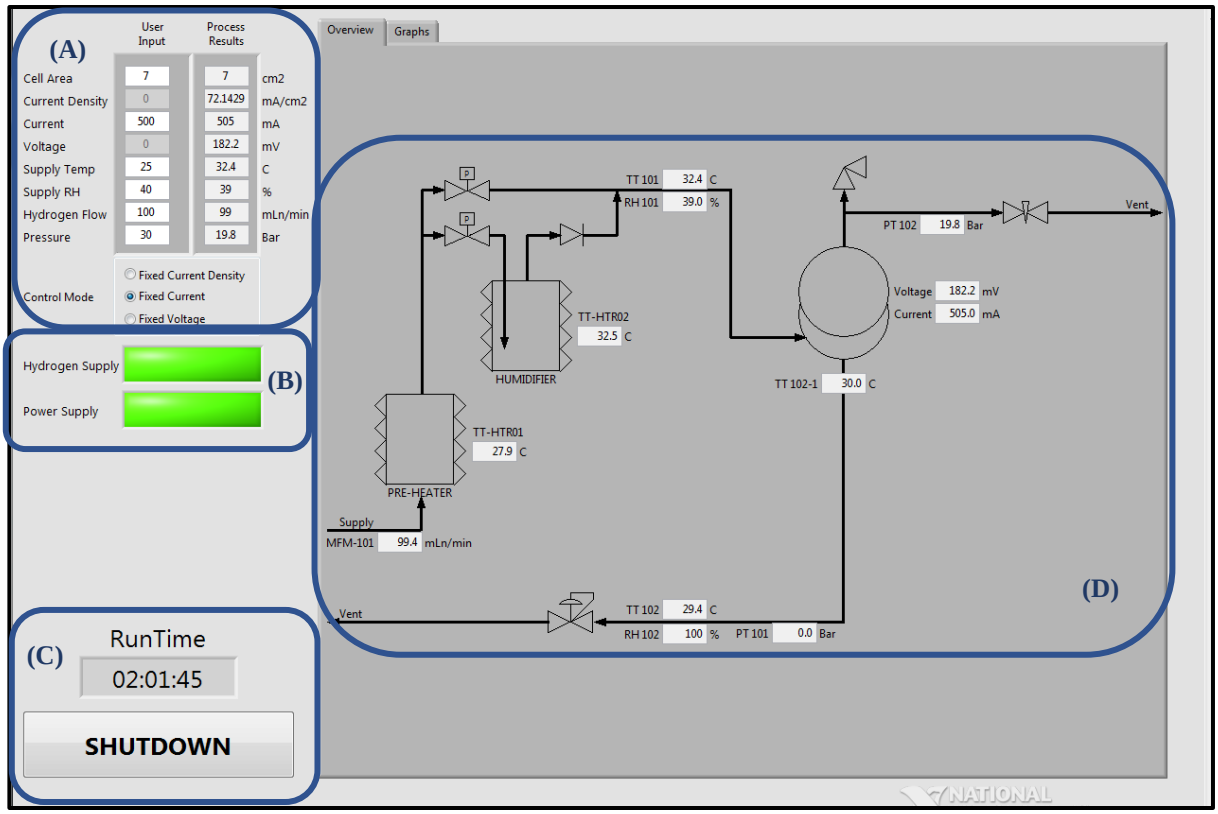

Figure 3-5: LabView Control Panel for the experimental setup

The commands are done through the LabView control panel **Figure 3-5** part (A), part (B) is used to start the power and the gas feed inlet and part (C) is where the recording of the data is launched which is quantified using a timer. For this experiment the input on the control panel is listed in **Table 3.2**.

Table 3.2: Input details

Cell area	7 cm^2
Current	1500 mA
Maximum Voltage	600 mV
Temperature	25°C - 40 °C -60°C
RH	20% - 40% -70% - 100%
Hydrogen inlet flow	100 mLn/min
Cathode Pressure	10bars - 20bars - 30bars

As illustrated in **Figure 3-5** part (D), the anode gas supply sub-system can receive hydrogen or a gas mixture. First the gas would flow through a thermal mass flow meter, followed by a pressure regulating valve and a preheater. At the exit of the preheater, the gas supply line is split into two. Both lines contain a proportional solenoid valve which is used to control the total gas supply rate, as well as the flow ratio of the two lines. From here each line is routed into an oven. One of the gas lines is en route to a bubbler (located inside the oven). The two gas lines are recombined at the exit of the bubbler and supplied to a humidity sensor, which measures the relative humidity and temperature of the gas. The relative humidity of the gas supply is controlled by adjusting the flow ratio of the two pipelines. The temperature of the gas supply is controlled by adjusting the oven set temperature. From here, the gas is routed to the anode cavity of the EHC cell, which is also located in the oven. The excess gas is routed from the outlet of the anode cell to a second humidity/temperature sensor. The line that is connected to the cathode cavity, exits the oven before it is split in two lines. The one line is connected to a pressure relief line and the other line is connected to a pressure sensor followed by a mass flow controller. The cathode pressure is controlled by adjusting the set-point of pressure.

3.2 Polymer Electrolyte Membrane Conductivity: Results and discussion

The development of the PEM devices is going along with the different requirements of an optimal and durable functioning membrane [6]. One of the most important aspects of these membranes is the proton conductivity or the resistance. These are both a function of material properties and the conditions such as temperature and relative humidity (RH) [7]. As shown in **Figure 3-6**, the conductivity can be measured within the plane (in-plane direction, IP) or via the thickness of the membrane (through-plane orientation, TP) [8]. Through-plane is more suitable for PEM devices. Therefore, the measurements were conducted using the through-plane electrochemical method.

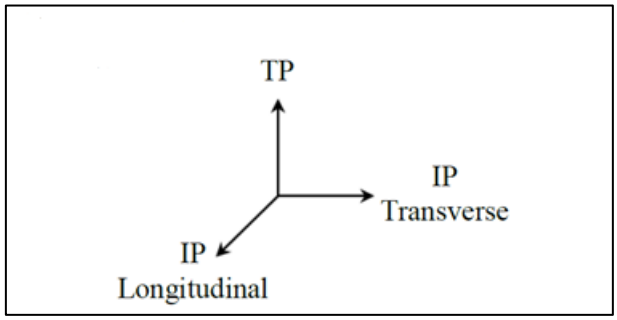

Figure 3-6: The difference between in-plane (IP) and through-plane conductivity [8]

The Nyquist plot of the EIS (**Figure 3-7**), provided at the end of each test, allows to determine the membrane resistance from the intersection between the curve plot and the real axis at high frequency [9].

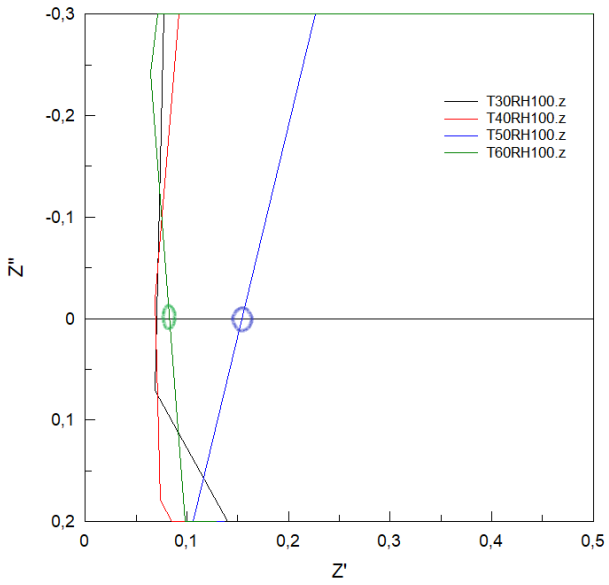

Figure 3-7: Nyquist plot for N117 Nafion® membrane RH 100% and different temperatures at 10^5 Hz

According to Anantaraman *et al.* [10] and Hung-Chung Chien *et al.* [11] the Nafion® membrane conductivity is around 10^{-4} S.cm^{-1} and 10^{-2} S.cm^{-1}. However, other studies such as Heimerdinger *et al.* [7] the conductivity is around 10^{-2} S.cm^{-1}. These values' differences are mostly due to the measurement method and the experimental set up. In the case of this current study, the measurements have been recorded between 10^{-4} S.cm^{-1} and 10^{-3} S.cm^{-1}. The main purpose of these experiment is to analyze the different effects of thickness, temperature, and RH on the Nafion® membrane conductivity. Specially that even if the values differ the growing pattern as a function of the RH tends to be remarkably similar between the measurements and the literature (**Figure 3-8**).

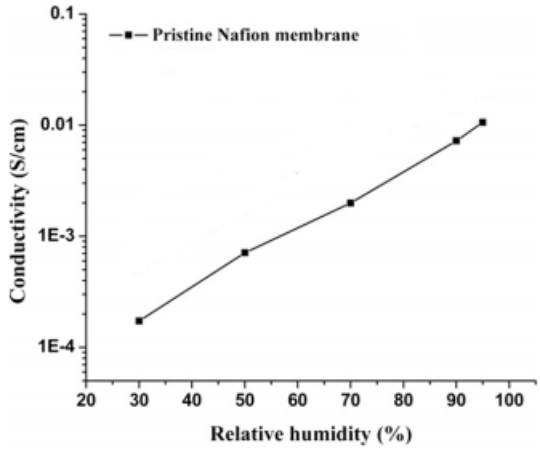

Figure 3-8: Proton conductivity of a pristine Nafion® 211 at 70°C [11]

3.2.1 Conductivity measurements for PEM membrane Nafion®

The main measurements were done using a Nafion® N117 membrane. However, some temperature and RH test were also conducted on the Nafion® N115 since these two membranes are more frequently found in the literature.

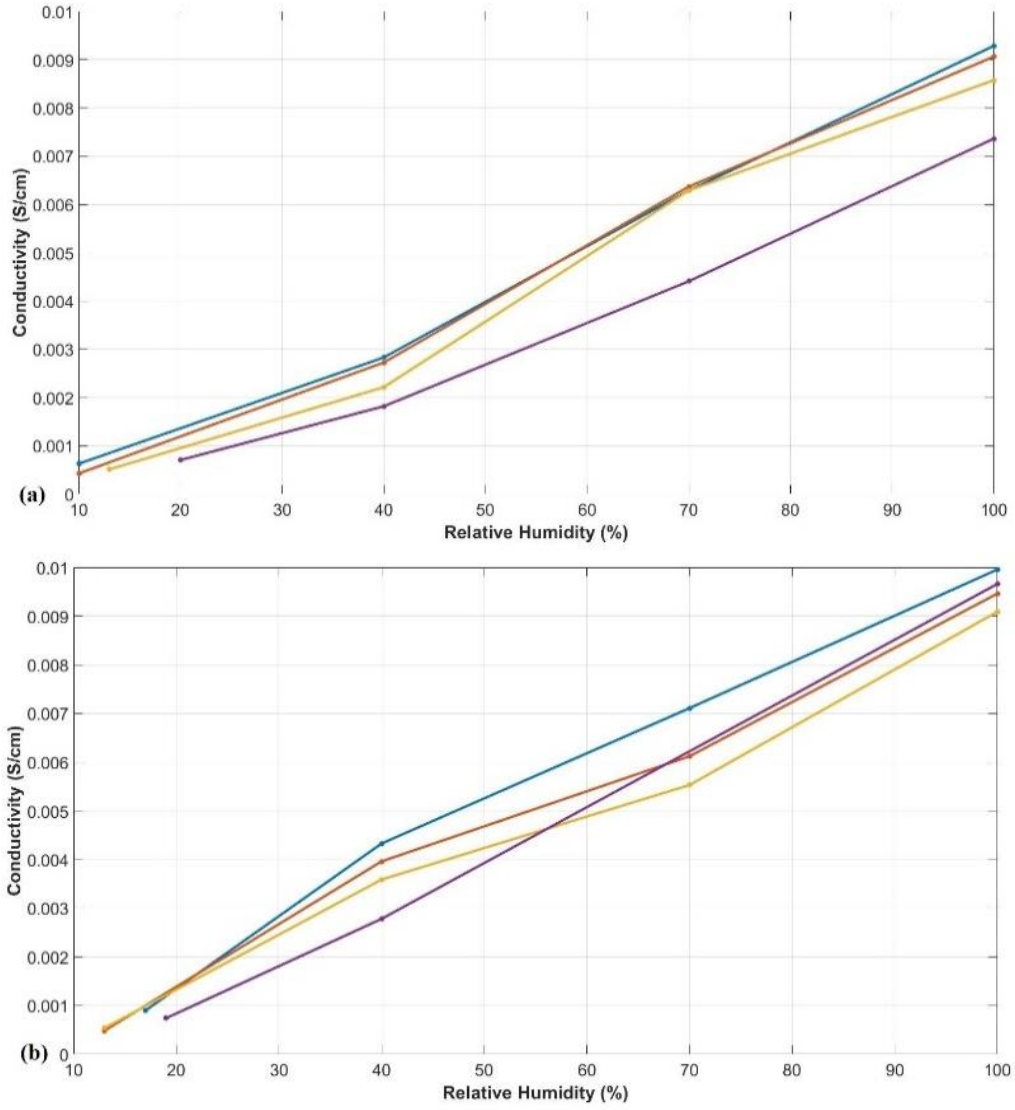

Figure 3-9: Nafion® Membrane conductivity for different RH and Temperature (T=60°C (-•-);T=50°C (-•-);T=40°C (-•-);T=30°C (-•-)) : (a) N115 & (b) N117

As shown in **Figure 3-9**, the behaviors of both membranes are random for the temperature. Except for the 60°C, which is clearly higher than the others no matter which RH it is. This randomness can be because neither of these membranes were pretreated. Essentially, before using a Nafion® in any devices, it needs to be activated. This enhances the conductivity with the different temperature and RH [12].

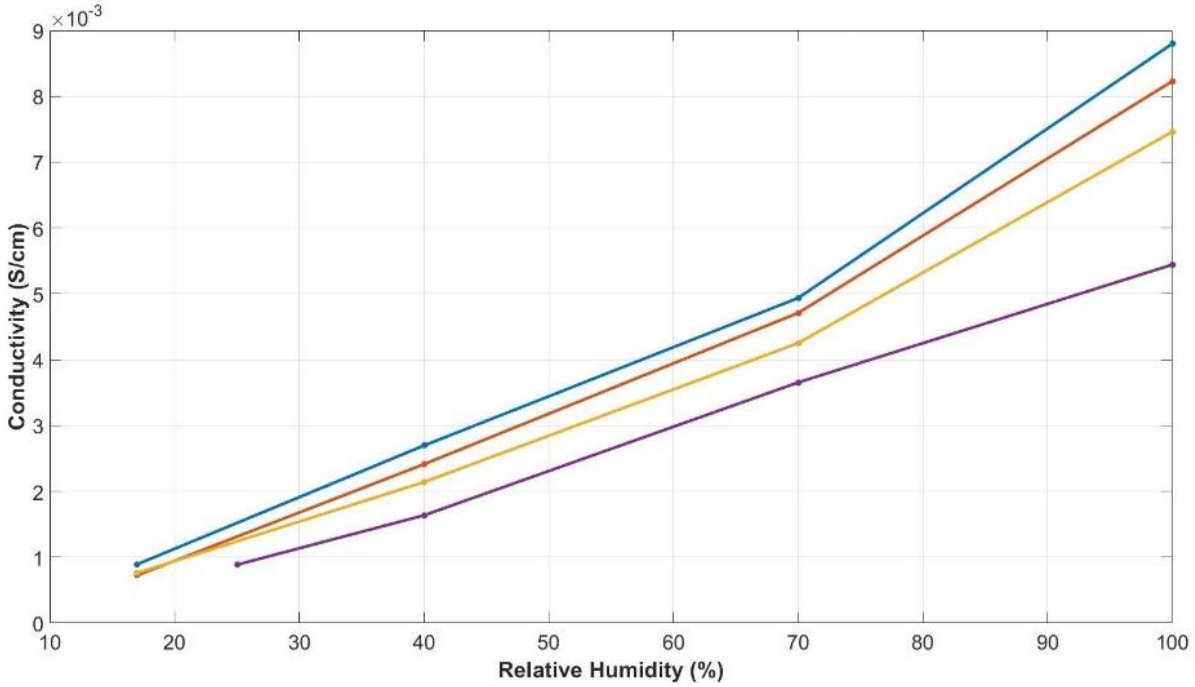

Figure 3-10: Nafion® N117 Membrane conductivity for different RH and Temperatures: HCl Pretreated membrane (T=60°C (-•-);T=50°C (-•-);T=40°C (-•-);T=30°C (-•-))

This membrane was pretreated or prepared, or some might say activated beforehand. As exhibited in **Figure 3-10**, the values of conductivity depend strongly on the RH and temperature. The conductivity increases with temperature and RH, between RH of 30% and 60%, that means that the conductivity has doubled. The correlation between these conditions and the ultimate value of resistance strongly depends on the usage of this type of membranes which is essential and conditions the performance of the cell. By that, it means that the configuration of temperature and RH should be provided to create that efficient performance. The plots do not intertwine like the previous measurements in **Figure 3-9**. This both proves the strong dependence on the cell functioning environment and conditions but also the state of the material itself.

3.2.2 Measurements for PEM membrane Nafion® N117: active layer effect and thickness

On these following measurements, the purpose was to test both the effect of the membrane thickness (multilayer assembly) and the catalyst layer's orientation (Figure 3-11).

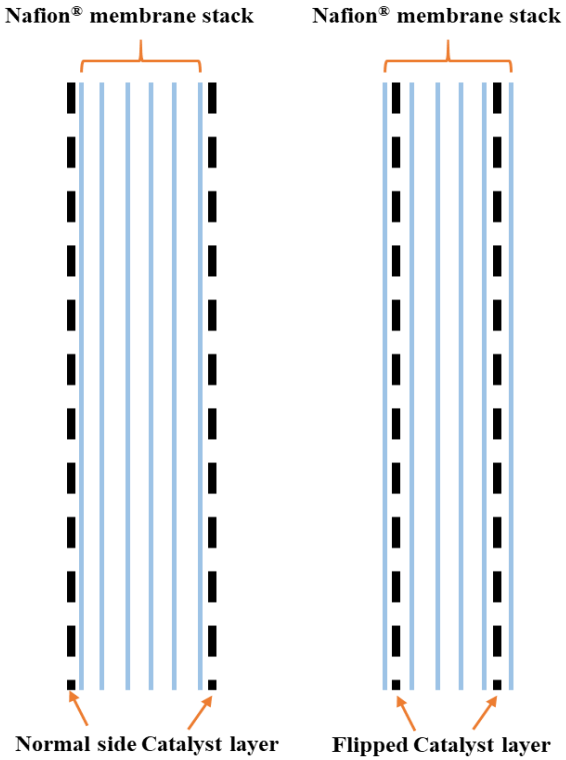

Figure 3-11: Schematic sketch representation of the catalyst layer orientation tested

The previous tests were conducted on clear uncoated membrane. Besides the preparation process there is also the catalyst coat limitation. For the membrane to be operational in PEM devices a small layer of catalytic loading is added to exploit the electrochemical functionalities. In this case, a few nanometers Pt/C load was added only on one side of two membranes. A stack of 4 other clean uncoated N117 membranes were put in between these two on side coated ones, as a sandwich structure (***Figure 3-11***). Each time one of those four clean ones were taken out and another test was done to measure the resistance. The orientation of the catalyst was also inspected. If it was facing the GDL or the membrane does it, affect the general measured conductivity.

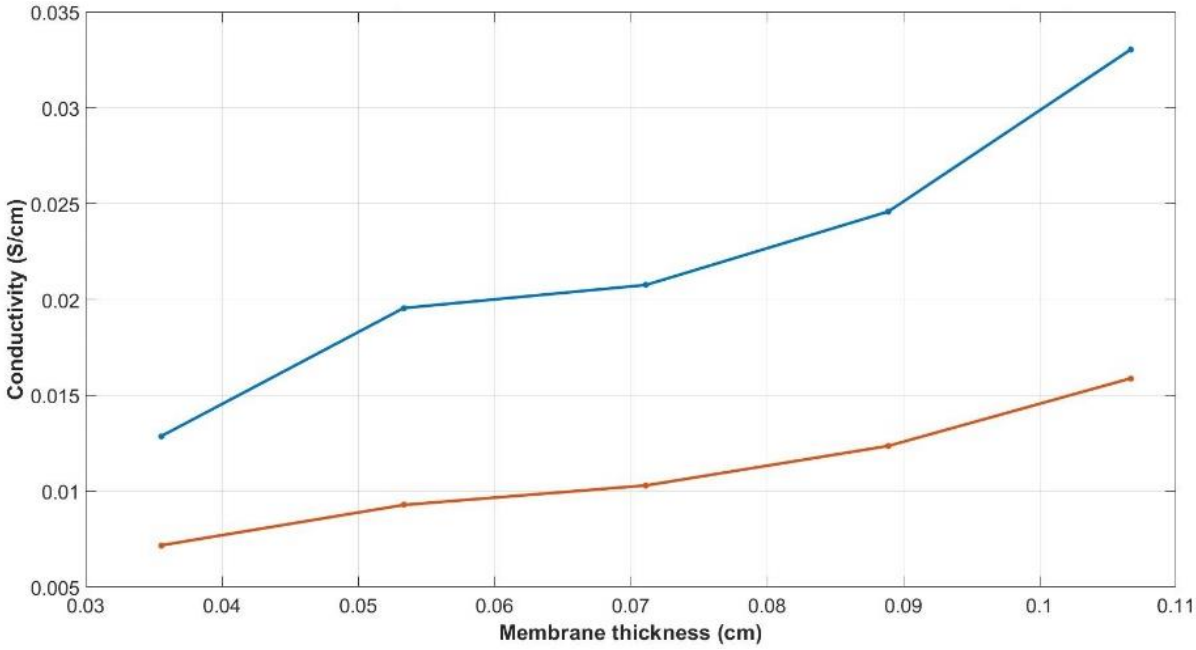

Figure 3-12: Nafion® Membrane conductivity for different thicknesses at 25°C & RH 100% (Normal catalyst orientation (-•-); Catalyst flipped to the inside (-•-))

The thickness can have a big effect on the resistance, not the conductivity. However, in **Figure 3-12**, the thicker the stack, the bigger the conductivity. This can be due the contact resistance between the stacked membrane or the non-homogeneity of the humidity in the stack. For the flipped catalyst, a barrier is created which lowers the conductivity. Even though the loading was only a few nanometers, it created a blockage in the measurements by adding an additional resistance. The catalytic layer is a poor ionic conductor. As a result, the thickness does not have as much effect as the normal catalyst orientation. Thus, the thickness pile to measure the conductivity is not the ideal method.

3.2.3 Measurements for PEM membrane Nafion® N117: Ammonia (NH_3) effects

According to Uribe *et al.* [13] the NH_4^+ generated by the NH_3 can cause a significant decrease of the conductivity. Gomez *et al.* [14] confirms experimentally that the ammonia affects tremendously the performance of the fuel cell causing drastic damages to both the membrane and the catalyst. Regarding this possibility, the following experiments were done to verify this hypothesis in the case of a clean uncoated membrane in a cell whose only goal is to measure the membrane's resistance. In order to do that, three N117 membranes were dipped directly in liquid NH_3 while three others were exposed to vapor NH_3. These six membranes were later cleaned in 10% boiling HCl for two hours and rinsed for an hour with boiling water and were left to dry at room temperature. This cleaning process was done to verify the conductivity of these membranes in order to determine if the ammonia damages were permanent. These were compared to a clean unused membrane to see the difference. Each time a stack of three uncoated membranes were placed in a cell and after each measurement one of the membranes is retrieved to test for three different thicknesses.

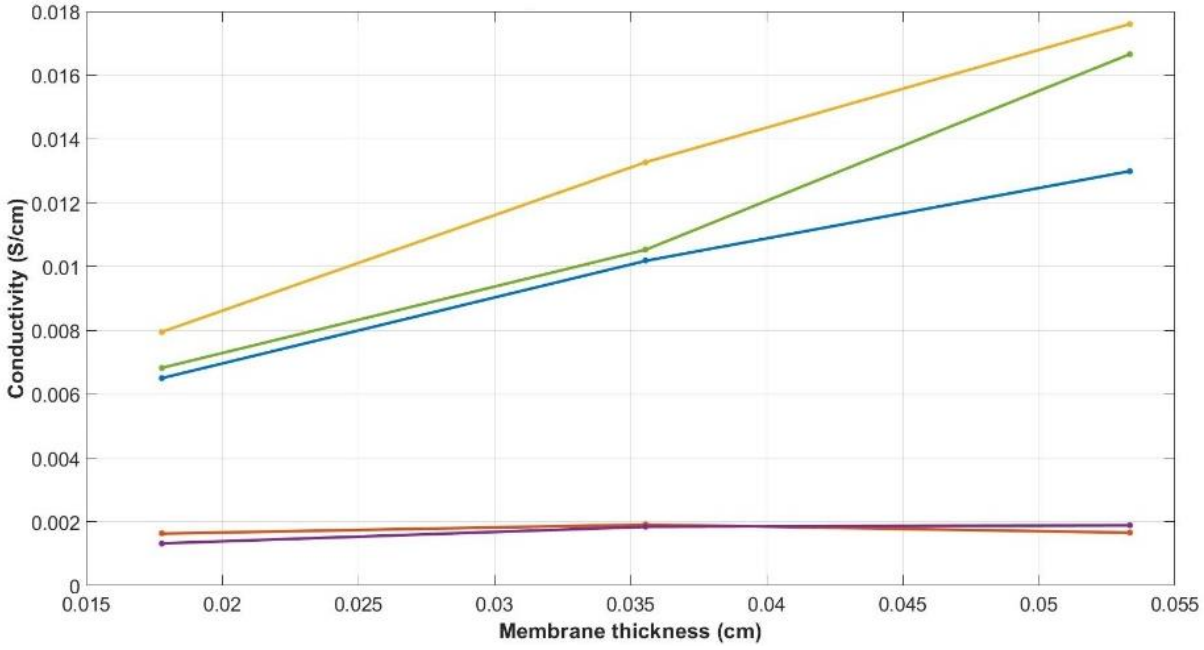

Figure 3-13: Nafion® N117 Membrane conductivity comparison on the effect of ammonia for different thicknesses at 25°C & RH 100% (Clean unused membrane (-•-); Dipped in liquid NH_3 (-•-);Cleaned with HCl after liquid NH_3 (-•-); Exposed to vapor NH_3 (-•-) ;Cleaned with HCl after Vapor NH_3 (-•-))

Figure 3-13 demonstrates how low the conductivity drops whether it was exposed to vapor NH_3 or dipped in the liquid itself. The values are even extremely close. This indicates that the statement of Gomez *et al.* and Uribe *et al.* [15] is not limited to fuel cells but concerns every PEM device who might be exposed to ammonia. However, the cleaned membrane after NH_3 behaved better than the new one which might be because the new membrane was not pretreated. Therefore, it can be assumed that there is a negative effect on the conductivity in the presence of the NH_3, nevertheless it seems to be reversible. On the other hand, this does not confirm that the NH_3 did not damage the material on a microscopic level.

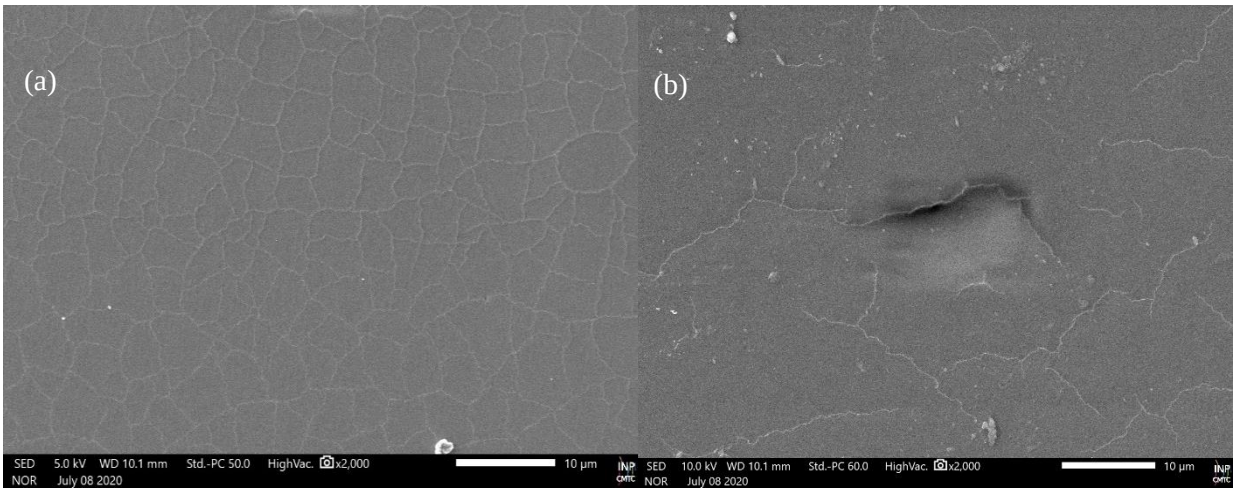

Figure 3-14: SEM imaging of a Nafion® membrane N117 after the conductivity measurements: (a) clean and unused & (b) dipped in liquid NH_3

As illustrated in **Figure 3-14**, although the membrane has similar conductivity after it was cleaned, the microscopic imaging shows a clear sign of a minor deterioration in the membrane dipped in liquid NH_3.

Since this membrane was only dipped once in NH_3, a generalized conclusion cannot be drawn. However, this can trigger an assumption worth testing in the future. That maybe the long time use of a membrane in NH_3 can cause a complete degradation after a certain number of uses.

These conductivity measurements highlighted the limiting processes when hydrogen contains impurities.

3.3 Electrochemical Hydrogen Compression: results

In this section, the EHC measurements will be discussed. In this case, the main phenomena are proton diffusion, electrochemical kinetics, water transport: diffusion, electro-osmotic and osmotic pressure transport in the membrane [16]. According to Dawn M. Bernardi and Mark W. Verbrugge [23] in the PEM devices, water management and temperature are the key parameters. Water management affects the proton conductivity, and the temperature increase improves both electro catalyst kinetics and membrane conductivity.

Then, the EHC measurements were done at different pressures (10 bars - 20 bars - 30 bars), These experiments were conducted at 3 temperatures (25°C - 40°C - 60°C) and four relative humidity (20% - 40% - 70% - 100%). It was done for both pure H_2 and N_2/H_2 gas mixtures (75%/25%). For the gas mixture experiments, the N1110 Nafion® membrane had to be changed mid-tests due to degradation and poisoning. EIS measurements were performed before and after a compression at 30 bars. Due to the large number of experiments, the proposed methodology is based on resistance and EIS analysis. Obviously, online, and postmortem investigations could provide some indications of the processes occurring in EHC.

3.3.1 Online results: Pressure variation

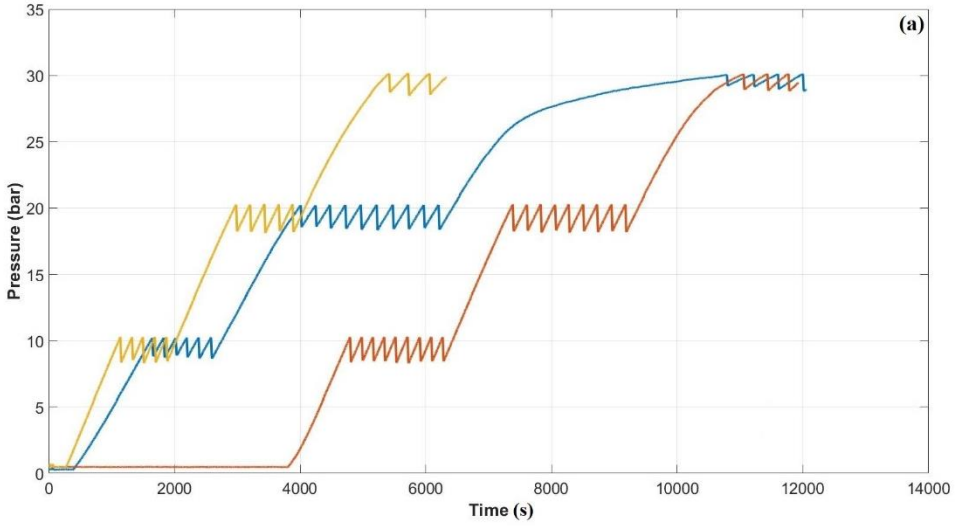

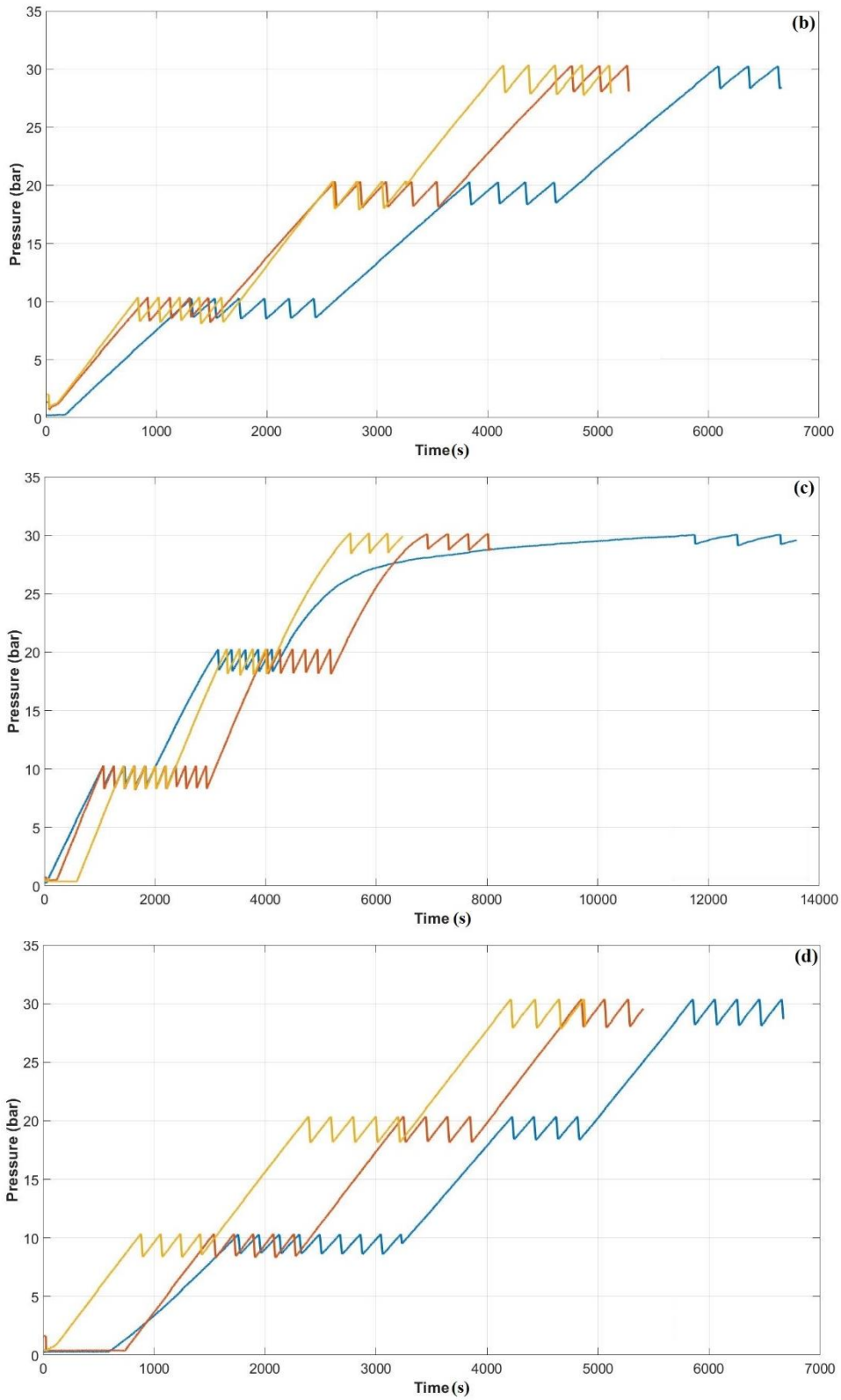

Figure 3-15: Pressure as function of time with varying gas composition and RH and temperature (T=25°C (-•-);T=40°C (-•-);T=60°C (-•-)): (a) Pure H_2 at RH 40% & (b) N_2/H_2 gas mixture at RH 40% & (c) Pure H_2 at RH 70% & (d) N_2/H_2 gas mixture at RH 70%

In **Figure 3-15** the effect of the inlet gas composition was only observed at low relative humidity. Due to safety reasons on the experimental bench the voltage was fixed at a maximum of 600 mV, it was laborious to fix the pressure close to 30 bars with low humidity with an inlet mixture of nitrogen and hydrogen compared to pure hydrogen. Other tests have given similar results (Appendix B): for RH > 20%, it was recorded that the increase of temperature seems to have a positive effect on the compression speed. The separation process did not affect the performance of the compression since the cell was able to reach 30 bars.

3.3.2 Membrane resistance analysis for in situ experiment of EHC

As noticed above EIS measurements are performed at open circuit voltage (OCV) before and after the compression procedure for both pure H_2 and gas mixtures. In the Nyquist plot, EIS spectra provide a good assessment of the membrane resistivity. The PEM membrane is directly affected by inlet RH, water transport due to the diffusion, the electro-osmotic and the osmotic pressure transport [16]. As expected, the temperature ranges and relative humidity (operating conditions) play a substantial role in the EHC performances. On **Table 3.3** resistance measurements are scrutinized as a function of humidification and temperature during compression of pure hydrogen. The membrane conductivity increases after compression which might be due to better humidification caused by water transport during the operation. This effect is less observed for high humidification, for 70% RH and 100% RH the conductivity was stable. As it was observed during the conductivity measurements, the conductivity increases with inlet RH and the temperature.

Table 3.4 presents the same results but this time for a N_2/H_2 gas mixture (75%/25%). Surprisingly, no correlation was between the resistance and the humidification during the electrochemical compression/separation of hydrogen for the nitrogen mixture at RH below 40% (**Table 3.4**). In addition, for higher RH the resistance was stable, the transition of stable conductivity appears at lower RH for the gas mixture (around 40%) than for pure hydrogen (around RH 70%).

Table 3.3: Membrane resistance measured before and after compression (up to 30 bar) for different relative humidity and temperature for pure H_2

Experiments	Membrane resistances Ω	Membrane resistance decrease%
RH=20% & T=25°C & Before compression	0,5162051	52,37% ↘
RH=20% & T=25°C & After compression	0,2458817	
RH=20% & T=40°C & Before compression	0,976546	80,33% ↘
RH=20% & T=40°C & After compression	0,1920664	
RH=20% & T=60°C & Before compression	0,756445	75,98% ↘
RH=20% & T=60°C & After compression	0,1816946	
RH=40% & T=25°C & Before compression	0,328155	66,13% ↘
RH=40% & T=25°C & After compression	0,1111525	
RH=40% & T=40°C & Before compression	0,3034591	66,02% ↘
RH=40% & T=40°C & After compression	0,1031014	
RH=40% & T=60°C & Before compression	0,2542501	58,33% ↘
RH=40% & T=60°C & After compression	0,1059386	
RH=70% & T=25°C & Before compression	0,1232285	22,65% ↘
RH=70% & T=25°C & After compression	0,095312	
RH=70% & T=40°C & Before compression	0,0861506	5,12% ↘
RH=70% & T=40°C & After compression	0,0817399	
RH=70% & T=60°C & Before compression	0,0752786	7,99% ↘
RH=70% & T=60°C & After compression	0,0692642	
RH=100% & T=25°C & Before compression	0,1032728	12,19% ↘
RH=100% & T=25°C & After compression	0,0906802	
RH=100% & T=40°C & Before compression	0,086604	8,25% ↘
RH=100% & T=40°C & After compression	0,0794604	
RH=100% & T=60°C & Before compression	0,070391	-2,30% ≅
RH=100% & T=60°C & After compression	0,0720115	

Table 3.4: Membrane resistance measured before and after compression for different relative humidity and temperature for N_2/H_2 gas mixture (25% N_2 and 75% H_2)

Experiments	Membrane resistances Ω	Membrane resistance decrease %
RH=20% & T=25°C & Before compression	0,2394895	-20,08% ↗
RH=20% & T=25°C & After compression	0,2875854	
RH=20% & T=40°C & Before compression	0,7241763	67,40% ↘
RH=20% & T=40°C & After compression	0,2361013	
RH=20% & T=60°C & Before compression	0,1391278	-172,24%↗
RH=20% & T=60°C & After compression	0,378758	
RH=40% & T=25°C & Before compression	0,1299256	-16,89% ↗
RH=40% & T=25°C & After compression	0,1518643	
RH=40% & T=40°C & Before compression	0,1545895	2,14% ≅
RH=40% & T=40°C & After compression	0,1512819	
RH=40% & T=60°C & Before compression	0,1817256	14,57% ↘
RH=40% & T=60°C & After compression	0,1552566	
RH=70% & T=25°C & Before compression	0,8963493	86,76%↘
RH=70% & T=25°C & After compression	0,1187045	
RH=70% & T=40°C & Before compression	0,1058912	0,07% ≅
RH=70% & T=40°C & After compression	0,1058131	
RH=70% & T=60°C & Before compression	0,0921294	5,72% ↘ ≅
RH=70% & T=60°C & After compression	0,0868637	
RH=100% & T=25°C & Before compression	0,115419	5,48% ↘ ≅
RH=100% & T=25°C & After compression	0,1090989	
RH=100% & T=40°C & Before compression	0,0976181	6,80%↘ ≅
RH=100% & T=40°C & After compression	0,090983	
RH=100% & T=60°C & Before compression	0,076549	1,99% ↘ ≅
RH=100% & T=60°C & After compression	0,0750262	

3.4 Data analysis & discussion

3.4.1 Entropy analysis

The experimental test bench exhibited many commands and safety thresholds to regulate the behavior of the EHC using control loops. Therefore, it was not trivial to evaluate the EHC cell state of health and performance. The calculation of the energy contributions is also commonly used to extract features and then perform a diagnosis. This methodology is employed in the works of Damour *et al.* and applies to a proton exchange membrane fuel cell investigation [17]. The topographies extraction for fault detection of the electrochemical cell was achieved by the generalized composite multi-scale symbol dynamic entropy that had provided an accurate assessment of the cell behavior [18]. According to this methodology, the average value of cell power at each step of fixed relative pressure has been scrutinized: 0 bars – 10 bars – 20 bars – 30 bars. Assuming that the Nernst potential is negligible, this total power corresponds to an entropic dissipation effect. This power is calculated using the following formula:

$$P_i = \frac{E_{cell}}{\Delta t_{i+1}} \left(\int_{ti}^{ti+1=ti+\tau i} |i_{cell}(t)|\, dt \right) \tag{3.2}$$

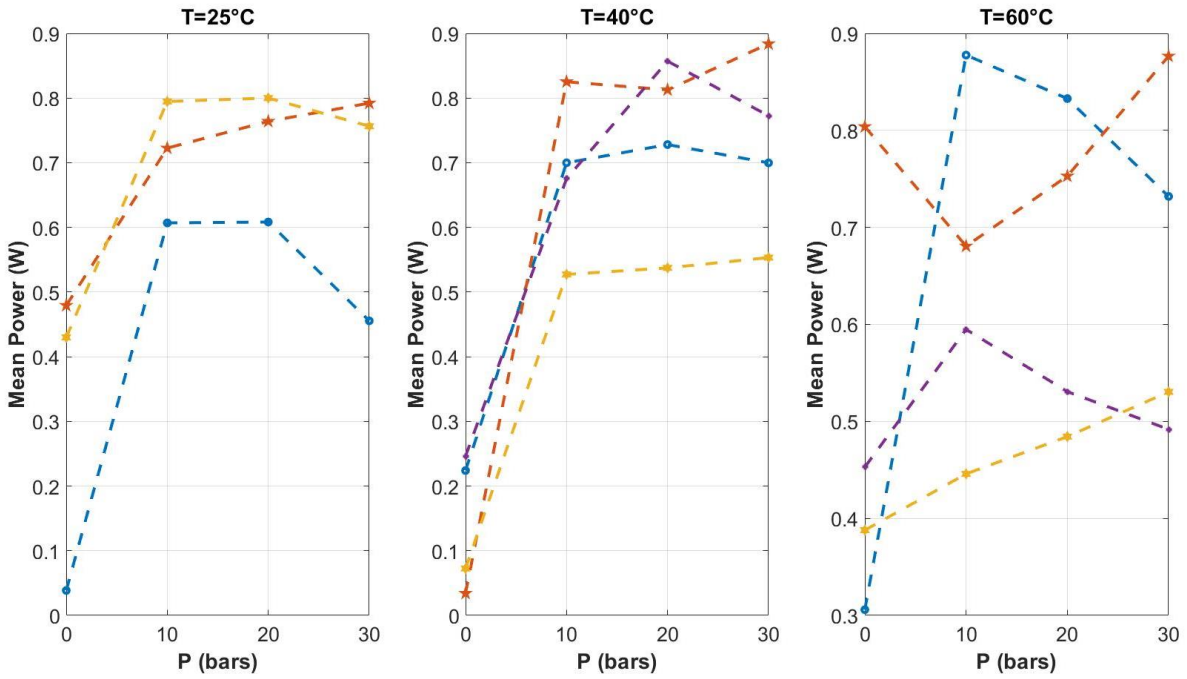

Figure 3-16: Mean power (Mean voltage*Mean current) as a function of Pressure for pure H_2 for different RH (RH 20% (-•-); RH 40% (-•-); RH 70% (-•-); RH 100% (-•-)) and temperatures: (a) T=25°C & (b) T=40°C& (c) T=60°C

Entropy analysis shown in **Figure 3-16** an increasing value until a plateau for different relative humidity and temperature. According to the membrane resistance analysis previously discussed, the conductivity usually increases with RH and the temperature, yet the mean power drops after reaching a maximum. This behavior was not recorded at high temperature. The hydration effect played a more critical impact on the cell's behavior with lower power for higher humidity ((c) T=60°C). At higher temperatures, the power was not correlated to the relative humidity.

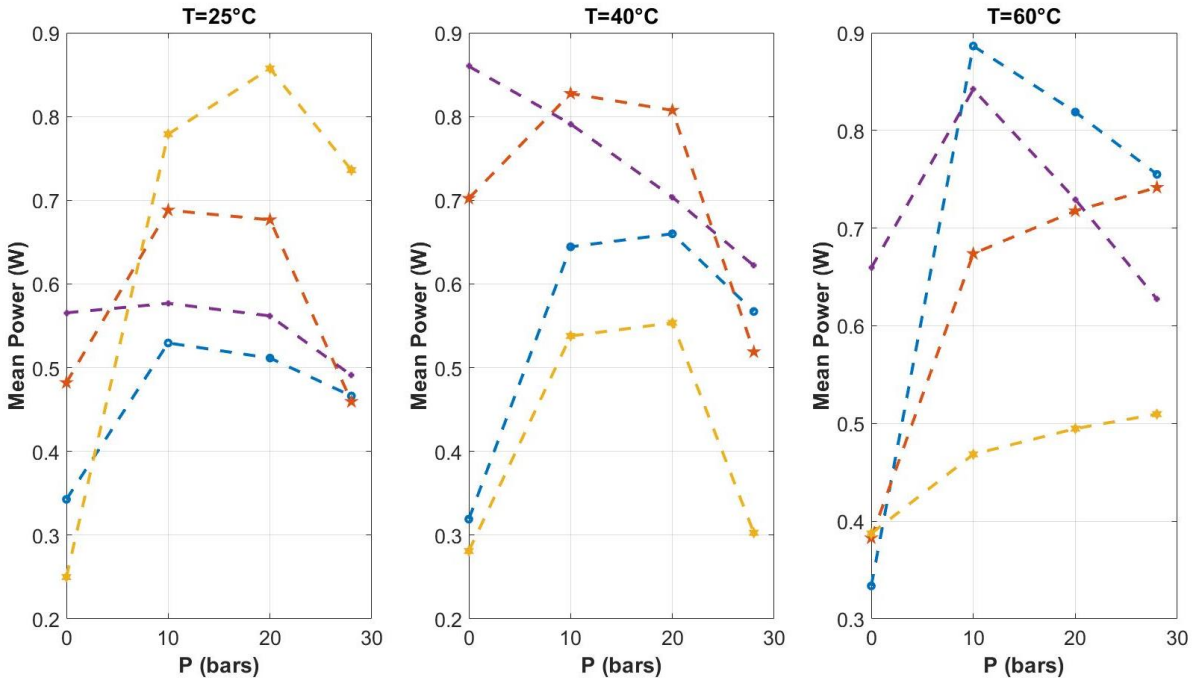

Figure 3-17: Mean power (Mean voltage*Mean current) as a function of Pressure for N_2/H_2 gas mixture for different RH (RH 20% (-•-); RH 40% (-•-); RH 70% (-•-); RH 100% (-•-)) and temperatures: (a) T=25°C & (b) T=40°C & (c) T=60°C

On **Figure 3-17** reverse "V" or "U" shapes were clearly illustrated; these topographies were not correlated to the humidity or temperature but only to the pressure. Therefore, the entropic analysis provides relevant characteristics comparing between EHC using pure H_2 and N_2/H_2 gas mixture.

According to the previous mathematical approach (Chapter 2), the dimensionless β_m is a function of the mass transport, the pressure gradient (Darcy law), the electro osmotic transport, and the back diffusion ($\beta_m = \frac{\delta_m}{D_{H_2O}}(\frac{\kappa_\Phi}{\mu} z_f c_f F \frac{J_0}{\sigma^m} + \frac{\kappa_p}{\mu}\nabla p)$). As expected for a constant value of current density the increase of cathode pressure can provide water back flow toward the anode. Only the anode side are freshly humidified, the plateau shape for pure H_2 compression confirms this description. However, water management does not describe the reverse "V" or "U" shapes. Only a new chemical process can explain this phenomenon.

3.4.2 Electrochemical Impedance Spectroscopy (EIS) comparison

Indeed, Electrochemical Impedance Spectroscopy (EIS) based approaches are widespread diagnosis methods [19]. EIS is a powerful tool to analyze physical processes. However, to perform a correct interpretation it is required to use an adapted model [20].

Figure 3-18 shows EIS diagrams performed at OCV before and after compression process until 30 bars. These diagrams exhibited the same shape and the same magnitude of capacitive loop; they were not correlated to the gas composition but to the temperature (diagrams in Appendix B of this manuscript). In addition, only the relative humidity affected the EIS capacitive loop. Therefore, the apex frequencies (Appendix B), which is the frequency at the minimum of the imaginary value Z(imag), could provide more elements to ensure a correct interstation.

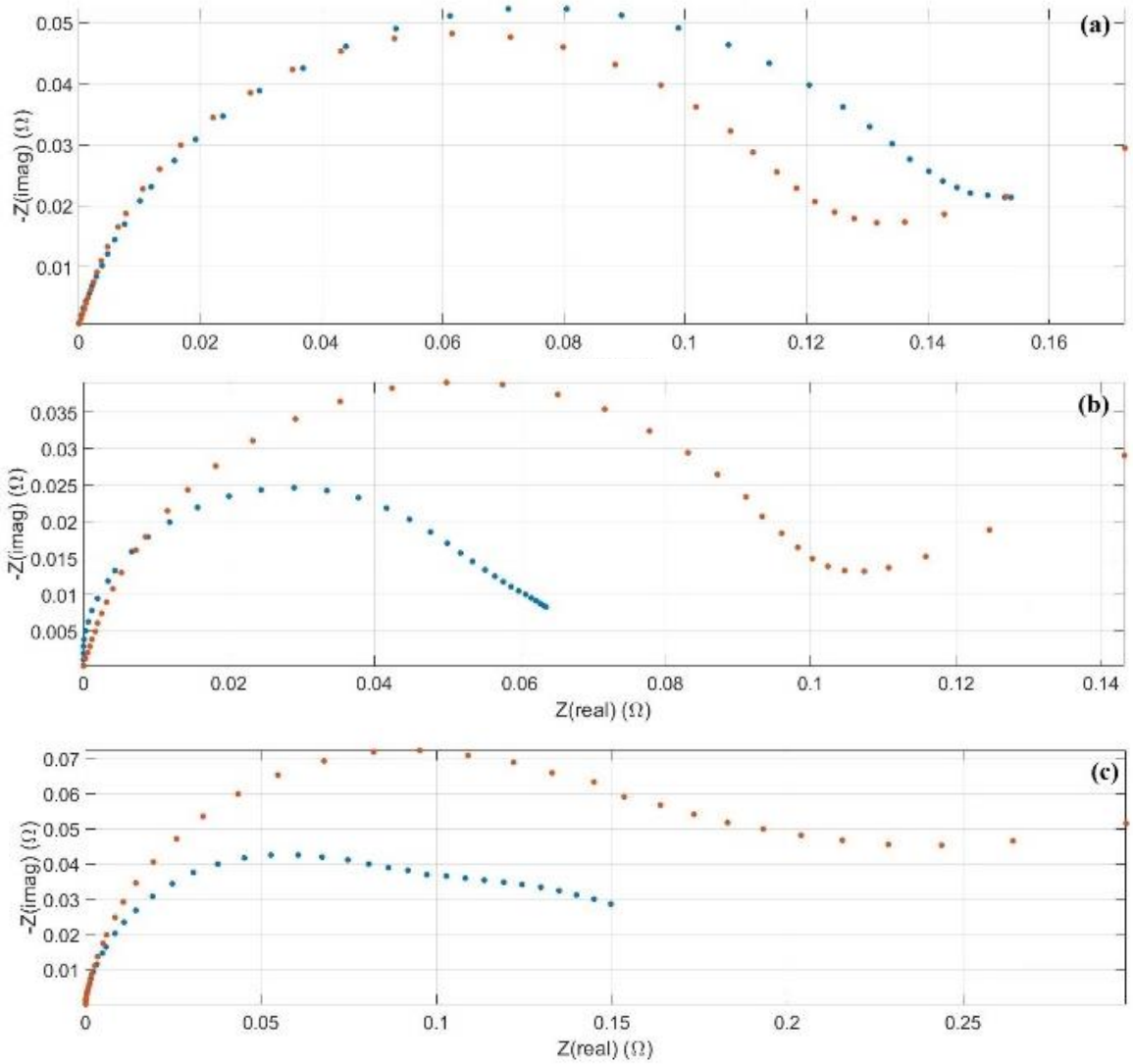

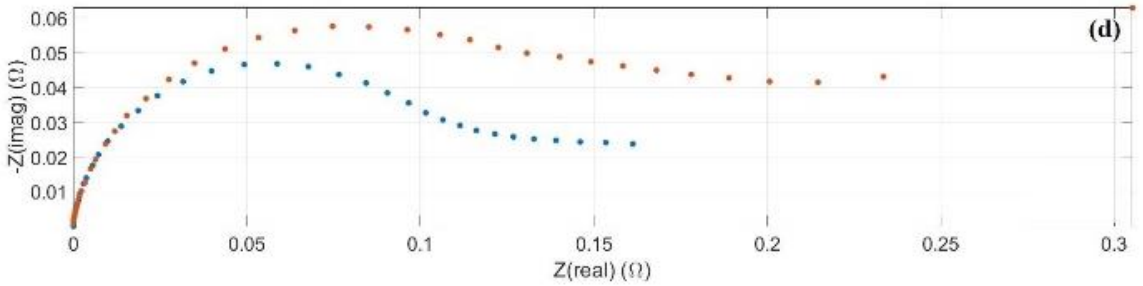

Figure 3-18: EIS diagrams at 40°C for (-•-) H_2 pure and (-•-) N_2/H_2 gas mixture: (a) before compression at RH 40% & (b) After compression at RH 40% & (c) before compression at RH 100% & (d) After compression at RH 100%

Under both pure H_2 and the gas mixture of H_2 and N_2, the apex frequencies increased after the compression for RH below 70%. For high hydration, the apex frequency after compression remains stable. The same observations were made for the membrane conductivity. Nevertheless, in **Table 3.5**, a comparison of apex frequencies after compression for pure H_2 and gas mixture N_2/H_2 is provided. To compare the evolution of these parameters, a logarithm ratio was performed as follow:

$$LnA = \ln\left(\frac{\text{Apex frequency } (H_2)}{\text{Apex frequency } (N_2/H_2)}\right) \tag{3.3}$$

Table 3.5: Apex frequencies comparison after compression under pure H_2 and gas mixture N_2/H_2

Experiments (After compression)	LnA
RH=20% & T=25°C	-0,299
RH=20% & T=40°C	-0,500
RH=20% & T=60°C	-0,699
RH=40% & T=25°C	-0,699
RH=40% & T=40°C	-0,300
RH=40% & T=60°C	-0,300
RH=70% & T=25°C	-2,401
RH=70% & T=40°C	-0,997
RH=70% & T=60°C	-1,901
RH=100% & T=25°C	0,298
RH=100% & T=40°C	-1,601
RH=100% & T=60°C	-1,301

Table 3.5 exhibits that the N_2/H_2 mixture provides higher values of apex frequencies than pure H_2. There are two possible phenomena to explain these values:

(i) When the MEA is locally dried, the frequencies increase [21] : This phenomenon due to water management during the compression explains the behavior difference between low and high hydration. High hydrations promote a stable and low value.

(ii) A modification of TPB (Triple Phase boundary) at the interface between catalyst and polymeric ionic conductor should occur and explain the increase of apex frequencies.

3.5 Postmortem characterization and online gas detection for N_2/H_2 mixture separation compression.

The evolution of apex frequency on impedance diagrams is because a new electrochemical reaction appeared at TPB which could be explained by a side reaction. In addition, an entropic analysis was conducted using the calculation of the mean power used by the cell in the compression process. The entropic evolution as a function of pressure had a "U" or "V" shape, which can be a result of the NH_3 synthesis enhanced by the increasing pressure.

The analysis of the results led to considering the appearance of a side reaction during the compression of the mixture. Kordali *et al.* [22] have demonstrated the electrochemical synthesis of ammonia at atmospheric pressures and below 100 °C. Their cell involved ruthenium catalyst deposited on a carbon felt on the cathode with Nafion® membrane and platinum catalyst on the anode. The authors have observed maximum rate of ammonia synthesis was 2.12×10^{-11} mol cm^{-2} s^{-1} at 90 °C at a cathode voltage of −0.81 V (vs NHE), but the faradaic efficiency was only equal to 0.24%. This kinetic of ammonia synthesis exhibited an Arrhenius function of temperature. However, the electrolyte solution was 2 M KOH solution. Subsequently, the synthesis of ammonia during compression was thermodynamically possible. The ammonium ion exchange with protons results in reduction of the membrane conductivity by as much as 75% – 98% compared to proton-form membrane [23].

Gas chromatography (GC) analysis was conducted, at the cathode side, to prove the NH_3 synthesis. The GC was cleaned twice before this measurement to ensure that it was not due to a previous experiment. After the compression, the gas from the cathode was released in a pipeline directly to the GC. It recorded a signature of NH_3 in the cathodic compartment during the electrochemical compression at 30 bars

(**Figure 3-19**). The value was exceedingly small compared to the hydrogen yet still considerable compared to the nitrogen.

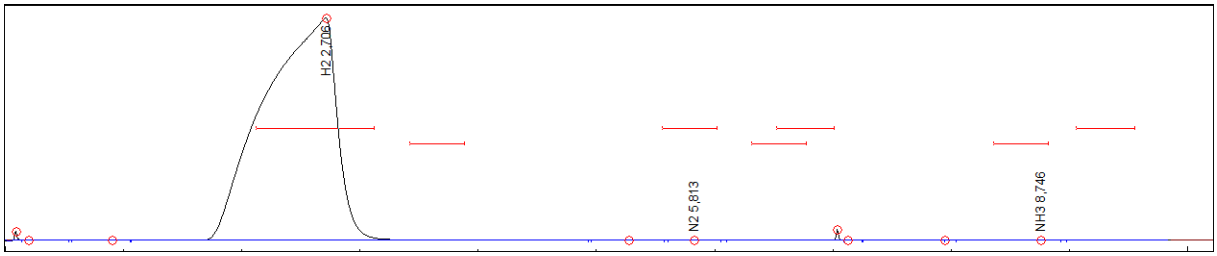

Figure 3-19: GC measurements of the gas post compression at the cathode side

This observation is quite difficult because the amount of NH_3 is very low and the reproducibility of this experiment was not efficient. However, an IR analyst of membrane after compression exhibited similar transmittance behavior to the membrane that was dipped in NH_3 (**Figure 3-20**). The comparison was done using a N1110 membrane that was dipped directly in liquid NH_3 and the membrane that was used for the GC measurements. The dipped membrane and the used one showed a similar pattern behavior which can corroborate the existence of ammonia at the surface of the membrane.

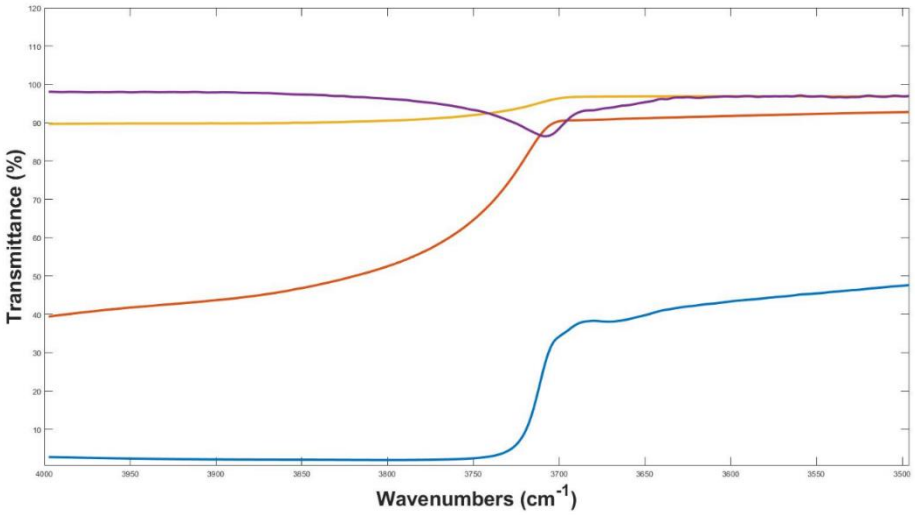

Figure 3-20: Transmittance plot of the FTIR imaging of a Nafion® membrane N1110 used for compression/separation gas mixture N_2/H_2 (Uncoated & dipped in NH_3 (-•-); Uncoated & dipped in NH_3 & cleaned (-•-); Used for the compression/separation of gas mixture (-•-); Uncoated & Unused (-•-))

According to these assumptions of NH_3 production at the membrane, the catalyst layer can be damaged early on.

Figure 3-21 and **Figure 3-22** shows the damage involved during purification/compression of N_2/H_2 mixture. This damage can be due to both the pressure applied both the membrane and the catalyst and the contaminations of what was assumed to be the ammonia. In all the pictures taken by the SEM, the material damage is very visible. Some of the catalyst load was taken off the membrane which can also be seen by the naked eye. However microscopically, the rounded shapes of a new load were completely gone. The surface was flattened which is mechanically logical due to the high pressure reached by the cell during all the compression process and specially this membrane was used every day to compress up to 30 bars for a week.

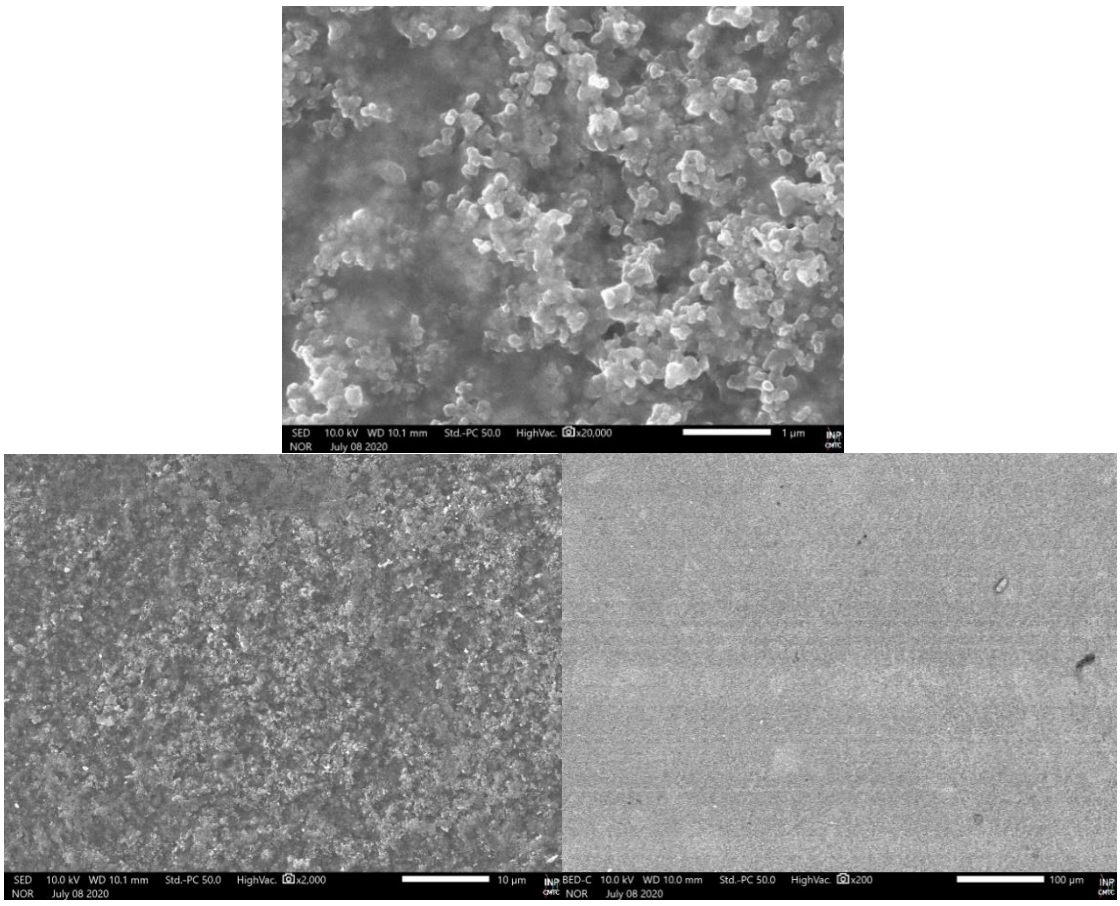

Figure 3-21: SEM imaging of catalyst layer for a clean unused coated Nafion® membrane N1110

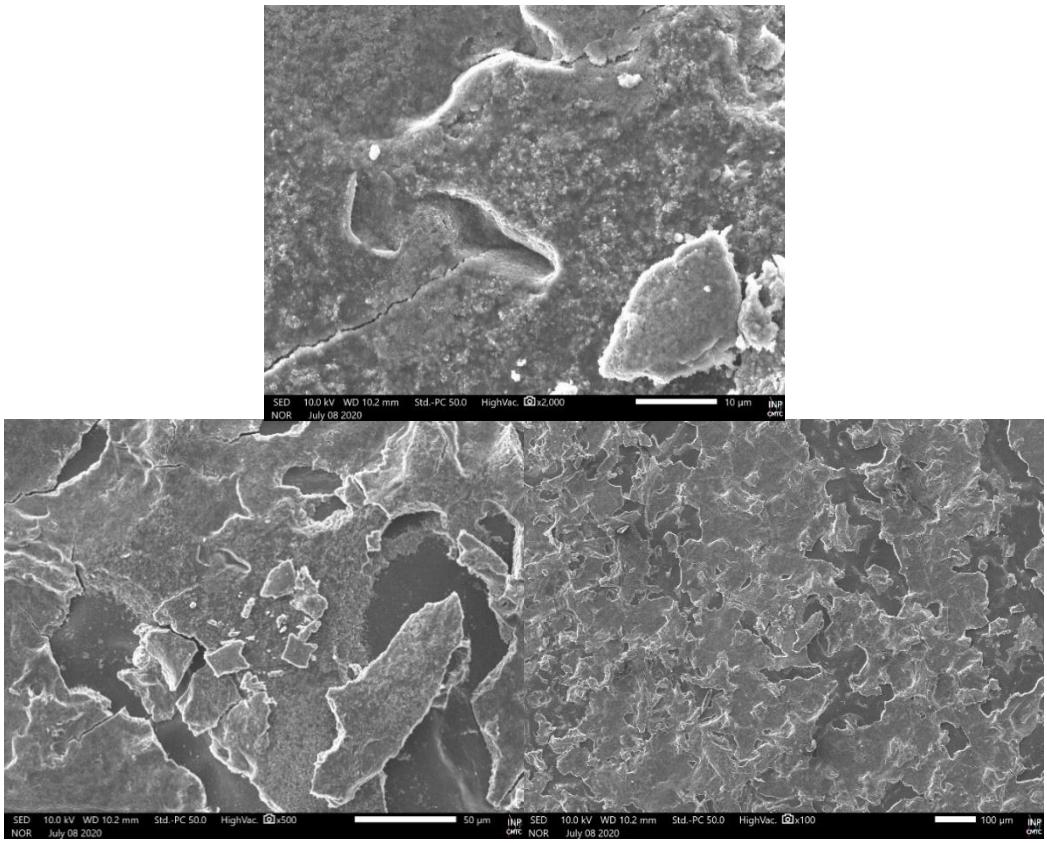

Figure 3-22: SEM imaging of catalyst layer for coated Nafion® membrane N1110 used for compression/separation gas mixture N_2/H_2

3.6 Further investigation with different mixture

After the compression of pure hydrogen and the compression/separation of the N_2/H_2 gas mixture using two different N1110 membranes with the same catalyst load. The results showed that running the cell on 75% H_2 and 25% N_2 lowered the ability to compress with time due to a strong deterioration. It was assumed to be due to the ammonia contamination. However, it was able to compress up to 27 bars, yet the cell struggled to reach 30 bars. A few last tests were done to estimate the operation for low hydrogen concentrations and methanol contamination.

3.6.1 Pressure variation for low hydrogen concentration

As stated before, a low hydrogen compression/separation test was conducted for 1% H_2 and 99% N_2. The cell went already through multiple gas mixture tests. The run time was around four hours. The results were compared to pure hydrogen and (75% H_2 / 25% N_2) compression.

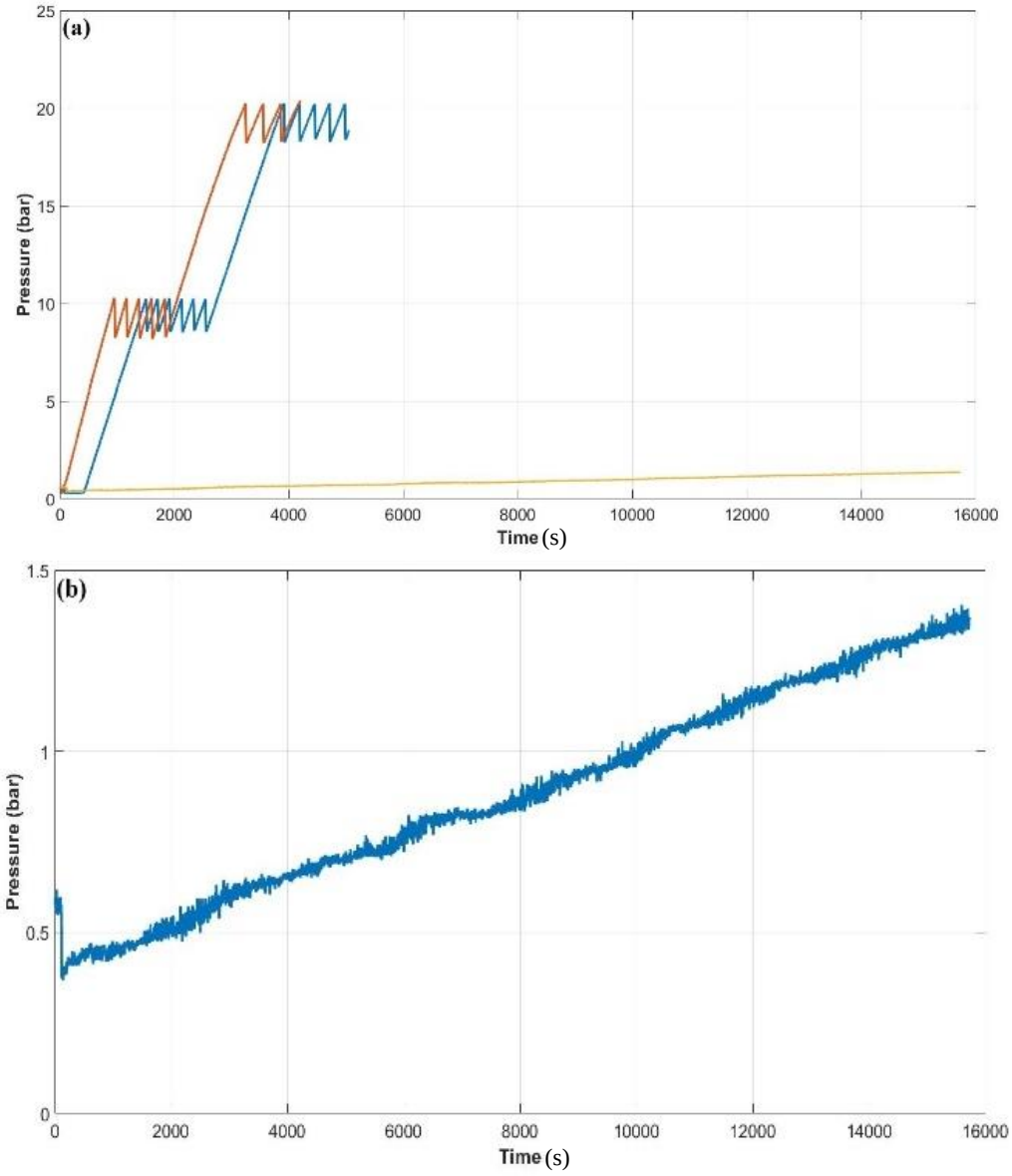

Figure 3-23: Pressure as function of time at RH 100% and T=25°C with varying gas composition: (a) Pure H_2 (-•-); Gas mixture 75% H_2 and 25% N_2 (-•-); Gas mixture 1% H_2 and 99% N_2 (-•-) & (b) Gas mixture 1% H_2 and 99% N_2

Figure 3-23, (a) and (b), exhibits the cell behavior depending on the gas feed. For pure hydrogen and high hydrogen concentration in a gas mixture, the device can reach 20 bars in less than two hours.

However, in low hydrogen concentration even after four hours the maximum pressure achieved less than 1.5 bars. This caused an aggressive damage to the membrane. Even with pure hydrogen, the cell was not able to compress anymore due to the high contamination rate caused by the high nitrogen concentration in the gas feed. There was no time to verify if HCl treatment can help the membrane recover after this damage.

3.6.2 Pressure variation with methanol contamination

An additional humidifier was added to the gas feed pipeline. Inside it was a mixture of 30% methanol and 70% water. Before feeding the cell with a gas, it must pass through this additional humidifier.

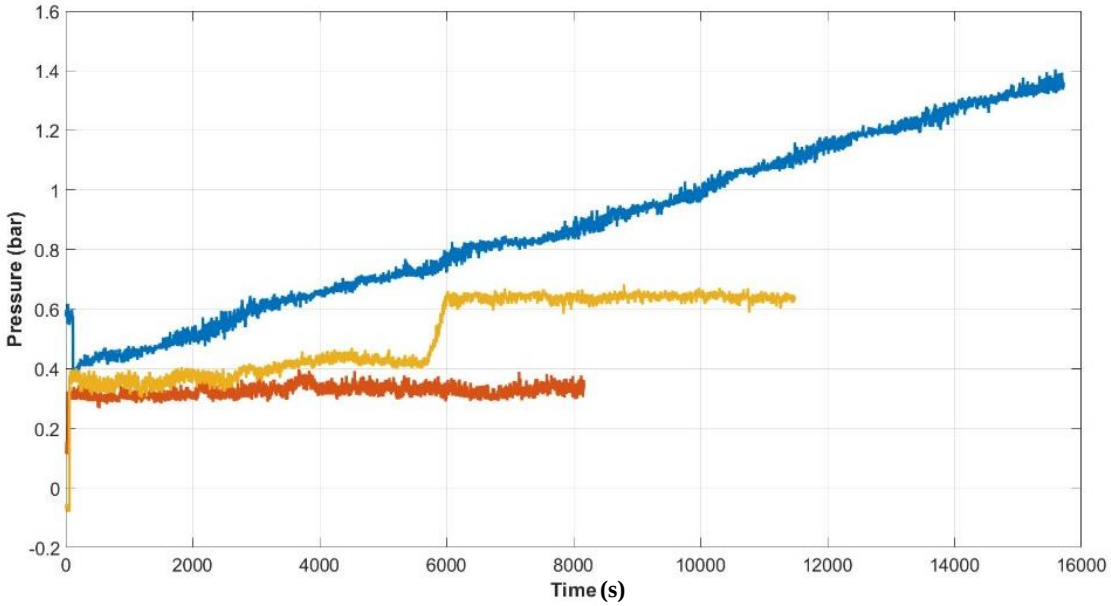

Figure 3-24 : Pressure as function of time at RH 100% and T=25°C with varying gas composition: Gas mixture 1% H_2 and 99% N_2 (-•-); Pure H_2 + Methanol (-•-); Gas mixture 75% H_2 and 25% N_2 + Methanol (-•-)

In the previous section, the cell struggled with the low hydrogen mixture. Without changing the membrane after the two (N_2/H_2) gas mixtures (25%/75%) and (99%/1%), the cell was tested again by feeding the gas feed with MeOH. Whether it is pure hydrogen or high hydrogen concentration gas mixture, the pressure cannot even reach 1 bar (**Figure 3-24**).

In the Chapter 1 (1.3.2.1. subsection) , according to Catalano *et al.* [24], the efficiency (η) of electrochemical gas compressors, depends on β values which is the figure-of-merit for electro-kinetic compression in the gas phase:

$$\beta = (RT/F^2)(t_n{}^2\,\sigma/\kappa_n) \tag{3.4}$$

with R is the gas constant (8.31 J mol^{-1} K^{-1}), *T* is the temperature (K), *F* is the faraday constant (96487 C mol^{-1}), t_n is the dimensionless transference coefficient of the volatile species (H_2 and methanol), σ is the ionic conductivity (S m^{-1}) and κ_n is the molar permeability coefficient (mol s^{-1} m^{-1}) for zero current density.

Using the estimation for the gas transport properties of Nafion® with pure H_2 from Sakai *et al.* [25] and with H_2 and methanol transport from [26], the square value transference coefficient acts on of β. Therefore, anomia synthesis is not the only chemical phenomena. A possible transference of N_2 was also possible. This effect has never been reported in the literature.

DISPOSITO (conclusions and perspectives)

In many cases, hydrogen is mixed with other gas such as nitrogen (N_2): in the case of hydrogen produced using ammonia (NH_3) reforming. Ammonia shows a volumetric energy density equal to 4325 Wh/L versus only 1305 Wh/L for hydrogen (700 bars). Therefore, NH_3 becomes especially competitive and it is an inexpensive fuel. The usual price range in North America from 2008 to 2018 is from $400-600/ton for anhydrous ammonia [27]. The average market price of NH_3 and with other reported studies, $500/ton with a world value of about $250 billion [28]. Nevertheless, the Haber-Bosch process using steam methane reforming process to produce hydrogen generates large quantities (1500 kg-CO_2/ton-NH_3) of greenhouse gases (GHG). According to Wang et al. [29], it proves possible to produce solar ammonia from just N_2, H_2O, and sunlight on an industrially significant scale, efficiency, and cost. Ammonia supply chain has an extensive and well-developed manufacturing distribution infrastructure worldwide to guarantee uninterrupted fuel quantity. NH_3 decomposition is a processing technology for PEM fuel cell applications. Several technical and economic reasons confirm the sustainability of the route of NH_3 decomposition for distributed H_2 generation.

The catalyst of ammonia decomposition reaction has long been studied. The commercially used catalyst for ammonia decomposition is nickel on alumina, which is mechanically strong and heat resistant, and their development and optimization are well established [30]. NH_3 decomposition has a single feed stream and is therefore accomplished in a single step. Which is a cost advantage in consequence of reduced balance-of-plant (BOP) as compared to the multi-step process of methane steam reforming [31]. Produced H_2 from NH_3 conversion exhibits high selectivity and high efficiency [32]. However, for a PEM device this synthesis can be poisonous. As it has been said in the introduction for the first chapter, for PEMFC automotive applications the level of purity required is as follows: $H_2 > 99.97$ mol%, $NH_3 < 0.1$ ppm (mol), and $N_2 < 300$ ppm (mol) ([33], [34]).

Direct electrochemical compression of the hydrogen process has been successfully seen through the final state of the membrane after the experiments. According to the resistive energy losses associated with proton diffusion through the electrochemical cell: doubling the current density, doubles the hydrogen flow, but quadruples the dissipated power. The specific resistance of the membrane is the main parameter of the electrochemical cell. The overall resistance depends on cell materials as well as operating conditions such as pressure gradient, contact resistance, and at the selected current density. Due to the multiple parameters that might not be known in this study which complicates the interpretation of the results. This was done using perfluoro-sulfonic acid (PFSA) membranes with a Pt/C supported catalyst. Other tests were conducted on a clean membrane to measure the conductivity for different thicknesses in different temperatures and relative humidity (RH).

The post analysis of the data collected through the experiments have mainly shown that:

- The cell was able to successfully compress the hydrogen up to 30 bars whether it is pure H_2 or (N_2/H_2) gas mixture.
- The membrane resistance analysis has shown that the conductivity increased after pure H_2 compression which might be due to better humidification. However, no correlation was between the resistance and the humidification during the electrochemical compression/separation of (N_2/H_2) gas mixture.
- A new investigation method of the entropy analysis using the cell mean power was conducted to highlight the effect of the gas mixture on the operating cell. This has revealed a possibility of a new chemical process.
- EIS measurement showed that the nitrogen impacts the performance of the catalyst layer during electrochemical compression.
- Postmortem analyses (SEM, IR spectroscopy) of MEA and GC online have confirmed the possible electro synthesis of NH_3. Also, these analyses have shown a clear sign of contamination and deterioration.
- An abusive test with a higher concentration of nitrogen revealed the difficulties of the cell's ability to both purify the hydrogen and compress it.
- A parametric optimization was conducted using the second chapter 2 model, the Wagner number values are provided in the Appendix B. The results have shown an increase of the Wagner number with pressure. This behavior highlights the decrease of charge transfer resistance along with the partial pressure increase. However, there was no significant difference between the pure H_2 and the (N_2/H_2) gas mixture.

In conclusion, the differences in EHC performance that were investigated in this chapter as a function of nitrogen concentration is not linked to water management through the membrane. The Hydrogen/Nitrogen mixture's separation process had affected the membrane resistance. This was exhibited by the weak increase of membrane resistance. Hydrogen/Nitrogen mixture involved an additional limitation conceivably at the membrane electrode interface.

References

[1] M. Suermann, T. Kiupel, T. J. Schmidt, et F. N. Büchi, "Electrochemical Hydrogen Compression: Efficient Pressurization Concept Derived from an Energetic Evaluation," *J. Electrochem. Soc.*, vol. 164, nº 12, p. F1187–F1195, 2017, doi: 10.1149/2.1361712jes.

[2] G. Sdanghi, G. Maranzana, A. Celzard, et V. Fierro, "Review of the current technologies and performances of hydrogen compression for stationary and automotive applications," *Renew. Sustain. Energy Rev.*, vol. 102, p. 150-170, Mar. 2019, doi: 10.1016/j.rser.2018.11.028.

[3] "HySa Infrastructure." https://hysainfrastructure.com/exchange_student/maha-rhandi/.

[4] "ion power." https://ion-power.com/nafion-membranes/.

[5] "SH-222 Model Details." https://espec.com/na/products/model/sh_221.

[6] W. Germer, C. Harms, V. Tullius, J. Leppin, et A. Dyck, "Comparison of conductivity measurement systems using the example of nafion and anion exchange membrane," *Solid State Ion.*, vol. 275, p. 71-74, Jul. 2015, doi: 10.1016/j.ssi.2015.02.023.

[7] P. Heimerdinger, A. Rosin, M. A. Danzer, et T. Gerdes, "A Novel Method for Humidity-Dependent Through-Plane Impedance Measurement for Proton Conducting Polymer Membranes," *Membranes*, vol. 9, nº 5, p. 62, May 2019, doi: 10.3390/membranes9050062.

[8] K. Cooper, "Characterizing Through-Plane and In-Plane Ionic Conductivity of Polymer Electrolyte Membranes," *ECS Trans.*, vol. 41, nº 1, p. 1371-1380, Dec. 2019, doi: 10.1149/1.3635668.

[9] C. L. Gardner et A. V. Anantaraman, "Studies on ion-exchange membranes. II. Measurement of the anisotropic conductance of Nafion®," *J. Electroanal. Chem.*, vol. 449, nº 1-2, p. 209-214, Jun. 1998, doi: 10.1016/S0022-0728(97)00408-7.

[10] A. V. Anantaraman et C. L. Gardner, "Studies on ion-exchange membranes. Part 1. Effect of humidity on the conductivity of Nafion®," *J. Electroanal. Chem.*, vol. 414, nº 2, p. 115-120, Jan. 1996, doi: 10.1016/0022-0728(96)04690-6.

[11] H.-C. Chien, L.-D. Tsai, C.-M. Lai, J.-N. Lin, C.-Y. Zhu, et F.-C. Chang, "Characteristics of high-water-uptake activated carbon/Nafion hybrid membranes for proton exchange membrane fuel cells," *J. Power Sources*, vol. 226, p. 87-93, Mar. 2013, doi: 10.1016/j.jpowsour.2012.10.017.

[12] R. Kuwertz, C. Kirstein, T. Turek, et U. Kunz, "Influence of acid pretreatment on ionic conductivity of Nafion® membranes," *J. Membr. Sci.*, vol. 500, p. 225-235, Fer. 2016, doi: 10.1016/j.memsci.2015.11.022.

[13] F. A. Uribe, S. Gottesfeld, et T. A. Zawodzinski, "Effect of Ammonia as Potential Fuel Impurity on Proton Exchange Membrane Fuel Cell Performance," *J. Electrochem. Soc.*, vol. 149, nº 3, p. A293, 2002, doi: 10.1149/1.1447221.

[14] Y. A. Gomez, A. Oyarce, G. Lindbergh, et C. Lagergren, "Ammonia Contamination of a Proton Exchange Membrane Fuel Cell," *J. Electrochem. Soc.*, vol. 165, nº 3, Art. nº 3, 2018, doi: 10.1149/2.0761803jes.

[15] Y. A. Gomez, A. Oyarce, G. Lindbergh, et C. Lagergren, "Ammonia Contamination of a Proton Exchange Membrane Fuel Cell," *J. Electrochem. Soc.*, vol. 165, nº 3, p. F189–F197, 2018, doi: 10.1149/2.0761803jes.

[16] F. Aubras *et al.*, "Two-dimensional model of low-pressure PEM electrolyser: Two-phase flow regime, electrochemical modelling and experimental validation," *Int. J. Hydrog. Energy*, vol. 42, nº 42, p. 26203-26216, oct. 2017, doi: 10.1016/j.ijhydene.2017.08.211.

[17] C. Damour, M. Benne, B. Grondin-Perez, M. Bessafi, D. Hissel, et J.-P. Chabriat, "Polymer electrolyte membrane fuel cell fault diagnosis based on empirical mode decomposition," *J. Power Sources*, vol. 299, p. 596-603, déc. 2015, doi: 10.1016/j.jpowsour.2015.09.041.

[18] J. Zheng, J. Cheng, Y. Yang, et S. Luo, "A rolling bearing fault diagnosis method based on multi-scale fuzzy entropy and variable predictive model-based class discrimination," *Mech. Mach. Theory*, vol. 78, p. 187-200, Aug. 2014, doi: 10.1016/j.mechmachtheory.2014.03.014.

[19] J. C. Garcia-Navarro, M. Schulze, et K. A. Friedrich, "Measuring and modeling mass transport losses in proton exchange membrane water electrolyzers using electrochemical impedance

spectroscopy," *J. Power Sources*, vol. 431, p. 189-204, août 2019, doi: 10.1016/j.jpowsour.2019.05.027.
[20] S. J. Andreasen, J. L. Jespersen, E. Schaltz, et S. K. Kaer, "characterization and Modelling of a High Temperature PEM Fuel Cell Stack using Electrochemical Impedance Spectroscopy," *Fuel Cells*, vol. 9, nº 4, p. 463-473, août 2009, doi: 10.1002/fuce.200800137.
[21] J. Deseure, " Coupling RTD and EIS modelling to characterize operating non-uniformities on PEM cathodes," *J. Power Sources*, vol. 178, nº 1, p. 323-333, Mar. 2008, doi: 10.1016/j.jpowsour.2007.11.071.
[22] V. Kordali, G. Kyriacou, et Ch. Lambrou, "Electrochemical synthesis of ammonia at atmospheric pressure and low temperature in a solid polymer electrolyte cell," *Chem. Commun.*, nº 17, p. 1673-1674, 2000, doi: 10.1039/b004885m.
[23] K. Hongsirikarn, J. G. Goodwin, S. Greenway, et S. Creager, « Influence of ammonia on the conductivity of Nafion membranes », *J. Power Sources*, vol. 195, nº 1, p. 30-38, janv. 2010, doi: 10.1016/j.jpowsour.2009.07.013.
[24] J. Catalano, A. Bentien, D. N. Østedgaard-Munck, et S. Kjelstrup, « Efficiency of electrochemical gas compression, pumping and power generation in membranes », *J. Membr. Sci.*, vol. 478, p. 37-48, mars 2015, doi: 10.1016/j.memsci.2014.12.042.
[25] T. Sakai, "Gas Permeation Properties of Solid Polymer Electrolyte (SPE) Membranes," *J. Electrochem. Soc.*, vol. 132, nº 6, p. 1328, 1985, doi: 10.1149/1.2114111.
[26] R. P. W. J. Struis, S. Stucki, et M. Wiedorn, "A membrane reactor for methanol synthesis," *J. Membr. Sci.*, vol. 113, nº 1, p. 93-100, May 1996, doi: 10.1016/0376-7388(95)00222-7.
[27] G. Schnitkey, "Fertilizer Prices Higher for 2019 Crop ," Sept. 25, 2018. https://farmdocdaily.illinois.edu/2018/09/fertilizer-prices-higher-for-2019-crop.html.
[28] G. Schnitkey, "Fertilizer Costs in 2017 and 2018," Jul. 11, 2017. https://farmdocdaily.illinois.edu/2017/07/fertilizer-costs-in-2017-and-2018.html.
[29] L. Wang *et al.*, "Greening Ammonia toward the Solar Ammonia Refinery," *Joule*, vol. 2, nº 6, p. 1055-1074, Jun. 2018, doi: 10.1016/j.joule.2018.04.017.
[30] A. Klerke, C. H. Christensen, J. K. Nørskov, et T. Vegge, "Ammonia for hydrogen storage: challenges and opportunities," *J. Mater. Chem.*, vol. 18, nº 20, p. 2304, 2008, doi: 10.1039/b720020j.
[31] S. Chiuta, R. C. Everson, H. W. J. P. Neomagus, P. van der Gryp, et D. G. Bessarabov, "Reactor technology options for distributed hydrogen generation via ammonia decomposition: A review," *Int. J. Hydrog. Energy*, vol. 38, nº 35, p. 14968-14991, Nov. 2013, doi: 10.1016/j.ijhydene.2013.09.067.
[32] S. Chiuta, R. C. Everson, H. W. J. P. Neomagus, L. A. Le Grange, et D. G. Bessarabov, "A modelling evaluation of an ammonia-fuelled microchannel reformer for hydrogen generation", *Int. J. Hydrog. Energy*, vol. 39, nº 22, p. 11390-11402, Jul. 2014, doi: 10.1016/j.ijhydene.2014.05.146.
[33] "ISO 14687-2:2012: Hydrogen fuel -- Product specification -- Part 2: Proton exchange membrane (PEM) fuel cell applications for road vehicles". 2012, [En ligne]. Disponible sur: https://www.iso.org/standard/55083.html.
[34] "ISO 14687-3:2014: Hydrogen fuel -- Product specification -- Part 3: Proton exchange membrane (PEM) fuel cell applications for stationary appliances". 2014, [En ligne]. Disponible sur: https://www.iso.org/standard/55078.html.

Chapter 4: Polymer Electrolyte Membrane Cells Electrochemical Impedance Spectroscopy Modeling

4. Polymer Electrolyte Membrane Cells Electrochemical Impedance Spectroscopy Modeling

Electrochemical Impedance Spectroscopy (EIS) is a common experimental method to characterize the electrochemical reactions. Currently, not many EIS numerical and mathematical models exist specifically for EHC. The mathematical model not only helps to characterize the phenomena but also helps to separate the physics and electrochemical processes in each part of the cell (anode, cathode, and membrane). The aim of this chapter is to define the basic of Electrochemical Impedance Spectroscopy and adapt this method to a Polymer Electrolyte Membrane Cell used in EHC.

4.1 State of art on Electrochemical Impedance Spectroscopy modeling and applications

4.1.1 The Principle of the Electrochemical Impedance Spectroscopy

EIS was founded by Heaviside in the late 19th century (1880-1900). He focused on the advancement of electric circuit theory by introducing the Laplace frequency "s" (s = d/dt & 1/s= $\int$ dt). He revolutionized the era by transforming complicated equations into simple solvable ones. He also introduced the words "impedance" which he defined as follow [1]:

$$Z(s) = \frac{\overline{V}(s)}{\overline{I}(s)} \tag{4.1}$$

Where, $\overline{I}(s)$ is the Laplace transforms of the current and $\overline{V}(s)$ is the one for the voltage.

This started the current methods of resolution by transforming a normal complicated equation into Laplace or Fourier spaces allowing a simpler equation solving and transforming the results back to the original temporal space. This granted the development of many fields such as the EIS.

EIS can be applied to any electrochemical system. However, the electrochemical systems are non-stationary and non-linear. Therefore, the measurements are done through a transfer function that is assumed quasi-stationary during the time of measurements (Figure 4-1). Under these assumptions, the system's behavior can be considered to be similar to a linear time-invariant system (LTI system) [2].

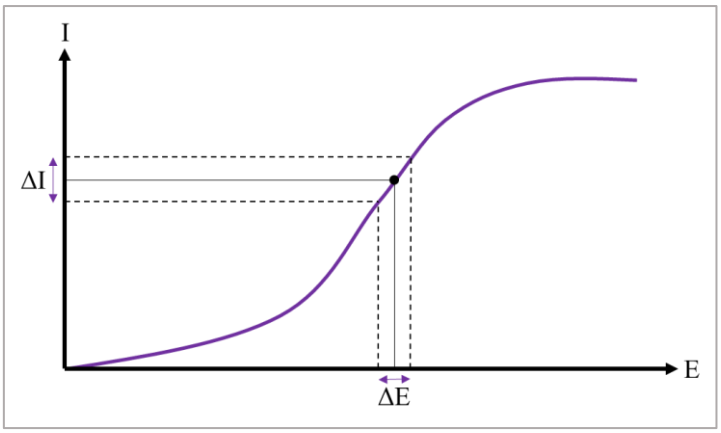

Figure 4-1: an example of a stationary operating point in a non-linear non-stationary system

The Electrochemical Impedance Spectroscopy is an extraordinarily strong characterization method which inclines both theoretical and experimental approaches by modeling the different physics and electrochemical processes into a very complex system. That is simplified and solved using Laplace and/or Fourier's transforms, analyzed using electrical analogs and, measured using a frequency response analyzer. Depending on the studies, some papers might change this order or remove a step completely. Most published studies rely on the electrical analogs or previous standard diagrams to interpret their results. However, the theoretical/numerical background calculation and simulation allow a more accurate analysis and validation. Thus, the intention behind this study is to model a closer theoretical understanding of the EIS of an EHC.

4.1.2 The Electrochemical Impedance Spectroscopy approach methodology

The current measured at the electrodes in an electrochemical system depends on the different phenomena in the electrode materials, the electrolyte, and the interfaces: Thermodynamics and electro kinetics of reactions, mass transfer, and flow dynamics.

The impedance framework is defined only within a linear system theory. This imposes four restrictions on the current work [3]:

- Linearity: the system must be represented by linear differential equations.
- Stability: the system must be stable and stationary.
- Causality: the response of the system must be integrally related to the applied signal.
- Finite impedance: the values of the real and imaginary parts of the impedance must be finite.

If these four conditions are not met the classical analytical EIS methods are impossible to apply. Therefore, the system cannot be represented by an equivalent electrical circuit and the equations cannot be solved by operational calculation or decomposed into a sum of independent contributions.

There are several methods of measuring an EIS, but the most common one is to apply a sinusoidal voltage (or current) with a pulse $\omega = 2\pi f$ where f is the frequency.

If a voltage is applied, it can be represented by the complex number:

$$\Delta E = \bar{E} e^{i\omega t} \tag{4.2}$$

This the response is:

$$\Delta I = \bar{I} e^{i\omega t} \tag{4.3}$$

The complex impedance is written as bellow:

$$Z = \frac{\Delta E}{\Delta I} = |Z| e^{i\emptyset t} \tag{4.4}$$

Where the argument ϕ is the phase shift created by the system which depend on the pulse and the modulus $|Z|$.

The EIS is obtained by sweeping over a range of frequencies. The reason is that each phenomenon might have a different relaxation time which implies a different frequency.

4.1.3 Resolution example:

The applied signal around the stationary state during the EIS defines the potential as $E = E + \Delta E$ and the current as $I = I + \Delta I$.

The total current at the electrode surface is formulated as bellow:

$$I = I_F + \Delta I_F + \Delta I_{Cdl} = I_F + \frac{\partial I_F}{\partial \eta}\Delta\eta + C_{dl}\frac{d}{dt}\Delta\eta \quad (4.5)$$

ΔI_{Cdl} is the charging current of the double capacitive layer, which only available the transitional regime, and $\frac{\partial I_F}{\partial \eta}\Delta\eta$ comes from first-order development of the faradic current using Taylor series. Helmholtz initially theorized the double layer (dl) which is the accumulation of positive and negative charges on both sides of the electrode/electrolyte interface due to the potential difference [4]. Any potential variation causes a variation in the charges accumulated on each side, without these being able to pass from one medium to the other. This induces a charging current ΔI_{Cdl} similar to the charge of a capacitance C_{dl} which cannot be observed using only a polarization curve. Gouy-Chapman-Stern (GCS) model is one of models representing the double layer and allowing to evaluate the value of the parameter C_{dl}. It is based on the long-distance electrostatic interactions between the electrode and the ions of the electrolyte but also by effects related to short-range interactions [4]. The capacitance can for example be altered by a specific ion adsorption on the electrode surface or by the surface condition of the electrodes.

The limiting condition is therefore the current variation:

$$\Delta I = \frac{\partial I_F}{\partial \eta}\Delta\eta + C_{dl}\frac{d}{dt}\Delta\eta \quad (4.6)$$

By integrating over the thickness of the electrode δ_{act}, the potential variation is therefore:

$$\Delta E = R_{ohm}\Delta I + \Delta\eta \quad (4.7)$$

Where $\Delta\eta = \Delta\varphi_{elec} - \Delta\varphi_{x=0}$.

Over potential variation can also be written in a complex form:

$$\Delta\eta = \tilde{\eta}e^{i\omega t} \quad (4.8)$$

Where the notation $\tilde{X}$referrers to the Laplace variable.

Thus

$$\tilde{I} = \frac{\partial I_F}{\partial \eta}\tilde{\eta} + i\omega C_{dl}\tilde{\eta} \quad (4.9)$$

$$\tilde{E} = R_{ohm}\tilde{I} + \tilde{\eta} \tag{4.10}$$

The impedance is written finally as follow:

$$Z(\omega) = \frac{\Delta E}{\Delta I} = \frac{R_{ohm}(\frac{\partial I_F}{\partial \eta}\tilde{\eta} + i\omega C_{dl}\tilde{\eta}) + \tilde{\eta}}{\frac{\partial I_F}{\partial \eta}\tilde{\eta} + i\omega C_{dl}\tilde{\eta}} = R_{ohm} + \frac{1}{\frac{1}{R_f} + i\omega C_{dl}} \tag{4.11}$$

Where the charge transfer resistance is $R_f = \frac{\partial I_F}{\partial \eta}$.

From this approach, two things are obvious. If the equations used are linearized, their resolution in Fourier space can greatly simplify the impedance calculation. And secondly, electrochemical impedance resembles in some cases the impedances of electrical circuits. Equation (4.11) corresponds for example to the transfer function of a resistance in series with an RC circuit.

Electrochemical impedances can therefore be represented by equivalent electrical diagrams in some cases to facilitate their interpretation [3].

4.1.4 Equivalent electrical circuit

In electricity, the behavior of a linear passive dipole can characterize in a sinusoidal regime with a complex number called complex impedance. It measures the opposition of an electrical circuit to the passage of a sinusoidal alternating current. Equivalent electric circuit can be very practical. The impedance presented in equation (4.11) can be represented by a resistance in series with a resistance/capacitance pair in parallel. The results are mainly presented in the form of a Bode diagram or, as in Figure 4-2,by a Nyquist diagram on which the negative of the imaginary part ($-Z''$) is plotted against the real part (Z') of the impedance [3].

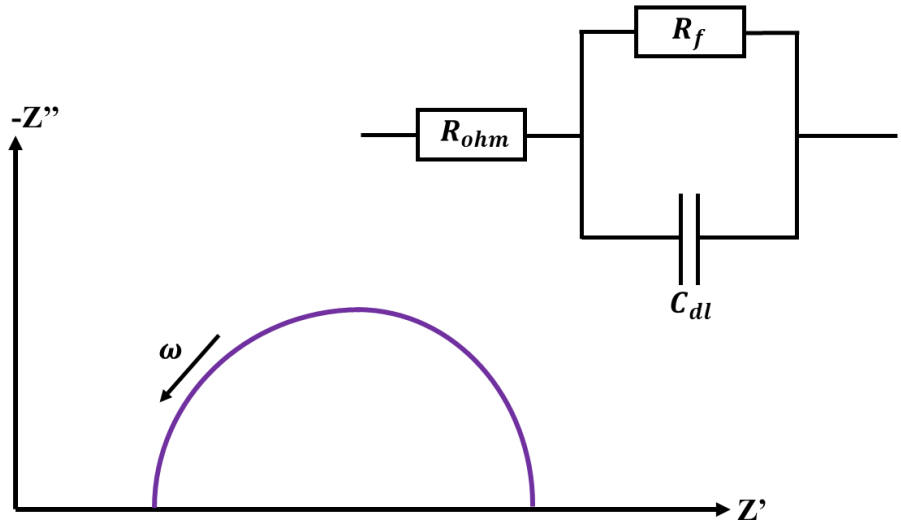

Figure 4-2: Schematic Nyquist diagram and the equivalent electrical circuit for (4.11)

It is then easy to assume that a two-electrode system could be represented by a linear combination of resistances and capacitances. However, it should be noted that using analog circuits must be distinguished from physical models. Indeed, a sufficient number of resistances, capacitances and inductances (RCL) allows to simulate any spectrum respecting the constraints of linear systems theory but might lead to physical analogy incoherence. D.D. Macdonald [1] stated that the representation of an electric circuit equivalent must be coupled with a reliable physics model and must be made of the smallest number of RCL elements possible.

4.2 Electrochemical Impedance Spectroscopy model: equations system & solving

The purpose of this work is to build an equivalent circuit to characterize the different phenomena in each part of the device (Figure 4-3).

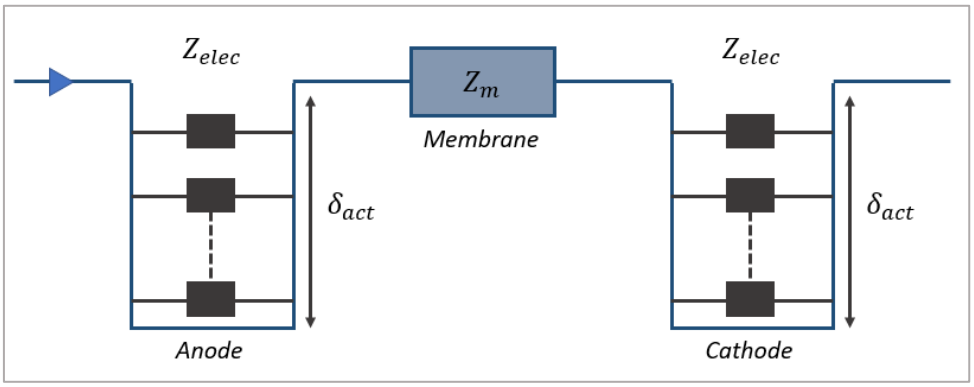

Figure 4-3: The equivalent circuit of the device

The definition of impedance is a generalization of Ohm's law:

$$\overline{U} = Z\overline{I} = \frac{\overline{I}}{Y} \tag{4.12}$$

Indeed, in a sinusoidal alternating signal, it is found that other elements, which are not resistances, also respond to this law. The admittance (Figure 4-5) is the reverse of the impedance (Figure 4-4) for an alternating current. For simplification reasons the following calculations will be done using the admittance instead of the impedance:

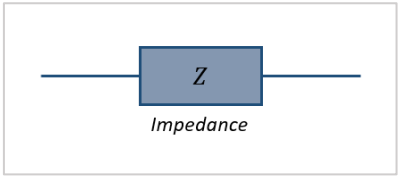

Figure 4-4: Electrical impedance

$$Z_T = \frac{1}{Y_T} \leftrightarrow Y_T = \sum Y_x \tag{4.13}$$

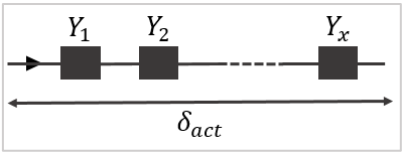

Figure 4-5: Electrical admittance

This method allows one to characterize an electrode behavior under various conditions of flow feeding and applied current density. The approach provides the impedance distribution in the active layer as function of the spatial variation x.

4.2.1 The equation system development at the active layer

The electrodes equation considered in this method is:

$$\frac{\partial\left(\sigma_{H^+,k}^{eff}\partial\eta_k\right)}{\partial x^2} - \frac{\gamma}{\delta_{act}} i_{k,f} = \frac{\gamma}{\delta_{act}} C_{dl}\frac{\partial\eta_k}{\partial t} \tag{4.14}$$

Laplace transform will be applied to the second equation of the system, introducing p = jω where ω is the angular frequency of the time-dependent perturbed variables with an overbar. The Laplace form $\overline{\eta_k}$ will be assigned to η_k. Due to notation problems, since "i" refers to the current density in this work, the "j" will be used instead to describe the methodical "i" that defines a complex number. The x will be the spatial variation along the electrode thickness δ_{act}. The GDL/electrode interface is at x=0 and the electrode/membrane interface is at $x=\delta_{act}$.

The Laplace transform equation will be written as follow:

$$\frac{\partial\left(\sigma_{H^+,k}^{eff}\partial\overline{\eta_k}\right)}{\partial x^2} - \frac{\gamma}{\delta_{act}}\overline{i_{k,f}} = \frac{\gamma}{\delta_{act}} C_{dl}\overline{\eta_k}p \tag{4.15}$$

The charge transfer resistance is defined as: $\frac{1}{R_{k,f}} = \frac{\overline{i_{k,f}}}{\overline{\eta_k}}$ and p = jω thus:

$$\frac{\partial^2\overline{\eta_k}}{\partial x^2} - \frac{\gamma}{\sigma_{H^+,k}^{eff}\delta_{act}}\left(\frac{1}{R_{k,f}} + C_{dl}p\right)\overline{\eta_k} = 0 \tag{4.16}$$

Where $\overline{\eta_k} = z = a(x) + jb(x)$

4.2.2 Analytical solution of the equation

This equation can be written as follow:

$$\frac{\partial^2 z}{\partial x^2} - \frac{\gamma}{\sigma_{H^+,k}^{eff}\delta_{act}R_{k,f}} z - j\omega C_{dl} z = 0 \tag{4.17}$$

Thus:

$$\left(\frac{\partial^2 a(x)}{\partial x^2} - \frac{\gamma}{\sigma_{H^+,k}^{eff}\delta_{act}R_{k,f}} a(x) + \omega C_{dl} b(x)\right) + j\left(\frac{\partial^2 b(x)}{\partial x^2} - \frac{\gamma}{\sigma_{H^+,k}^{eff}\delta_{act}R_{k,f}} b(x) - \omega C_{dl} a(x)\right) = 0 \tag{4.18}$$

A complex number is equal to zero if and only if his imaginary and real parts are equal to zero. Therefore, the differential equation system obtained is:

$$\begin{cases} \dfrac{\partial^2 a(x)}{\partial x^2} - \dfrac{\gamma}{\sigma_{H^+,k}^{eff}\delta_{act}R_{k,f}} a(x) + \omega C_{dl} b(x) = 0 \\ \dfrac{\partial^2 b(x)}{\partial x^2} - \dfrac{\gamma}{\sigma_{H^+,k}^{eff}\delta_{act}R_{k,f}} b(x) - \omega C_{dl} a(x) = 0 \end{cases} \tag{4.19}$$

$a(x)$ & $b(x)$ needed to be determined to have a full expression of the over potential $\overline{\eta_k}$. To do so, the system needs to be rewritten to have each equation depending only on one of the variables.

$$\begin{cases} b(x) = -\dfrac{1}{\omega C_{dl}} \dfrac{\partial^2 a(x)}{\partial x^2} + \dfrac{\gamma}{\omega C_{dl}\sigma_{H^+,k}^{eff}\delta_{act}R_{k,f}} a(x) \\ a(x) = \dfrac{1}{\omega C_{dl}} \dfrac{\partial^2 b(x)}{\partial x^2} - \dfrac{\gamma}{\omega C_{dl}\sigma_{H^+,k}^{eff}\delta_{act}R_{k,f}} b(x) \end{cases} \tag{4.20}$$

The (4.19) expression will be then replaced in the equation system (4.18):

$$\begin{cases} \dfrac{\partial^2\left(\frac{1}{\omega C_{dl}}\frac{\partial^2 b(x)}{\partial x^2} - \frac{\gamma}{\omega C_{dl}\sigma_{H^+,k}^{eff}\delta_{act}R_{k,f}} b(x)\right)}{\partial x^2} - \dfrac{\gamma}{\sigma_{H^+,k}^{eff}\delta_{act}R_{k,f}}\left(\dfrac{1}{\omega C_{dl}}\dfrac{\partial^2 b(x)}{\partial x^2} - \dfrac{\gamma}{\omega C_{dl}\sigma_{H^+,k}^{eff}\delta_{act}R_{k,f}} b(x)\right) + \omega C_{dl} b(x) = 0 \\ \dfrac{\partial^2\left(-\frac{1}{\omega C_{dl}}\frac{\partial^2 a(x)}{\partial x^2} + \frac{\gamma}{\omega C_{dl}\sigma_{H^+,k}^{eff}\delta_{act}R_{k,f}} a(x)\right)}{\partial x^2} - \dfrac{\gamma}{\sigma_{H^+,k}^{eff}\delta_{act}R_{k,f}}\left(-\dfrac{1}{\omega C_{dl}}\dfrac{\partial^2 a(x)}{\partial x^2} + \dfrac{\gamma}{\omega C_{dl}\sigma_{H^+,k}^{eff}\delta_{act}R_{k,f}} a(x)\right) - \omega C_{dl} a(x) = 0 \end{cases}$$

Thus:

$$\begin{cases} \frac{1}{\omega C_{dl}}\frac{\partial^4 b(x)}{\partial x^4} - \frac{\gamma}{\omega C_{dl}\sigma^{eff}_{H^+,k}\delta_{act}R_{k,f}}\frac{\partial^2 b(x)}{\partial x^2} - \frac{\gamma}{\omega C_{dl}\sigma^{eff}_{H^+,k}\delta_{act}R_{k,f}}\frac{\partial^2 b(x)}{\partial x^2} + \frac{\gamma^2}{\omega C_{dl}\left(\sigma^{eff}_{H^+,k}\delta_{act}R_{k,f}\right)^2}b(x) + \omega C_{dl}b(x) = 0 \\ -\frac{1}{\omega C_{dl}}\frac{\partial^4 a(x)}{\partial x^4} + \frac{\gamma}{\omega C_{dl}\sigma^{eff}_{H^+,k}\delta_{act}R_{k,f}}\frac{\partial^2 a(x)}{\partial x^2} + \frac{\gamma}{\omega C_{dl}\sigma^{eff}_{H^+,k}\delta_{act}R_{k,f}}\frac{\partial^2 a(x)}{\partial x^2} - \frac{\gamma^2}{\omega C_{dl}\left(\sigma^{eff}_{H^+,k}\delta_{act}R_{k,f}\right)^2}a(x) - \omega C_{dl}a(x) = 0 \end{cases}$$

Therefore, the new system of equation is:

$$\begin{cases} \frac{\partial^4 b(x)}{\partial x^4} - \frac{2\gamma}{\omega C_{dl}\sigma^{eff}_{H^+,k}\delta_{act}R_{k,f}}\frac{\partial^2 b(x)}{\partial x^2} + \left((\omega C_{dl})^2 + \frac{\gamma^2}{\left(\sigma^{eff}_{H^+,k}\delta_{act}R_{k,f}\right)^2}\right)b(x) = 0 \\ \frac{\partial^4 a(x)}{\partial x^4} + \frac{2\gamma}{\omega C_{dl}\sigma^{eff}_{H^+,k}\delta_{act}R_{k,f}}\frac{\partial^2 a(x)}{\partial x^2} - \left((\omega C_{dl})^2 + \frac{\gamma^2}{\left(\sigma^{eff}_{H^+,k}\delta_{act}R_{k,f}\right)^2}\right)a(x) = 0 \end{cases} \quad (4.21)$$

Thus:

$$\begin{cases} \frac{\partial^4 y_1}{\partial x^4} - K'\frac{\partial^2 y_1}{\partial x^2} + Ky_1 = 0 \\ \frac{\partial^4 y_2}{\partial x^4} + K'\frac{\partial^2 y_2}{\partial x^2} - Ky_2 = 0 \end{cases} \quad (4.22)$$

Where $K = (\omega C_{dl})^2 + \frac{\gamma^2}{\left(\sigma^{eff}_{H^+,k}\delta_{act}R_{k,f}\right)^2}$ and $K' = \frac{2\gamma}{\omega C_{dl}\sigma^{eff}_{H^+,k}\delta_{act}R_{k,f}}$

The characteristic equation system to solve is:

$$\begin{cases} r^4 - K'r^2 + K = 0 \\ m^4 + K'm^2 - K = 0 \end{cases} \quad (4.23)$$

Where $r = y_1 = b(x)$, $m = y_2 = a(x)$

$$K = (\omega C_{dl})^2 + \frac{\gamma^2}{\left(\sigma^{eff}_{H^+,k}\delta_{act}R_{k,f}\right)^2} \; and \; K' = \frac{2\gamma}{\omega C_{dl}\sigma^{eff}_{H^+,k}\delta_{act}R_{k,f}}$$

If the system (4.22) is a biquadratic equation system that can be simplified using change of variable as $X=r^2$ and $Y = m^2$, it will be a conventional second order equations:

$$\begin{cases} a:\ X^2 - K'X + K = 0 \\ b:\ Y^2 + K'Y - K = 0 \end{cases} \quad (4.24)$$

First step would be to calculate the discriminant to find the expression of the roots of the two equations:

$$\begin{cases} a:\ \Delta_a = K'^2 - 4K \\ b:\ \Delta_b = K'^2 + 4K \end{cases} \quad (4.25)$$

In the case of the second equation (b) of Y the discriminant Δ is always positive given that K is always positive. Therefore, Y is a real number that can be written as follows:

$$Y_{1,2} = \frac{-K' \pm \sqrt{\Delta_b}}{2} = \frac{-K' \pm \sqrt{K'^2 + 4K}}{2} \tag{4.26}$$

Y is equal to m², thus the roots need to solve the initial system are the roots of m:

$$\begin{cases} Y_1 = \dfrac{-K' + \sqrt{\Delta_b}}{2} \rightarrow \begin{cases} if\ (K' > \sqrt{\Delta_b}) \rightarrow m_{1,2} = \pm j\sqrt{\dfrac{-K' + \sqrt{\Delta_b}}{2}} & (4.27) \\ if\ (K' < \sqrt{\Delta_b}) \rightarrow m_{1,2} = \pm\sqrt{\dfrac{-K' + \sqrt{\Delta_b}}{2}} & (4.28) \end{cases} \\ Y_2 = \dfrac{-K' - \sqrt{\Delta_b}}{2} \rightarrow m_{3,4} = \pm j\sqrt{\dfrac{K' + \sqrt{\Delta_b}}{2}} & (4.29) \end{cases}$$

For (4.26) : $K' > \sqrt{\Delta_b} \rightarrow K' > \sqrt{K'^2 + 4K} \rightarrow K'^2 > K'^2 + 4K \rightarrow 0 > 4K\ but\ K > 0$ thus this case is not possible. Therefore, the possible roots of $b(x)$ are:

$$m_{1,2} = \pm\sqrt{\frac{-K' + \sqrt{\Delta_b}}{2}} \quad \& \quad m_{3,4} = \pm j\sqrt{\frac{K' + \sqrt{\Delta_b}}{2}} \tag{4.30}$$

Thus, the solution of the equation (4.30) for b(x) will be written as follow:

$$\mathrm{b}(x) = C_6 e^{x\sqrt{\frac{-K' + \sqrt{\Delta_b}}{2}}} + C_7 e^{-x\sqrt{\frac{-K' + \sqrt{\Delta_b}}{2}}} + C_8 \sin\left(x\sqrt{\frac{K' + \sqrt{\Delta_b}}{2}}\right) + C_9 \cos\left(x\sqrt{\frac{K' + \sqrt{\Delta_b}}{2}}\right) \tag{4.31}$$

For the equation a(x) of the system (4.23) the discriminant is $\Delta_a = K'^2 - 4K$ there is two possible cases:

If $K'^2 > 4K$:

X is a real number and can be written as follows:

$$X_{1,2} = \frac{K' \pm \sqrt{\Delta_a}}{2} = \frac{K' \pm \sqrt{K'^2 - 4K}}{2} \tag{4.32}$$

X is equal to r², thus the roots need to solve the initial system are the roots of r:

$$\begin{cases} X_1 = \dfrac{K' + \sqrt{\Delta_a}}{2} \rightarrow r_{1,2} = \pm\sqrt{\dfrac{K' + \sqrt{\Delta_a}}{2}} & (4.33) \\ X_2 = \dfrac{K' - \sqrt{\Delta_a}}{2} \rightarrow \begin{cases} if\ (K' < \sqrt{\Delta_a}) \rightarrow r_{3,4} = \pm j\sqrt{\dfrac{K' - \sqrt{\Delta_a}}{2}} & (4.34) \\ if\ (K' > \sqrt{\Delta_a}) \rightarrow r_{3,4} = \pm\sqrt{\dfrac{K' - \sqrt{\Delta_a}}{2}} & (4.35) \end{cases} \end{cases}$$

For (4.32) : $K' < \sqrt{\Delta_a} \rightarrow K' < \sqrt{K'^2 - 4K} \rightarrow K'^2 < K'^2 - 4K \rightarrow 0 < -4K \; but \; K > 0$ thus this case is not possible. Therefore, the possible roots of $a(x)$ are:

$$r_{1,2} = \pm\sqrt{\frac{K' + \sqrt{\Delta_a}}{2}} \;\; \& \;\; r_{3,4} = \pm\sqrt{\frac{K' - \sqrt{\Delta_a}}{2}} \tag{4.36}$$

Thus, the solution of the equation (4.20) for a(x) will be written as follow:

$$a(x) = C_1 e^{x\sqrt{\frac{K'+\sqrt{\Delta_a}}{2}}} + C_2 e^{-x\sqrt{\frac{K'+\sqrt{\Delta_a}}{2}}} + C_3 e^{x\sqrt{\frac{K'-\sqrt{\Delta_a}}{2}}} + C_4 e^{-x\sqrt{\frac{K'-\sqrt{\Delta_a}}{2}}} \tag{4.37}$$

If $K'^2 < 4K$:

X is a complex number and can be written as follows:

$$X_{1,2} = r^2 = \frac{K' \pm j\sqrt{|\Delta_a|}}{2} = \frac{K' \pm j\sqrt{|K'^2 - 4K|}}{2} \tag{4.38}$$

X = r², thus the roots need to solve the initial system are the roots of r. Given the fact that X is a complex the method used to find the roots will not be the same:

$$X_{1,2} = r^2 = \frac{K' \pm j\sqrt{|\Delta_a|}}{2} \;\; \& \;\; r = \alpha + j\beta \;\; \rightarrow \begin{cases} \alpha^2 - \beta^2 = \dfrac{K'}{2} \\ 2\alpha\beta = \pm\dfrac{\sqrt{|\Delta_a|}}{2} \\ \alpha^2 + \beta^2 = \sqrt{\dfrac{K'^2 + |\Delta_a|}{4}} \end{cases} \tag{4.39}$$

$$\rightarrow \begin{cases} \alpha^2 = \dfrac{K'}{2} + \sqrt{\dfrac{K'^2 + |\Delta_a|}{4}} \\ 2\alpha\beta = \pm\dfrac{\sqrt{|\Delta_a|}}{2} \end{cases} \tag{4.40}$$

$$\rightarrow \begin{cases} \alpha = \pm\sqrt{\dfrac{K'}{2} + \sqrt{\dfrac{K'^2 + |\Delta_a|}{4}}} \\ 2\alpha\beta = \pm\dfrac{\sqrt{|\Delta_a|}}{2} \end{cases} \tag{4.41}$$

For $X_1 = \frac{K'+j\sqrt{|\Delta_a|}}{2} \;\; \& \;\; r_{1,2} = \alpha_{1,2} + j\beta_{1,2}$ and for $X_2 = \frac{K'+j\sqrt{|\Delta_a|}}{2} \;\; \& \;\; r_{3,4} = \alpha_{3,4} + j\beta_{3,4}$

$$r_{1,2} = \alpha_{1,2} + j\beta_{1,2} \rightarrow \begin{cases} \alpha_1 = \sqrt{\frac{K'}{2} + \sqrt{\frac{K'^2 + |\Delta_a|}{4}}} \rightarrow \beta_1 = \frac{\sqrt{|\Delta_a|}}{4\sqrt{\frac{K'}{2} + \sqrt{\frac{K'^2 + |\Delta_a|}{4}}}} \\ \alpha_2 = -\sqrt{\frac{K'}{2} + \sqrt{\frac{K'^2 + |\Delta_a|}{4}}} \rightarrow \beta_2 = -\frac{\sqrt{|\Delta_a|}}{4\sqrt{\frac{K'}{2} + \sqrt{\frac{K'^2 + |\Delta_a|}{4}}}} \end{cases} \quad (4.42)$$

$$r_{3,4} = \alpha_{3,4} + j\beta_{3,4} \rightarrow \begin{cases} \alpha_3 = \sqrt{\frac{K'}{2} + \sqrt{\frac{K'^2 + |\Delta_a|}{4}}} \rightarrow \beta_3 = -\frac{\sqrt{|\Delta_a|}}{4\sqrt{\frac{K'}{2} + \sqrt{\frac{K'^2 + |\Delta_a|}{4}}}} \\ \alpha_4 = -\sqrt{\frac{K'}{2} + \sqrt{\frac{K'^2 + |\Delta_a|}{4}}} \rightarrow \beta_4 = \frac{\sqrt{|\Delta_a|}}{4\sqrt{\frac{K'}{2} + \sqrt{\frac{K'^2 + |\Delta_a|}{4}}}} \end{cases} \quad (4.43)$$

Thus, the solution of the equation (4.20) for a(x) will be written as follow:

$$a(x) = e^{x\sqrt{\frac{K'}{2}+\sqrt{\frac{K'^2+|\Delta_a|}{4}}}}\left(C_1 \sin\left(x\sqrt{\frac{K' + \sqrt{\Delta_b}}{2}}\right) + C_2 \cos\left(x\sqrt{\frac{K' + \sqrt{\Delta_b}}{2}}\right)\right) + e^{-x\sqrt{\frac{K'}{2}+\sqrt{\frac{K'^2+|\Delta_a|}{4}}}}\left(C_3 \sin\left(x\sqrt{\frac{K' + \sqrt{\Delta_b}}{2}}\right) + C_4 \cos\left(x\sqrt{\frac{K' + \sqrt{\Delta_b}}{2}}\right)\right) \quad (4.44)$$

To summarize $\overline{\eta_k} = z = a(x) + jb(x)$ is the analytical solution for the initial equation. The b(x) depends on K' and a(x) depends on the value of the discriminant (Δ_a). Therefore, the expression of z is a combination of the previous solutions.

If $K'^2 > 4K$:

$$\overline{\eta_k} = \left(C_1 e^{x\sqrt{\frac{K'+\sqrt{\Delta_a}}{2}}} + C_2 e^{-x\sqrt{\frac{K'+\sqrt{\Delta_a}}{2}}} + C_3 e^{x\sqrt{\frac{K'-\sqrt{\Delta_a}}{2}}} + C_4 e^{-x\sqrt{\frac{K'-\sqrt{\Delta_a}}{2}}}\right) + j\left(C_5 e^{x\sqrt{\frac{-K'+\sqrt{\Delta_b}}{2}}} + C_6 e^{-x\sqrt{\frac{-K'+\sqrt{\Delta_b}}{2}}} + C_7 \sin\left(x\sqrt{\frac{K' + \sqrt{\Delta_b}}{2}}\right) + C_8 \cos\left(x\sqrt{\frac{K' + \sqrt{\Delta_b}}{2}}\right)\right) \quad (4.45)$$

If $K'^2 < 4K$:

$$\overline{\eta_k} = \left(e^{x\sqrt{\frac{K'}{2}+\sqrt{\frac{K'^2+|\Delta_a|}{4}}}} \left(C_1 \sin\left(x\sqrt{\frac{K'+\sqrt{\Delta_b}}{2}} \right) + C_2 \cos\left(x\sqrt{\frac{K'+\sqrt{\Delta_b}}{2}} \right) \right) \right.$$
$$+ e^{-x\sqrt{\frac{K'}{2}+\sqrt{\frac{K'^2+|\Delta_a|}{4}}}} \left(C_3 \sin\left(x\sqrt{\frac{K'+\sqrt{\Delta_b}}{2}} \right) + C_4 \cos\left(x\sqrt{\frac{K'+\sqrt{\Delta_b}}{2}} \right) \right) \Bigg) \quad (4.46)$$
$$+ j\left(C_5 e^{x\sqrt{\frac{-K'+\sqrt{\Delta_b}}{2}}} + C_6 e^{-x\sqrt{\frac{-K'+\sqrt{\Delta_b}}{2}}} + C_7 \sin\left(x\sqrt{\frac{K'+\sqrt{\Delta_b}}{2}} \right) + C_8 \cos\left(x\sqrt{\frac{K'+\sqrt{\Delta_b}}{2}} \right) \right)$$

$\frac{\partial \overline{\eta_k}}{\partial x}$ the derivative of $\overline{\eta_k}$ is:

If $K'^2 > 4K$:

$$\frac{\partial \overline{\eta_k}}{\partial x} = \left(C_1\sqrt{\frac{K'+\sqrt{\Delta_a}}{2}} e^{x\sqrt{\frac{K'+\sqrt{\Delta_a}}{2}}} - C_2\sqrt{\frac{K'+\sqrt{\Delta_a}}{2}} e^{-x\sqrt{\frac{K'+\sqrt{\Delta_a}}{2}}} + C_3\sqrt{\frac{K'-\sqrt{\Delta_a}}{2}} e^{x\sqrt{\frac{K'-\sqrt{\Delta_a}}{2}}} \right.$$
$$\left. - C_4\sqrt{\frac{K'-\sqrt{\Delta_a}}{2}} e^{-x\sqrt{\frac{K'-\sqrt{\Delta_a}}{2}}} \right)$$
$$+ j\left(C_5\sqrt{\frac{-K'+\sqrt{\Delta_b}}{2}} e^{x\sqrt{\frac{-K'+\sqrt{\Delta_b}}{2}}} - C_6\sqrt{\frac{-K'+\sqrt{\Delta_b}}{2}} e^{-x\sqrt{\frac{-K'+\sqrt{\Delta_b}}{2}}} \right. \quad (4.47)$$
$$\left. + C_7\sqrt{\frac{K'+\sqrt{\Delta_b}}{2}} \cos\left(x\sqrt{\frac{K'+\sqrt{\Delta_b}}{2}} \right) - C_8\sqrt{\frac{K'+\sqrt{\Delta_b}}{2}} \sin\left(x\sqrt{\frac{K'+\sqrt{\Delta_b}}{2}} \right) \right)$$

If $K'^2 < 4K$:

$$\begin{aligned}\frac{\partial\overline{\eta_k}}{\partial x} = C_1&\left(\sqrt{\frac{K'}{2}+\sqrt{\frac{K'^2+|\Delta_a|}{4}}}\,e^{x\sqrt{\frac{K'}{2}+\sqrt{\frac{K'^2+|\Delta_a|}{4}}}}\sin\left(x\sqrt{\frac{K'+\sqrt{\Delta_b}}{2}}\right)+\sqrt{\frac{K'+\sqrt{\Delta_b}}{2}}\,e^{x\sqrt{\frac{K'}{2}+\sqrt{\frac{K'^2+|\Delta_a|}{4}}}}\cos\left(x\sqrt{\frac{K'+\sqrt{\Delta_b}}{2}}\right)\right)\\&+C_2\left(\sqrt{\frac{K'}{2}+\sqrt{\frac{K'^2+|\Delta_a|}{4}}}\,e^{x\sqrt{\frac{K'}{2}+\sqrt{\frac{K'^2+|\Delta_a|}{4}}}}\cos\left(x\sqrt{\frac{K'+\sqrt{\Delta_b}}{2}}\right)-\sqrt{\frac{K'+\sqrt{\Delta_b}}{2}}\,e^{x\sqrt{\frac{K'}{2}+\sqrt{\frac{K'^2+|\Delta_a|}{4}}}}\sin\left(x\sqrt{\frac{K'+\sqrt{\Delta_b}}{2}}\right)\right)\\&+C_3\left(-\sqrt{\frac{K'}{2}+\sqrt{\frac{K'^2+|\Delta_a|}{4}}}\,e^{-x\sqrt{\frac{K'}{2}+\sqrt{\frac{K'^2+|\Delta_a|}{4}}}}\sin\left(x\sqrt{\frac{K'+\sqrt{\Delta_b}}{2}}\right)+\sqrt{\frac{K'+\sqrt{\Delta_b}}{2}}\,e^{-x\sqrt{\frac{K'}{2}+\sqrt{\frac{K'^2+|\Delta_a|}{4}}}}\cos\left(x\sqrt{\frac{K'+\sqrt{\Delta_b}}{2}}\right)\right)\\&+C_4\left(-\sqrt{\frac{K'}{2}+\sqrt{\frac{K'^2+|\Delta_a|}{4}}}\,e^{-x\sqrt{\frac{K'}{2}+\sqrt{\frac{K'^2+|\Delta_a|}{4}}}}\cos\left(x\sqrt{\frac{K'+\sqrt{\Delta_b}}{2}}\right)-\sqrt{\frac{K'+\sqrt{\Delta_b}}{2}}\,e^{-x\sqrt{\frac{K'}{2}+\sqrt{\frac{K'^2+|\Delta_a|}{4}}}}\sin\left(x\sqrt{\frac{K'+\sqrt{\Delta_b}}{2}}\right)\right)\\&+j\left(C_5\sqrt{\frac{-K'+\sqrt{\Delta_b}}{2}}\,e^{x\sqrt{\frac{-K'+\sqrt{\Delta_b}}{2}}}-C_6\sqrt{\frac{-K'+\sqrt{\Delta_b}}{2}}\,e^{-x\sqrt{\frac{-K'+\sqrt{\Delta_b}}{2}}}+C_7\sqrt{\frac{K'+\sqrt{\Delta_b}}{2}}\cos\left(x\sqrt{\frac{K'+\sqrt{\Delta_b}}{2}}\right)\right.\\&\left.-C_8\sqrt{\frac{K'+\sqrt{\Delta_b}}{2}}\sin\left(x\sqrt{\frac{K'+\sqrt{\Delta_b}}{2}}\right)\right)\end{aligned} \tag{4.48}$$

In order to modelize $\frac{\frac{\partial\overline{\eta_k}}{\partial x}}{\overline{\eta_k}}$, the integration constantes needs to be either determined or eliminated in order to simplify the mathematical expression using boundary conditions and the physics of the problem.

The first simplification is that when x approaches infinity, tends toward a constant and can never be infinite.

Therefore, the new expression of $\overline{\eta_k}$ is:

If $K'^2 > 4K$:

$$\overline{\eta_k} = \left(C_2 e^{-x\sqrt{\frac{K'+\sqrt{\Delta_a}}{2}}} + C_4 e^{-x\sqrt{\frac{K'-\sqrt{\Delta_a}}{2}}}\right) + jC_6 e^{-x\sqrt{\frac{-K'+\sqrt{\Delta_b}}{2}}} \tag{4.49}$$

If $K'^2 < 4K$:

$$\overline{\eta_k} = \left(e^{-x\sqrt{\frac{K'}{2}+\sqrt{\frac{K'^2+|\Delta_a|}{4}}}}\left(C_3\sin\left(x\sqrt{\frac{K'+\sqrt{\Delta_b}}{2}}\right)+C_4\cos\left(x\sqrt{\frac{K'+\sqrt{\Delta_b}}{2}}\right)\right)\right) + jC_6 e^{-x\sqrt{\frac{-K'+\sqrt{\Delta_b}}{2}}} \tag{4.50}$$

And the new expression of $\frac{\partial\overline{\eta_k}}{\partial x}$ is:

If $K'^2 > 4K$:

$$\frac{\partial\overline{\eta_k}}{\partial x} = \left(-C_2\sqrt{\frac{K'+\sqrt{\Delta_a}}{2}}e^{-x\sqrt{\frac{K'+\sqrt{\Delta_a}}{2}}} - C_4\sqrt{\frac{K'-\sqrt{\Delta_a}}{2}}e^{-x\sqrt{\frac{K'-\sqrt{\Delta_a}}{2}}}\right) - jC_6\sqrt{\frac{-K'+\sqrt{\Delta_b}}{2}}e^{-x\sqrt{\frac{-K'+\sqrt{\Delta_b}}{2}}} \tag{4.51}$$

If $K'^2 < 4K$:

$$\begin{aligned}\frac{\partial\overline{\eta_k}}{\partial x} = C_3\Bigg(&-\sqrt{\frac{K'}{2}+\sqrt{\frac{K'^2+|\Delta_a|}{4}}}e^{-x\sqrt{\frac{K'}{2}+\sqrt{\frac{K'^2+|\Delta_a|}{4}}}}\sin\left(x\sqrt{\frac{K'+\sqrt{\Delta_b}}{2}}\right)\\ &+\sqrt{\frac{K'+\sqrt{\Delta_b}}{2}}e^{-x\sqrt{\frac{K'}{2}+\sqrt{\frac{K'^2+|\Delta_a|}{4}}}}\cos\left(x\sqrt{\frac{K'+\sqrt{\Delta_b}}{2}}\right)\Bigg)\\ &+C_4\Bigg(-\sqrt{\frac{K'}{2}+\sqrt{\frac{K'^2+|\Delta_a|}{4}}}e^{-x\sqrt{\frac{K'}{2}+\sqrt{\frac{K'^2+|\Delta_a|}{4}}}}\cos\left(x\sqrt{\frac{K'+\sqrt{\Delta_b}}{2}}\right)\\ &-\sqrt{\frac{K'+\sqrt{\Delta_b}}{2}}e^{-x\sqrt{\frac{K'}{2}+\sqrt{\frac{K'^2+|\Delta_a|}{4}}}}\sin\left(x\sqrt{\frac{K'+\sqrt{\Delta_b}}{2}}\right)\Bigg) - jC_6\sqrt{\frac{-K'+\sqrt{\Delta_b}}{2}}e^{-x\sqrt{\frac{-K'+\sqrt{\Delta_b}}{2}}}\end{aligned} \tag{4.52}$$

The boundary conditions (4.53) in this case will be used to simplify the set of equations by eliminating a few integration constants.

$$\begin{cases}\left.\frac{\partial\overline{\eta_k}}{\partial x}\right|_{x=L} = 0\\ \left.\overline{\eta_k}\right|_{x=0} = \Delta E e^{i\omega} = \Delta E\cos\omega + j\Delta E\sin\omega\end{cases} \tag{4.53}$$

Thus:

$$\left.\frac{\partial\overline{\eta_k}}{\partial x}\right|_{x=L} = 0 \rightarrow \begin{cases}\boldsymbol{K'^2 > 4K}: \begin{cases}\boldsymbol{Re}\left(\left.\frac{\partial\overline{\eta_k}}{\partial x}\right|_{x=L}\right) = 0\\ \boldsymbol{Im}\left(\left.\frac{\partial\overline{\eta_k}}{\partial x}\right|_{x=L}\right) = 0\end{cases}\\ \boldsymbol{K'^2 < 4K}: \begin{cases}\boldsymbol{Re}\left(\left.\frac{\partial\overline{\eta_k}}{\partial x}\right|_{x=L}\right) = 0\\ \boldsymbol{Im}\left(\left.\frac{\partial\overline{\eta_k}}{\partial x}\right|_{x=L}\right) = 0\end{cases}\end{cases} \tag{4.54}$$

This hypothesis is only valid for the real part of $\left.\frac{\partial \overline{\eta_k}}{\partial x}\right/_{x=L}$ due to the mathematical ambiguity of the expression of the imaginary part. Therefore:

$$\boldsymbol{K'^2 > 4K}: C_2\sqrt{\frac{K'+\sqrt{\Delta_a}}{2}}e^{-L\sqrt{\frac{K'+\sqrt{\Delta_a}}{2}}}+C_4\sqrt{\frac{K'-\sqrt{\Delta_a}}{2}}e^{-L\sqrt{\frac{K'-\sqrt{\Delta_a}}{2}}}=0 \tag{4.55}$$

$$\begin{aligned}\boldsymbol{K'^2 < 4K}: C_3&\left(-\sqrt{\frac{K'}{2}+\sqrt{\frac{K'^2+|\Delta_a|}{4}}}e^{-L\sqrt{\frac{K'}{2}+\sqrt{\frac{K'^2+|\Delta_a|}{4}}}}\sin\left(L\sqrt{\frac{K'+\sqrt{\Delta_b}}{2}}\right)\right.\\&\left.+\sqrt{\frac{K'+\sqrt{\Delta_b}}{2}}e^{-L\sqrt{\frac{K'}{2}+\sqrt{\frac{K'^2+|\Delta_a|}{4}}}}\cos\left(L\sqrt{\frac{K'+\sqrt{\Delta_b}}{2}}\right)\right)\\&+C_4\left(-\sqrt{\frac{K'}{2}+\sqrt{\frac{K'^2+|\Delta_a|}{4}}}e^{-L\sqrt{\frac{K'}{2}+\sqrt{\frac{K'^2+|\Delta_a|}{4}}}}\cos\left(L\sqrt{\frac{K'+\sqrt{\Delta_b}}{2}}\right)\right.\\&\left.-\sqrt{\frac{K'+\sqrt{\Delta_b}}{2}}e^{-L\sqrt{\frac{K'}{2}+\sqrt{\frac{K'^2+|\Delta_a|}{4}}}}\sin\left(L\sqrt{\frac{K'+\sqrt{\Delta_b}}{2}}\right)\right)=0\end{aligned} \tag{4.56}$$

For $\overline{\eta_k}$:

$$\left.\overline{\eta_k}\right/_{x=0}=\Delta E e^{j\omega}=\Delta E\cos\omega+j\Delta E\sin\omega\rightarrow\begin{cases}\boldsymbol{K'^2>4K}:\begin{cases}\boldsymbol{Re}\left(\left.\overline{\eta_k}\right/_{x=0}\right)=\Delta E\cos\omega\\\boldsymbol{Im}\left(\left.\overline{\eta_k}\right/_{x=0}\right)=\Delta E\sin\omega\end{cases}\\\boldsymbol{K'^2<4K}:\begin{cases}\boldsymbol{Re}\left(\left.\overline{\eta_k}\right/_{x=0}\right)=\Delta E\cos\omega\\\boldsymbol{Im}\left(\left.\overline{\eta_k}\right/_{x=0}\right)=\Delta E\sin\omega\end{cases}\end{cases} \tag{4.57}$$

Than:

$$\rightarrow\begin{cases}\boldsymbol{K'^2>4K}:\begin{cases}C_2+C_4=\Delta E\cos\omega\\C_6=\Delta E\sin\omega\end{cases}\\\boldsymbol{K'^2<4K}:\begin{cases}C_4=\Delta E\cos\omega\\C_6=\Delta E\sin\omega\end{cases}\end{cases} \tag{4.58}$$

Using the previous solving simplifications and boundary conditions, the integration constants can be written as follow:

$$\begin{cases} \boldsymbol{K'^2 > 4K}: \begin{cases} C_2 + C_4 = \Delta E \cos\omega \ \ and \ \ C_2 = -C_4 \dfrac{\sqrt{K' - \sqrt{\Delta_a}}}{\sqrt{K' + \sqrt{\Delta_a}}} e^{-L\left(\sqrt{\frac{K' - \sqrt{\Delta_a}}{2}} - \sqrt{\frac{K' + \sqrt{\Delta_a}}{2}}\right)} \\ C_6 = \Delta E \sin\omega \end{cases} \\ \boldsymbol{K'^2 < 4K}: \begin{cases} C_4 = \Delta E \cos\omega \ \ and \ C_3 = C_4 \dfrac{\sqrt{\frac{K'}{2} + \sqrt{\frac{K'^2 + |\Delta_a|}{4}}} \cos\left(L\sqrt{\frac{K' + \sqrt{\Delta_b}}{2}}\right) \sqrt{\frac{K' + \sqrt{\Delta_b}}{2}} \sin\left(L\sqrt{\frac{K' + \sqrt{\Delta_b}}{2}}\right)}{-\sqrt{\frac{K'}{2} + \sqrt{\frac{K'^2 + |\Delta_a|}{4}}} \sin\left(L\sqrt{\frac{K' + \sqrt{\Delta_b}}{2}}\right) + \sqrt{\frac{K' + \sqrt{\Delta_b}}{2}} \cos\left(L\sqrt{\frac{K' + \sqrt{\Delta_b}}{2}}\right)} \\ C_6 = \Delta E \sin\omega \end{cases} \end{cases} \quad (4.59)$$

Thus:

If $\boldsymbol{K'^2 > 4K}$:

$$\begin{cases} C_4 = \dfrac{\Delta E \cos\omega}{1 - \dfrac{\sqrt{K' - \sqrt{\Delta_a}}}{\sqrt{K' + \sqrt{\Delta_a}}} e^{-L\left(\sqrt{\frac{K' - \sqrt{\Delta_a}}{2}} - \sqrt{\frac{K' + \sqrt{\Delta_a}}{2}}\right)}} \\ C_2 = -\dfrac{\Delta E \cos\omega}{1 - \dfrac{\sqrt{K' - \sqrt{\Delta_a}}}{\sqrt{K' + \sqrt{\Delta_a}}} e^{-L\left(\sqrt{\frac{K' - \sqrt{\Delta_a}}{2}} - \sqrt{\frac{K' + \sqrt{\Delta_a}}{2}}\right)}} \dfrac{\sqrt{K' - \sqrt{\Delta_a}}}{\sqrt{K' + \sqrt{\Delta_a}}} e^{-L\left(\sqrt{\frac{K' - \sqrt{\Delta_a}}{2}} - \sqrt{\frac{K' + \sqrt{\Delta_a}}{2}}\right)} \\ C_6 = \Delta E \sin\omega \end{cases} \quad (4.60)$$

If $\boldsymbol{K'^2 < 4K}$:

$$\begin{cases} C_3 = \Delta E \cos\omega \dfrac{\sqrt{\frac{K'}{2} + \sqrt{\frac{K'^2 + |\Delta_a|}{4}}} \cos\left(L\sqrt{\frac{K' + \sqrt{\Delta_b}}{2}}\right) \sqrt{\frac{K' + \sqrt{\Delta_b}}{2}} \sin\left(L\sqrt{\frac{K' + \sqrt{\Delta_b}}{2}}\right)}{-\sqrt{\frac{K'}{2} + \sqrt{\frac{K'^2 + |\Delta_a|}{4}}} \sin\left(L\sqrt{\frac{K' + \sqrt{\Delta_b}}{2}}\right) + \sqrt{\frac{K' + \sqrt{\Delta_b}}{2}} \cos\left(L\sqrt{\frac{K' + \sqrt{\Delta_b}}{2}}\right)} \\ C_4 = \Delta E \cos\omega \\ C_6 = \Delta E \sin\omega \end{cases} \quad (4.61)$$

The previous calculations were simplified using:

$$K = (\omega C_{dl})^2 + \frac{\gamma^2}{\left(\sigma^{eff}_{H^+,k} \delta_{act} R_{k,f}\right)^2} \text{ and } K' = \frac{2\gamma}{\omega C_{dl} \sigma^{eff}_{H^+,k} \delta_{act} R_{k,f}}$$

An asymptotic calculation is done to verify and compare K and K' using both the values of the literature and the values used in the modeling code stated in Table 4-1:

Table 4-1 : Parameters constant verification

Parameter	Value
$\boldsymbol{\delta_{act}}$	10^{-6} m
$\boldsymbol{\gamma}$	100
$\boldsymbol{C_{dl}}$	32.10^{-6} F/m²
$\boldsymbol{\omega}$	$[10^{-2},10^{3}]$ Hz
σ	0.1024 S.m
$\mathbf{R_f}$	0.1 Ω.m²

The previous calculations gave two possible solution depending if the discriminant Δ_a is positive or negative. Therefore, an order of magnitude is needed to see which of these two cases is possible in reality:

For low frequencies:

$$[K] = ([\omega][C_{dl}])^2 + \frac{[\gamma]^2}{\left(\left[\sigma_{H^+,k}^{eff}\right][\delta_{act}][R_{k,f}]\right)^2} \rightarrow [K] = (10^{-2}10^{-6})^2 + \frac{(10^2)^2}{(10^{-1}10^{-6}10^{-1})^2}$$

$$\rightarrow [K] \approx 10^{20}$$

$$\rightarrow [4K] \approx 10^{20}$$

$$[K'] = \frac{[2\gamma]}{[\omega][C_{dl}]\left[\sigma_{H^+,k}^{eff}\right][\delta_{act}][R_{k,f}]} \rightarrow [K'] = \frac{10^2}{10^{-2}10^{-6}10^{-1}10^{-6}10^{-1}} \rightarrow [K'] \approx 10^{18}$$

$$\rightarrow \left[K'^2\right] \approx 10^{36}$$

Thus at low frequencies: K'² > 4K

For high frequencies:

$$[K] = ([\omega][C_{dl}])^2 + \frac{[\gamma]^2}{\left(\left[\sigma_{H^+,k}^{eff}\right][\delta_{act}][R_{k,f}]\right)^2} \rightarrow [K] = (10^{3}10^{-6})^2 + \frac{(10^2)^2}{(10^{-1}10^{-6}10^{-1})^2}$$

$$\rightarrow [K] \approx 10^{20}$$

$$\rightarrow [4K] \approx 10^{20}$$

$$[K'] = \frac{[2\gamma]}{[\omega][C_{dl}]\left[\sigma_{H^+,k}^{eff}\right][\delta_{act}][R_{k,f}]} \rightarrow [K'] = \frac{10^2}{10^{3}10^{-6}10^{-1}10^{-6}10^{-1}} \rightarrow [K'] \approx 10^{16}$$

$$\rightarrow \left[K'^2\right] \approx 10^{32}$$

Thus at high frequencies: K'² > 4K

According to the values usually encountered in PEM devices , the only possible case for the chosen parameters is the discriminant Δ_a is positive (K'² > 4K).

4.3 Electrochemical Impedance Spectroscopy: Modeling Results at the active layer

This model is based on a single volumetric electrode to obtain a local impedance along x. For the rest of this study, the only exploited version of the mathematical model will be for the case of K'² > 4K. Most of the parameters used in this section are from the literature [5] [6].

The parameter chosen for the model are as follow (Table 4-2):

Table 4-2 : Model parameters

Parameter	Value
$\boldsymbol{T}$	25°C
$\boldsymbol{\delta_{act}}$	10^{-6} m
$\boldsymbol{\gamma}$	100
$\boldsymbol{C_{dl}}$	32.10^{-6} F/m²
$\boldsymbol{\omega}$	$[10^{-2},10^{3}]$ Hz

4.3.1 Electrochemical Impedance Spectroscopy: Frequency behaviors

The model seems to struggle with low frequencies depending on the value of the chosen parameters. Started the plots first by the basic values stated in the literature: $\sigma = 0.1024$ S.m^{-1} & $R_f = 0.1$ Ω.cm². To facilitate the interpretation all, the impedance values are normalized (using the maximum value of the real or the imaginary part). The thickness variable x will be referred to as δ_{act}.

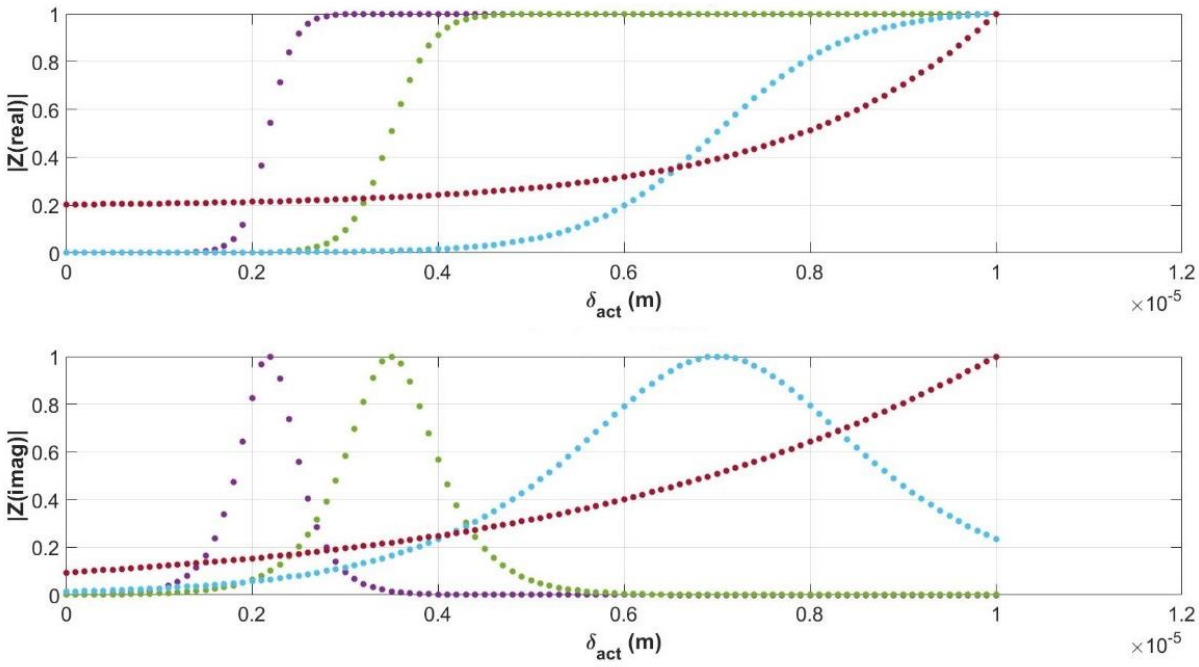

Figure 4-6 : Impedance real and imaginary parts plots as a function of δ_{act} for different frequencies: (-•-) 4 Hz (-•-) 10 Hz (-•-) 100 Hz (-•-) 1000 Hz

Figure 4-6 exhibits the absolute value of the real and imaginary parts of the impedance across the catalytic layer for different frequencies. The lowest frequency the model was able to reach was 4 Hz.

Impedance simulation will be done with a variation of two parameters R_f (0.05 Ω.cm², 0.1 Ω.cm², 0.2 Ω.cm², 0.5 Ω.cm²) & σ (0.01024 S.m^{-1}, 0.05108 S.m^{-1}, 0.1024 S.m^{-1}, 0.2048 S.m^{-1}). To facilitate the effect of these two parameters, a dimensionless number (ratio of charge transfer resistance to ohmic resistance) will be introduced:

$$\Psi = \frac{R_f \sigma}{\delta_{act}} \tag{4.62}$$

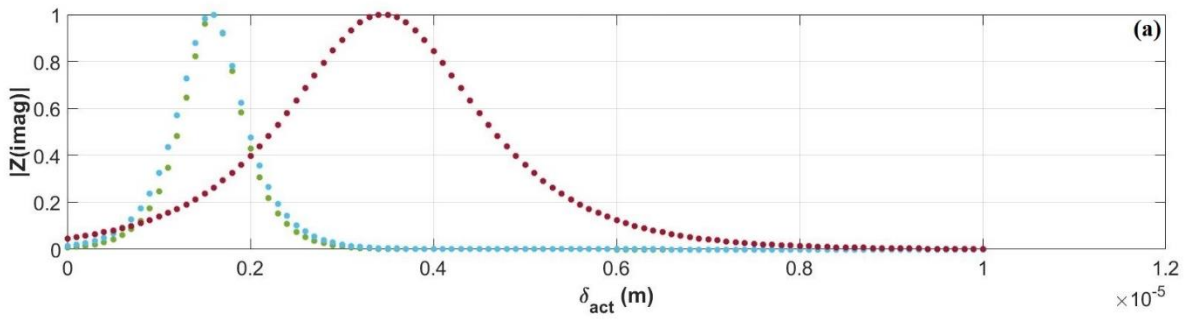

Figure 4-7: Impedance imaginary part plot as a function of δ_{act} for different frequencies for the smallest Ψ = 512: (-•-) 95 Hz (-•-) 100 Hz (-•-) 1000 Hz

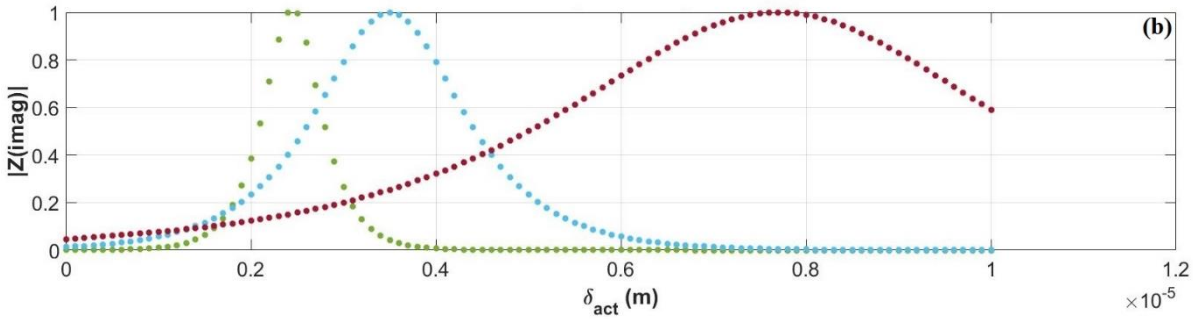

Figure 4-8: Impedance imaginary part plot as a function of δ_{act} for different frequencies for the average Ψ = 2554: (-•-) 16 Hz (-•-) 100 Hz (-•-) 1000 Hz

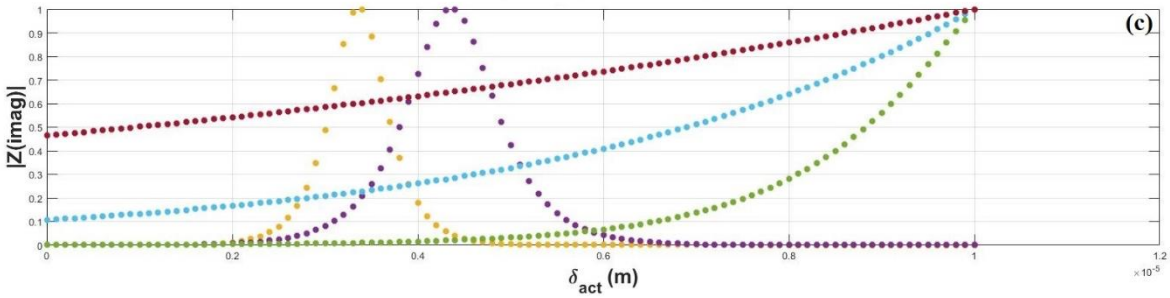

Figure 4-9 Impedance imaginary part plot as a function of δ_{act} for different frequencies for the biggest Ψ = 102400: (-•-) 0.4 Hz (-•-) 1 Hz (-•-) 10 Hz (-•-) 100 Hz (-•-) 1000 Hz

Figure 4-7 is a plot of the smallest Ψ (σ = 0.01024 S.m^{-1} & R_f = 0.05 Ω.cm²). This displays that at lower frequency the imaginary part of the impedance behavior tends to be more homogenous than higher frequency. This might explain the flatten spectrum by the high frequency deformation which is due to low conductivity. However, for Figure 4-9 the higher frequencies are more homogenous than lower frequency. For the smallest Ψ the plots are deformed at high frequencies but the biggest Ψ the values are homogenous at high frequencies. This pattern was observed in the literature for PEMFC and solid oxide fuel cell SOFC due to the heterogeneity at the active layer [7] [6].

4.3.2 Electrochemical Impedance Spectroscopy: Influence of σ and R_f

In this paragraph, the aim was to fix either conductivity (σ) or charge transfer resistance (R_f) with their values in the literature respectively and variate the other one in order to evaluate the impact of these two parameters. According to Boyer *et al.* [8] the catalyst layer ionic conductivity affects the electrodes' electrochemical performance. Yuan *et al.* [9] states that the charge transfer resistance is the leading contributor, at low over potential, to the impedance. These comparisons will be done at high frequency (1000 Hz).

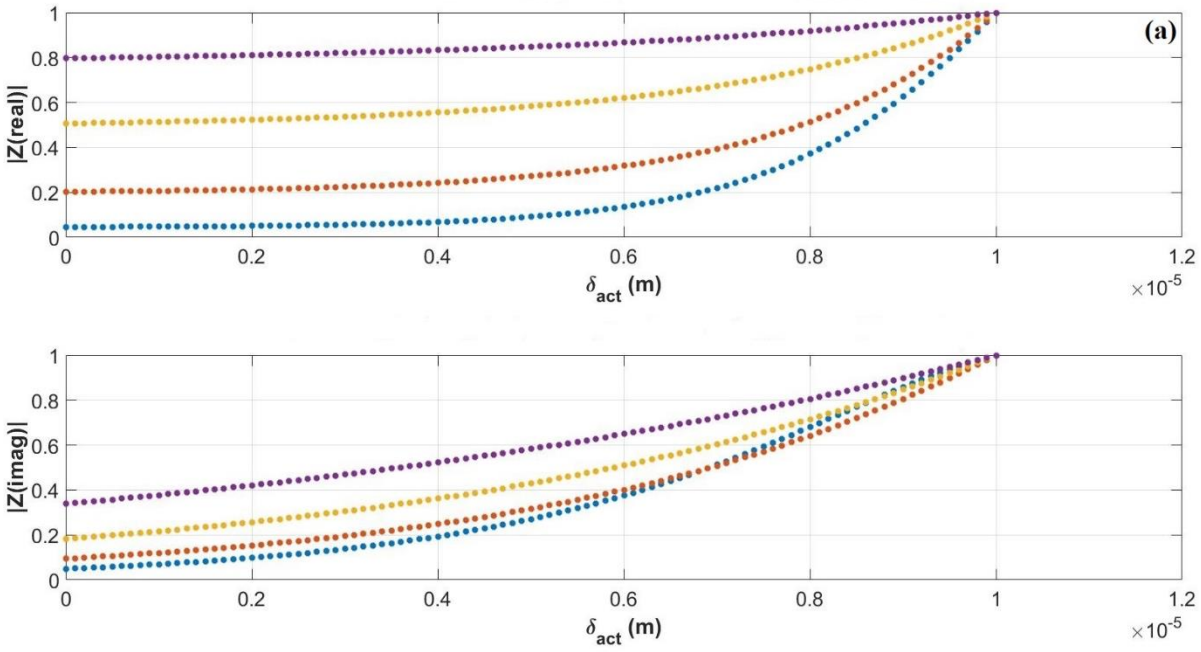

Figure 4-10 : Impedance real and imaginary parts plots as a function of δ_{act} at σ = 0.1024 S.m^{-1}: (-•-) R_f = 0.05 Ω.cm² (-•-) R_f = 0.1 Ω.cm² (-•-) R_f = 0.2 Ω.cm² (-•-) R_f = 0.5 Ω.cm²

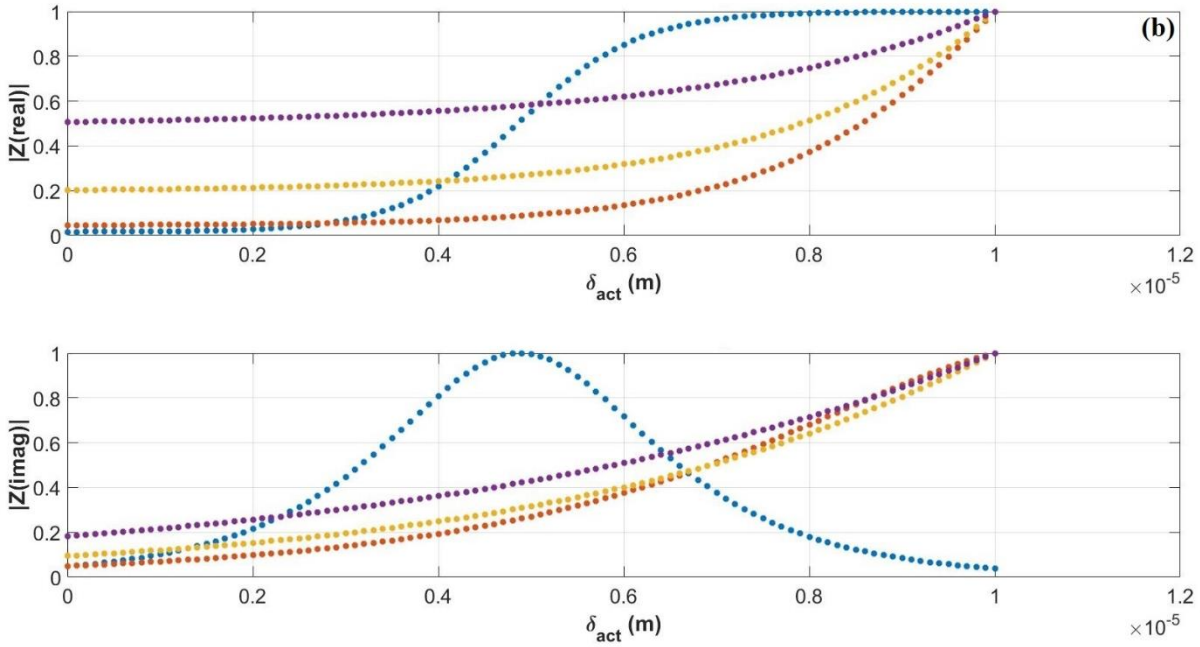

Figure 4-11: Impedance real and imaginary parts plots as a function of δ_{act} at R_f = 0.1 Ω.cm²: (-•-) σ = 0.01024 S.m^{-1} (-•-) σ = 0.05108 S.m^{-1} (-•-) σ = 0.1024 S.m^{-1} (-•-) σ = 0.2048 S.m^{-1}

Figure 4-10 represents the Impedance real and imaginary plots for different charge transfer resistance values and Figure 4-11 exhibits the same functions for different conductivities. The variation of the conductivity seems to have more a heterogeneous effect specially for a low conductivity. However, for the variation of charge transfer the impedance tends to keep the same pattern for different R_f values with a more homogeneous behavior.

4.3.3 Electrochemical Impedance Spectroscopy: Experimental analysis

According to Bao *et al.* [10], high frequencies the cell impedance is dominated by the charge at the catalyst layer. However, at medium and low frequencies the mass transfer and the water transport in the membrane and the diffusion layer has a bigger impact. Rozain *et al.* [11] have illustrated that EIS measurements allow the evaluation of the electrical environment homogeneity in PEMWE stacks and can track degradation processes.

The Figure 4-12 plots of EIS measurements from the previous chapter will be analyzed based on the previous observation of the effect of the resistance and the conductivity. It was noticed that at low temperatures the gas mixture (N_2/H_2) shows a deformation at low temperature and high frequency (Figure 4-12 (a) & (b)). This pattern is similar to what was observed for the simulation of the active layer behavior at low conductivity value. This behavior might also be a sign of presence of the ammonia. However, this does not exclude the deterioration of the catalytic layer. Nevertheless at higher temperatures (Figure 4-12 (c)) the EIS is not deformed but it seems to have compensated the heterogeneities noticed before. This proves that there was no catalyst layer degradation instead a conductivity issue.

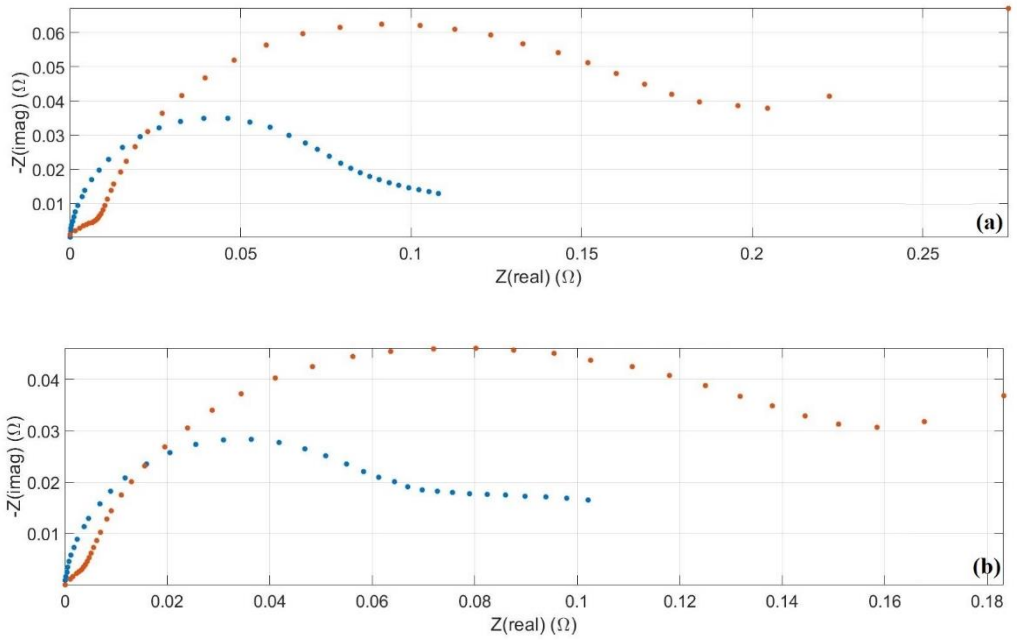

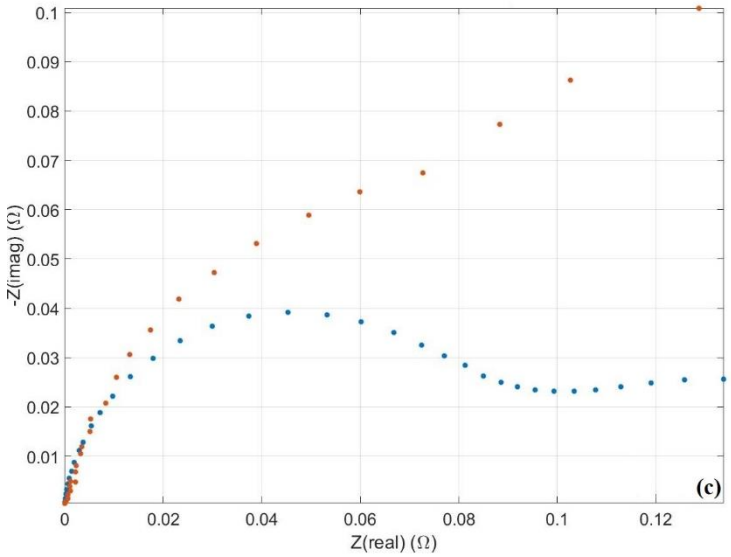

Figure 4-12: EIS diagrams For 70% RH for (-•-) H_2 pure and (-•-) H_2/N_2 gas mixture: (a) at 25°C (b) at 40°C & (c) at 60°C

CONCLUSIONS

The purpose of this chapter was to create a simplified model of Electrochemical Impedance Spectroscopy of a Proton Electrolyte Membrane device. A first step towards developing a thorough analytical model was made by focusing on a single volumetric electrode model.

Electrochemical impedance spectroscopy has proven to be remarkably interesting if the model is clearly formulated. The variation of values of resistance and conductivity showed as expected a tremendous effect on the impedance behavior of the active layer. This can be used to explain the different EIS measurements. However, this model is limited to mainly high frequency and seems to struggle on covering low frequencies depending on the different values of the parameters used. An analysis was made using different values of charge transfer resistance and conductivity to investigate the effect of these two parameters. The values found in the literature have shown very coherent results. Finally, the very low (R_f, σ) values greatly complicate the analysis of impedance.

It would be an interesting perspective to develop a full model of the cell and validate the model using experimental data and see how it can be optimized to cover low frequencies. The continuation of this study, always in connection with numerical methods, will undoubtedly allow a better understanding of the performance of a PEM cell.

References

[1] D. D. Macdonald, "Reflections on the history of electrochemical impedance spectroscopy," *Electrochimica Acta*, vol. 51, nº 8-9, p. 1376-1388, janv. 2006, doi: 10.1016/j.electacta.2005.02.107.

[2] J.-P. Diard, *Cinétique électrochimique*. Paris: Hermann, 1996.

[3] J. SCHILLINGS, « Etude numérique et expérimentale d'écoulements diphasiques Application aux écoulements à bulles générées par voie électrochimique », Université Grenoble Alpes, 2017.

[4] A. J. Bard et L. R. Faulkner, *Electrochemical methods: fundamentals and applications*, 2nd ed. New York: Wiley, 2001.

[5] M.-T. Nguyen, S. A. Grigoriev, A. A. Kalinnikov, A. A. Filippov, P. Millet, et V. N. Fateev, "Characterization of a electrochemical hydrogen pump using electrochemical impedance spectroscopy," *J. Appl. Electrochem.*, vol. 41, nº 9, p. 1033-1042, sept. 2011, doi: 10.1007/s10800-011-0341-9.

[6] J. Deseure, Y. Bultel, L. Dessemond, E. Siebert, et P. Ozil, "Modelling the porous cathode of a SOFC: oxygen reduction mechanism effect," *J. Appl. Electrochem.*, vol. 37, nº 1, p. 129-136, déc. 2006, doi: 10.1007/s10800-006-9208-x.

[7] J. Deseure, "Coupling RTD and EIS modelling to characterize operating non-uniformities on PEM cathodes." *J. Power Sources*, vol. 178, nº 1, Art. nº 1, mars 2008, doi: 10.1016/j.jpowsour.2007.11.071.

[8] C. Boyer, S. Gamburzev, O. Velev, S. Srinivasan, et A. J. Appleby, "Measurements of proton conductivity in the active layer of PEM fuel cell gas diffusion electrodes," *Electrochimica Acta*, vol. 43, nº 24, p. 3703-3709, août 1998, doi: 10.1016/S0013-4686(98)00128-5.

[9] X. Yuan, H. Wang, J. Colinsun, et J. Zhang, "AC impedance technique in PEM fuel cell diagnosis—A review," *Int. J. Hydrog. Energy*, vol. 32, nº 17, p. 4365-4380, déc. 2007, doi: 10.1016/j.ijhydene.2007.05.036.

[10] C. Bao et W. G. Bessler, "Two-dimensional modeling of a polymer electrolyte membrane fuel cell with long flow channel. Part II. Physics-based electrochemical impedance analysis," *J. Power Sources*, vol. 278, p. 675-682, mars 2015, doi: 10.1016/j.jpowsour.2014.12.045.

[11] C. Rozain et P. Millet, "Electrochemical characterization of Polymer Electrolyte Membrane Water Electrolysis Cells," *Electrochimica Acta*, vol. 131, p. 160-167, juin 2014, doi: 10.1016/j.electacta.2014.01.099.

General Conclusion

The main purpose of this research thesis entitled “Modeling of Polymer Electrolyte Membrane devices for hydrogen energy carrier”, is characterizing a few unexploited aspects of these machines. After a full bibliographical research, this study was focused on the pressurizing point of view specially with the Proton Electrolyte Membrane Water Electrolysis (PEMWE) and the Electrochemical Hydrogen Compressor (EHC).

Two main models were developed. The first model was a dimensionless steady state approach of a general PEM cell that was applied to a PEMWE in collaboration with the LE2P at the Reunion university and the Electrochemical Innovation Lab (EIL) in University College London (UCL). The second model is an electrochemical impedance spectroscopy (EIS) one-dimensional analytical model describing the electrochemical kinetics of the cell in the EIS regime. Experiments were also performed within the facilities of Hydrogen South Africa (HySA) Infrastructure at the North-West University (NWU) to study the PEM conductivity and the compression and separation aspects on the EHC.

For the steady state DC modeling of a PEM cell, this was done to investigate the multiple phenomena in the MEA. This included the water diffusion, the proton diffusion, the electro-osmotic transport, the pressure gradient, and the electrochemical kinetics. Each of this limiting physics contributed to a global mass balance or charge balance equations that was only studied on a one-dimensional scale. Dimensionless numbers were introduced along with boundary conditions to solve the equations. The dimensionless parameter ω, β, and γ allows to represent the influence of the water content and the over potential on the MEA. Even though the experiments validated the model it is still only valid for a steady state with multiple assumptions that were based on a PEM cell general behavior and on the PEMWE. A parametric optimization was conducted using this model with the EHC data. The results have shown an increase of the Wagner number with pressure. This behavior highlights the decrease of charge transfer resistance along with the partial pressure increase.

As for the experimental aspect of this thesis. Multiple measurements were conducted within this framework. First a through-plane conductivity measurement for different types of Nafion® commercial membranes and different conditions and backgrounds. Which indicated the importance of the pretreatment on the membrane conductivity and how the temperature, RH and thickness also played a

drastic role in the PEM resistance. Then the EHC experiments were performed between 0 bars and 30 bars for pure H_2 and a H_2/N_2 gas mixture for different RH and temperatures. The analysis of these measurements was based on the pressure variation as a function of time, the entropic analysis using the calculated power for each compression step and the EIS comparison before and after compression for different gas inlets. These analyses were studied at different RH and temperature. The cell was able to successfully compress the hydrogen up to 30 bars whether it is pure H_2 or (N_2/H_2) gas mixture. The membrane resistance analysis, the entropy analysis, the EIS measurements, the postmortem analyses (SEM, IR spectroscopy) of MEA and GC measurements all have shown a clear sign of contamination and deterioration due to the nitrogen impact. This has revealed a possibility of a new chemical process, a plausible electro synthesis of NH_3.

For the Polymer Electrolyte Membrane Cells Electrochemical Impedance Spectroscopy Modeling, this work has focused on the contribution of the active layer on the EIS. The model offers to help with the analysis of experimental behavior. This was a first step towards developing a thorough analytical model of PEM devices.

This thesis's work gives a general phenomenological understanding of Polymer Electrolyte Membrane devices, especially for the PEMWE and the EHC. By identifying the physics and the different phenomena which affect the operational parameters and the cell's performance.

APPENDIX A: Modeling of Polymer Electrolyte Membrane cells (steady state, DC modeling)

Dimensionless approach of a PEM Water Electrolysis:

1. **Electrochemical approach**

- At the anode

Butler-Volmer's law describes electrochemical kinetics at the electrode

In the 1D approach $\vec{\nabla}$ becomes $\nabla_x \vec{\imath} = \frac{d}{dx}\vec{\imath}$

$$\nabla_x i_a = \frac{di_a}{dx} = \frac{\gamma_a}{\delta_{act,a}} i_{0,a} \left(e^{\frac{\alpha_a F \eta_a}{RT_a}} - e^{\frac{-(1-\alpha_a)F\eta_a}{RT_a}} \right) \quad \text{(A1)}$$

However, when PEM electrolysis operates at cell potential quite far from the equilibrium potential $E_{eq}^{a,c}$, Butler Volmer's law is simplified by Tafel's approximation:

$$e^{\frac{\alpha_a F \eta_a}{RT_a}} \gg e^{\frac{-(1-\alpha_a)F\eta_a}{RT_a}}$$

$$\nabla_x i_a = \frac{di_a}{dx} = \frac{\gamma_a}{\delta_{act,a}} i_{0,a} e^{\frac{\alpha_a F \eta_a}{RT_a}} \quad \text{(A2)}$$

The electrochemical kinetics is then written as follows:

$$\frac{di_a}{dx} = \frac{\gamma_a}{\delta_{act,a}} i_{0,a} e^{\frac{\alpha_a F \eta_a}{RT_a}} \quad \text{(A3)}$$

The catalytic layer is composed of an ionic phase and an electric phase. The over potential at the active layer is the difference between the ionic potential Φ_{ionic} and the electric potential Φ_{elec}:

$$\eta_a = \Phi_{elec} - \Phi_{ionic} - E_{eq}^{a} \quad \text{(A4)}$$

Ohm's law:

$$\begin{cases} \nabla_x \Phi_{elec} = -\frac{i_a}{\sigma_{elec,a}^{eff}} \\ \nabla_x \Phi_{ionic} = -\frac{i_a}{\sigma_{H^+,a}^{eff}} \end{cases} \quad \text{(A5)}$$

In 1D, the derivative of the equation (A4) is:

$$\nabla_x \eta_a = \nabla_x \Phi_{elec} - \nabla_x \Phi_{ionic} \quad \text{(A6)}$$

As it has been mentioned in the assumptions, the protonic conductivity is negligible compared to the electrical conductivity:

$$\sigma_{elec,a}^{eff} \gg \sigma_{H^+,a}^{eff}$$

As a result:

$$\nabla_x \eta_a = -\frac{i_a}{\sigma_{elec,a}^{eff}} + \frac{i_a}{\sigma_{H^+,a}^{eff}} \rightarrow \nabla_x \eta_a = \frac{i_a}{\sigma_{H^+,a}^{eff}}\left(1 - \frac{\sigma_{H^+,a}^{eff}}{\sigma_{elec,a}^{eff}}\right) \rightarrow \nabla_x \eta_a = \frac{i_a}{\sigma_{H^+,a}^{eff}} \quad \text{(A7)}$$

The effective protonic conductivity of the ionic polymer phase of the active layer $\sigma_{H^+,a}^{eff}$ is obtained by the Neubrand model of protonic conductivity (A8) and corrected using properties (porosity, electrolyte content, *etc.*) of the active layer [20].

$$\sigma_{H^+} = (0.0013\lambda^3 + 0.0298\lambda^2 + 0.2658\lambda)\exp\left(EA\left(\frac{1}{353} - \frac{1}{T}\right)\right) \quad \text{(A8)}$$

By associating the following equations:

$$\begin{cases} \nabla_x i_a = \frac{di_a}{dx} = \frac{\gamma_a}{\delta_{act,a}} i_{0,a} e^{\frac{\alpha_a F \eta_a}{RT_a}} \\ \nabla_x \eta_a = \frac{d\eta_a}{dx} = \frac{i_a}{\sigma_{H^+,a}^{eff}} \end{cases} \quad \text{(A9)}$$

The result is a nonlinear second order differential equation, involving the current density at the active layer i_a:

$$\frac{d^2 i_a}{dx^2} = \frac{\gamma_a i_{0,a}}{\delta_{act,a}} \frac{\alpha_a F \eta_a}{RT_a} e^{\frac{\alpha_a F \eta_a}{RT_a}} \frac{d\eta_a}{dx} \rightarrow \frac{d^2 i_a}{dx^2} = \frac{\alpha_a F}{RT_a} \cdot \frac{\gamma_a}{\delta_{act,a}} i_{0,a} e^{\frac{\alpha_a F \eta_a}{RT_a}} \cdot \frac{i_a}{\sigma_{H^+,a}^{eff}} \rightarrow \quad \frac{d^2 i_a}{dx^2} = \frac{\alpha_a F}{RT_a \sigma_{H^+,a}^{eff}} \cdot \frac{di_a}{dx} \cdot i_a \quad \text{(A10)}$$

In order that the previous differential equation to be valid, the $\sigma_{H^+,a}^{eff}$ is consider constant, therefore it doesn't depend on neither λ nor T. Same assumption will be taken at the cathode side.

The differential equation of the anodic current density at the active layer can be written as follows:

$$i_a'' = \frac{\alpha_a F}{RT_a \sigma_a^{H^+}} i_a' i_a \quad \text{(A11)}$$

- At the cathode

As it has been done for the anodic active layer, the electrochemical kinetics at the cathode is obtained by a Tafel law. Using the similar development as the anode side, the differential equation of the electrochemical kinetics of the cathodic current density at the active layer is written as follows:

$$i_c'' = \frac{\alpha_c F}{RT_c \sigma_c^{H^+}} i_c' i_c \quad \text{(A12)}$$

- At the membrane

The membrane is electrically isolated. Only protons can migrate from the anodic side to the cathodic side. In a case of a theoretically perfect functioning, the accumulation of protons is not taken into consideration. The distribution of the over potential is written using charge balance:

$$\frac{\mathrm{d}\eta_m}{\mathrm{d}x} = -\frac{i_m}{\sigma_{H^+,m}^{eff}} \quad \text{(A13)}$$

The current density at the membrane is considered constant and equal to the operating current density imposed by the user J_0:

$$i_m = J_0 \quad \text{(A14)}$$

A differential equation of the first order is obtained:

$$\frac{\mathrm{d}\eta_m}{\mathrm{d}x} = -\frac{J_0}{\sigma_{H^+,m}^{eff}} \quad \text{(A15)}$$

The effective proton conductivity $\sigma_{H^+,m}^{eff}$is calculated from the proton conductivity σ_{H^+}defined by equation (A8) and corrected with the properties of the membrane. In the following calculation $\sigma_{H^+,m}^{eff}$ will be mentioned as σ^m to simplify the notation.

2. Mass balance

- At the membrane

The conservation of mass for water is defined using the following equation:

$$\frac{\partial c_{H_2O}}{\partial t} + \vec{\nabla} \cdot \vec{N}_{H_2O} = 0 \quad \text{(A16)}$$

The flux, $\vec{N}_{H_2O}$, is defined using the following equation:

$$\vec{N}_{H_2O} = -D_{H_2O}\vec{\nabla}c_{H_2O} + \vec{v}_m c_{H_2O} \quad \text{(A17)}$$

The steady-state material balance expression:

$$\vec{\nabla} \cdot \vec{N}_{H_2O} = 0$$

$$\leftrightarrow \ \vec{\nabla} \cdot \left(-D_{H_2O}\vec{\nabla}c_{H_2O} + \vec{v}_m c_{H_2O}\right) = 0$$

$$\leftrightarrow \ -D_{H_2O}\Delta c_{H_2O} + \vec{\nabla}.\vec{v}_m c_{H_2O} + \vec{v}_m.\vec{\nabla}c_{H_2O} = 0 \quad \text{(A18)}$$

D_{H_2O} the diffusion coefficient is considered constant in this work.

The equation of continuity for incompressible fluid flow at the membrane:

$$\vec{\nabla}.\vec{v}_m = 0 \quad \text{(A19)}$$

This means that ($A18$) can be simplified as:

$$D_{H_2O}\Delta c_{H_2O} = \vec{v}_m.\vec{\nabla}c_{H_2O} \quad \text{(A20)}$$

The fluid dynamics are described by a form of Schlögl's equation of motion; electric potential and pressure gradients generate convection within the pores of the ion-exchange membrane [14]:

$$\vec{v}_m = \frac{\kappa_\Phi}{\mu} z_f c_f F \vec{\nabla}\Phi - \frac{\kappa_p}{\mu}\vec{\nabla}p \quad \text{(A21)}$$

The current is represented using the Ohm's law:

$$\vec{J} = -\sigma^m \vec{\nabla}\Phi \quad \text{(A22)}$$

And the current conservation for one dimensional approach, expressed as:

$$\vec{\nabla}.\vec{J} = 0 \;\leftrightarrow\; \Delta\Phi = 0 \;\leftrightarrow\; \vec{\nabla}\Phi = cste \quad \text{(A23)}$$

The $\vec{\nabla}p$ is also constant and that can be proven using both the current conservation and the continuity equation for one dimensional approach:

$$\Delta\Phi = 0 \;\&\; \vec{\nabla}.\vec{v}_m = 0 \;\leftrightarrow\; \vec{\nabla}.\vec{v}_m = \frac{\kappa_\Phi}{\mu} z_f c_f F \Delta\Phi - \frac{\kappa_p}{\mu}\Delta p \;\leftrightarrow\; \Delta p = 0 \leftrightarrow \vec{\nabla}p = cste \quad \text{(A24)}$$

The equation (A20) becomes:

$$D_{H_2O}\Delta c_{H_2O} = -\frac{\kappa_\Phi}{\mu} z_f c_f F \frac{\vec{J}}{\sigma^m}.\vec{\nabla}c_{H_2O} - \frac{\kappa_p}{\mu}\vec{\nabla}p.\vec{\nabla}c_{H_2O} \quad \text{(A25)}$$

Water molecules that are transported through the PEM from the anode to the cathode along with protons (H^+) will be referred to as water content λ transport in the PEM, where λ is the dimensionless quantity defined as follows [22]:

$$\lambda_m = \frac{EWV_{ex}c_{H_2O}}{\rho^m_{dry}} \leftrightarrow c_{H_2O} = \frac{\rho^m_{dry}\lambda_m}{EWV_{ex}} \quad \text{(A26)}$$

The conservation of mass for water can be written as follows:

$$D_{H_2O}\Delta\lambda_m = -\frac{\kappa_\Phi}{\mu} z_f c_f F \frac{\vec{J}}{\sigma^m}.\vec{\nabla}\lambda_m - \frac{\kappa_p}{\mu}\vec{\nabla}p.\vec{\nabla}\lambda_m \quad \text{(A27)}$$

3. Dimensionless approach

The main objective is to obtain a set of dimensionless differential equations driven by dimensionless numbers representing the phenomenology of the PEM-E single cell core. In order to do so, a dimensionless method should be introduced using dimensionless parameters:

Table 1: Dimensionless parameters

Dimensionless current density	$i^*_{a,c,m} = \frac{i_{a,c,m}}{J_0}$
Dimensionless activation over potential	$\eta^*_{a,c} = \frac{\eta_{a,c}}{\frac{RT_{a,c}}{\alpha_{a,c}F}}$
Dimensionless ohmic voltage drop	$\eta^*_m = \frac{\eta_m}{\frac{RT_m}{F}}$
Characteristic length	$x^*_{a,c,m} = \frac{x_{a,c,m}}{\delta_{a,c,m}}$
Dimensionless water content	$\lambda^*_m = \frac{\lambda_m}{\lambda^{sat}_m}$
Dimensionless pressure	$p^*_m = \frac{p_m}{p^0_m}$

a. Dimensionless electrochemistry

- At the anode

According to table (1) and the differential equation of the anodic current density at the reaction layer ($A11$):

$$i''_a = \frac{\alpha_a F}{RT_a \sigma^{eff}_{H^+,a}} i'_a i_a \quad \& \quad i^*_a = \frac{i_a}{J_0} \quad \& \; x^*_a = \frac{x_a}{\delta_a} \tag{A28}$$

In other terms:

$$\frac{d^2 i_a}{dx^2} = \frac{\alpha_a F}{RT_a \sigma^{eff}_{H^+,a}} \cdot \frac{di_a}{dx} \cdot i_a \quad \leftrightarrow \quad \frac{J_0}{{\delta_a}^2} \frac{d^2 i^*_a}{d{x^*_a}^2} = \frac{\alpha_a F}{RT_a \sigma^{eff}_{H^+,a}} \cdot \frac{{J_0}^2}{\delta_a} \frac{di^*_a}{dx^*_a} \cdot i^*_a \quad \leftrightarrow \quad \frac{d^2 i^*_a}{d{x^*_a}^2} = 2\beta_a \frac{di^*_a}{dx^*_a} \cdot i^*_a \tag{A29}$$

Where

$$\beta_a = \frac{\boldsymbol{\alpha_a} J_0 \delta_a F}{2RT_a \sigma^{eff}_{H^+,a}} \tag{A30}$$

The dimensionless over potential is obtained by Tafel's law and table (1):

$$\frac{di_a}{dx} = \frac{\gamma_a}{\delta_{act,a}} i_{0,a} e^{\frac{\alpha_a F \eta_a}{RT_a}} \;\&\; i_a^* = \frac{i_a}{J_0} \;\&\; x_a^* = \frac{x_a}{\delta_a} \;\&\; \eta_a^* = \frac{\eta_a}{\frac{RT_a}{\alpha_a F}} \tag{A31}$$

Then:

$$\frac{J_0}{\delta_a}\frac{di_a^*}{dx_a^*} = \frac{\gamma_a}{\delta_{act,a}} i_{0,a} e^{\frac{\alpha_a F R T_a}{RT_a \alpha_a F}\eta_a^*} \leftrightarrow \frac{di_a^*}{dx_a^*} = \frac{\gamma_a \delta_a i_{0,a}}{\delta_{act,a} J_0} e^{\eta_a^*} \leftrightarrow \frac{di_a^*}{dx_a^*} = \zeta_a e^{\eta_a^*} \tag{A32}$$

Where

$$\zeta_a = \frac{\delta_a}{\delta_{act,a}} \frac{\gamma_a i_{0,a}}{J_0} \tag{A33}$$

- At the cathode

The approach is similar at the cathode side:

$$i_c'' = \frac{\alpha_c F}{RT_c \sigma_{c,H^+}^{eff}} i_c' i_c \;\&\; i_c^* = \frac{i_c}{J_0} \;\&\; x_c^* = \frac{x_c}{\delta_c} \tag{A34}$$

In other terms:

$$\frac{d^2 i_c}{dx^2} = \frac{\alpha_c F}{RT_c \sigma_{c,H^+}^{eff}} . \frac{di_c}{dx} . i_c \leftrightarrow \frac{J_0}{{\delta_c}^2}\frac{d^2 i_c^*}{dx_c^{*2}} = \frac{\alpha_c F}{RT_c \sigma_{c,H^+}^{eff}} . \frac{{J_0}^2}{\delta_c} . \frac{di_c^*}{dx_c^*} . i_c^* \leftrightarrow \frac{d^2 i_c^*}{dx_c^{*2}} = 2\beta_c . \frac{di_c^*}{dx_c^*} . i_c^* \tag{A35}$$

Where

$$\beta_c = \alpha_c \frac{J_0 \delta_c F}{2RT_c \sigma_{c,H^+}^{eff}} \tag{A36}$$

The dimensionless over potential is:

$$\frac{di_c}{dx} = -\frac{\gamma_c}{\delta_{act,c}} i_{0,c} e^{-\frac{\alpha_c F \eta_c}{RT_c}} \;\&\; i_c^* = \frac{i_c}{J_0} \;\&\; x_c^* = \frac{x_c}{\delta_c} \;\&\; \eta_c^* = \frac{\eta_c}{\frac{RT_c}{\alpha_c F}} \tag{A37}$$

$$\frac{di_c}{dx} = -\frac{\gamma_c}{\delta_{act,c}} i_{0,c} e^{-\frac{\alpha_c F \eta_c}{RT_c}} \leftrightarrow \frac{J_0}{\delta_c}\frac{di_c^*}{dx_c^*} = -\frac{\gamma_c}{\delta_{act,c}} i_{0,c} e^{-\frac{\alpha_c F}{RT_c}\frac{RT_c}{\alpha_c F}\eta_c^*} \leftrightarrow \frac{di_c^*}{dx_c^*} = -\zeta_c e^{-\eta_c^*} \tag{A38}$$

Where

$$\zeta_c = \frac{\delta_c}{\delta_{act,c}} \frac{\gamma_c}{J_0} i_{0,c} \tag{A39}$$

a. Dimensionless mass transport in the membrane

By associating equation (A27) with the dimensionless numbers described by the parameters of table (1), the mass transport at the membrane is written as follows:

$$D_{H_2O}\Delta\lambda_m = -\frac{\kappa_\Phi}{\mu} z_f c_f F \frac{\vec{J}}{\sigma^m}.\vec{\nabla}\lambda_m - \frac{\kappa_p}{\mu}\vec{\nabla}p.\vec{\nabla}\lambda_m \quad \text{(A40)}$$

For the one dimensional approach:

$$D_{H_2O}\frac{d^2\lambda_m}{dx^2} = \mp\frac{\kappa_\Phi}{\mu} z_f c_f F \frac{J}{\sigma^m}.\frac{d\lambda_m}{dx} \mp \frac{\kappa_p}{\mu}\frac{dp_m}{dx}.\frac{d\lambda_m}{dx} \quad \text{(A41)}$$

And according to Table (1):

$$\lambda_m^* = \frac{\lambda_m}{\lambda_m^{sat}} \;\&\; x_m^* = \frac{x_m}{\delta_m} \;\&\; p_m^* = \frac{p_m}{p_m^0} \;\&\; {J_m}^* = \frac{J}{J_m} \quad \text{(A42)}$$

Thus:

$$\frac{D_{H_2O}\lambda_m^{sat}}{{\delta_m}^2}\frac{d^2\lambda_m^*}{{dx_m^*}^2} = \mp\frac{\kappa_\Phi}{\mu} z_f c_f F \frac{J_m\lambda_m^{sat}}{\delta_m\sigma^m}.{J_m}^*\frac{d\lambda_m^*}{dx_m^*} \mp \frac{\kappa_p}{\mu}.\frac{p_m^0\lambda_m^{sat}}{{\delta_m}^2}\frac{dp_m^*}{dx_m^*}.\frac{d\lambda_m^*}{dx_m^*} \quad \text{(A43)}$$

Therefore:

$$\frac{d^2\lambda_m^*}{{dx_m^*}^2} = \frac{{\delta_m}^2}{D_{H_2O}\delta_m}\left(\mp\frac{\kappa_\Phi}{\mu} z_f c_f F \frac{J_m}{\sigma^m}.{J_m}^* \mp \frac{\kappa_p}{\mu}.\frac{p_m^0}{\delta_m}\frac{dp_m^*}{dx_m^*}\right).\frac{d\lambda_m^*}{dx_m^*} \quad \leftrightarrow \quad \frac{d^2\lambda_m^*}{{dx_m^*}^2} = \beta_m.\frac{d\lambda_m^*}{dx_m^*} \quad \text{(A44)}$$

Avec

$$\beta_m = \frac{\delta_m}{D_{H_2O}}\left(\mp\frac{\kappa_\Phi}{\mu} z_f c_f F \frac{J_m}{\sigma^m}.{J_m}^* \mp \frac{\kappa_p}{\mu}.\frac{p_m^0}{\delta_m}\frac{dp_m^*}{dx_m^*}\right) \quad \text{(A45)}$$

4. Analytical solution

In this section, the previously obtained differential equations are solved, in order to obtain the spatial distributions and the averaged values of the current densities, over potential and water content at the membrane.

a. Electrochemical approach

i. Over potential at the catalytic layer

At the anode and the cathode, the limiting processes taken into account are the electrochemical reactions and the proton resistance of the Nafion phase. The coupling of these two phenomena is at the origin of the over potential at the catalytic layers named $\eta_{a,c}^*$. obtained previously with the differential equations involving the current density $\boldsymbol{i_{a,c}}$.

At the anode, according to the equation (A29):

$$\frac{d^2 i_a^*}{dx_a^{*2}} = 2\beta_a \frac{di_a^*}{dx_a^*}.i_a^* \qquad \text{where} \quad \beta_a = \frac{\alpha_a J_0 \delta_a F}{2RT_a \sigma_{H^+,a}^{eff}} \tag{A46}$$

Then:

$$\frac{d^2 i_a^*}{dx_a^{*2}} = \frac{d}{dx_a^*}\left(\beta_a.i_a^{*2}\right) \rightarrow \frac{d}{dx_a^*}\left(\frac{di_a^*}{dx_a^*} - \beta_a.i_a^{*2}\right) = 0 \rightarrow \frac{di_a^*}{dx_a^*} - \beta_a.i_a^{*2} = K_1^a \tag{A47}$$

The equation $(A47)$ is a non-linear, therefore in order to solve it, the problem-solving method of Riccati equation will be used in order to have an approximated analytical solution to the current density differential equation. The general solution is obtained as:

$$i_a^* = z_a^* + i_{a_p}^* \quad where \;\; i_{a_p}^* = cste \tag{A48}$$

At first, the particular solution needs to be defined:

$$\frac{di_{a_p}^*}{dx_a^*} - \beta_a.{i_{a_p}^*}^2 = -(K_1^a)^2 \;\rightarrow\; {i_{a_p}^*}^2 - \frac{(K_1^a)^2}{\beta_a} = 0 \;\rightarrow\; i_{a_p}^* = \pm\frac{|K_1^a|}{\sqrt{\beta_a}} \tag{A49}$$

Combining $(A47)$ and the equation $(A48)$:

$$\frac{di_a^*}{dx_a^*} - \beta_a.i_a^{*2} = K_1^a \rightarrow \frac{d\left(z_a^* + i_{a_p}^*\right)}{dx_a^*} - \beta_a.\left(z_a^* + i_{a_p}^*\right)^2 = -(K_1^a)^2 \tag{A50}$$

Therefore:

$$\frac{dz_a^*}{dx_a^*} - \beta_a.z_a^{*2} - 2\beta_a.i_{a_p}^*.z_a^* - \beta_a.{i_{a_p}^*}^2 = -(K_1^a)^2 \tag{A51}$$

According to $(A49)$:

$${i_{a_p}^*}^2 - \frac{(K_1^a)^2}{\beta_a} = 0 \tag{A52}$$

Thus:

$$\frac{dz_a^*}{dx_a^*} - 2\beta_a.i_{a_p}^*.z_a^* - \beta_a.z_a^{*2} = 0 \tag{A53}$$

Assuming:

$$z_a^* = \frac{1}{u_a^*} \rightarrow \frac{dz_a^*}{dx_a^*} = -\frac{1}{u_a^{*2}}\frac{du_a^*}{dx_a^*} \tag{A54}$$

The equation $(A53)$ can be written as follow:

$$\frac{dz_a^*}{dx_a^*} - 2\beta_a.i_{a_p}^*.z_a^* - \beta_a.z_a^{*2} = 0 \rightarrow -\frac{1}{u_a^{*2}}\frac{du_a^*}{dx_a^*} - 2\frac{\beta_a.i_{a_p}^*}{u_a^*} - \frac{\beta_a}{u_a^{*2}} = 0 \rightarrow \frac{du_a^*}{dx_a^*} + 2\beta_a.i_{a_p}^* u_a^* + \beta_a = 0 \tag{A55}$$

Where

$$u_a^* = u_{a_H}^* + u_{a_p}^* \;\&\; u_{a_p}^* = cste \tag{A56}$$

The particular solution of the equation is:

$$\frac{du_{a_p}^*}{dx_a^*} + 2\beta_a . i_{a_p}^* u_{a_p}^* = -\beta_a \rightarrow u_{a_p}^* = -\frac{1}{2i_{a_p}^*} \tag{A57}$$

Therefore, the general solution is:

$$\frac{du_a^*}{dx_a^*} + 2\beta_a . i_{a_p}^* u_a^* = 0 \rightarrow \frac{du_{a_H}^*}{dx_a^*} + 2\beta_a . i_{a_p}^* u_{a_H}^* = 0 \rightarrow u_{a_H}^* = K_2^a e^{-2\beta_a . i_{a_p}^* . x_a^*} \tag{A58}$$

Thereby:

$$u_a^* = K_2^a e^{-2\beta_a . i_{a_p}^* . x_a^*} - \frac{1}{2i_{a_p}^*} \tag{A59}$$

It was assumed that:

$$z_a^* = \frac{1}{u_a^*} \rightarrow z_a^* = \frac{1}{K_2^a e^{-2\beta_a . i_{a_p}^* . x_a^*} - \frac{1}{2i_{a_p}^*}} \tag{A60}$$

Therefore, the current density's analytical solution obtained is:

$$i_a^* = z_a^* + i_{a_p}^* \rightarrow i_a^* = \frac{1}{K_2^a e^{-2\sqrt{\beta_a} . |K_1^a| . x_a^*} - \frac{\sqrt{\beta_a}}{2|K_1^a|}} + \frac{|K_1^a|}{\sqrt{\beta_a}} \tag{A61}$$

<u>The result verification</u>

Preserving the term $i_{a_p}^*$, the analytical solution is as follow:

$$\rightarrow i_a^* = \frac{1}{K_2^a e^{-2\beta_a . i_{a_p}^* . x_a^*} - \frac{1}{2i_{a_p}^*}} + i_{a_p}^*$$

$$\rightarrow i_a^* = \frac{2i_{a_p}^*}{2i_{a_p}^* K_2^a e^{-2\beta_a . i_{a_p}^* . x_a^*} - 1} + i_{a_p}^*$$

$$\rightarrow i_a^* = i_{a_p}^* \left(\frac{2}{2i_{a_p}^* K_2^a e^{-2\beta_a . i_{a_p}^* . x_a^*} - 1} + 1 \right)$$

$$\rightarrow i_a^* = i_{a_p}^* \left(\frac{2i_{a_p}^* K_2^a e^{-2\beta_a . i_{a_p}^* . x_a^*} + 1}{2i_{a_p}^* K_2^a e^{-2\beta_a . i_{a_p}^* . x_a^*} - 1} \right)$$

$$\rightarrow i_a^* = i_{a_p}^* \left(\frac{Ae^{-B.x_a^*} + 1}{Ae^{-B.x_a^*} - 1} \right) \tag{A62}$$

Where $A = 2i_{a_p}^* K_2^a \;\&\; B = 2\beta_a . i_{a_p}^*$ (A63)

At the anode, according to the differential equation (A29):

$$\frac{d^2 i_a^*}{dx_a^{*2}} = 2\beta_a \frac{di_a^*}{dx_a^*}.i_a^* \quad \text{(A64)}$$

Verification:

The first derivative:

$$\frac{di_a^*}{dx_a^*} = i_{a_p}^* \frac{-ABe^{-B.x_a^*}\left(Ae^{-B.x_a^*}-1\right)+ABe^{-B.x_a^*}\left(Ae^{-B.x_a^*}+1\right)}{\left(Ae^{-B.x_a^*}-1\right)^2} = i_{a_p}^* \frac{2ABe^{-B.x_a^*}}{\left(Ae^{-B.x_a^*}-1\right)^2} \quad \text{(A65)}$$

The second derivative:

$$\frac{d^2 i_a^*}{dx_a^{*2}} = i_{a_p}^* \frac{-\left(2AB^2e^{-B.x_a^*}\right)\left(Ae^{-B.x_a^*}-1\right)^2+\left(2ABe^{-B.x_a^*}\right).2.\left(Ae^{-B.x_a^*}-1\right)ABe^{-B.x_a^*}}{\left(Ae^{-B.x_a^*}-1\right)^4}$$

$$\rightarrow \frac{d^2 i_a^*}{dx_a^{*2}} = i_{a_p}^* \frac{-\left(2AB^2e^{-B.x_a^*}\right)\left(Ae^{-B.x_a^*}-1\right)+2\left(2ABe^{-B.x_a^*}\right)ABe^{-B.x_a^*}}{\left(Ae^{-B.x_a^*}-1\right)^3}$$

$$\rightarrow \frac{d^2 i_a^*}{dx_a^{*2}} = i_{a_p}^* \frac{\left(2AB^2e^{-B.x_a^*}\right)\left(-Ae^{-B.x_a^*}+1+2Ae^{-B.x_a^*}\right)}{\left(Ae^{-B.x_a^*}-1\right)^3}$$

$$\rightarrow \frac{d^2 i_a^*}{dx_a^{*2}} = i_{a_p}^* \frac{\left(2AB^2e^{-B.x_a^*}\right)\left(1+Ae^{-B.x_a^*}\right)}{\left(Ae^{-B.x_a^*}-1\right)^3} \quad \text{(A66)}$$

The second part of the differential equation can also be calculated accordingly:

$$\beta_a \frac{di_a^*}{dx_a^*}.i_a^* = \beta_a {i_{a_p}^*}^2 \frac{2ABe^{-B.x_a^*}}{\left(Ae^{-B.x_a^*}-1\right)^2}.\left(\frac{Ae^{-B.x_a^*}+1}{Ae^{-B.x_a^*}-1}\right) = \beta_a {i_{a_p}^*}^2 \frac{2ABe^{-B.x_a^*}.\left(Ae^{-B.x_a^*}+1\right)}{\left(Ae^{-B.x_a^*}-1\right)^3} \quad \text{(A67)}$$

Combining the two sides $(A66)$ & $(A67)$ of the differential equation $(A29)$:

$$\frac{d^2 i_a^*}{dx_a^{*2}} = 2\beta_a \frac{di_a^*}{dx_a^*}.i_a^*$$

$$\rightarrow i_{a_p}^* \frac{\left(2AB^2e^{-B.x_a^*}\right)\left(1+Ae^{-B.x_a^*}\right)}{(Ae^{-B.x_a^*}-1)^3} = 2\beta_a {i_{a_p}^*}^2 \frac{2ABe^{-B.x_a^*}.\left(Ae^{-B.x_a^*}+1\right)}{(Ae^{-B.x_a^*}-1)^3}$$

$$\rightarrow i_{a_p}^*\left(2AB^2e^{-B.x_a^*}\right)\left(1+Ae^{-B.x_a^*}\right) = 4\beta_a i_{a_p}^* ABe^{-B.x_a^*}.\left(Ae^{-B.x_a^*}+1\right)$$

$$\rightarrow B\left(1+Ae^{-B.x_a^*}\right) = 2\beta_a i_{a_p}^*.\left(Ae^{-B.x_a^*}+1\right) \quad \text{(A68)}$$

It has been assumed that: $A = 2i_{a_p}^* K_2^a$ & $B = 2\beta_a.i_{a_p}^*$ (A69)

Therefore:

$$B\left(1+Ae^{-B.x_a^*}\right)=2\beta_a i_{a_p}^*.\left(Ae^{-B.x_a^*}+1\right)\rightarrow 2\beta_a.i_{a_p}^*\left(1+Ae^{-B.x_a^*}\right)=2\beta_a i_{a_p}^*.\left(Ae^{-B.x_a^*}+1\right)$$

(A70)

It is verified thus that the current density's analytical solution is:

$$i_a^*=z_a^*+i_{a_p}^*\rightarrow i_a^*=\frac{1}{K_2^a e^{-2\sqrt{\beta_a}.|K_1^a|.x_a^*}-\frac{\sqrt{\beta_a}}{2|K_1^a|}}+\frac{|K_1^a|}{\sqrt{\beta_a}}$$

(A71)

At the cathode, the same equation form and problem-solving method using Riccati equation and Bernoulli equation, the current density's analytical solution will be written as follows:

$$i_c^*=\frac{1}{K_2^c e^{-2\sqrt{\beta_c}.|K_1^c|.x_c^*}-\frac{\sqrt{\beta_c}}{2|K_1^c|}}+\frac{|K_1^c|}{\sqrt{\beta_c}}$$

(A72)

,k

With K_a^1, K_a^2, K_c^1 and K_c^2 integration constants. In order to determine this constants, the boundary conditions will be used:

Table 1: Boundary conditions

a theoretically perfect operation, the protonic current is zero at the interface diffusion layer / anodic reaction layer	$i_a^*(0)=0$
At the diffusion layer / cathodic catalytic layer interface, the protonic current will be considered as zero	$i_c^*(1)=0$
Considering a constant current at the membrane equal to the operating current density	$i_a^*(1)=-1$
	$i_c^*(0)=1$

Using this previous table, a system of equation will be defined at both the anode and the cathode side:

At the anode:

$$\begin{cases} i_a^*(0)=\frac{1}{K_2^a-\frac{\sqrt{\beta_a}}{2|K_1^a|}}+\frac{|K_1^a|}{\sqrt{\beta_a}}=0 \\ i_a^*(1)=\frac{1}{K_2^a e^{-2\sqrt{\beta_a}.|K_1^a|}-\frac{\sqrt{\beta_a}}{2|K_1^a|}}+\frac{|K_1^a|}{\sqrt{\beta_a}}=-1 \end{cases}$$

(A73)

After a few simplifications, the system will be written as follows:

$$i_a^*(0) = \frac{1}{K_2^a - \frac{\sqrt{\beta_a}}{2|K_1^a|}} + \frac{|K_1^a|}{\sqrt{\beta_a}} = 1 + \frac{|K_1^a|}{\sqrt{\beta_a}} K_2^a - \frac{|K_1^a|}{\sqrt{\beta_a}} \frac{\sqrt{\beta_a}}{2|K_1^a|} = 1 + \frac{|K_1^a|}{\sqrt{\beta_a}} K_2^a - \frac{1}{2} = 0$$

(A74)

Using the first boundary condition the expression of K_2^a is easily determined :

$$K_2^a = -\frac{\sqrt{\beta_a}}{2|K_1^a|}$$

(A75)

This formula will be inserted in the second part of the system in order to simplify it:

$$i_a^*(1) = \frac{1}{K_2^a e^{-2\sqrt{\beta_a}\cdot|K_1^a|} - \frac{\sqrt{\beta_a}}{2|K_1^a|}} + \frac{|K_1^a|}{\sqrt{\beta_a}} = \frac{1}{-\frac{\sqrt{\beta_a}}{2|K_1^a|} e^{-2\sqrt{\beta_a}\cdot|K_1^a|} - \frac{\sqrt{\beta_a}}{2|K_1^a|}} + \frac{|K_1^a|}{\sqrt{\beta_a}} = -1$$

$$\rightarrow i_a^*(1) = \frac{1 - \frac{|K_1^a|\sqrt{\beta_a}}{\sqrt{\beta_a} 2|K_1^a|} e^{-2\sqrt{\beta_a}\cdot|K_1^a|} - \frac{|K_1^a|\sqrt{\beta_a}}{\sqrt{\beta_a} 2|K_1^a|}}{-\frac{\sqrt{\beta_a}}{2|K_1^a|} e^{-2\sqrt{\beta_a}\cdot|K_1^a|} - \frac{\sqrt{\beta_a}}{2|K_1^a|}} = \frac{1 - \frac{1}{2} e^{-2\sqrt{\beta_a}\cdot|K_1^a|} - \frac{1}{2}}{-\frac{\sqrt{\beta_a}}{2|K_1^a|} e^{-2\sqrt{\beta_a}\cdot|K_1^a|} - \frac{\sqrt{\beta_a}}{2|K_1^a|}} = -1$$

$$\rightarrow i_a^*(1) = \frac{\frac{1}{2} - \frac{1}{2} e^{-2\sqrt{\beta_a}\cdot|K_1^a|}}{-\frac{\sqrt{\beta_a}}{2|K_1^a|}\left(e^{-2\sqrt{\beta_a}\cdot|K_1^a|} + 1\right)} = -1$$

$$\rightarrow \frac{\frac{1}{2} - \frac{1}{2} e^{-2\sqrt{\beta_a}\cdot|K_1^a|}}{\left(e^{-2\sqrt{\beta_a}\cdot|K_1^a|} + 1\right)} = \frac{\sqrt{\beta_a}}{2|K_1^a|}$$

$$\rightarrow \frac{1 - e^{-2\sqrt{\beta_a}\cdot|K_1^a|}}{1 + e^{-2\sqrt{\beta_a}\cdot|K_1^a|}} = \frac{\sqrt{\beta_a}}{|K_1^a|} \qquad \text{(A76)}$$

The integration constant definition system is:

$$\begin{cases} i_a^*(0) = 0 \rightarrow K_2^a = -\frac{\sqrt{\beta_a}}{2|K_1^a|} \\ i_a^*(1) = 1 \rightarrow \frac{1 - e^{-2\sqrt{\beta_a}\cdot|K_1^a|}}{1 + e^{-2\sqrt{\beta_a}\cdot|K_1^a|}} = \frac{\sqrt{\beta_a}}{|K_1^a|} \end{cases}$$

(A77)

At the cathode $(A72)$:

$$i_c^* = \frac{1}{K_2^c e^{-2\sqrt{\beta_c}\cdot|K_1^c|\cdot x_c^*} - \frac{\sqrt{\beta_c}}{2|K_1^c|}} + \frac{|K_1^c|}{\sqrt{\beta_c}} \qquad \text{(A78)}$$

Using the same simplification of the boundary conditions at the cathode side, the simplified system will be written as follows:

$$\begin{cases} i_c^*(0) = \frac{1}{K_2^c - \frac{\sqrt{\beta_c}}{2|K_1^c|}} + \frac{|K_1^c|}{\sqrt{\beta_c}} = 1 \\ i_c^*(1) = \frac{1}{K_2^c e^{-2\sqrt{\beta_c}\cdot|K_1^c|} - \frac{\sqrt{\beta_c}}{2|K_1^c|}} + \frac{|K_1^c|}{\sqrt{\beta_c}} = 0 \end{cases} \tag{A79}$$

Using the first boundary condition the expression of K_2^c is easily determined :

$$i_c^*(0) = \frac{1}{K_2^c - \frac{\sqrt{\beta_c}}{2|K_1^c|}} + \frac{|K_1^c|}{\sqrt{\beta_c}} = \frac{1 + \frac{|K_1^c|}{\sqrt{\beta_c}} K_2^c - \frac{|K_1^c|\sqrt{\beta_c}}{\sqrt{\beta_c} 2|K_1^c|}}{K_2^c - \frac{\sqrt{\beta_c}}{2|K_1^c|}} = \frac{1 + \frac{|K_1^c|}{\sqrt{\beta_c}} K_2^c - \frac{1}{2}}{K_2^c - \frac{\sqrt{\beta_c}}{2|K_1^c|}} = 1$$

$$\rightarrow \frac{1}{2} + \frac{|K_1^c|}{\sqrt{\beta_c}} K_2^c = K_2^c - \frac{\sqrt{\beta_c}}{2|K_1^c|}$$

$$\rightarrow \frac{1}{2} + \frac{\sqrt{\beta_c}}{2|K_1^c|} = K_2^c - \frac{|K_1^c|}{\sqrt{\beta_c}} K_2^c$$

$$\rightarrow 1 + \frac{\sqrt{\beta_c}}{|K_1^c|} = 2K_2^c \left(1 - \frac{|K_1^c|}{\sqrt{\beta_c}}\right)$$

$$\rightarrow K_2^c = \frac{1 + \frac{\sqrt{\beta_c}}{|K_1^c|}}{2\left(1 - \frac{|K_1^c|}{\sqrt{\beta_c}}\right)} \tag{A80}$$

This formula will be inserted in the second part of the system in order to simplify it:

$$i_c^*(1) = \frac{1}{K_2^c e^{-2\sqrt{\beta_c}\cdot|K_1^c|} - \frac{\sqrt{\beta_c}}{2|K_1^c|}} + \frac{|K_1^c|}{\sqrt{\beta_c}} = \frac{1}{\frac{1 + \frac{\sqrt{\beta_c}}{|K_1^c|}}{2\left(1 - \frac{|K_1^c|}{\sqrt{\beta_c}}\right)} e^{-2\sqrt{\beta_c}\cdot|K_1^c|} - \frac{\sqrt{\beta_c}}{2|K_1^c|}} + \frac{|K_1^c|}{\sqrt{\beta_c}} = 0$$

$$\rightarrow i_c^*(1) = \frac{2\left(1 - \frac{|K_1^c|}{\sqrt{\beta_c}}\right)}{\left(1 + \frac{\sqrt{\beta_c}}{|K_1^c|}\right) e^{-2\sqrt{\beta_c}\cdot|K_1^c|} - \frac{\sqrt{\beta_c}}{2|K_1^c|} 2\left(1 - \frac{|K_1^c|}{\sqrt{\beta_c}}\right)} + \frac{|K_1^c|}{\sqrt{\beta_c}} = 0$$

$$\rightarrow 2\left(1 - \frac{|K_1^c|}{\sqrt{\beta_c}}\right) + \frac{|K_1^c|}{\sqrt{\beta_c}} \left(1 + \frac{\sqrt{\beta_c}}{|K_1^c|}\right) e^{-2\sqrt{\beta_c}\cdot|K_1^c|} - \frac{|K_1^c|}{\sqrt{\beta_c}} \frac{\sqrt{\beta_c}}{|K_1^c|} \left(1 - \frac{|K_1^c|}{\sqrt{\beta_c}}\right) = 0$$

$$\rightarrow 2\left(1 - \frac{|K_1^c|}{\sqrt{\beta_c}}\right) + \left(1 + \frac{|K_1^c|}{\sqrt{\beta_c}}\right) e^{-2\sqrt{\beta_c}\cdot|K_1^c|} - \left(1 - \frac{|K_1^c|}{\sqrt{\beta_c}}\right) = 0$$

$$\rightarrow 2 - 2\frac{|K_1^c|}{\sqrt{\beta_c}} + \left(1 + \frac{|K_1^c|}{\sqrt{\beta_c}}\right) e^{-2\sqrt{\beta_c}\cdot|K_1^c|} - 1 + \frac{|K_1^c|}{\sqrt{\beta_c}} = 0$$

$$\rightarrow 1 - \frac{|K_1^c|}{\sqrt{\beta_c}} + \left(1 + \frac{|K_1^c|}{\sqrt{\beta_c}}\right) e^{-2\sqrt{\beta_c}\cdot|K_1^c|} = 0$$

$$\rightarrow 1 = \frac{|K_1^c|}{\sqrt{\beta_c}} - \left(1 + \frac{|K_1^c|}{\sqrt{\beta_c}}\right) e^{-2\sqrt{\beta_c}\cdot|K_1^c|} \tag{A81}$$

The integration constant definition system is:

$$\begin{cases} i_c^*(0) = 1 \rightarrow K_2^c = \frac{1+\frac{\sqrt{\beta_c}}{|K_1^c|}}{2\left(1-\frac{|K_1^c|}{\sqrt{\beta_c}}\right)} \\ i_c^*(1) = 0 \rightarrow \frac{|K_1^c|}{\sqrt{\beta_c}} - \left(1+\frac{|K_1^c|}{\sqrt{\beta_c}}\right) e^{2\sqrt{\beta_c}\cdot|K_1^c|} = 1 \end{cases}$$

(A82)

Giving the complexity of these systems $(A77)$ & $(A82)$, the integration constants will be determined using a numerical solving method.

i. Activation over potential

The over potential will firstly be defined using the equations (A35) & (A38) allow to write that:

$$\eta_a^* = \ln\left(\frac{i_a^{*\prime}}{\zeta_a}\right) = \ln\left(\frac{\sqrt{\beta_a}K_a^2K_a^1}{\zeta_a}\frac{\exp\left(-\sqrt{\beta_a}K_a^2x_a^*\right)}{\left(K_a^1\exp\left(-\sqrt{\beta_a}K_a^2x_a^*\right)-\frac{\sqrt{\beta_a}}{2K_a^2}\right)^2}\right) \quad where\ \zeta_a = \frac{\gamma_a}{J_0}i_{0,a}$$

(A83)

$$\eta_c^* = -\ln\left(-\frac{i_c^{*\prime}}{\zeta_c}\right) = -\ln\left(\frac{\sqrt{\beta_c}K_c^2K_c^1}{\zeta_c}\frac{\exp\left(-\sqrt{\beta_c}K_c^2x_c^*\right)}{\left(K_c^1\exp\left(-\sqrt{\beta_c}K_c^2x_c^*\right)-\frac{\sqrt{\beta_c}}{2K_c^2}\right)^2}\right) \quad where\ \zeta_c = \frac{\gamma_c}{J_0}i_{0,c}$$

(A84)

The average anodic and cathodic activation over potential are obtained by the relation:

$$\overline{\eta_{a,c}^*} = \int_0^1 \eta_{a,c}^*\, dx_{a,c}^* \qquad (A85)$$

The calculation of this average will be done also using an analytical solving method, due to complexity of this integration, for example at the anode side the average anodic activation over potential is calculated as follows:

$$\overline{\eta_a^*} = \int_0^1 \eta_a^*\, dx_a^* = \int_0^1 \ln\left(\frac{\sqrt{\beta_a}K_a^2K_a^1}{\zeta_a}\frac{\exp\left(-\sqrt{\beta_a}K_a^2x_a^*\right)}{\left(K_a^1\exp\left(-\sqrt{\beta_a}K_a^2x_a^*\right)-\frac{\sqrt{\beta_a}}{2K_a^2}\right)^2}\right) dx_a^*$$

$$= \int_0^1 \ln\left(\frac{\sqrt{\beta_a}K_a^2K_a^1}{\zeta_a}\right) + \ln\left(exp\left(-\sqrt{\beta_a}K_a^2x_a^*\right)\right) - 2\ln\left(K_a^1\, exp\left(-\sqrt{\beta_a}K_a^2x_a^*\right)-\frac{\sqrt{\beta_a}}{2K_a^2}\right) dx_a^*$$

$$= \int_0^1 \ln\left(\frac{\sqrt{\beta_a}K_a^2K_a^1}{\zeta_a}\right) dx_a^* + \int_0^1 -\sqrt{\beta_a}K_a^2x_a^*\ dx_a^*$$

$$+ \int_0^1 2\ln\left(K_a^1\ exp\left(-\sqrt{\beta_a}K_a^2x_a^*\right) - \frac{\sqrt{\beta_a}}{2K_a^2}\right) dx_a^*$$

$$= \ln\left(\frac{\sqrt{\beta_a}K_a^2K_a^1}{\zeta_a}\right) + \frac{-\sqrt{\beta_a}K_a^2x_a^*}{2} + \int_0^1 2\ln\left(K_a^1\ exp\left(-\sqrt{\beta_a}K_a^2x_a^*\right) - \frac{\sqrt{\beta_a}}{2K_a^2}\right) dx_a^*$$

(A86)

The last term of this integral is the part where the analytical calculation will be needed. The same thing goes for the cathode side.

ii. Over potential through the membrane

The distribution of the ohmic drop to the membrane is written as follows:

$$\eta_m = -\frac{i_m}{\sigma_{H^+,m}^{eff}}x_m + K \quad \leftrightarrow \quad \eta_m^*$$

$$= \frac{-\frac{i_m}{\sigma_{H^+,m}^{eff}}}{\frac{RT_m}{F}}\delta_m\ x_m^* + \frac{RT_m}{F}K$$

$$\leftrightarrow \quad \eta_m^* = K_m^1\ x_m^* + K_m^2 \quad where \quad K_m^1 = \frac{-\frac{i_m}{\sigma_{H^+,m}^{eff}}}{\frac{RT_m}{F}}\delta_m \ \&\ K_m^2 = \frac{RT_m}{F}K$$

(A87)

Therefore, the distribution of the dimensionless ohmic drop to the membrane is written as follows:

$$\eta_m^* = -K_m^1x_m^* + K_m^2 \quad where\ K_m^2 = \eta_a^*(1)$$

(A88)

iii. Total over potential

The total dimensionless theoretical over potential of a single cell is the sum of the activation over potential and the ohmic drop:

$$\overline{\eta_t^*} = \overline{\eta_a^*} + \overline{\eta_c^*} + \overline{\eta_m^*}$$

(A89)

b. Mass transport in the membrane

The characteristic equation of the equation (A44) can be written as follows:

$$ar^2 + br + c = 0 \ \ where\ a = 1, b = \beta_m\ and\ c = 0 \ \ \leftrightarrow \Delta = B^2 > 0$$

(A90)

The solution in this case is written as follows:

$$\lambda_m^* = C_1 e^{r_1 z} + C_2 e^{r_2 z} \ \ (C_1, C_2 \in \mathbb{R})\ and\ (r_1 = 0, r_2 = -\beta_m\ are\ the\ equation\ roots)$$

$$\lambda_m^* = C_1 \left(1 + \frac{C_2}{C_1} e^{-\beta_m x_m^*}\right) \ \ (C_1, C_2 \in \mathbb{R}) \tag{A91}$$

For C_1 and C_2:

At x_m^* =0:

$$\lambda_a{}^* = 0.3 + 10.8\left(\frac{P_{H_2O}}{P_{sat}}\right) - 16\left(\frac{P_{H_2O}}{P_{sat}}\right)^2 + 14.1\left(\frac{P_{H_2O}}{P_{sat}}\right)^3 = C_1 + C_2 \quad \left(a_a = \frac{P_{H_2O}}{P_{sat}} = 0.5\right)$$

(A92)

At x_m^* = 1:

$$\lambda_c{}^* = 0.3 + 10.8\left(\frac{P_{H_2O}}{P_{sat}}\right) - 16\left(\frac{P_{H_2O}}{P_{sat}}\right)^2 + 14.1\left(\frac{P_{H_2O}}{P_{sat}}\right)^3 = C_1\left(1 + \frac{C_2}{C_1} e^{-\beta_m L_m}\right) \quad \left(a_c = \frac{P_{H_2O}}{P_{sat}} = 1\right)$$

(A93)

Therefore:

$$\begin{cases} C_1 = \lambda_a{}^* - \frac{\lambda_c{}^* - \lambda_a{}^*}{e^{-\beta_m} - 1} \\ C_2 = \frac{\lambda_c{}^* - \lambda_a{}^*}{e^{-\beta_m} - 1} \end{cases} \tag{A94}$$

The distribution of water content to the membrane is written as follows:

$$\lambda_m^* = C_1\left(1 + \frac{C_2}{C_1} e^{-\beta_m x_m^*}\right) \quad where \begin{cases} C_1 = \lambda_a{}^* - \frac{\lambda_c{}^* - \lambda_a{}^*}{e^{-\beta_m} - 1} \\ C_2 = \frac{\lambda_c{}^* - \lambda_a{}^*}{e^{-\beta_m} - 1} \end{cases}$$

(A95)

The dimensionless water content averaged to the membrane is:

$$\overline{\lambda_m^*} = \int_0^1 \lambda_m^*\, dx_m^*$$

$$= \int_0^1 C_1\left(1 + \frac{C_2}{C_1} e^{-\beta_m x_m^*}\right) dx_m^*$$

$$= \int_0^1 C_1\, dx_m^* + \int_0^1 C_2 e^{-\beta_m x_m^*}\, dx_m^*$$

$$= C_1 - \frac{C_2}{\beta_m}\left(e^{-\beta_m} - 1\right) \quad \text{(A96)}$$

The verification of the numerical results is needed in order to verify the accuracy of the model:

$$\frac{\partial \eta_t}{\partial \zeta_a} = \frac{\partial \eta_t}{\partial \beta_a}\frac{\partial \beta_a}{\partial \zeta_a}$$

$$\frac{\partial \eta_t}{\partial \zeta_a} = \frac{\partial(\overline{\eta^*_{act,a}} + \overline{\eta^*_{act,c}} + \overline{\eta^*_{m,ohm}})}{\partial \zeta_a}$$

$\overline{\eta^*_{act,c}}, \overline{\eta^*_{m,ohm}}$ are independent of ζ_a :

$$\frac{\partial \eta_t}{\partial \zeta_a} = \frac{\partial(\overline{\eta^*_{act,a}})}{\partial \zeta_a}$$

According to (A96), (A93), (A94) and (A60)

$$\frac{\partial \overline{\eta_t{}^*}}{\partial \zeta_a} = -\frac{1}{\zeta_a}$$

$$-\frac{\partial \zeta_a}{\partial \beta_a}\frac{1}{\zeta_a} = \frac{\partial \eta_t}{\partial \beta_{a,exp}}$$

$$-\frac{\partial ln\zeta_a}{\partial \beta_a} = \frac{\partial \eta_t}{\partial \beta_{a,exp}}$$

$\frac{\partial \eta_t}{\partial \beta_{a,exp}}$ is calculated using the experimental data from the EIL at UCL.

$$-\frac{ln{\zeta_a}^{n+1} - ln{\zeta_a}^{n}}{{\beta_a}^{n+1} - {\beta_a}^{n}} = \frac{{\eta_t}^{n+1} - {\eta_t}^{n}}{{\beta_{a,exp}}^{n+1} - {\beta_{a,exp}}^{n}}$$

$$ln{\zeta_a}^{n+1} - ln{\zeta_a}^{n} = \frac{{\eta_t}^{n+1} - {\eta_t}^{n}}{{\beta_{a,exp}}^{n+1} - {\beta_{a,exp}}^{n}}(-{\beta_a}^{n+1} + {\beta_a}^{n})$$

$$ln{\zeta_a}^{n+1} = \frac{{\eta_t}^{n+1} - {\eta_t}^{n}}{{\beta_{a,exp}}^{n+1} - {\beta_{a,exp}}^{n}}\left(-{\beta_a}^{n+1} + {\beta_a}^{n}\right) + ln{\zeta_a}^{n}$$

$${\zeta_a}^{n+1} = \exp\left(\left(\frac{{\eta_t}^{n+1} - {\eta_t}^{n}}{{\beta_{a,exp}}^{n+1} - {\beta_{a,exp}}^{n}}\right)\left(-{\beta_a}^{n+1} + {\beta_a}^{n}\right) + ln{\zeta_a}^{n}\right)$$

Results at low pressure:

ω_a	β_a
$7.768260411916915.10^{-4}$	0.028315864
$2.8738075404688884.10^{-6}$	0.054453584
$1.3583974735736218.10^{-7}$	0.080591304
$1.6416666888119432.10^{-8}$	0.106729024
$2.43588005864023.10^{-9}$	0.132866745
$4.796971475358472.10^{-10}$	0.159004465
$7.469698037543124.10^{-11}$	0.185142185
$1.3364594298190756.10^{-11}$	0.211279905
$2.300656164056259.10^{-12}$	0.237417625

APPENDIX B: Polymer Electrolyte Membrane Cells Experimental Application: Electrochemical hydrogen compression

Conductivity measurement Setup (Cell components)

Electrochemical Hydrogen Compression: Pressure Variation for Different RH & Temperature

Pressure Variation for Different RH & Temperature: Pure H_2

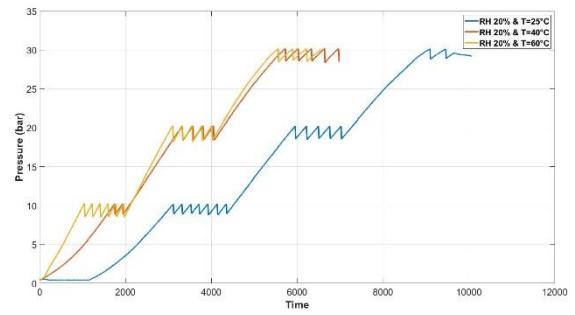

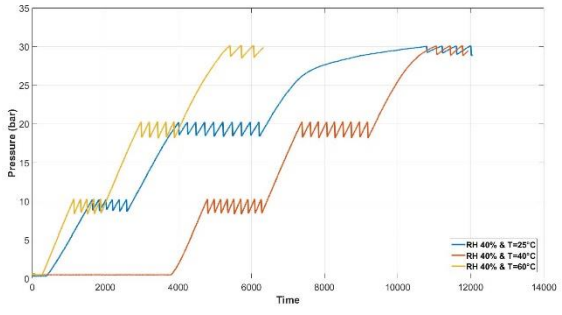

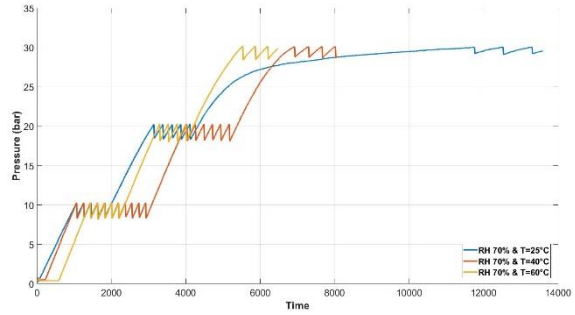

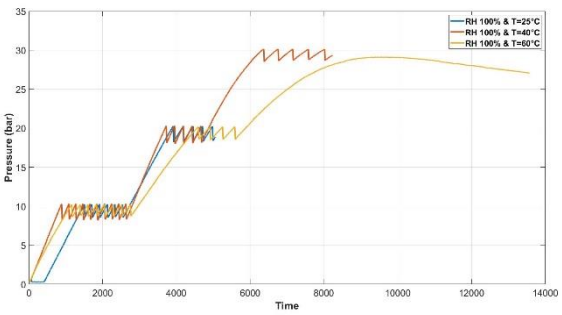

Pressure Variation for Different RH & Temperature:

H_2 gas mixture (75% H_2 & 25% N_2)

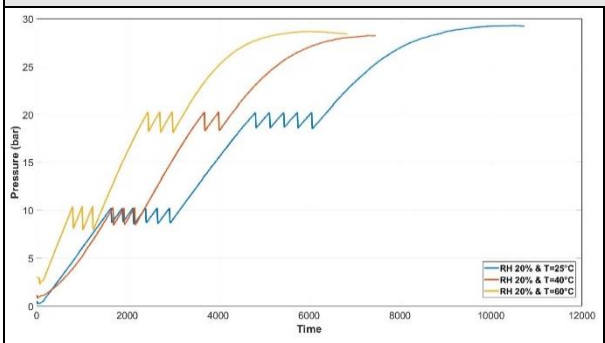

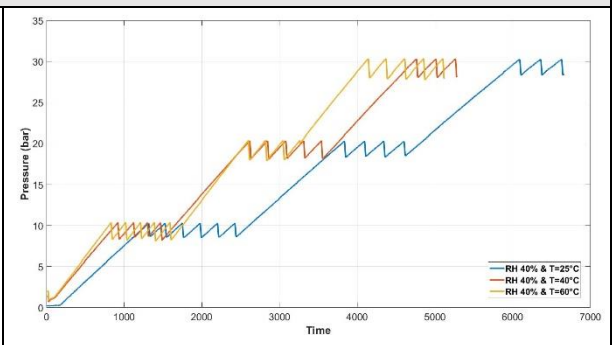

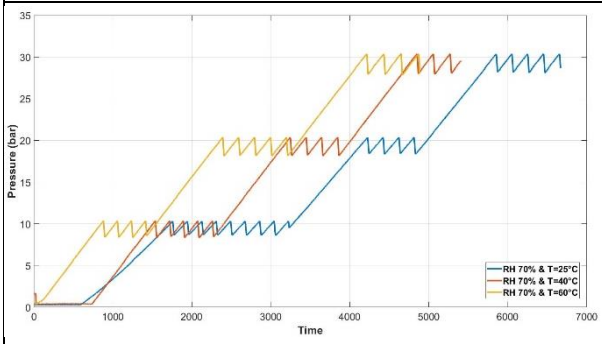

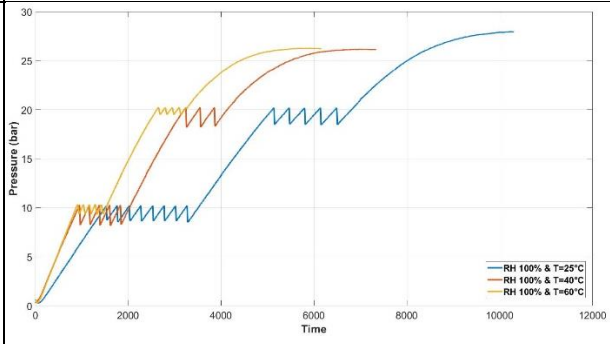

Electrochemical Hydrogen Compression: Current & Voltage Variation for Different RH & Temperature

Current & Voltage Variation for Different RH & Temperature: Pure H_2

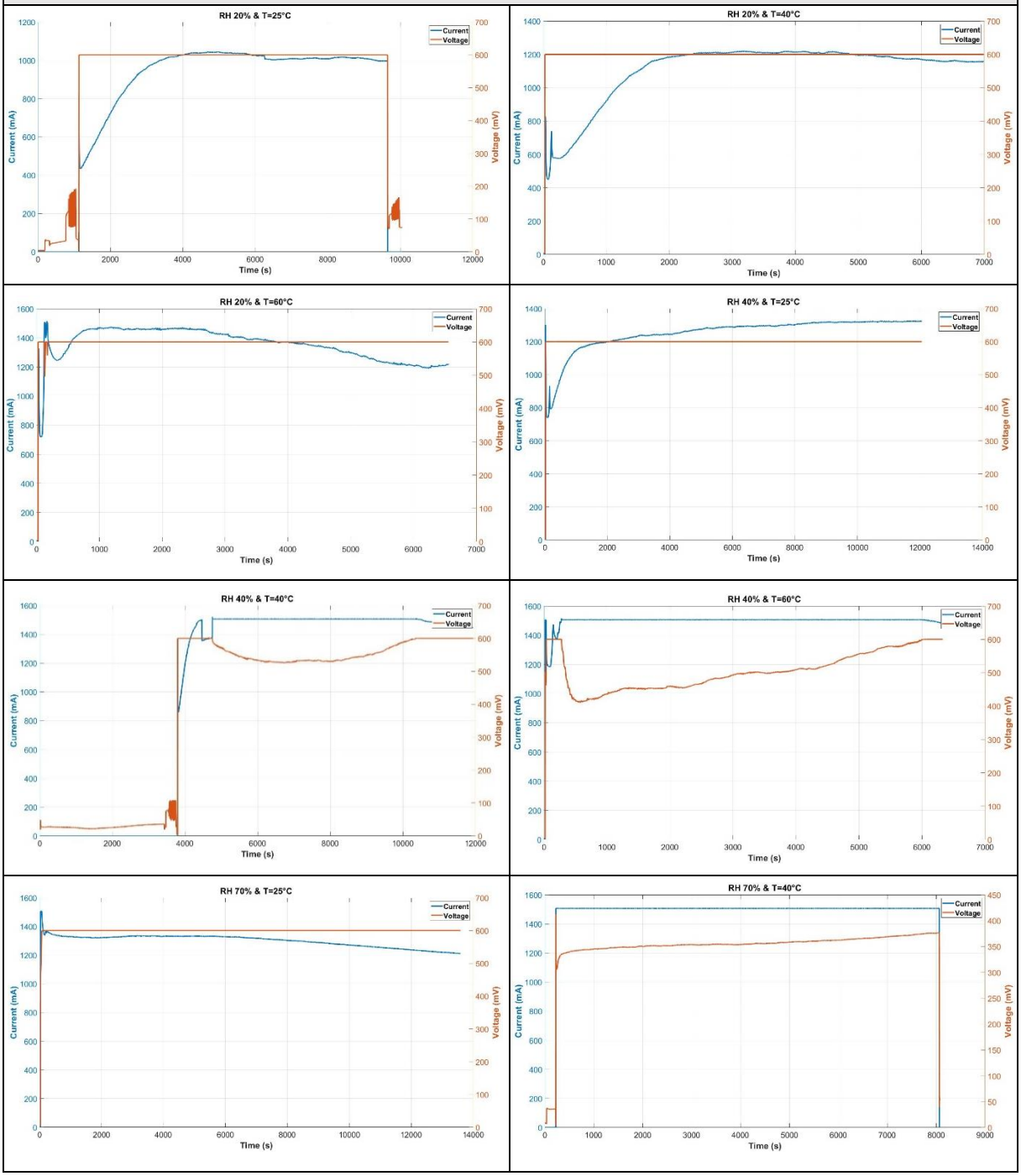

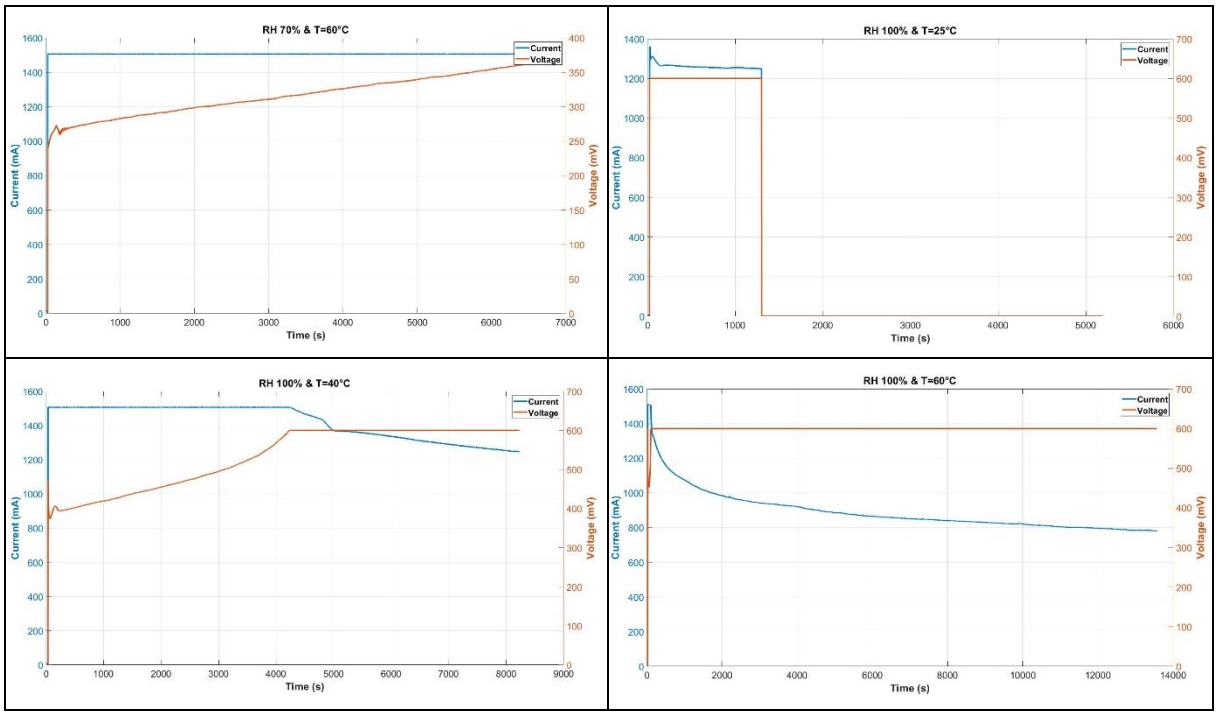

Current & Voltage Variation for Different RH & Temperature:

H_2 gas mixture (75% H_2 & 25% N_2)

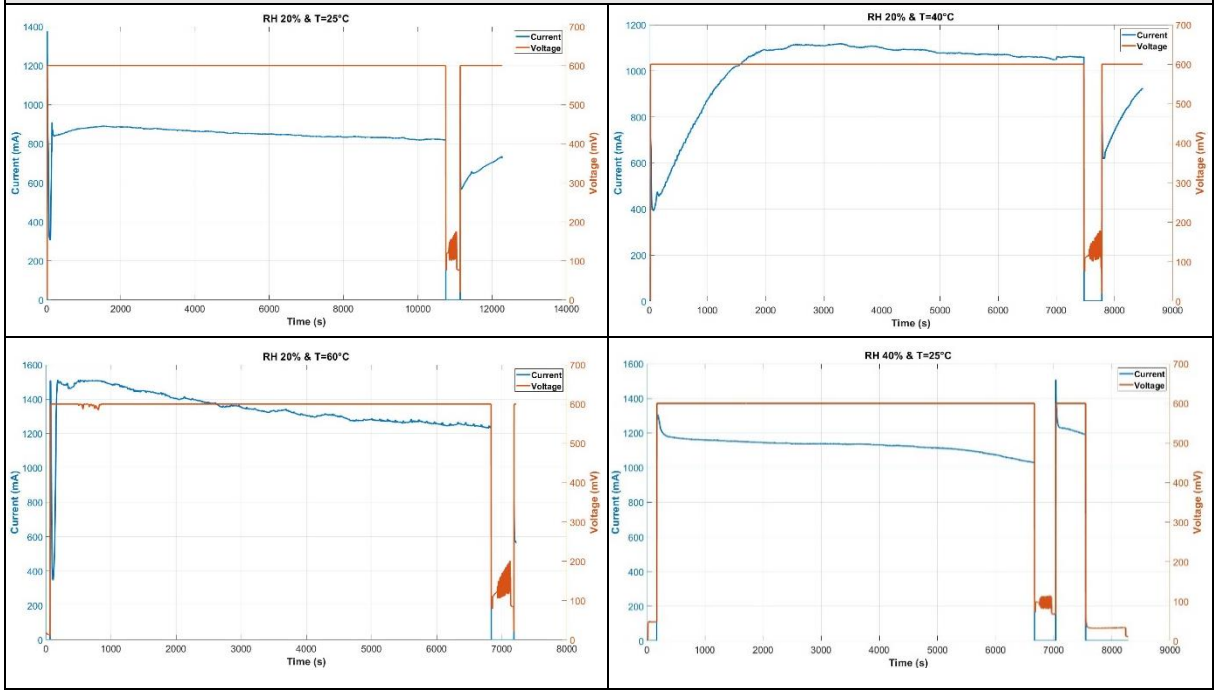

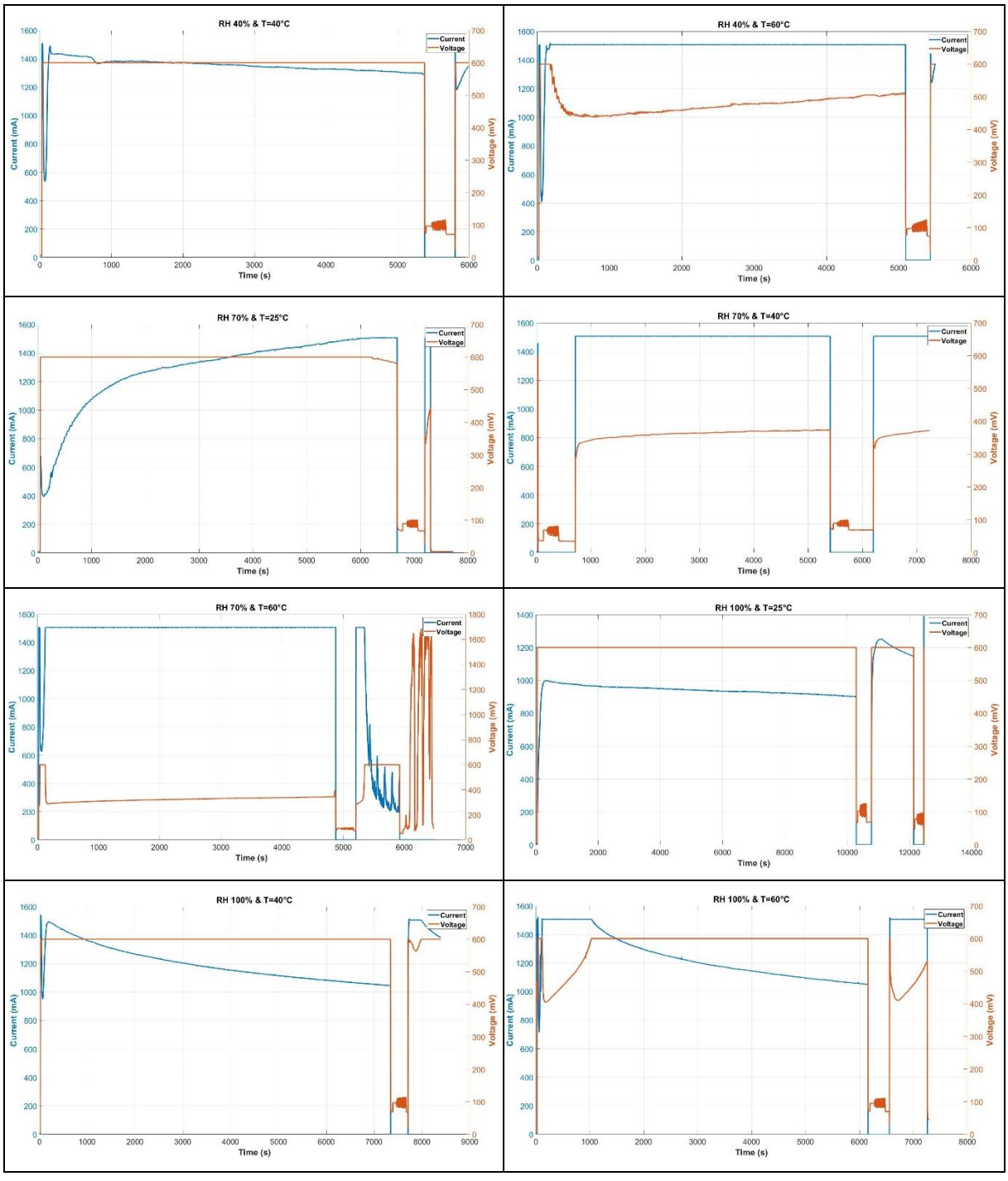
RH 40% & T=40°C
RH 40% & T=60°C
RH 70% & T=25°C
RH 70% & T=40°C
RH 70% & T=60°C
RH 100% & T=25°C
RH 100% & T=40°C
RH 100% & T=60°C
Current
Voltage
Current (mA)
Voltage (mV)
Time (s)

Electrochemical Hydrogen Compression: Electrochemical Impedance Spectroscopy (EIS) for Different RH & Temperature

Electrochemical Impedance Spectroscopy
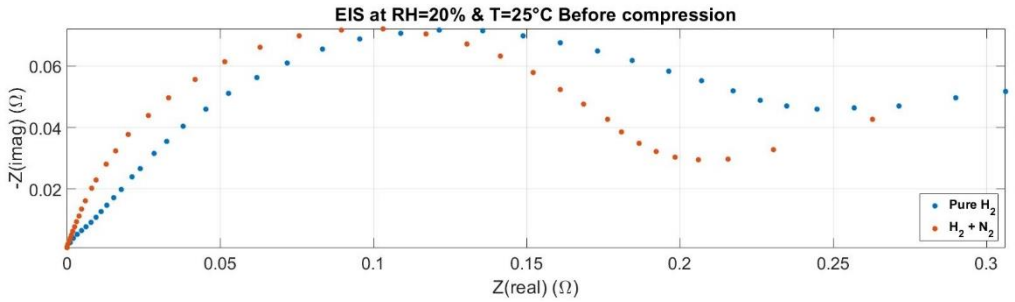
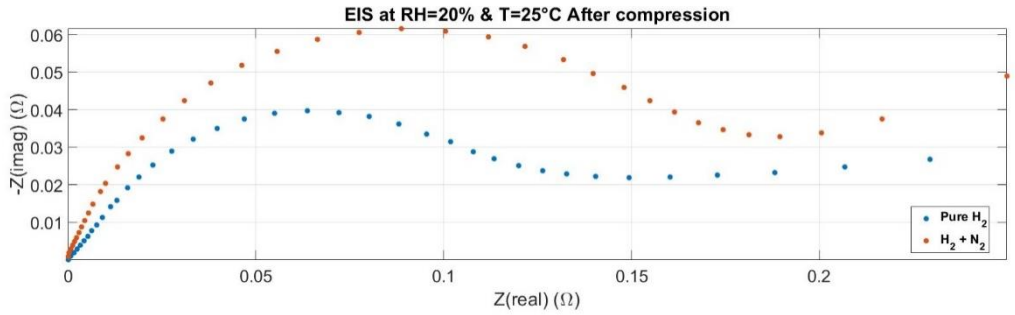
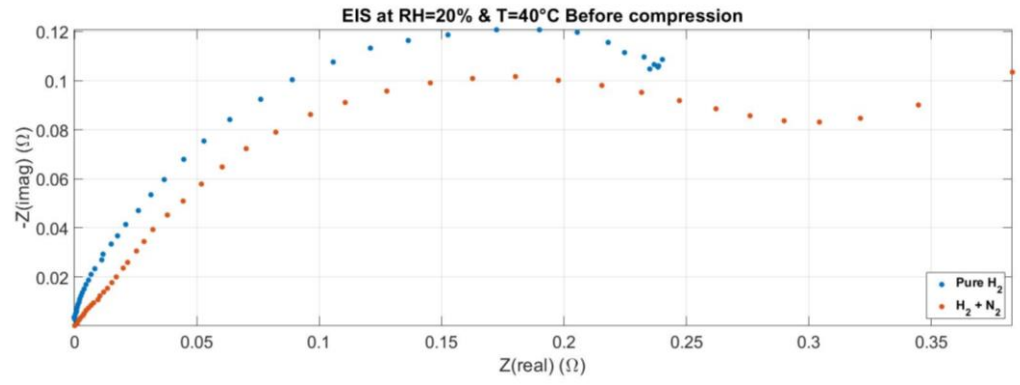

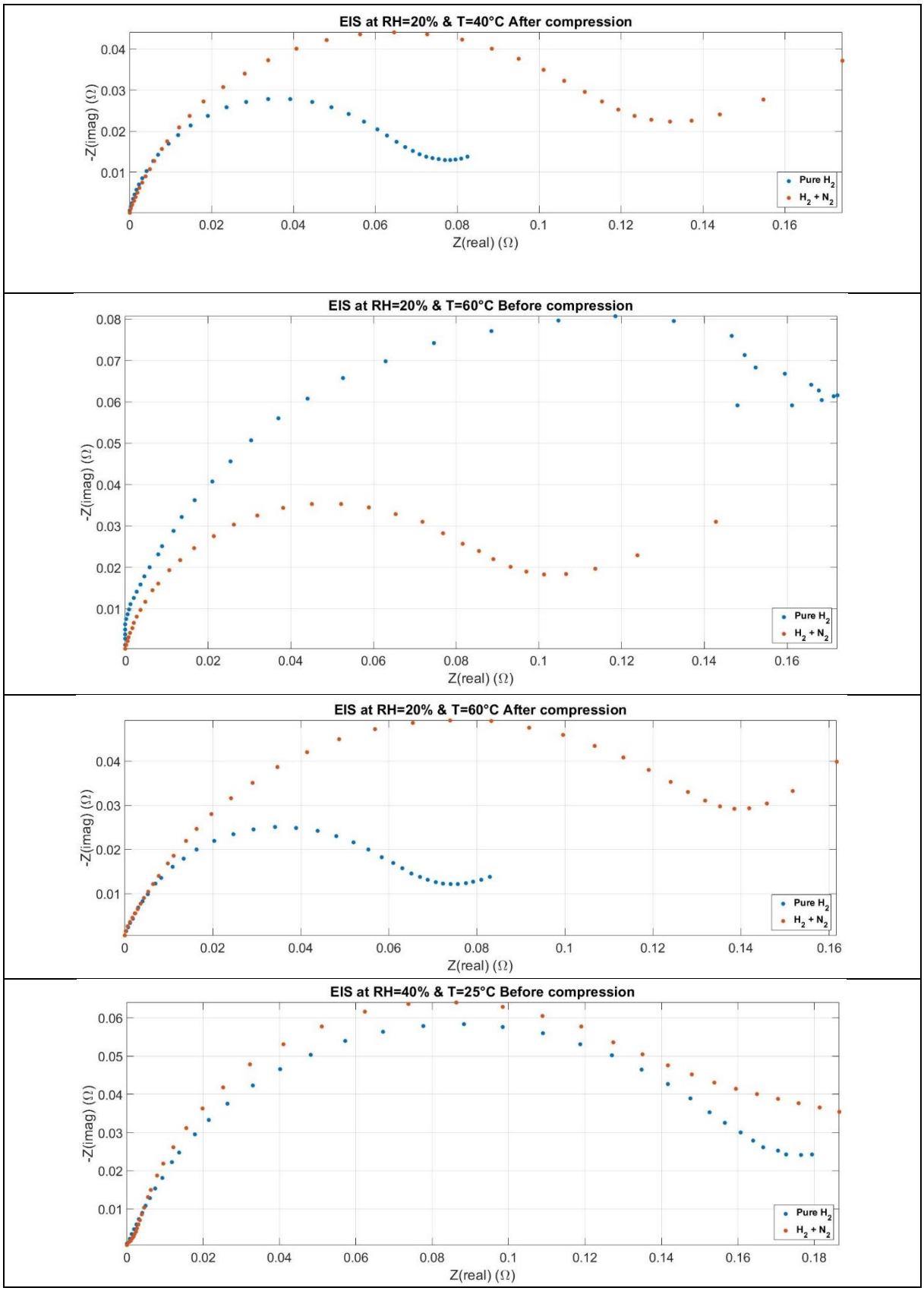
EIS at RH=20% & T=40°C After compression
-Z(imag) (Ω)
Z(real) (Ω)
Pure H2
H2 + N2
EIS at RH=20% & T=60°C Before compression
-Z(imag) (Ω)
Z(real) (Ω)
Pure H2
H2 + N2
EIS at RH=20% & T=60°C After compression
-Z(imag) (Ω)
Z(real) (Ω)
Pure H2
H2 + N2
EIS at RH=40% & T=25°C Before compression
-Z(imag) (Ω)
Z(real) (Ω)
Pure H2
H2 + N2

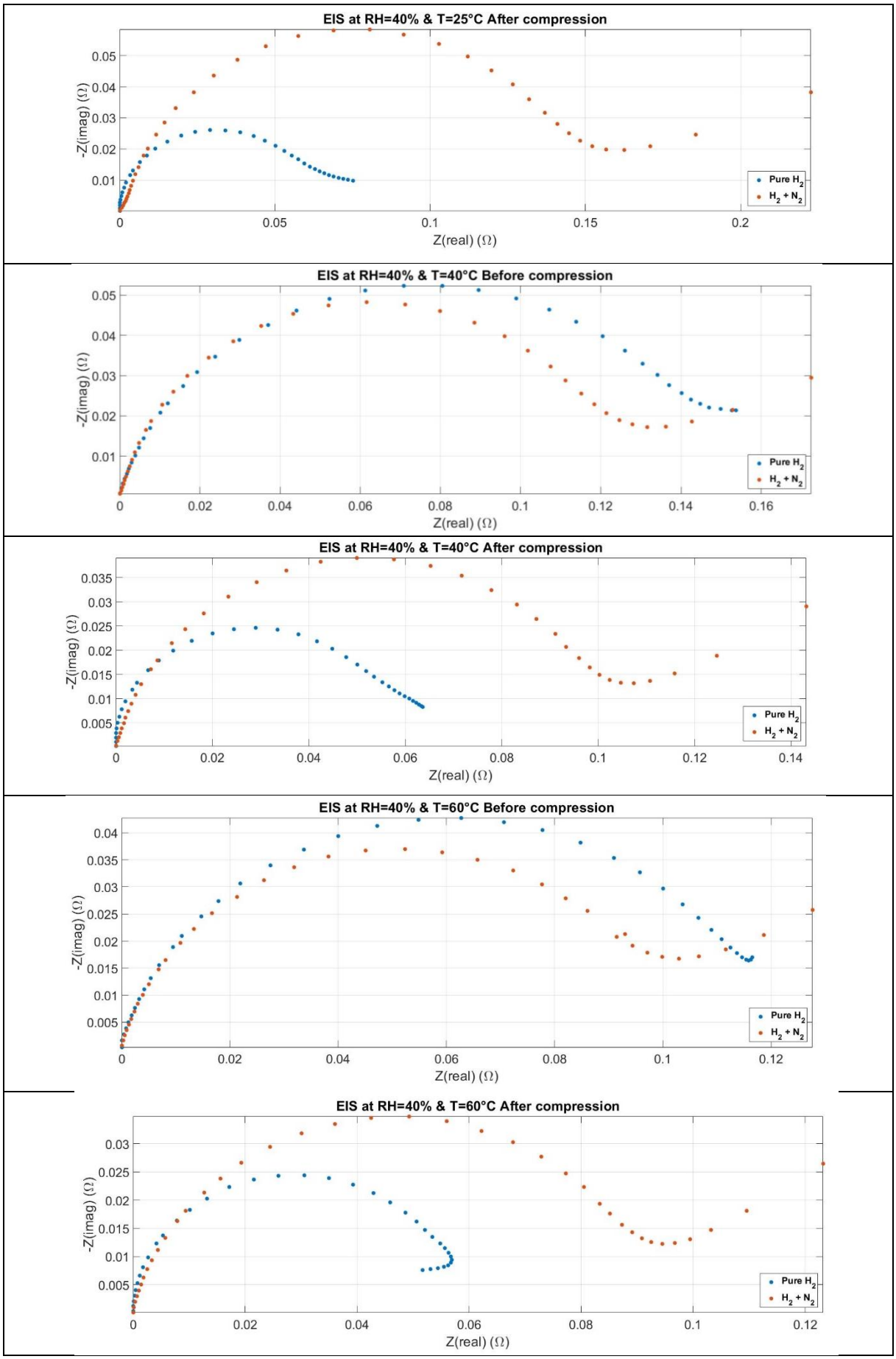
EIS at RH=40% & T=25°C After compression
-Z(imag) (Ω)
Z(real) (Ω)
Pure H2
H2 + N2
EIS at RH=40% & T=40°C Before compression
-Z(imag) (Ω)
Z(real) (Ω)
Pure H2
H2 + N2
EIS at RH=40% & T=40°C After compression
-Z(imag) (Ω)
Z(real) (Ω)
Pure H2
H2 + N2
EIS at RH=40% & T=60°C Before compression
-Z(imag) (Ω)
Z(real) (Ω)
Pure H2
H2 + N2
EIS at RH=40% & T=60°C After compression
-Z(imag) (Ω)
Z(real) (Ω)
Pure H2
H2 + N2

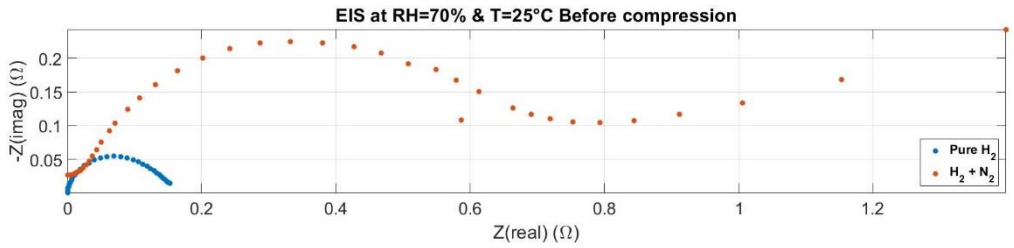
EIS at RH=70% & T=25°C Before compression
-Z(imag) (Ω)
Z(real) (Ω)
Pure H2
H2 + N2

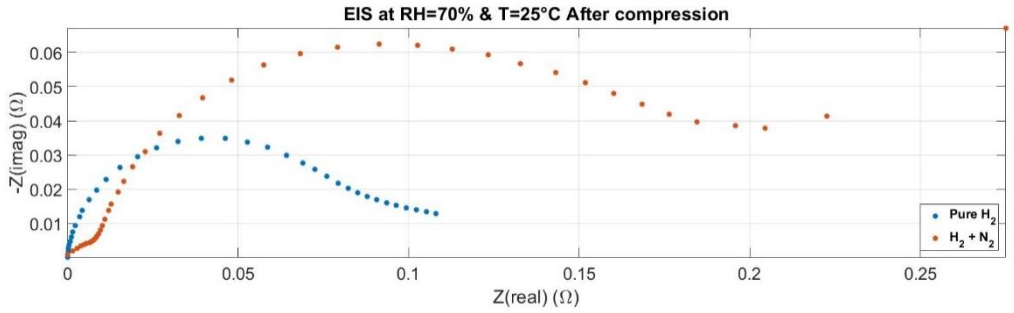
EIS at RH=70% & T=25°C After compression
-Z(imag) (Ω)
Z(real) (Ω)
Pure H2
H2 + N2

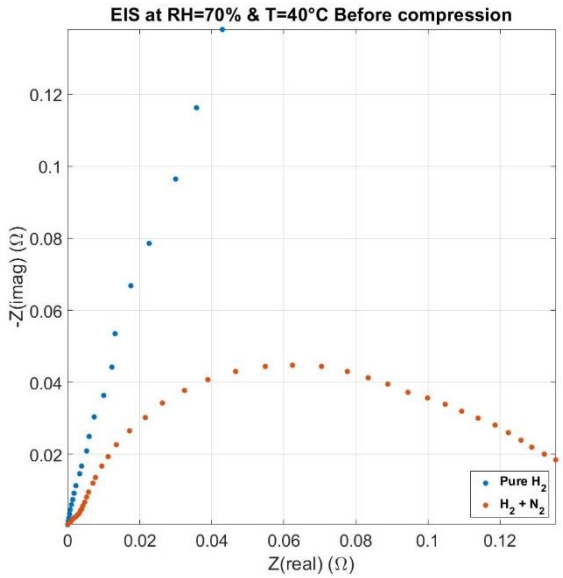
EIS at RH=70% & T=40°C Before compression
-Z(imag) (Ω)
Z(real) (Ω)
Pure H2
H2 + N2

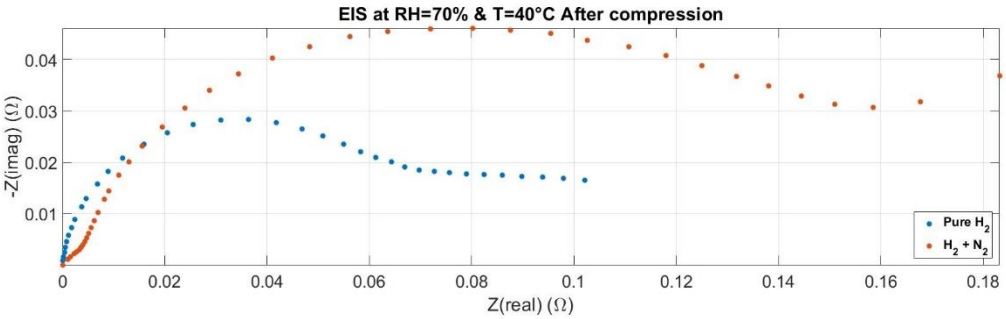
EIS at RH=70% & T=40°C After compression
-Z(imag) (Ω)
Z(real) (Ω)
Pure H2
H2 + N2

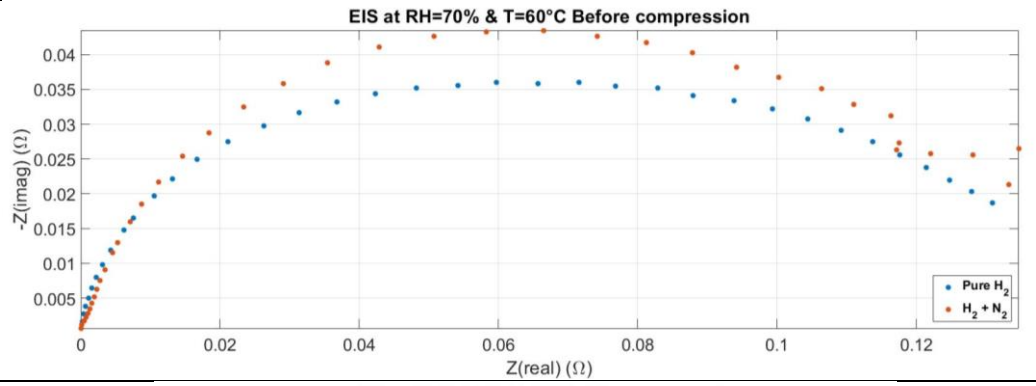
EIS at RH=70% & T=60°C Before compression
-Z(imag) (Ω)
Z(real) (Ω)
Pure H2
H2 + N2

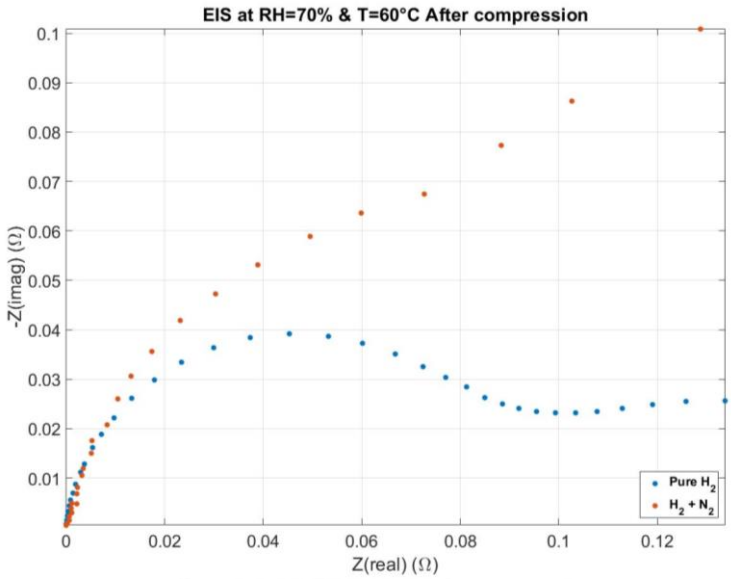
EIS at RH=70% & T=60°C After compression
-Z(imag) (Ω)
Z(real) (Ω)
Pure H2
H2 + N2

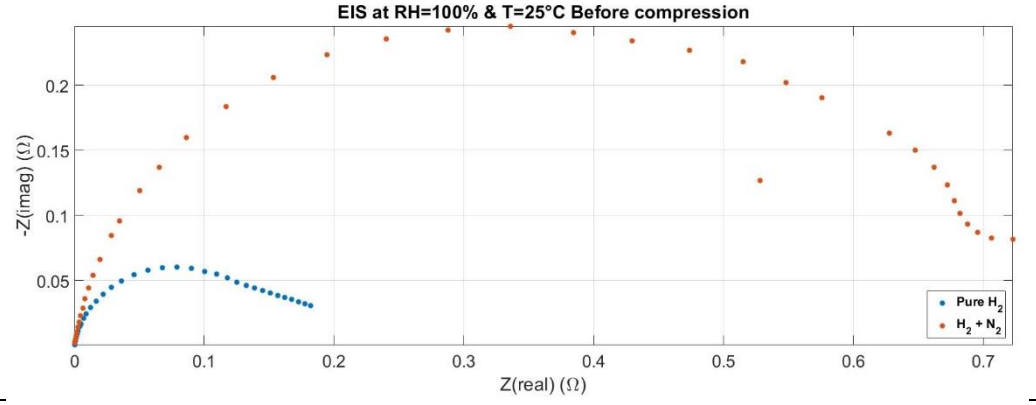
EIS at RH=100% & T=25°C Before compression
-Z(imag) (Ω)
Z(real) (Ω)
Pure H2
H2 + N2

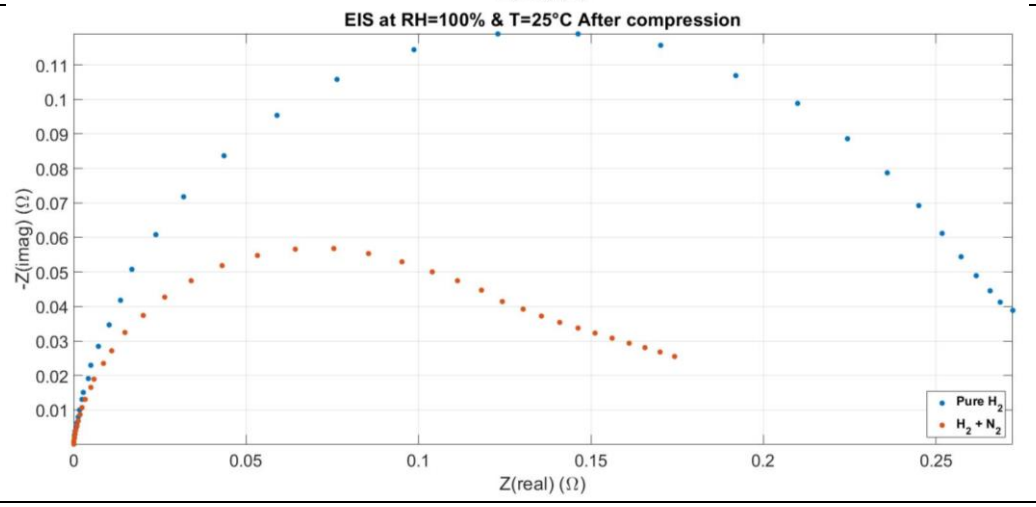
EIS at RH=100% & T=25°C After compression
-Z(imag) (Ω)
Z(real) (Ω)
Pure H2
H2 + N2

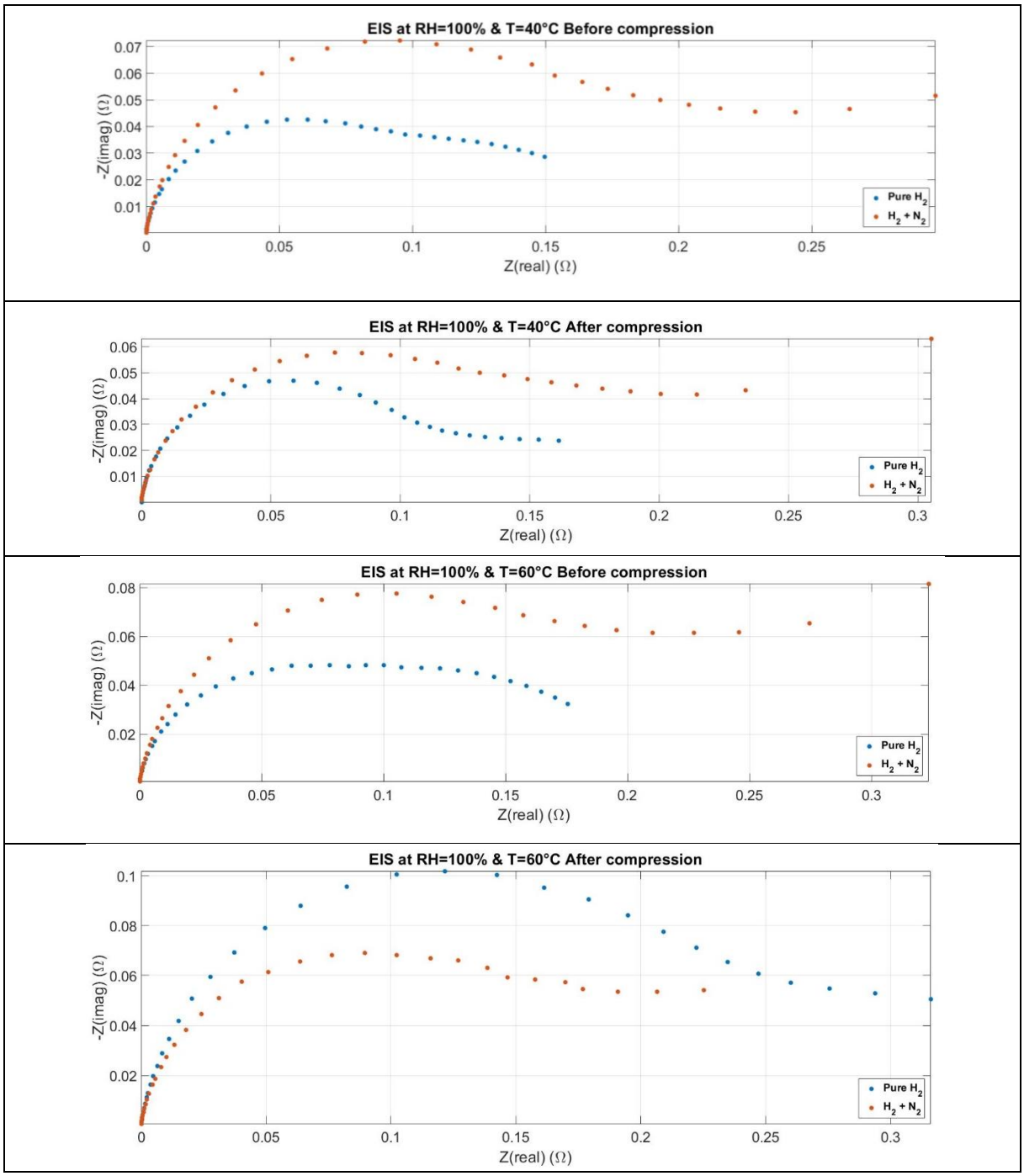
EIS at RH=100% & T=40°C Before compression
-Z(imag) (Ω)
Z(real) (Ω)
Pure H2
H2 + N2
EIS at RH=100% & T=40°C After compression
-Z(imag) (Ω)
Z(real) (Ω)
Pure H2
H2 + N2
EIS at RH=100% & T=60°C Before compression
-Z(imag) (Ω)
Z(real) (Ω)
Pure H2
H2 + N2
EIS at RH=100% & T=60°C After compression
-Z(imag) (Ω)
Z(real) (Ω)
Pure H2
H2 + N2

Scanning Electron Microscope (SEM) Images

(1) Membrane N117 clear & clean & unused

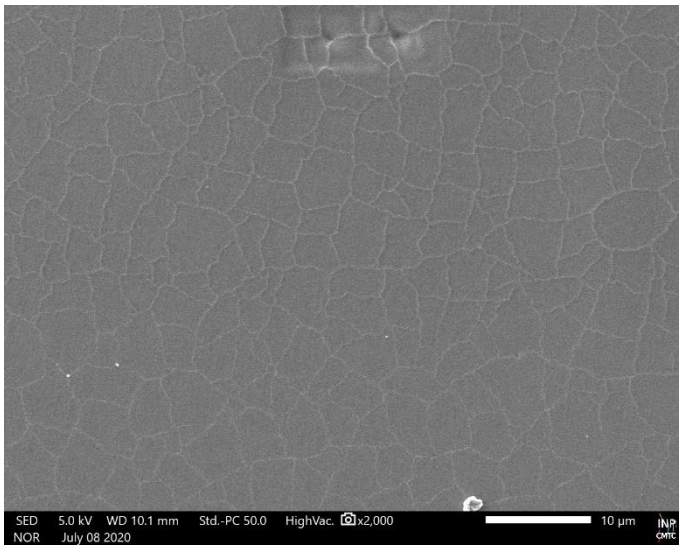

(2) Membrane N117 clear & Dipped in Liquid NH_3

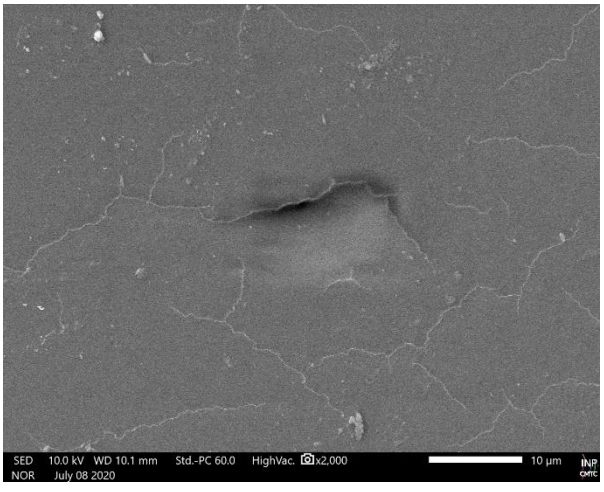

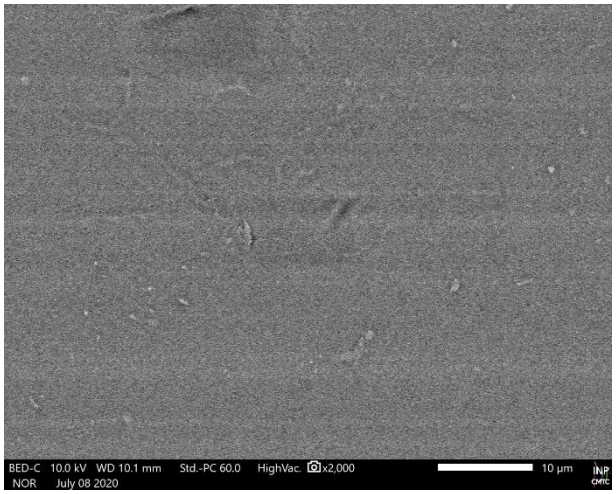

(3) Membrane N117 coated used for separation experiments (Ammonia 3000PPM)

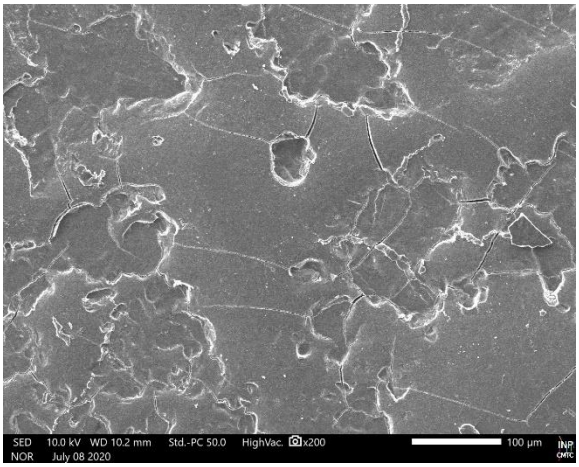

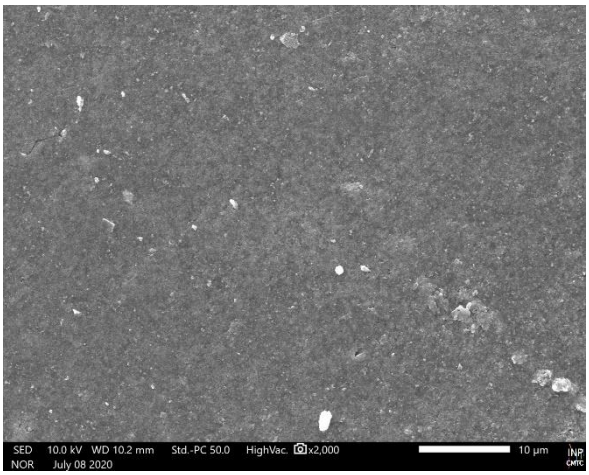

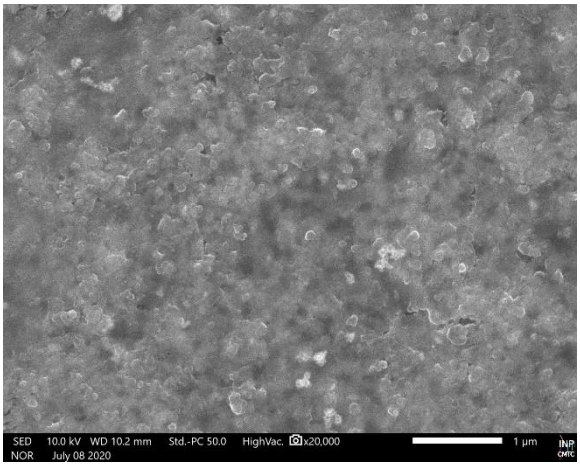

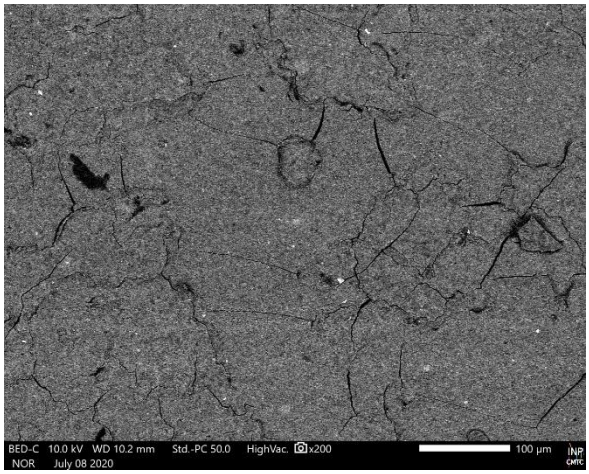

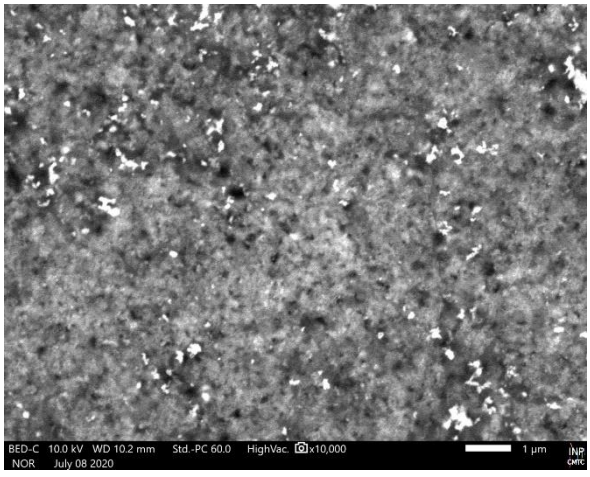

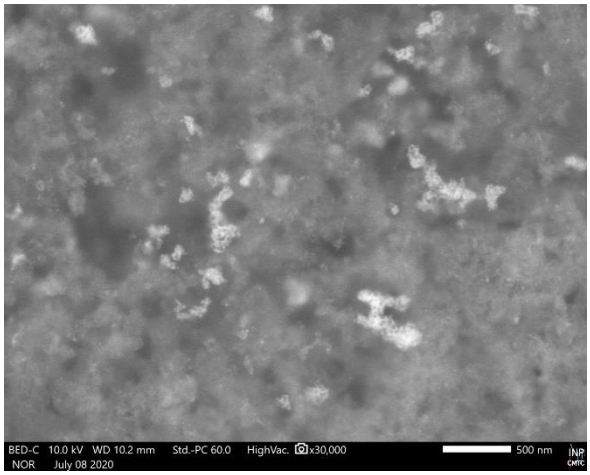

(4) Membrane N117 coated & clean & unused

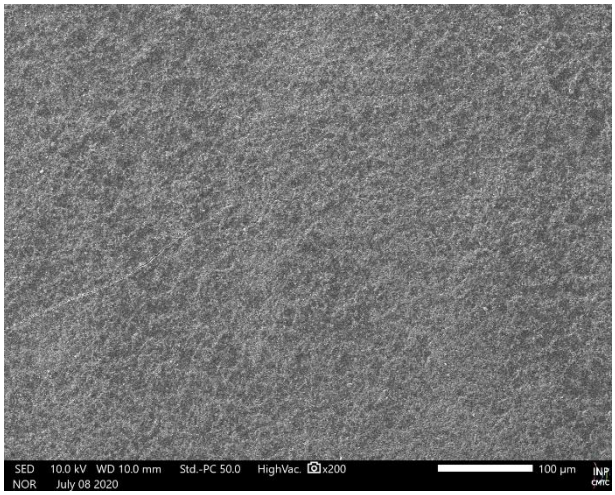

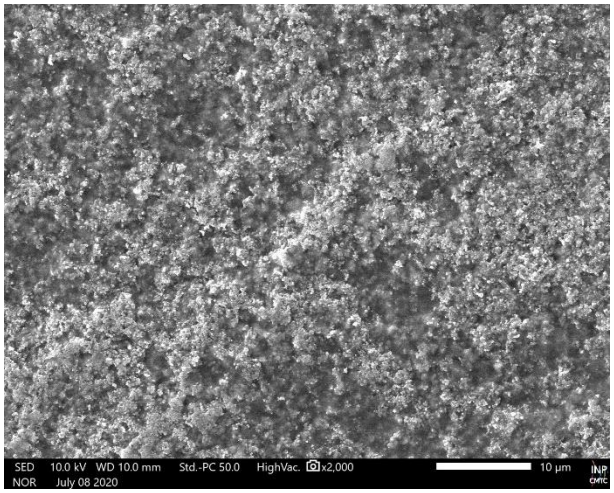

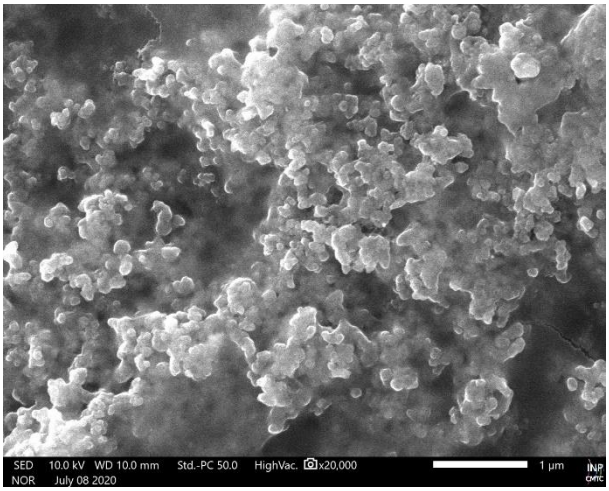

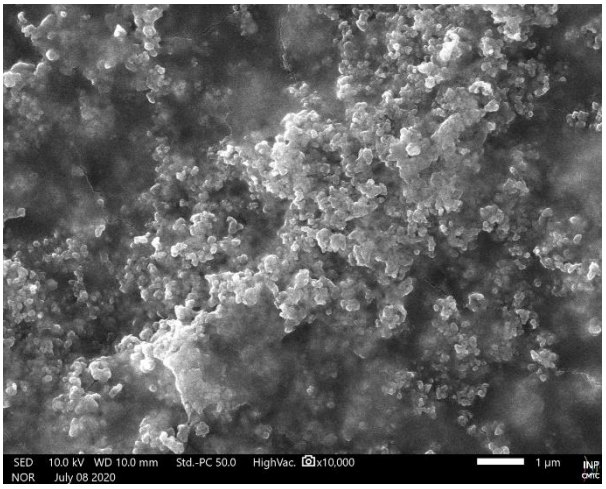

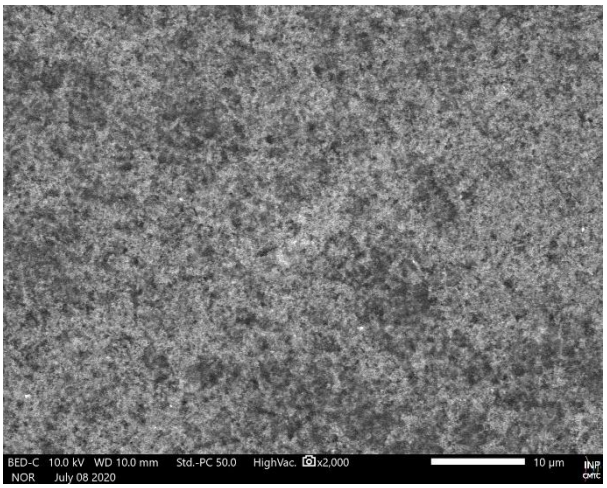

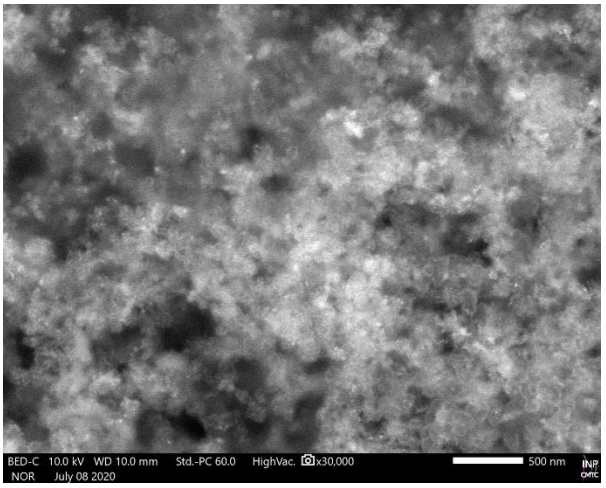

(5) Membrane N1110 clear & clean & unused

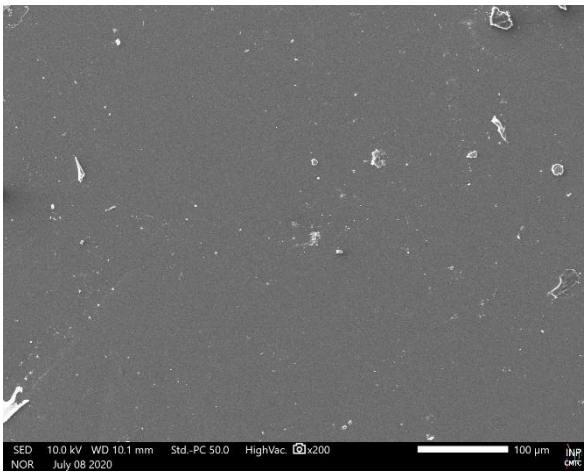

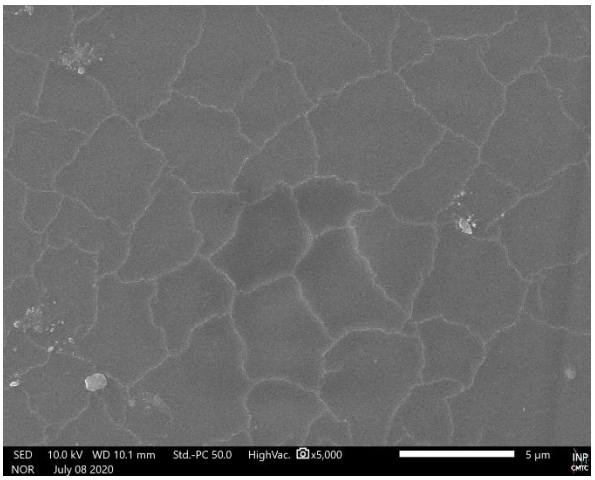

(6) Membrane N1110 clear & Dipped in Liquid NH_3

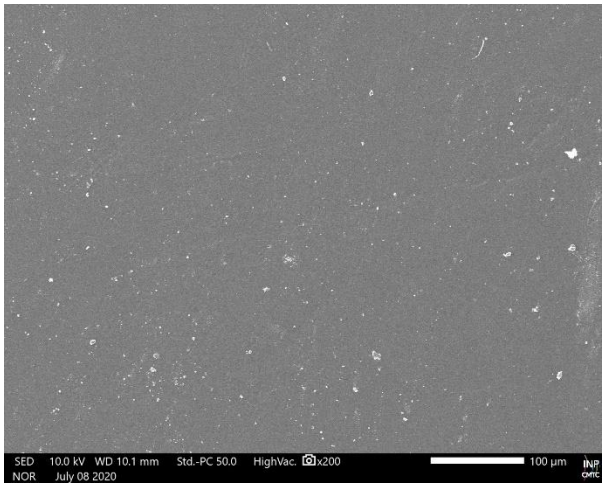

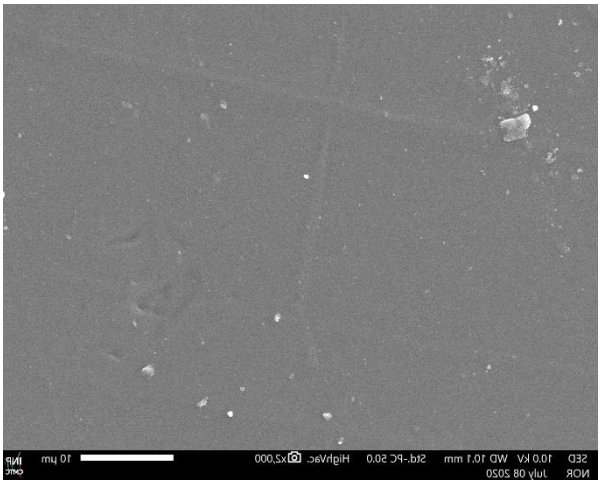

(7) Membrane N1110 used for compression/separation (pure H_2, 75%, 1%)

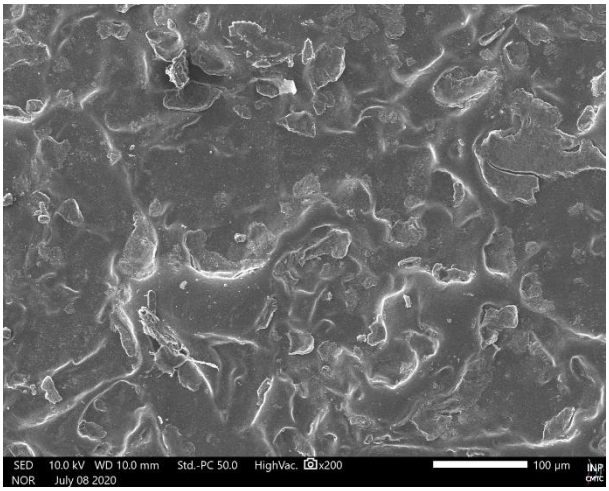

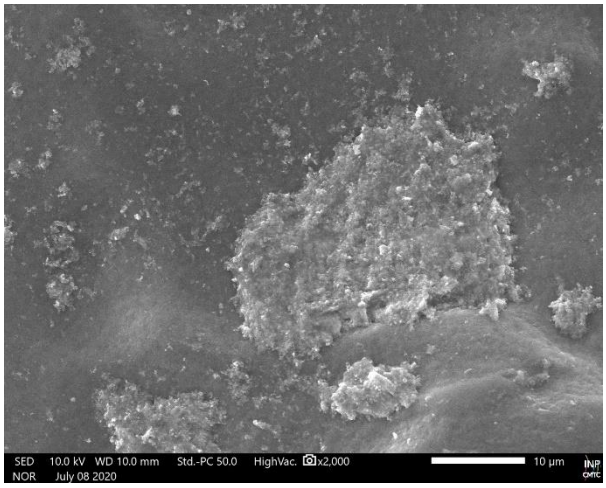

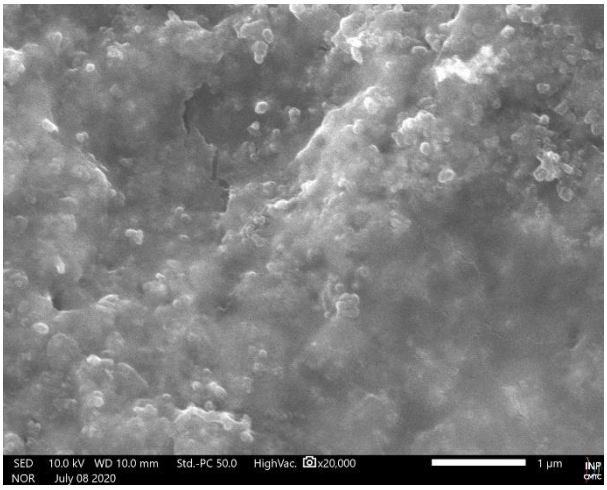

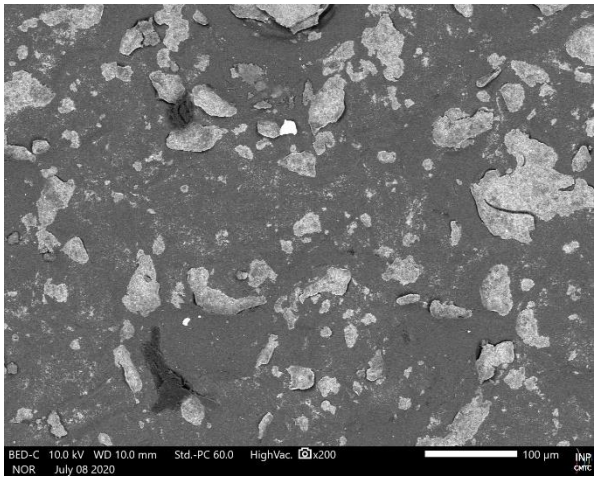

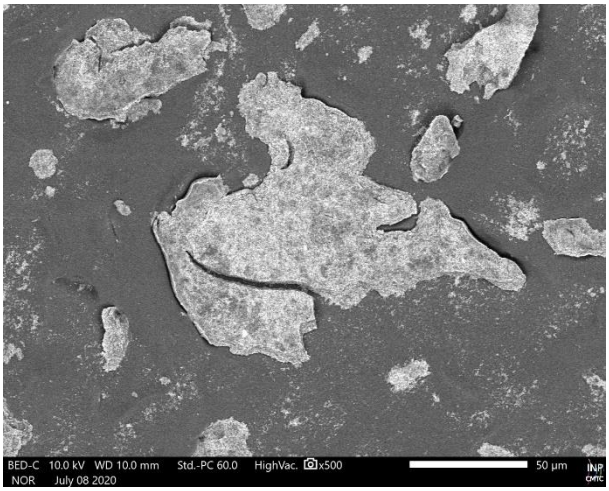

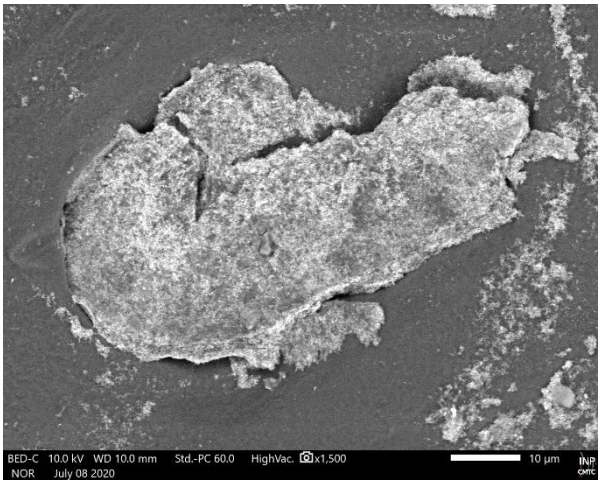

(8) Membrane N1110 coated used for compression/separation (75% H_2)

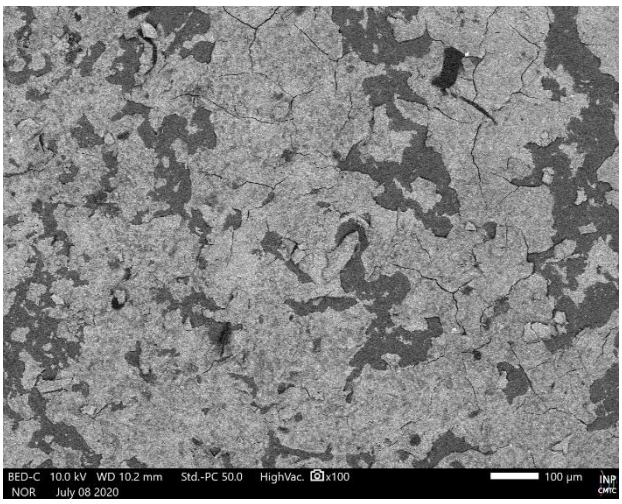

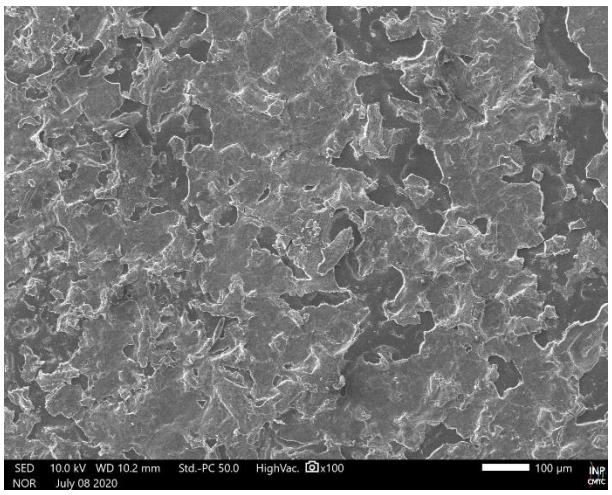

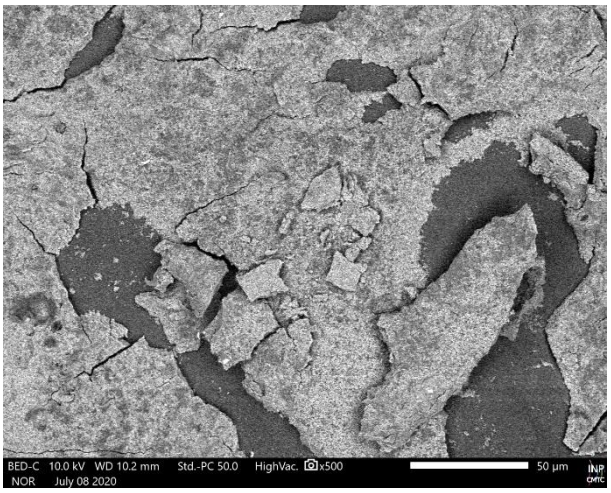

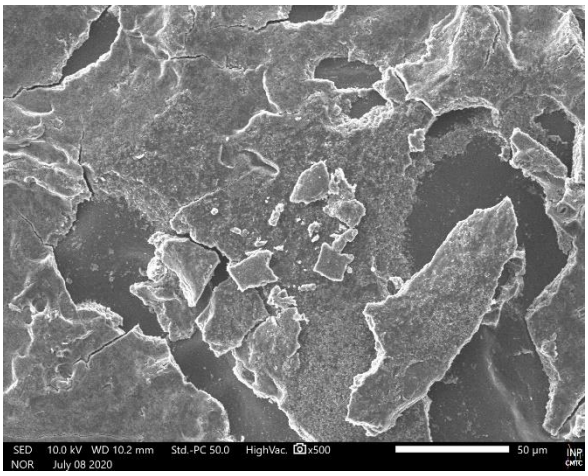

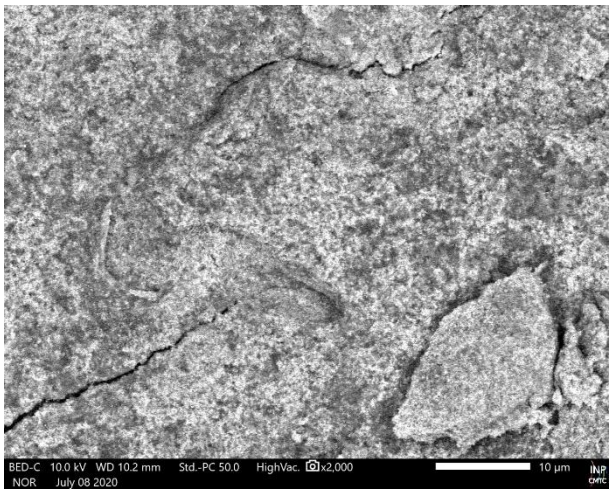

(9) Membrane N1110 coated & clean & unused

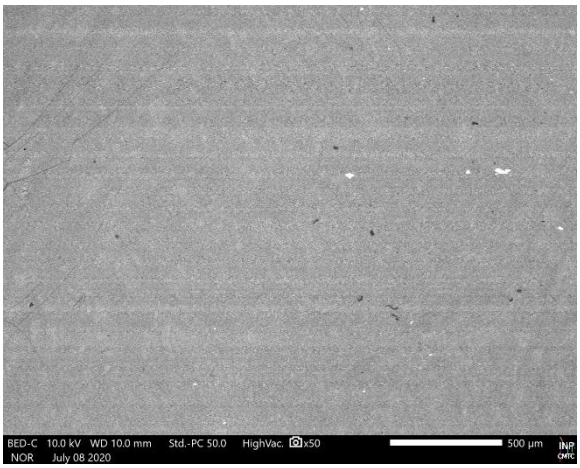

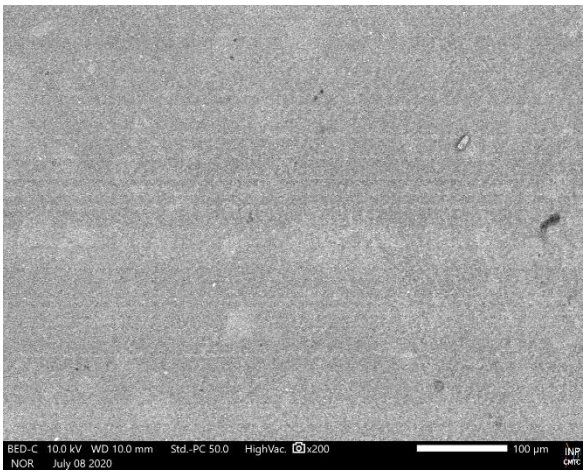

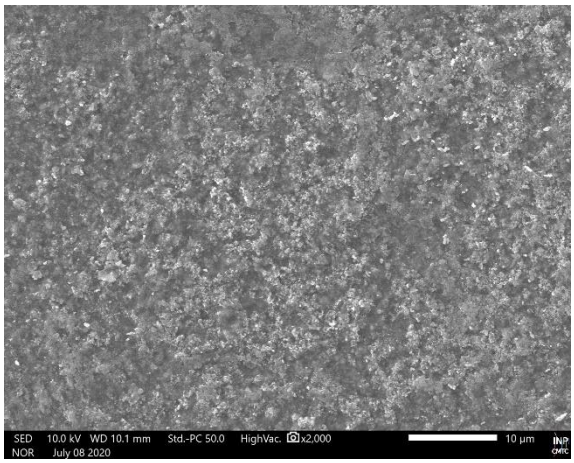

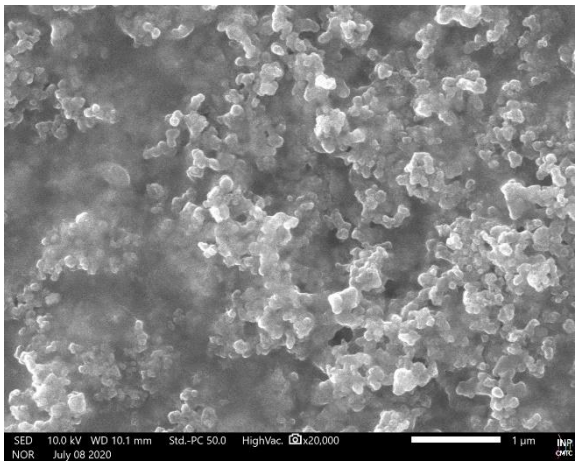

Wagner number: Compression Pure H_2

% RH=20% & T=25°C

	w_a	w_c	f_{val}
Pressure < 12	7.272×10^{-16}	1.114×10^{-3}	545.074
12 < Pressure < 22	1.501×10^{-15}	1.343×10^{-3}	1.729
22 < Pressure	1.585×10^{-15}	1.378×10^{-3}	1.097

% RH=20% & T=40°C

	w_a	w_c	f_{val}
Pressure < 12	9.859×10^{-16}	1.151×10^{-3}	56.850
12 < Pressure < 22	2.008×10^{-15}	1.401×10^{-3}	1.644
22 < Pressure	2.027×10^{-15}	1.411×10^{-3}	1.736

% RH=20% & T=60°C

	w_a	w_c	f_{val}
Pressure < 12	2.954×10^{-15}	1.113×10^{-3}	27.806
12 < Pressure < 22	3.070×10^{-15}	1.133×10^{-3}	2.716
22 < Pressure	2.343×10^{-15}	1.197×10^{-3}	4.986

% RH=40% & T=25°C

	w_a	w_c	f_{val}
Pressure < 12	1.405×10^{-15}	1.110×10^{-3}	35.739
12 < Pressure < 22	1.933×10^{-15}	1.216×10^{-3}	4.991
22 < Pressure	2.274×10^{-15}	1.298×10^{-3}	3.706

% RH=40% & T=40°C

	w_a	w_c	f_{val}
Pressure < 12	5.098×10^{-15}	1.203×10^{-3}	52.514
12 < Pressure < 22	9.188×10^{-15}	1.385×10^{-3}	10.785
22 < Pressure	2.724×10^{-15}	1.535×10^{-3}	6.451

% RH=40% & T=60°C

	w_a	w_c	f_{val}
Pressure < 12	3.178×10^{-14}	1.136×10^{-3}	48.180
12 < Pressure < 22	1.566×10^{-14}	1.319×10^{-3}	11.813
22 < Pressure	4.594×10^{-15}	1.462×10^{-3}	23.609

% RH=70% & T=25°C

	w_a	w_c	f_{val}
Pressure < 12	1.774×10^{-15}	1.118×10^{-3}	17.582
12 < Pressure < 22	2.122×10^{-15}	1.149×10^{-3}	1.546
22 < Pressure	2.109×10^{-15}	1.192×10^{-3}	13.624

% RH=70% & T=40°C

	w_a	w_c	f_{val}
Pressure < 12	2.409×10^{-13}	1.101×10^{-3}	3.618
12 < Pressure < 22	2.462×10^{-13}	1.139×10^{-3}	1.913
22 < Pressure	2.206×10^{-13}	1.193×10^{-3}	15.051

% RH=70% & T=60°C

	w_a	w_c	f_{val}
Pressure < 12	4.313×10^{-13}	1.103×10^{-3}	23.374
12 < Pressure < 22	3.368×10^{-13}	1.188×10^{-3}	5.382
22 < Pressure	2.183×10^{-13}	1.324×10^{-3}	6.913

% RH=100% & T=40°C

	w_a	w_c	f_{val}
Pressure < 12	4.401×10^{-14}	1.165×10^{-3}	52.134
12 < Pressure < 22	4.163×10^{-15}	1.338×10^{-3}	39.134
22 < Pressure	1.824×10^{-15}	1.475×10^{-3}	4.519

% RH=100% & T=60°C

	w_a	w_c	f_{val}
Pressure < 12	7.874×10^{-16}	1.123×10^{-3}	27.429
12 < Pressure < 22	6.878×10^{-16}	1.179×10^{-3}	2.963
22 < Pressure	6.021×10^{-16}	1.260×10^{-3}	11.478

Wagner number: Compression/Separation H_2/N_2

% RH=20% & T=25°C

	w_a	w_c	f_{val}
Pressure < 12	1.005×10^{-15}	1.136×10^{-3}	14.427
12 < Pressure < 22	1.071×10^{-15}	1.172×10^{-3}	1.083
22 < Pressure	1.083×10^{-15}	1.184×10^{-3}	1.198

% RH=20% & T=40°C

	w_a	w_c	f_{val}
Pressure < 12	1.076×10^{-15}	1.132×10^{-3}	58.811
12 < Pressure < 22	1.816×10^{-15}	1.282×10^{-3}	1.136
22 < Pressure	1.789×10^{-15}	1.305×10^{-3}	1.161

% RH=20% & T=60°C

	w_a	w_c	f_{val}
Pressure < 12	5.905×10^{-15}	1.214×10^{-3}	46.812
12 < Pressure < 22	5.387×10^{-15}	1.297×10^{-3}	2.851
22 < Pressure	4.443×10^{-15}	1.341×10^{-3}	4.592

% RH=40% & T=25°C

	w_a	w_c	f_{val}
Pressure < 12	1.465×10^{-15}	1.119×10^{-3}	78.901
12 < Pressure < 22	1.620×10^{-15}	1.175×10^{-3}	1.088
22 < Pressure	1.575×10^{-15}	1.213×10^{-3}	1.621

% RH=40% & T=40°C

	w_a	w_c	f_{val}
Pressure < 12	2.379×10^{-15}	1.110×10^{-3}	19.579
12 < Pressure < 22	2.536×10^{-15}	1.190×10^{-3}	0.965
22 < Pressure	2.579×10^{-15}	1.213×10^{-3}	0.453

% RH=40% & T=60°C

	w_a	w_c	f_{val}
Pressure < 12	3.891×10^{-14}	1.147×10^{-3}	41.243
12 < Pressure < 22	3.023×10^{-14}	1.241×10^{-3}	4.157
22 < Pressure	2.142×10^{-14}	1.312×10^{-3}	5.721

% RH=70% & T=25°C

	w_a	w_c	f_{val}
Pressure < 12	1.649×10^{-15}	1.104×10^{-3}	73.339
12 < Pressure < 22	2.635×10^{-15}	1.249×10^{-3}	2.798
22 < Pressure	3.281×10^{-15}	1.321×10^{-3}	3.971

% RH=70% & T=40°C

	w_a	w_c	f_{val}
Pressure < 12	2.261×10^{-13}	1.141×10^{-3}	439.266
12 < Pressure < 22	2.226×10^{-13}	1.154×10^{-3}	1.099
22 < Pressure	2.197×10^{-13}	1.181×10^{-3}	0.468

% RH=70% & T=60°C

	w_a	w_c	f_{val}
Pressure < 12	3.653×10^{-13}	1.116×10^{-3}	34.858
12 < Pressure < 22	3.085×10^{-13}	1.170×10^{-3}	2.974
22 < Pressure	2.709×10^{-13}	1.222×10^{-3}	1.351

% RH=100% & T=25°C

	w_a	w_c	f_{val}
Pressure < 12	8.081×10^{-16}	1.145×10^{-3}	28.811
12 < Pressure < 22	8.736×10^{-16}	1.211×10^{-3}	1.251
22 < Pressure	8.749×10^{-16}	1.262×10^{-3}	0.645

% RH=100% & T=40°C

	w_a	w_c	f_{val}
Pressure < 12	1.748×10^{-15}	1.105×10^{-3}	17.376
12 < Pressure < 22	1.507×10^{-15}	1.147×10^{-3}	2.448
22 < Pressure	1.279×10^{-15}	1.191×10^{-3}	3.151

% RH=100% & T=60°C

	w_a	w_c	f_{val}
Pressure < 12	4.088×10^{-15}	1.140×10^{-3}	71.541
12 < Pressure < 22	1.469×10^{-15}	1.292×10^{-3}	2.914
22 < Pressure	1.129×10^{-15}	1.416×10^{-3}	4.097

Modélisation de procédés électrochimiques de type PEM (Proton Electrolyte Membrane) pour le développement du vecteur Hydrogène

Actuellement, l'hydrogène est considéré comme un vecteur d'énergie prometteur. Cependant, il est préalablement produit par une électrolyse, une photo-catalyse, ou des procédés thermochimiques, biologiques. En suit une étape de stockage/conditionnement se réalisant par une compression, une liquéfaction, une physisorption ou une chimisorption. Enfin, la conversion quand elle est électrochimique, a lieu dans les piles à combustible. L'hydrogène remplit les principales caractéristiques pour atteindre les performances requises comme vecteur énergétique efficace, mais sa faible densité volumique reste un point faible. L'étape de compression reste nécessaire et doit avoir un rendement énergétique élevé. De plus, la purification est également essentielle notamment pour des applications comme la mobilité.

Le but de ce travail est d'étudier les dispositifs à électrolyte type membrane polymère (PEM : proton exchange membrane) que l'on retrouve fréquemment dans la filière hydrogène. Plus précisément, l'électrolyse de l'eau (PEMWE, Proton exchange Membrane Water Electrolysis) pour la production d'hydrogène et le compresseur/concentrateur électrochimique d'hydrogène (EHC, Eletrochemical Hydrogen Compressor) pour le stockage et la purification de l'hydrogène. Dans un premier temps, une étude préliminaire a été réalisée à l'aide d'un modèle adimensionnel analytique en régime permanent. Ce dernier a été appliqué aux cellules d'électrolyse fonctionnant avec un gradient de pression important. Cette approche permet l'estimation des performances à l'aide de trois nombres adimensionnels qui sont régi par la cinétique électrochimique au niveau de la couche active et le transport de matière dans la membrane. Les nombres adimensionnels sont : (i) un nombre de type Wagner à l'anode et à la cathode qui représente le rapport entre la conductivité protonique et la cinétique électrochimique au niveau de la couche active, (ii) un nombre similaire au module de Thiele au niveau des couches actives qui décrit la conductivité protonique effective et la densité de courant opérationnel, (iii) un rapport sans dimension décrivant le processus de transport de l'eau à travers la membrane. Le modèle a été appliqué à l'électrolyse de l'eau et le modèle est en bonne adéquation avec les résultats expérimentaux.

Dans un second temps, une étude expérimentale de compression et de purification à l'aide d'une cellule EHC a été mise en œuvre. Lors de ces tests, la compression a été effectuée entre 0 et 30 bars pour différentes températures et humidité relative. De plus, une mesure par spectroscopie d'impédance électrochimique (SIE) a permis de caractériser la cellule EHC. Ces expériences ont été menées pour deux alimentations : hydrogène pur et un mélange d'hydrogène/azote. Grâce à l'analyse d'entropie des résultats expérimentaux et la caractérisation post mortem à l'aide de l'imagerie MEB et des spectres IRTF, il a été constaté que l'azote n'est pas inerte lors du processus électrochimique. De manière

surprenante, la présence de N_2 peut conduire à la dégradation de la membrane due à la synthèse locale de NH_3. Enfin, un modèle de spectroscopie d'impédance électrochimique (SIE) a été développé. La SIE est une méthode de caractérisation puissante qui inclue à la fois des approches théoriques et expérimentales en décrivant les différents processus physiques et électrochimiques dans un système complexe. Le modèle analytique monodimensionnel développé en régime dynamique permet de caractériser les phénomènes prenant place aux électrodes d'une cellule EHC. Cette méthode permet de mettre en évidence les processus limitants et de prédire les artefacts.

1. Modélisation des cellules à membrane électrolytique polymère (état d'équilibre, modélisation en courant continu)

Dans cette section, les différentes hypothèses formulées et équations utilisées seront présentées. L'objectif est d'obtenir un ensemble d'équations qui peuvent être résolues de manière analytique et de manière adimensionnelle. Dans le cadre de cette modélisation, le gradient de la teneur en eau est négligé dans la couche de diffusion et la couche active, le gradient des espèces électro actives (H_2, O_2) l'est également. Par conséquent, aucun bilan de matière n'est réalisé dans ces couches et on suppose que la teneur en eau est constante dans les couches actives. Par conséquent, la couche de diffusion n'est pas incluse dans ce modèle. Cette description phénoménologique est basée sur les bilans dans deux domaines : bilan de matière et bilan de charge dans la membrane et bilan de charge dans les couches actives.

Le modèle est monodimensionnel et considéré comme fonctionnant en régime permanent ($\frac{d}{dt} = 0$).Les couches actives et la membrane sont supposées isothermes. La chute ohmique dans la membrane est considérée comme étant uniquement due à la résistance protonique.

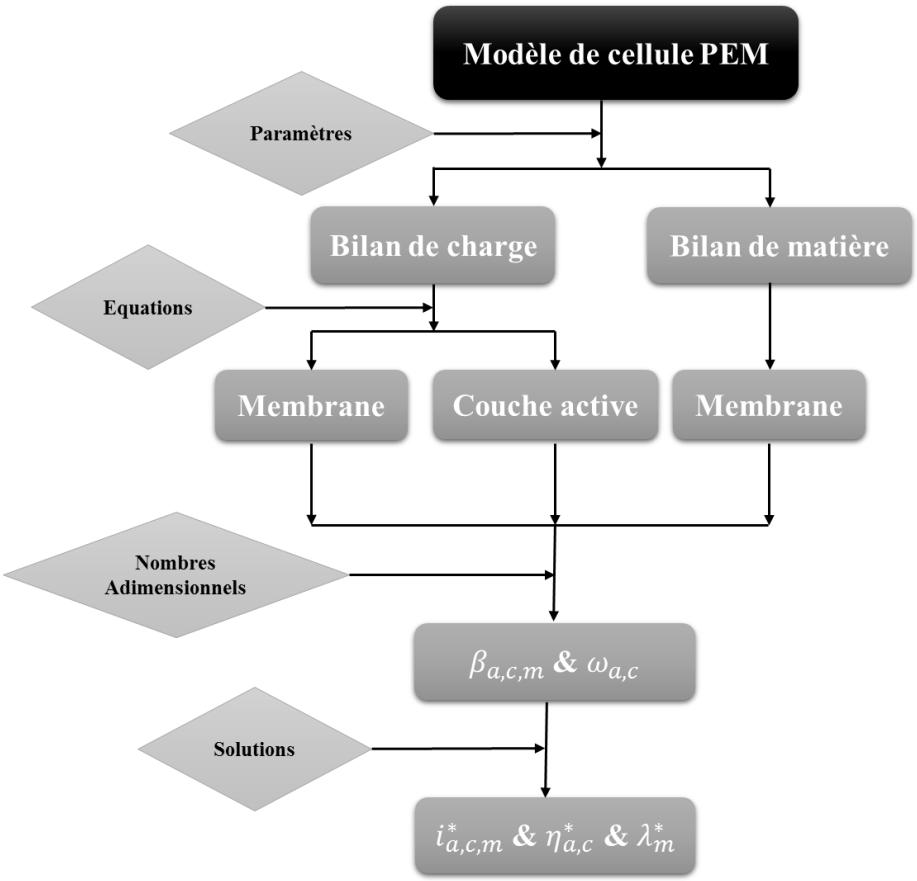

Figure 1.1 : Équations du modèle de cellule PEM et étapes de résolution

Comme le montre la Figure 1.1, le modèle repose sur plusieurs paramètres (conditions opératoires, géométrie de la cellule et caractéristiques du matériau). Les équations sont établies pour le bilan de matière dans la membrane et le bilan de charge dans la couche active et la membrane. Ensuite, en adimensionalisant ces équations un nouveau modèle est déterminé. Cela permet de définir les nombres adimensionnels pertinents qui décrivent les différents phénomènes d'une telle cellule électrochimique. Enfin, les nouvelles équations seront résolues à la fois analytiquement et numériquement pour donner une solution mathématique de ce système.

Les différents nombres adimensionnels sont les suivants :

$$\beta_m = \frac{\delta_m}{D_{H_2O}}\left(\frac{\kappa_\Phi}{\mu} z_f c_f F \frac{J_0}{\sigma^m} + \frac{\kappa_p}{\mu}\nabla p\right) \quad (1)$$

$$\beta_{a,c} = \frac{\alpha_{a,c} J_0 \delta_{a,c} F}{2RT\sigma^{eff}_{H^+,a,c}} \quad (2)$$

$$\omega_{a,c} = \frac{\gamma_{a,c} i_{0,a,c} \delta_{a,c} F}{2RT_{a,c}\sigma^{H^+}_{a,c}} \quad (3)$$

1.1 Résultats de simulation appliquée à l'électrolyse de l'eau

L'approche sans dimension du PEMWE pressurisé n'a pas encore été proposée dans la littérature. Toutefois, trois régimes d'écoulement diphasique ont été mis en évidence [1] : un régime de bulles non coalescées (régime NCB) pour les petites densités de courant, un régime de bulles coalescées (régime CB) pour les densités de courant moyennes et un régime d'écoulement à poches et bouchons appelé "régime de slug flow" pour les densités de courant élevées. Les conditions aux limites de ce modèle 1D dépendent de ces régimes d'écoulement diphasique.

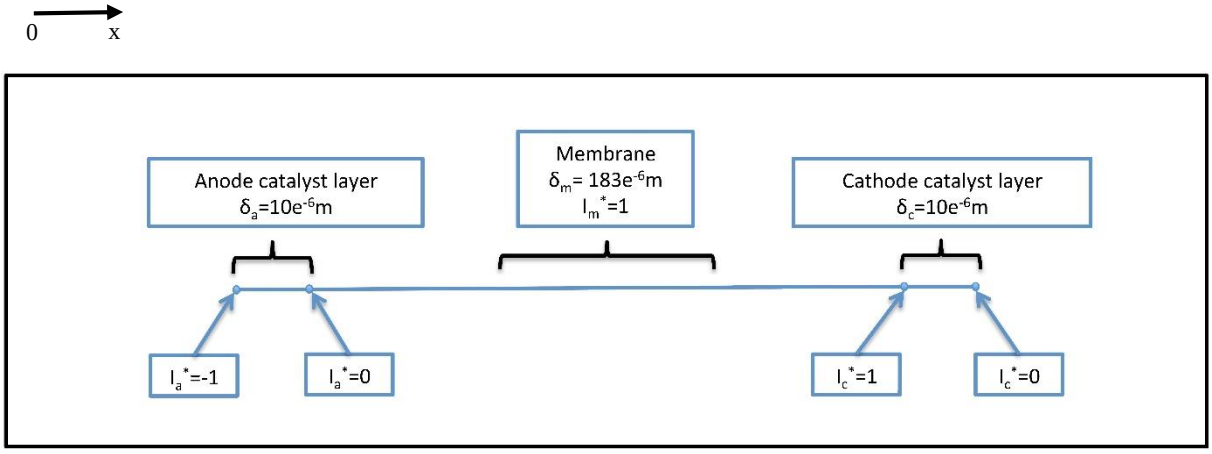

Figure 1.2: Représentation schématique unidimensionnelle de l'assemblage membrane électrode (MEA) d'une PEMWE avec $\delta_{a,c,m}$, les épaisseurs d'assemblage PEM classique

La Figure 1.2 montre la géométrie et les conditions limites de densité de courant sans dimension utilisées dans cette étude. Les couches de diffusion et les couches actives sont supposées complètement saturées en eau (cette hypothèse est largement admise pour le coté cathodique d'une PEMWE, c'est pourquoi seules les couches actives et la membrane sont représentées pour effectuer les bilans de charge et de masse.

- A l'anode

Comme indiqué dans les hypothèses du modèle, la couche anodique de diffusion et la couche active sont saturées d'eau, la teneur en eau de ces couches est donc constante et égale à la teneur en eau de saturation $\lambda_{a,c,m}^{sat}$. Cette teneur en eau à l'anode dépend des conditions de fonctionnement telles que le régime d'écoulement et les paramètres topologiques de la membrane. Selon des travaux expérimentaux [2], à l'interface canal/électrode, la teneur en eau de saturation apparaît en fonction du régime d'écoulement des bulles dans le canal anodique. On émet l'hypothèse que de faibles gradients de température dans la couche active impliquent une condition de non-équilibre dans la couche active parce que l'effet de refroidissement du flux d'eau pendant l'électrolyse est bloqué par de fines bulles comme un mince film de gaz. Par conséquent, de grosses bulles peuvent créer un renouvèlement d'eau dans la couche active : deux valeurs de saturation apparentes sont possibles $\lambda_a = \lambda_a^{sat,liq} = 22\ ou\ \lambda_a = \lambda_a^{sat,vap} = 18$.

- A la cathode

Au niveau de la cathode, on peut appliquer le même raisonnement. Dans le cas d'une cathode hydratée : $\lambda_c = \lambda_c^{sat,liq} = 22\ ou\ \lambda_c = \lambda_c^{sat,vap} = 18$.

Les paramètres choisis pour la simulation dans le cas de cette application sont les suivants (**Tableau 1**):

Tableau 1: Paramètres du modèle

Paramètre	Valeur
$\boldsymbol{T}$	58°C
$\boldsymbol{\delta_m}$	183.10-6 m
$\boldsymbol{F}$	96485 C.mol-1
$\boldsymbol{D_{H_2O}}$	3.10-10 m².s-1
$\boldsymbol{R}$	8.31
$\boldsymbol{\kappa_\Phi}$	1.13.10-19 m²
$\boldsymbol{\mu}$	3.565.10-4 kg.m-1.s-1
$\boldsymbol{z_f}$	1
$\boldsymbol{c_f}$	1.2.10-11 mol.cm-3
$\boldsymbol{\kappa_p}$	1.58.10-18 m²
$\boldsymbol{\sigma_{H^+,k}^{eff}}$	$(0.005139.22 - 0.00326) * exp(1268 * (\frac{1}{303} - \frac{1}{T}))$
$\boldsymbol{\delta_c}$	10-6 m

1.2 Distribution de la densité de courant ionique adimensionnel dans la couche active :

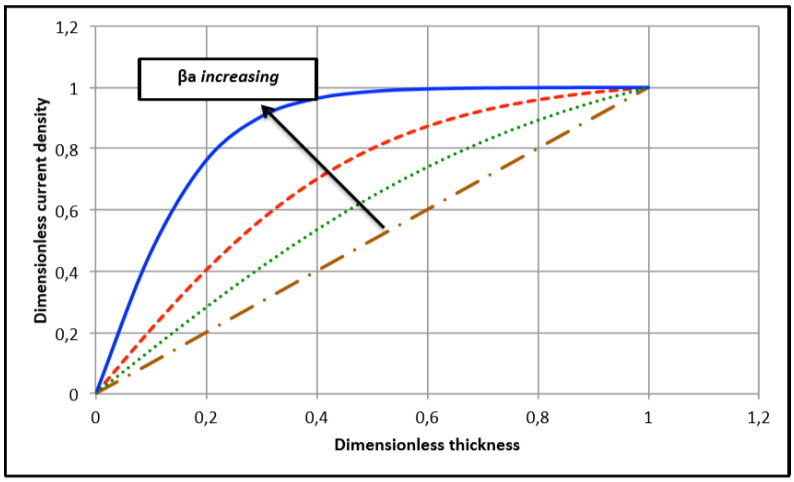

Figure 1.3: Distribution de la densité de courant adimensionnel pour β_a= 0,01 [---] ; β_a= 1 [-] ; β_a= 5 [- -] ; β_a= 10 [-] à la température ambiante et à la pression atmosphérique

La Figure 1.3 présente la distribution de la densité de courant du côté de l'anode en fonction de β_a. À mesure que β_a diminue, la distribution de la densité de courant dans l'épaisseur de l'électrode devient plus linéaire.

Ce résultat analytique montre que la valeur de β_a (2) estimé à partir de la conductivité protonique effective et la densité de courant (imposé par les conditions opératoires), affecte la distribution de la densité de courant ionique au niveau de la couche active.

Par conséquent, la couche active produit plus de courants faradiques sur toute son épaisseur à une densité de courant élevée (ce résultat est trivial). Le même résultat est également valable pour une faible conductivité ionique. Le rapport entre le courant appliqué et la conductivité ionique effective détermine donc les performances de l'anode. L'évolution de ce rapport (et de β_a) peut révéler les conditions de fonctionnement optimales de l'anode pour une température et une épaisseur de catalyseur données.

1.3 Conclusion : Modèle analytique

Cette approche, réalisée sur un modèle analytique sans dimension de PEMWE, permet de trouver les trois paramètres qui ont régi la réaction électrochimique au niveau de la couche active et le transport de masse à travers la membrane, à savoir les nombres de Wagner $\omega_{a,c}$ du côté de l'anode et de la cathode, $\beta_{a,c}$ des couches actives, et le rapport adimensionel du transport de l'eau à travers la membrane β_m.

Les données expérimentales, réalisée en collaboration avec Electrochemical Innovation Lab (EIL) à University College London (UCL), ont montré un bon accord avec les simulations. De plus, les calculs ont permis d'obtenir des solutions analytiques de la teneur en eau de la membrane, des surtensions et de la distribution de la densité de courant dans la membrane et les couches actives. Cette approche offre un outil adapté à l'étude la gestion de l'eau. La dépendance de l'hydratation de la membrane, de la surtension totale sur le nombre de Wagner $\omega_{a,c}$ et β_m a été estimé, ce qui permet d'évaluer la performance du système PEMWE.

La réduction exponentielle des nombres de Wagner au niveau de la couche active de l'anode, $\omega_{a,}$ montre l'impact du slug flow sur le rendement des cellules à haute densité de courant. Ce résultat semble montrer que la réaction électrochimique est fortement affectée par la génération du gaz pour les densités de courant élevées. En outre, cette approche est originale et constitue une méthode aisée à utiliser qui facilitera l'analyse expérimentale. Cette solution analytique d'un modèle adimensionnel a de nombreuses applications pour l'optimisation des performances des cellules :

- La capacité de calcul rapide de ce modèle adimensionnel fournira une grande quantité de données pour le « *deep learning* »
- Le modèle est adapté à la méthode avancée de contrôle des processus pour modéliser le contrôle prédictif (MPC)
- Cette approche peut être insérée dans une boucle de contrôle pour les méthodes de détection des défauts

2. Application expérimentale de cellules à membrane électrolytique polymère : Compression/concentration électrochimique d'hydrogène (ou purification)

La compression électrochimique de l'hydrogène est une technologie à fort potentiel : efficiente, respectueuse de l'environnement, nécessitant peu d'entretien et fonctionnant silencieusement, utilisée pour produire de l'hydrogène à haute pression [3].

Dans ce contexte, le compresseur électrochimique peut également servir de dispositif de purification, produisant de l'hydrogène pur [4].

En effet, le transfert de masse à travers la membrane ne permet que le transport sélectif de l'hydrogène, ce qui permet une purification simultanée à la compression. Malgré tous ces avantages, il reste quelques points à optimiser, comme la gestion de l'eau pour un taux élevé de compression/purification.

Cette partie se concentre sur l'examen de la compression de l'hydrogène pur et l'effet des impuretés telles que N_2 sur la cellule EHC pendant la compression/séparation d'un mélange de gaz N_2/H_2. Plusieurs mesures électrochimiques ont été réalisées afin d'observer le comportement de la cellule PEM pendant la compression.

Le travail a été effectué sur la plateforme de Hydrogen South Africa (HySA) à l'Université du Nord-Ouest (NWU), campus de Potchefstroom, en Afrique du Sud. [5].

Dans cette partie, on commence par présenter les dispositifs expérimentaux : le banc d'essai ainsi que la compression électrochimique de l'hydrogène en cellule unique. Suit la présentation des résultats de la compression de l'hydrogène pur. Pour ces expériences, une étude galvano statique a été utilisée et les conditions opératoires contrôlées (température, humidité relative, pression). En outre, une caractérisation par spectroscopie d'impédance électrochimique (SIE) a également été effectuée. Enfin, une discussion et une analyse des données sont effectuées, détaillant l'impact des impuretés d'azote sur le comportement de la cellule.

2.1 Dispositif expérimental : Compression électrochimique de l'hydrogène

Figure 2.1: Installation expérimentale de compression/séparation

La caractérisation électrochimique de la compression et de la séparation est caractérisée par une courbe courant-tension, des mesures galvano statiques et des mesures SIE (Figure 2.1). Ce banc a été utilisé pour les deux tests :

- Caractérisation de la compression avec de l'H_2 pur à différentes humidités, températures et pressions
- Caractérisation de la compression et de la séparation avec un mélange d'hydrogène (hydrogène dilué dans de l'azote) avec différentes humidités, températures et pressions

La compression électrochimique d'hydrogène (EHC) à cellule unique a été réalisée sur une membrane en Nafion® N1110 (δ=254 µm) avec une charge de catalyseur en platine (0,2045 ± 0,0065 mg Pt/cm²).

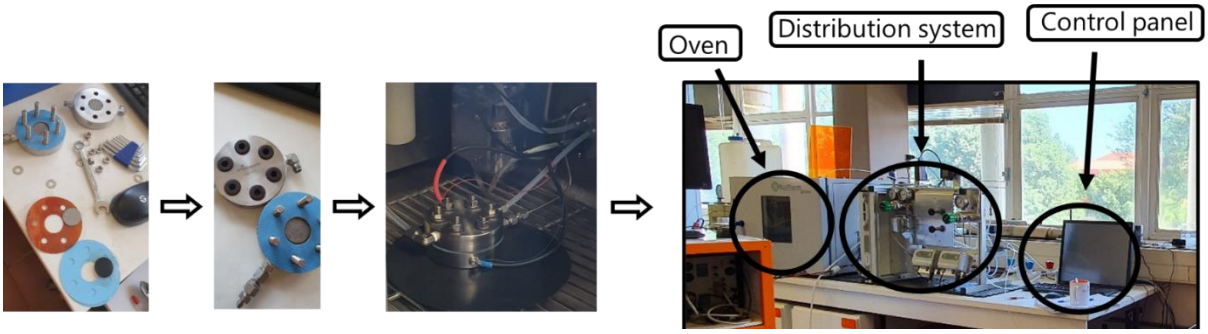

Figure 2.2: Installation expérimentale de compression électrochimique de l'hydrogène

La compression a été effectuée entre 0 et 30 bars. Pour des raisons de sécurité, le dispositif a été conçu pour atteindre une valeur de tension maximale de 600 mV lors des essais menés en mode galvano statique. La mesure par spectroscopie d'impédance électrochimique a été effectuée à l'aide d'un potentiostat Gamry avant et après chaque expérience de compression, la gamme de fréquences étant de [10^{-1} Hz – 3.10^{5} Hz]. Ces expériences ont été réalisées avec de l'hydrogène pur et un mélange

hydrogène/azote. Les expériences ont été réalisées pour trois températures imposées : 25°C - 40 °C - 60 °C et quatre humidités relatives : 20% - 40% - 70% - 100%. Habituellement, l'humidité relative était fixée le matin et les températures modifiées au cours de la journée. Un temps de stabilisation de 1h a été respecté avant chaque mesure. La cellule est scellée et placée dans l'enceinte et connectée à un humidificateur (Figure 2.2) pour contrôler l'humidité et la température.

Du côté de l'anode, ce système peut contrôler la température, l'humidité, la pression (jusqu'à 2 bars) et le débit massique de l'hydrogène ou du mélange gazeux qui est fourni à l'anode de la cellule ECH. Le système a également la fonctionnalité de contrôler la pression de la cathode (jusqu'à 30 bars).

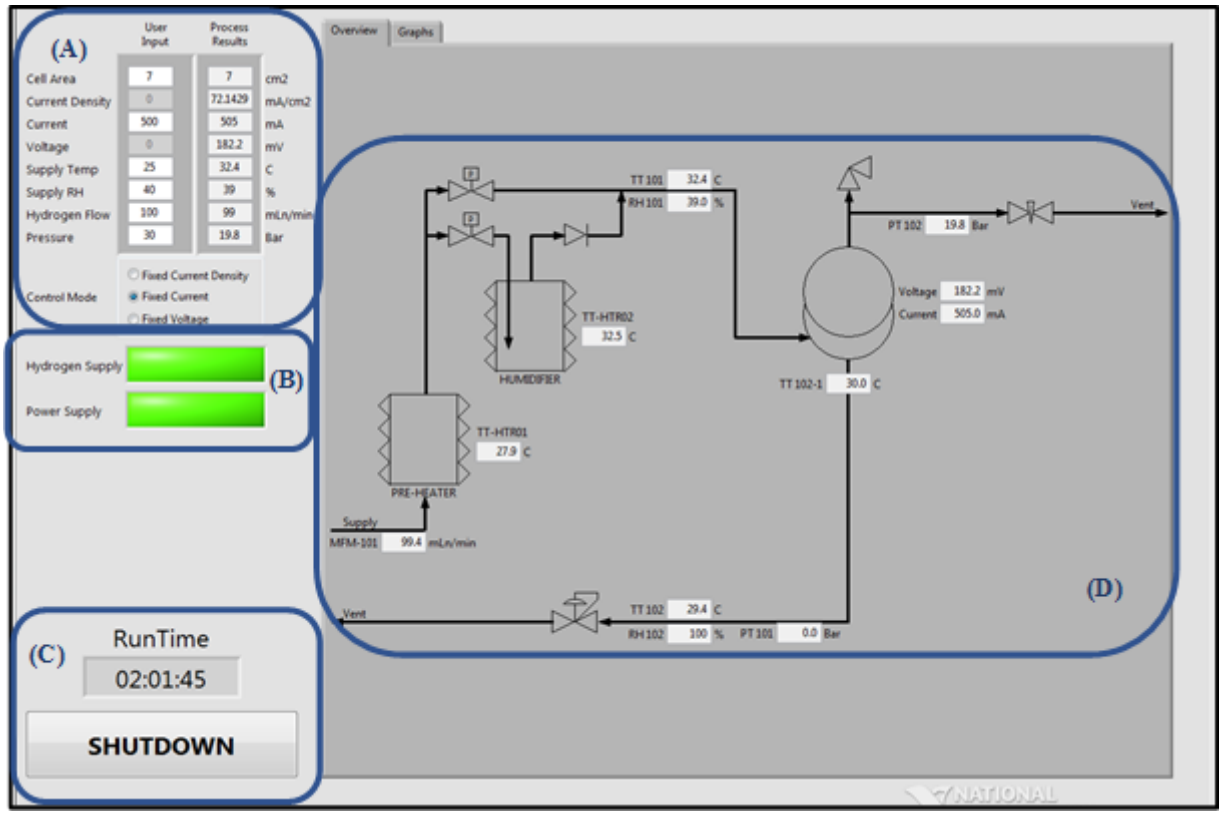

Figure 2.3: Panneau de contrôle LabView pour le dispositif expérimental

La Figure 2.3 montre le panneau de contrôle LabView, la partie (A) résume les conditions opératoires. Pour cette expérience, les conditions opératoires choisies sont rappelées dans le Tableau 2.

Tableau 2: Détails des entrées

Zone de cellule	7 cm^2
En cours	1500 mA
Tension maximale	600 mV
Température	25°C - 40 °C -60°C
RH	20% - 40% -70% - 100%
Débit d'entrée de l'hydrogène	100 NmL/min
Pression cathodique	10bars - 20bars - 30bars

2.2 Compression électrochimique de l'hydrogène : résultats

Dans cette section, les mesures de l'ECH sont discutées. Dans ce cas, les principaux phénomènes sont la diffusion des protons, la cinétique électrochimique, le transport de l'eau : diffusion, transport de pression électroosmotique et osmotique dans la membrane [2]. En effet, selon Dawn M. Bernardi et Mark W. Verbrugge [6] dans les dispositifs PEM, la gestion de l'eau et la température sont les paramètres clés. La gestion de l'eau affecte la conductivité des protons, et l'augmentation de la température améliore à la fois la cinétique de l'électro catalyseur et la conductivité de la membrane.

Ces expériences ont été effectuées pour des mélanges de gaz H_2 et N_2/H_2 purs (75 %/25 %). Pour les expériences sur les mélanges gazeux, la membrane N1110 Nafion® a dû être changée à mi-parcours en raison de sa dégradation et de son empoisonnement. Les mesures SIE ont été effectuées avant et après une compression à 30 bars. En raison du grand nombre d'expériences, la méthodologie proposée est

basée sur l'analyse de la résistance et de la SIE. Les analyses en ligne et post-mortem fourniront des indications complémentaires sur les processus qui se produisent dans les EHC.

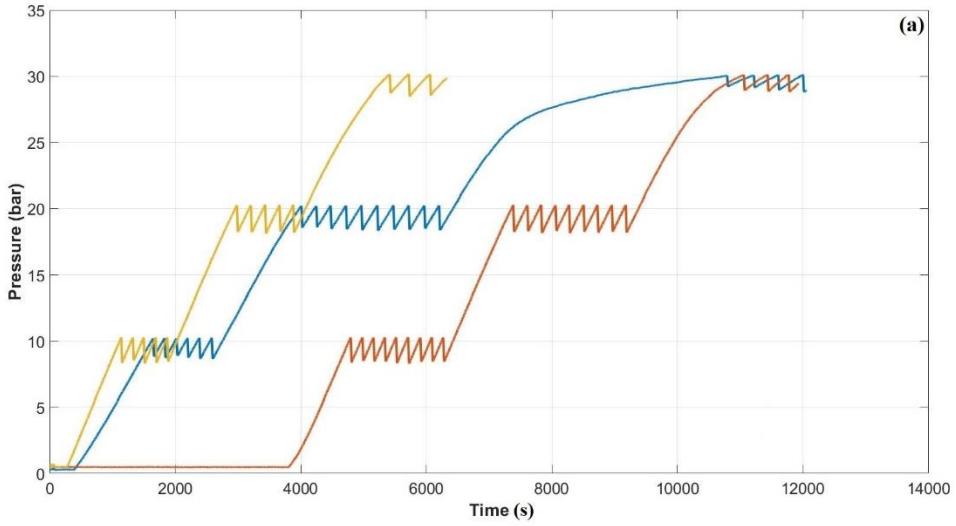

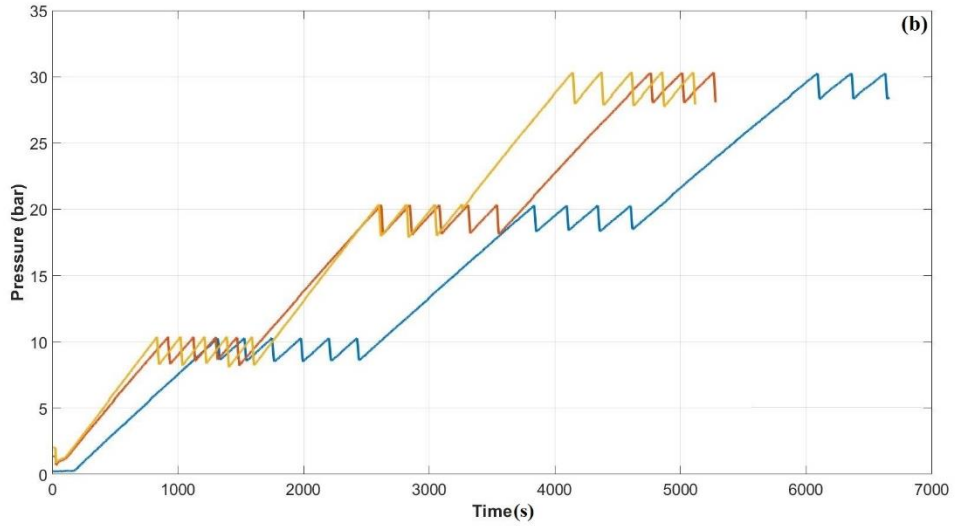

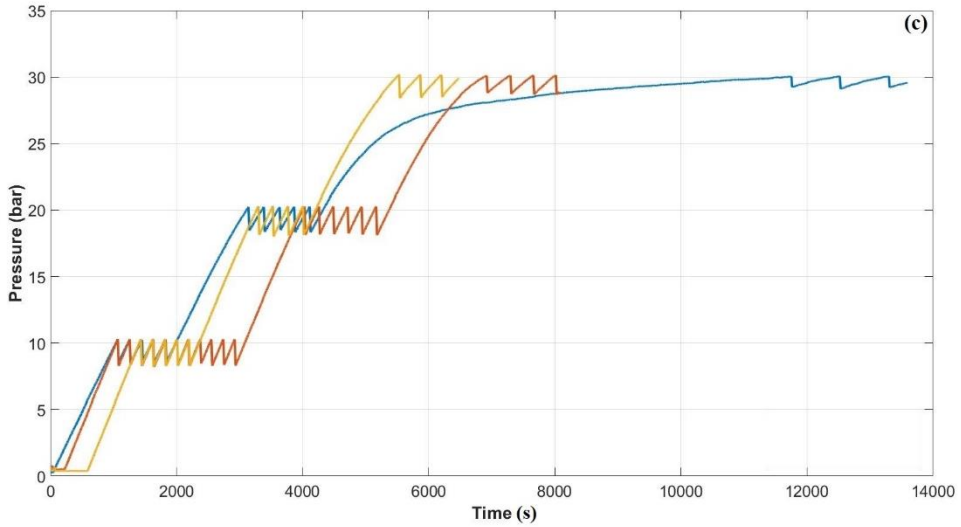

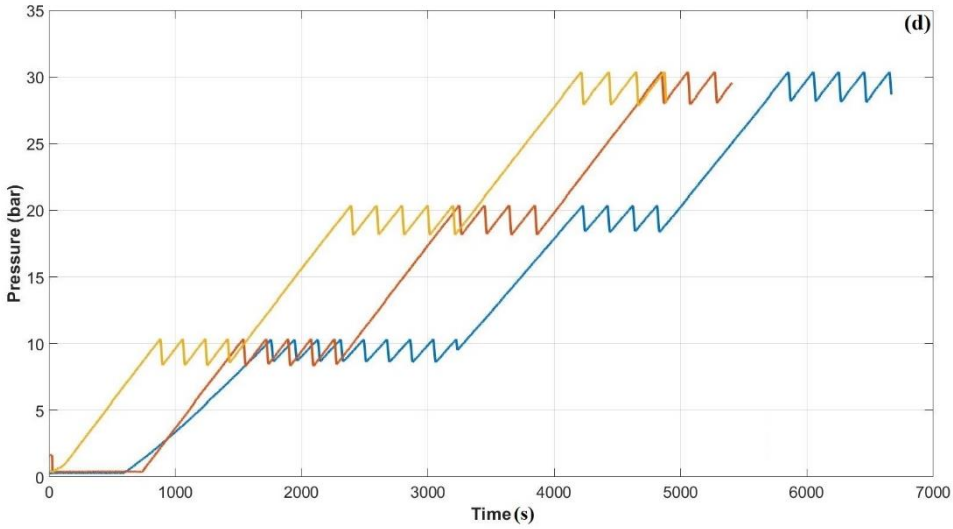

Figure 2.4 : Pression en fonction du temps avec une composition de gaz et une humidité relative et une température variables (T=25°C (---);T=40°C (---);T=60°C (---)) : (a) H_2 pur à HR 40% & (b) N_2/H_2 mélange gazeux à HR 40% & (c) Pur H_2 à HR 70% & (d) N_2/H_2 mélange gazeux à HR 70%

Dans la Figure 2.4, l'effet de la composition du gaz d'entrée n'a été observé que pour une faible humidité relative. Pour des raisons de sécurité sur le banc expérimental, la tension a été fixée à un maximum de 600 mV, il a été laborieux de fixer la pression proche de 30 bars à faible humidité avec un mélange d'entrée d'azote et d'hydrogène par rapport à l'hydrogène pur. D'autres essais ont donné des résultats similaires (Annexe B) : pour une HR > 20%, il a été enregistré que l'augmentation de la température semble avoir un effet positif sur la vitesse de compression. Le processus de séparation n'a pas affecté les performances de la compression puisque la cellule a pu atteindre 30 bars.

2.3 Conclusions

Cette étude a été réalisée en utilisant des membranes d'acide perfluorosulfonique (PFSA) avec un catalyseur supporté par du Pt/C. D'autres tests ont été effectués sur une membrane propre afin de mesurer la conductivité pour différentes épaisseurs à différentes températures et humidité relative (HR).

L'analyse a posteriori des données recueillies dans le cadre des expériences a principalement montré que

- La cellule a réussi à comprimer l'hydrogène jusqu'à 30 bars, qu'il s'agisse de H_2 pur ou d'un mélange gazeux (N_2/H_2).
- L'analyse de la résistance de la membrane a montré que la conductivité augmentait après la compression de H_2 pur, ce qui pourrait être dû à une meilleure humidification. Cependant,

aucune corrélation n'a été établie entre la résistance et l'humidification pendant la compression/séparation électrochimique du mélange gazeux (N_2/H_2).

- Une nouvelle méthode d'investigation de l'analyse de l'entropie utilisant la puissance moyenne de la cellule a été réalisée pour mettre en évidence l'effet du mélange gazeux sur la cellule en fonctionnement. Cela a révélé la possibilité d'un nouveau processus chimique.
- Les mesures de l'SIE ont montré que l'azote a un impact sur les performances de la couche de catalyseur lors de la compression électrochimique.
- Les analyses post mortem (MEB, spectroscopie IR) de MEA et GC en ligne ont confirmé la possibilité d'une électrosynthèse de NH_3. De plus, ces analyses ont montré un signe clair de contamination et de détérioration.
- Un test abusif avec une concentration plus élevée d'azote a révélé les difficultés de la capacité de la cellule à la fois à purifier l'hydrogène et à le comprimer.
- Une optimisation paramétrique a été réalisée à l'aide du deuxième modèle du chapitre 2, les valeurs des nombres de Wagner sont fournies à l'annexe B. Les résultats ont montré une augmentation du nombre de Wagner avec la pression. Ce comportement met en évidence la diminution de la résistance au transfert de charge en même temps que l'augmentation de la pression partielle. Cependant, il n'y avait pas de différence significative entre le H_2 pur et le mélange gazeux (N_2/H_2).

En conclusion, les différences de performances des EHC qui ont été étudiées en fonction de la concentration d'azote ne sont pas liées à la gestion de l'eau par la membrane. Le processus de séparation du mélange hydrogène/azote a affecté la résistance de la membrane. Cela s'est traduit par une faible augmentation de la résistance de la membrane. Le mélange hydrogène/azote impliquait une limitation supplémentaire concevable à l'interface membrane-électrode.

Références:

[1] F. Aubras *et al.*, « Two-dimensional model of low-pressure PEM electrolyser: Two-phase flow regime, electrochemical modelling and experimental validation », *Int. J. Hydrog. Energy*, vol. 42, nº 42, p. 26203-26216, oct. 2017, doi: 10.1016/j.ijhydene.2017.08.211.

[2] F. Aubras *et al.*, « Two-dimensional model of low-pressure PEM electrolyser: Two-phase flow regime, electrochemical modelling and experimental validation », *Int. J. Hydrog. Energy*, vol. 42, nº 42, p. 26203-26216, oct. 2017, doi: 10.1016/j.ijhydene.2017.08.211.

[3] M. Suermann, T. Kiupel, T. J. Schmidt, et F. N. Büchi, « Electrochemical Hydrogen Compression: Efficient Pressurization Concept Derived from an Energetic Evaluation », *J. Electrochem. Soc.*, vol. 164, nº 12, p. F1187–F1195, 2017, doi: 10.1149/2.1361712jes.

[4] G. Sdanghi, G. Maranzana, A. Celzard, et V. Fierro, « Review of the current technologies and performances of hydrogen compression for stationary and automotive applications », *Renew. Sustain. Energy Rev.*, vol. 102, p. 150-170, mars 2019, doi: 10.1016/j.rser.2018.11.028.

[5] « HySa Infrastructure ». https://hysainfrastructure.com/exchange_student/maha-rhandi/.

[6] D. M. Bernardi et M. W. Verbrugge, « Mathematical model of a gas diffusion electrode bonded to a polymer electrolyte », *AIChE J.*, vol. 37, nº 8, p. 1151-1163, août 1991, doi: 10.1002/aic.690370805.

Abstract: Modeling of Polymer Electrolyte Membrane devices for hydrogen energy carrier

Currently, hydrogen is considered as a promising energy carrier. However, it needs to be produced first using electrolysis, photo catalysis, thermochemical or biological processes. Then hydrogen is stored by compression, liquefaction, physisorption or chemisorption. Lastly, the conversion process occurs, which is based on using it as a product or a reactant in an application like Fuel Cells. Hydrogen fulfils the main characteristics to achieve the performance required for an efficient energy carrier, but its low volume density remains a weak point. An extremely high energy-efficient compression is a necessary step. On the other hand, the hydrogen purification step is also essential for several applications such as mobility.

The aim of this work is to investigate the Polymer Electrolyte Membrane (PEM) devices for hydrogen energy carrier. Specifically, PEM Water Electrolysis (PEMWE) for hydrogen production and Electrochemical Hydrogen Compressor/Concentrator (EHC) for hydrogen storage. First, a preliminary study was carried out using a dimensionless analytical steady state model of PEM electrolysis cells operating with large pressure gradients. This approach enables the estimation of performance using three dimensionless parameters that govern the electrochemical reaction at the catalyst layer and the mass transport through the membrane. The dimensionless numbers are: (i) a Wagner like numbers at the anode and cathode side which is the ratio between the protonic conductivity and the electrochemical kinetic at the catalyst layer, (ii) a number similar to Thiele modulus at the catalyst layers that describes the effective protonic conductivity and the operational current density, (iii) a dimensionless ratio describing the water transport process through the membrane. The model was applied to the PEMWE and it was in good agreement with the experimental data. Secondly, hydrogen compression and purification experiments were conducted using an EHC. During these tests, the compression was performed between 0 and 30 bars for different temperatures and relative humidity. In addition, an electrochemical impedance spectroscopy (EIS) measurement was also performed. These experiments ran on both pure hydrogen and hydrogen/nitrogen mixture. After the data entropy analysis and the postmortem characterization using FTIR and SEM imaging it was found that the azote is not a benign component for this application. Surprisingly, the N_2 can lead to the degradation of the membrane due to local NH_3 synthesis. Finally, an electrochemical impedance spectroscopy (EIS) model was developed. The EIS is a strong characterization method which inclines both theoretical and experimental approaches by modelling the different physics and electrochemical processes into a very complex system. The one-dimensional analytical model describes the electrochemical kinetics of the cell in the EIS regime. This method allows to highlight the limiting process and to predict the artefacts.

Keywords: Hydrogen, Polymer Electrolyte Membrane, Electrochemical Hydrogen Compression, PEM water electrolysis

---

Résumé : Modélisation de procédés électrochimiques de type PEM (Proton Electrolyte Membrane) pour le développement du vecteur Hydrogène

Actuellement, l'hydrogène est considéré comme un vecteur d'énergie prometteur. Cependant, il est préalablement produit par une électrolyse, une photo-catalyse, ou des procédés thermochimiques, biologiques. En suit une étape de stockage/conditionnement se réalisant par une compression, une liquéfaction, une physisorption ou une chimisorption. Enfin, la conversion quand elle est électrochimique et a lieu dans les piles à combustible. L'hydrogène remplit les principales caractéristiques pour atteindre les performances requises comme vecteur énergétique efficace, mais sa faible densité volumique reste un point faible. L'étape de compression reste nécessaire et doit avoir un rendement énergétique élevé. De plus, la purification est également essentielle notamment pour des applications comme la mobilité.

Le but de ce travail est d'étudier les dispositifs à électrolyte type membrane polymère (PEM : proton exchange membrane) que l'on retrouve fréquemment dans la filière hydrogène. Plus précisément, l'électrolyse de l'eau (PEMWE, Proton exchange Membrane Water Electrolysis) pour la production d'hydrogène et le compresseur/concentrateur électrochimique d'hydrogène (EHC, Eletrochemical Hydrogen Compressor) pour le stockage et la purification de l'hydrogène. Dans un premier temps, une étude préliminaire a été réalisée à l'aide d'un modèle adimensionnel analytique en régime permanent. Ce dernier a été appliqué aux cellules d'électrolyse fonctionnant avec un gradient de pression important. Cette approche permet l'estimation des performances à l'aide de trois nombres adimensionnels qui sont régi par la cinétique électrochimique au niveau de la couche active et le transport de matière dans la membrane. Les nombres adimensionnels sont : (i) un nombre de type Wagner à l'anode et à la cathode qui représente le rapport entre la conductivité protonique et la cinétique électrochimique au niveau de la couche active. (ii) un nombre similaire au module de Thiele au niveau des couches actives qui décrit la conductivité protonique effective et la densité de courant opérationnel, (iii) un rapport sans dimension décrivant le processus de transport de l'eau à travers la membrane. Le modèle a été appliqué à l'électrolyse de l'eau et le modèle est en bonne adéquation avec les résultats expérimentaux.

Dans un second temps, une étude expérimentale de compression et de purification à l'aide d'une cellule EHC a été mise en œuvre. Lors de ces tests, la compression a été effectuée entre 0 et 30 bars pour différentes températures et humidité relative. De plus, une mesure par spectroscopie d'impédance électrochimique (SIE) a permis de caractériser la cellule EHC. Ces expériences ont été menées pour deux alimentations : hydrogène pur et un mélange d'hydrogène/azote. Grâce à l'analyse d'entropie des résultats expérimentaux et la caractérisation post mortem à l'aide de l'imagerie MEB et des spectres IRTF, il a été constaté que l'azote n'est pas inerte lors du processus électrochimique. De manière surprenante, le N_2 peut conduire à la dégradation de la membrane due à la synthèse locale de NH_3. Enfin, un modèle de spectroscopie d'impédance électrochimique (SIE) a été développé. La SIE est une méthode de caractérisation puissante qui inclut à la fois des approches théoriques et expérimentales en décrivant les différents processus physiques et électrochimiques dans un système complexe. Le modèle analytique monodimensionnel développé en régime dynamique permet de caractériser les phénomènes prenant place aux électrodes d'une cellule EHC. Cette méthode permet de mettre en évidence les processus limitants et de prédire les artefacts.

Mots clés : hydrogène, membrane PEM, compression électrochimique d'hydrogène, électrolyse de l'eau PEM